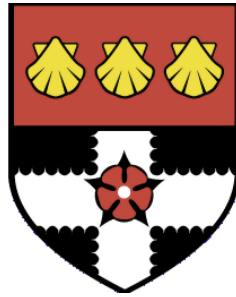


UNIVERSITY OF READING

Department of Meteorology



**On the Utilization of Aircraft
Derived Observations for
Operational Meteorology and
Numerical Weather Prediction.**

Andrew Karl Mirza

A thesis submitted for the degree of Doctor of Philosophy

January 2017

Declaration

I confirm that this is my own work and the use of all material from other sources has been properly and fully acknowledged.

This thesis contains extracts from the paper '*Comparison of aircraft derived observations with in situ research aircraft measurements,*' by Mirza, A. K.; Ballard, S. P.; Dance, S. L.; Maisey, P.; Rooney, G. G. and Stone, E. K. Published in the Quarterly Journal of the Royal Meteorological Society, John Wiley & Sons, Ltd, 2016.

My contributions to Mirza et al. (2016) are the original idea for the experiment, obtaining the experimental data and its subsequent analysis, wrote and prepared the paper for publication. I discussed my methods of analysis and my findings with my co-authors, who also reviewed drafts of the paper.

Andrew Karl Mirza

Copyright

© Andrew K. Mirza 2017 and Crown Copyright 2017.

Production of this thesis was part funded by the Met Office.

Abstract

This thesis analyses a new source of observations, Mode-Select Enhanced Surveillance (Mode-S EHS), obtained from reports exchanged between aircraft and air-traffic-control. These reports contain the aircrafts speed, direction, altitude and Mach number. Observations of temperature and horizontal wind can be derived from the reports. However, Mode-S EHS processing reduces the reporting precision from 16-bit to 10-bit representation. We aim to understand the observation errors that are due to the reduced precision of Mode-S EHS reports, how accurately these derived observations represent vertical profiles of wind and temperature and the benefit they bring to convection-permitting NWP.

We derive new models to estimate the observation errors and validate them using research grade instruments on board the Facility for Atmospheric Airborne Measurements. For the cases studied, the temperature observation error increases from 1.25 K to 2.5 K between an altitude of 10 km and the surface, due to its dependence on Mach number and Mode-S EHS precision. The zonal wind error is around 0.50 ms^{-1} and the meridional wind error is 0.25 ms^{-1} . The horizontal wind is also subject to directionally dependent systematic errors.

We aggregate Mode-S EHS reports from multiple aircraft to construct vertical profiles of temperature and demonstrate their ability to resolve temperature inversions. However, there are large errors in the aggregated observations that are still dominated by the effects of reduced precision.

We assess the benefits of Mode-S EHS for data assimilation in the Met Office convection-permitting NWP model. We find that assimilation of Mode-S EHS has a neutral impact. Using assimilation output statistics, we find that the observation uncertainties for AMDAR and Mode-S EHS horizontal wind are similar in magnitude, while for Mode-S EHS Mach temperature the diagnosed errors are similar to our new error model.

Our new results may assist with utilising Mode-S EHS reports in operational forecasting.

Acknowledgements

Firstly I would like to thank my academic supervisor Dr Sarah Dance, University of Reading, and to my Met Office supervisors Susan Ballard, MetOffice@Reading, Dr Gabriel Rooney and Dr Edmund Stone, Met Office, Exeter. Their support and guidance had been invaluable during this research.

Thanks also go to my colleagues at the Met Office, Exeter, Dr Paul Agnew, Dr Dave Jones, Dr Helen Wells, Dr Teil Howard and Paul Maisey for their support during the course of this research.

I would also like to thank the members of the Department of Mathematics and Statistics and the Data Assimilation Research Centre with whom I have had useful discussions.

Thanks must also go to my Mother and friends, David and Shan Mills, Mark and Camille Harrison, and Phil and Sue Lea, for their encouragement, support, tea and sympathy which have been a great help throughout the past few years. Without their support I could not have completed this work.

Finally I acknowledge the co-operation of National Air Traffic Services for providing Mode-S EHS data and the financial support of the Met Office and the Civil Aviation Authority.

Dedication

I dedicate this work to:

- the memory of my father, Raheem, and my brother, Adam;
- my mother, Eileen, who witnessed my joys, happiness, sorrows and frustrations encountered along my journey;
- my brothers: Antony, Lorne, Jason and Alan; and my sisters: Angela, Surriya, Nisa and Sofina, so that they can share in my achievement;
- my nieces: Jodi, Samantha, Stephanie, Sita, Natalie, Demi, Lydia and Charlotte; and my nephews: Devon, Aran, Daniel, Matthew, Benjamin, Thomas L., Robert, Thomas R., Jordan and Kristofer – let this work be a source of inspiration to you and to show you that with ambition and perseverance you too can achieve your goals;
- my friends Dave and Shan; Phil and Sue, for providing me with comfort and support;
- enfin, mes bons amis Mark et Camille, et leurs filles, Beatrice et Constance: deux étoiles scintillantes qui taient mon principal divertissement.

For me, this work marks the end of a long, long journey. Conceived during my darkest hour ...

[REDACTED]

*From 'The Love Song of J. Alfred Prufrock' By T. S. Eliot,
in Poetry: A Magazine of Verse (June 1915), pp. 130–135, Harriet Monroe (editor)*

impelled by my moment of spiritual faith

[REDACTED]

[REDACTED]

[REDACTED]

[REDACTED]

[REDACTED]

[REDACTED]

[REDACTED]

[REDACTED]

*From 'The Greater Thing' By Tom Godwin,
in Astounding Science Fiction (February 1954), pp. 108 – 132, John W. Campbell,
Jr. (Editor)*

to my enlightenment

[REDACTED]

[REDACTED]

*From 'The Hogfather' By Terry Pratchett,
Corgi Books (1997), pp. 421 - 423.*

Contents

List of Figures	v
List of Tables	ix
1 Introduction.	1
1.1 Motivation	1
1.2 Novel Observations	1
1.3 Numerical Weather Prediction	2
1.4 Thesis Aims	3
1.5 Principle Results	3
1.6 Thesis Outline	4
1.7 Data sets used in this study	6
2 Review of Meteorological Features, Aircraft-based Observations and Numerical Weather Prediction.	8
2.1 Introduction	8
2.2 Length Scales of Atmospheric Phenomenon	9
2.3 Temperature Inversions	9
2.4 Low-level Jets	12
2.5 In situ Observations	12
2.6 Introduction to Aircraft-based Observations	13
2.7 Mode Selective Enhanced Surveillance	15
2.8 Accuracy of Aircraft-based Observations	16
2.9 Numerical Weather Prediction Model Development	20
2.10 Limited Area NWP Model: UKV	22
2.11 Data Assimilation	25
2.12 3-D Variational Data Assimilation	27
2.13 Data Assimilation of Aircraft-based Observations	27

2.14	Summary	29
3	Initial Study on Utilising	
	Mode-S EHS Observations.	33
3.1	Introduction	33
3.2	National Air Traffic Services Secondary Surveillance Radar Mode-Select . .	34
3.3	Airport Domains	35
3.4	Deriving the Ambient Air-temperature from Mode-S EHS Reports of Mach Number and True Airspeed	37
3.5	Deriving the Horizontal Wind Vector from the Mode-S EHS Message	38
3.6	Aggregated Observations	39
3.7	Derived Vertical Profiles for Horizontal Wind and Temperature	41
3.7.1	Meteorological Conditions for the period 13 th to 15 th October 2012	41
3.7.2	Case Study: 14 th and 15 th October 2012, Aggregated Observations	47
3.8	Preliminary Analysis of Mode-S EHS Processing	48
3.9	Quantisation Error	51
3.10	Summary	53
4	Comparison of Aircraft Derived Observations with in situ Research Aircraft	
	Measurements.	55
4.1	Introduction	55
4.2	Facility for Atmospheric Airborne Measurements (FAAM BAe-146)	56
4.2.1	Aeronautical Radio Incorporated (ARINC) 429 Standard	56
4.2.2	The Mode-S EHS Message Format	57
4.2.3	Emulation of Mode-S EHS messages	59
4.2.4	Aircraft True Heading	60
4.3	Meteorological Research Measurements	61
4.4	Notation and Metrics	64
4.5	Quality of Derived Mach Temperature	66
4.5.1	Differences in T_{MACH} and T_{REF}	66
4.5.2	Estimated Error in T_{MACH}	66
4.6	Quality of Derived Horizontal-Wind Vector	71
4.7	Estimated Error in the Derived Horizontal-Wind Vector	75
4.8	Results Obtained for All Cases	82
4.9	Summary and Conclusions	87

5 Synoptic Meteorology and Distribution of Aircraft Observations for Case Studies.	91
5.1 Introduction	91
5.2 Summary of Meteorological Conditions 2 nd to 8 th January 2015	92
5.3 Meteorological Observations: Radiosondes	93
5.4 Numerical Weather Prediction Data: UKV	98
5.5 Met Office Mode-S EHS Receiver Network	99
5.6 Geographic Distribution of Aircraft	102
5.7 Aircraft-based Observations	105
5.8 Summary	107
6 Meteorological Information Contained in Mode-S EHS Derived Observations.	109
6.1 Introduction	109
6.2 Constructing Temperature Profiles using Mode-S EHS Reports	111
6.3 Time and Length Scales of Aircraft-based Observations	117
6.4 Derived Mode-S EHS Temperature Profiles	118
6.5 Low-pass-filters	126
6.5.1 Block-window average	127
6.5.2 Moving centred average	127
6.5.3 Linear regression	128
6.5.4 Exponential Moving Average	129
6.6 Time-series of Mode-S EHS Derived Mach Temperature	129
6.7 Variation in Mode-S EHS Derived Mach Temperature	136
6.8 Mach Temperature Differences	140
6.9 Temporal smoothing using low-pass-filters	142
6.9.1 Applying low-pass-filters to time-series of Mode-S EHS Reports	142
6.9.2 The Effect of Applying low-pass-filters to time-series of Mode-S EHS Reports	143
6.10 Estimating the Observation Error for Aggregated Mach Temperature	147
6.11 Summary and Conclusion	148
7 Assimilation of Aircraft Derived Observations using a Convection-Permitting Configuration of the Met Office Unified Model.	153
7.1 Introduction	153
7.2 Desroziers et al (2005) Diagnosis of Observation Errors	155
7.3 Experiment Design	157

7.3.1	Configuration of the UKV	157
7.3.2	Observation Operator	158
7.3.3	Observation Error Profiles	159
7.3.4	Mode-S EHS Observation Thinning	163
7.3.5	Quality Control	164
7.3.6	Trials of Data Assimilation Performance	164
7.3.7	Desroziers et al. (2005) Diagnostic Calculation	168
7.4	Results of Data Assimilation Experiments	172
7.4.1	Impact of Assimilated Mode-S EHS Observations on the Fit to Aircraft Observations	172
7.4.2	Impact of Assimilated Mode-S EHS Observations on the Fit to Non-aircraft Observations	173
7.4.3	Forecast Verification against Radiosonde	175
7.5	Diagnosed Observation Errors	179
7.6	Summary and Conclusions	186
8	Discussion and Further Work.	189
8.1	Summary of Results and Conclusion	190
8.2	Discussion of Results	191
8.2.1	Quality of Mode-S EHS Reports	192
8.2.2	Identifying Atmospheric Phenomena using Mode-S EHS Observations	193
8.2.3	Assimilation Experiments using Mode-S EHS Observations	195
8.3	Further work	196
	Appendix A Symbols and Abbreviations	199
	Bibliography	207

List of Figures

2-1	Idealised depictions of the temperature profiles.	10
2-2	Herstmonceux radiosonde temperature profiles showing radiation inversion.	11
2-3	Idealised evolution of the wind speed profiles for low-level jet.	13
2-4	Herstmonceux radiosonde windspeed profiles showing a low-level jet. . .	14
2-5	Illustration comparing development of spatial representation between the observation network and NWP limited area model for the UK. . . .	23
2-6	Domain of the Met Office UKV Numerical Weather Prediction Model. .	24
3-1	Location of NATS Secondary Surveillance Radars (SSR).	35
3-2	Horizontal domains for London Heathrow and London Gatwick with the airports at the centre of the domain.	36
3-3	Met Office Analysis Chart for NATS case study day.	42
3-4	Using NATS Mode-S EHS to construct temperature profiles for the London Heathrow domain.	43
3-4	continued from page 43	44
3-5	Using NATS Mode-S EHS to construct wind speed profiles for the London Heathrow domain.	45
3-5	continued from page 45	46
3-6	Time series plot of an aircraft track.	49
3-7	Analogue to digital conversion of continuous time-varying signals. . . .	50
4-1	Flight B787 (11 th July 2013) Vertical profile of reference temperature T_{REF} and derived Mach temperature	67
4-2	Vertical profile of the estimated error in the Mach temperature	69
4-3	Flight B787 (11 th July 2013) vertical profiles of box average statistics for temperature	70

4-4	Flight B787 (11 th July 2013) vertical profiles of the horizontal wind components.	72
4-5	Flight B787 (11 th July 2013) vertical profiles of the horizontal wind components difference between observed and derived.	73
4-6	Flight B787 (11 th July 2013) vertical profiles for the estimated error for the zonal wind component.	77
4-7	Flight B787 (11 th July 2013) vertical profiles for the box-average statistics for the effect of Mode-S EHS processing on the horizontal wind components.	79
4-8	Flight B787 (11 th July 2013) vertical profiles of the box-average statistics comparing measured and derived horizontal wind components.	80
4-9	Vertical profile of the box-average statistics for temperature (K) for all cases studied.	83
4-10	Vertical profile of the Mode-S EHS box-average statistics for horizontal wind components for all cases studied.	84
4-11	Vertical profile of the box-average statistics comparing Mode-S EHS processed with measured (REF) for horizontal wind components for all cases studied.	86
4-12	Systematic error related to the aircraft's heading.	88
5-1	Met Office surface analysis charts for case study days 3 rd and 4 th January 2015.	94
5-2	This sequence of significant weather charts shows the change in weather type for case study days 3 rd and 4 th January 2015.	96
5-3	Radiosonde vertical profiles for case study days 3 rd and 4 th January 2015.	97
5-4	The track of Herstmonceux 0600 UTC radiosonde, launched at 0530 UTC on 4 th January 2015	99
5-5	1-D column temperature profiles valid at 0600 UTC from the Met Office NWP UKV analysis at 0300 UTC 4 th January 2015	100
5-6	Spatial coverage of the Met Office Mode-S EHS receiver network.	102
5-7	Spatial distribution of aircraft on 4 th January 2015, 1200 to 1300 UTC for London Heathrow domain and London Gatwick domain.	104
5-8	Number of AMDAR (top panel) and Mode-S (bottom panel) EHS reports available for the data assimilation trials 0300 UTC 2 nd January 2015 to 0600 UTC 8 th January 2015.	106
5-9	Geographic distribution of observations from AMDAR and MODES for data assimilation trials.	107

6-1	Vertical profile of aggregated Mode-S EHS temperature for London Heathrow domain for altitude bin width 150 m	112
6-2	Vertical profile of aggregated Mode-S EHS temperature for London Heathrow domain for altitude bin widths 300 m and 75 m.	113
6-3	Histogram distribution of Mach Temperatures for different altitude bins.	115
6-3	Figure continued from page 115.	117
6-4	Horizontal sampling length scale along the aircraft's trajectory.	118
6-5	Mode-S EHS aggregated Mach Temperature vertical profiles for London Gatwick.	122
6-6	Mode-S EHS aggregated Mach Temperature vertical profiles for London Gatwick and London Heathrow domains at various times of the day. . .	123
6-7	Time-series plots of aircraft tracks that were present for the period 0530 to 0630 UTC in the London Heathrow domain on 4 th January 2015 . . .	132
6-8	Time-series plot of derived temperature for aircraft that were present for the period 0530 to 0630 UTC in the London Heathrow domain on 4 th January 2015	133
6-9	As for figure 6-7 except showing aircraft tracks as vertical profiles. . . .	134
6-10	As for figure 6-9	135
6-11	Scatter plot of True Airspeed v Mach number with the histograms showing the corresponding distributions for all aircraft ascents within the London Heathrow domain on 4th January 2015.	137
6-12	As for figure 6-11 except this is for aircraft descents.	138
6-13	Effect of applying a low-pass-filter on the Mode-S EHS reports of an aircraft track.	145
6-13	Figure continued from page 145.	146
6-14	Effect of applying low-pass-filter to the aggregated Mach Temperature. .	149
6-15	The effect of different low-pass-filter schemes on the (histogram) distribution of Mach Temperature reports.	150
6-15	Figure continued from page 150	151
7-1	Assumed observation error standard deviation, $\sigma_{A OBS}$, profiles for temperature and horizontal wind components as used in NWP models: UKV, HIRLAM and COSMO-KENDA	161
7-2	The mean observation-minus-background from observation monitoring of Mode-S EHS temperature for the period 2 nd to 8 th January 2015. . .	162
7-3	Time series of the total cost function at the start and end of data assimilation processing for the trials listed in table 7.3.	174

7-4	Assimilation cycle time series of the innovations and residuals at the start and end of data assimilation for 10 m horizontal wind component U and 2 m potential temperature.	176
7-5	Assimilation cycle time series of the innovations and residuals at the start and end of data assimilation for satellite and radar wind observations	177
7-6	Mean RMSE of forecast vertical temperature profile against radiosonde for data assimilation trials	180
7-7	Mean RMSE of forecast vertical wind profile against radiosonde for the data assimilation trials	181
7-8	Desroziers et al. (2005) diagnosed observation error standard deviation for horizontal u-wind component.	183
7-9	Desroziers et al. (2005) diagnosed observation error standard deviation for horizontal v-wind component.	184
7-10	Desroziers et al. (2005) diagnosed observation error standard deviation for temperature.	185

List of Tables

2.1	Summary of the results from previous studies on the root mean square accuracy of aircraft-based observations.	18
2.2	Summary of the results from previous studies on mean bias of aircraft-based observations.	19
2.3	Horizontal and vertical resolution for a selection of convection permitting numerical weather prediction models.	21
2.4	Extra observations used in the data assimilation processing for the Met Office limited area NWP model.	25
2.5	Observations Assimilated in each NWP Model used to evaluate Mode-S EHS observations.	29
2.6	Configuration of the NWP Models used for Data Assimilation of Mode-S EHS Observations.	30
4.1	Aircraft state parameters relevant for meteorological reporting using the ARINC-429 standard and for transmission by Mode-S EHS	58
4.2	Algorithm for Mode-S EHS processing.	60
4.3	Brief description of the six flights studied in chapter 4.	63
4.4	Accuracy of FAAM Aircraft Parameters.	64
4.5	Acceptance criteria used for filtering the FAAM aircraft data.	64
4.6	Notation used in chapter 4.	65
4.7	Outliers not displayed in plots shown in figure 4-5	74
5.1	World Meteorological Organisation present weather symbols used in significant weather charts shown in figure 5-2.	95
5.2	Mode-S EHS receiver locations for the Met Office network.	103
5.3	Quality control parameters used by the Met Office Mode-S EHS for gross error check	105

6.1	Statistics for histogram distributions shown in figure 6-3	116
6.2	The change in Mach Temperature is computed for discrete changes in Mach number at constant true airspeed and for true airspeed at constant Mach number.	141
7.1	List of technical trials for data assimilation of AMDAR and Mode-S EHS using the Met Office limited area model UKV-ps37.	169
7.2	Metrics for the technical trials for the data assimilation (DA) cycles 0300, 0600 and 0900 UTC for 2nd January 2015.	170
7.3	List of longer trials for data assimilation of AMDAR and Mode-S EHS using the Met Office limited area model UKV-ps37.	171
7.4	Met Office TRUI verification and comparison of forecasts from UKV trials, listed in table 7.3.	179

Chapter 1

Introduction.

1.1 Motivation

Weather impacts on airports are an important problem for society (Ball et al. 2007, Markovic et al. 2008, Barnhart et al. 2012). Fog and low visibility conditions reduce the capacity of airports as aircraft separations need to be increased to maintain safe operations. This increases costs in terms of the extra fuel that must be used, loss of revenue due to reduced capacity at airports, environmental impacts on local air quality and noise emissions, and climate impacts due increased emissions of nitrogen oxides and carbon dioxide (Mahashabde et al. 2011). Low level wind shear is a particular hazard to an aircraft that is ascending or descending (de Villiers & White 2014, Theodore & Caracena 1977). This may cause the pilot to lose control of an aircraft through insufficient acceleration during ascent or to descend too quickly. Therefore, observation monitoring and accurate forecasting of these weather phenomena is important to maintain safety of aircraft, minimise disruption to aviation operations and impacts on the environment.

1.2 Novel Observations

Radiosondes (World Meteorological Organisation 2008, Section 12.1.3) and Aircraft Meteorological Data Relay (AMDAR) (Stickland & Grooters 2005) are used to construct vertical profiles of the horizontal wind and temperature. These observations may provide relevant information but they are very infrequent. AMDAR reports are made hourly or 3-hourly but depend on the participation of airlines, which operate from specific airports. Radiosonde reports are made at 6-hourly or 12-hourly intervals. Their launch sites are determined by the requirements of the National Weather Service.

By contrast, observations derived from routine air-traffic communications (Boisvert & Orlando 1993), e.g., Mode-S EHS, are available at a high temporal-frequency, every 4 to 12 seconds, and have a high spatial-density, especially within the vicinity of major hub airports such as London Heathrow.

Mode-S EHS reports may be a useful source of wind and temperature observations (de Haan 2011), but this is an open question and forms the basis of this thesis. Recent studies by de Haan (2011) and Strajnar (2012) have shown that observations from Mode-S EHS are of similar quality to those obtained from AMDAR, which are routinely assimilated into numerical weather prediction (NWP) models. The advantage of Mode-S EHS over AMDAR and radiosondes is its higher temporal reporting, higher spatial density and lower operating costs. Furthermore Mode-S EHS reports may afford the opportunity to observe and classify the evolution of the boundary layer, the region of the atmosphere in which the adverse weather affecting airport operations tends to occur.

1.3 Numerical Weather Prediction

Forecasting wind is difficult since this requires an accurate representation of orography, surface characteristics, e.g., water, soil, grass, and the vertical temperature profile. These affect the horizontal wind speed and direction, and if these vary with height, can give rise to wind shear. A temperature inversion occurs where the temperature increases with height rather than decreases. The altitude, time of occurrence and its persistence may influence the formation and duration of low visibility conditions (Jacobs et al. 2005, 2008).

Weather forecasting uses a range of tools from routine observations to computer models of atmospheric phenomena. NWP models represent the state of the atmosphere in space and time. The NWP model is initialised using the best estimate of the atmospheric state known as an analysis (Daley 1991). The analysis is constructed through a process known as data assimilation which combines, in an optimal way, the last best estimate of the atmospheric state with the latest available observations (Kalnay 2003). NWP models represent atmospheric variables, such as temperature and wind, on a discrete grid and use a set of equations that describe physical dynamics to determine how these variables evolve over discrete intervals of time. However, a discrete system cannot fully represent a continuous system. So errors in the predictions increase due to uncertainties in the measured observations (Lorenz 1963) and the representativeness of the NWP model's state of the atmosphere (Daley 1991). Furthermore, mathematical modelling of some atmospheric variables is either incomplete or impractical so these

variables are parameterized which may result in systematic errors, e.g., the onset of convective turbulence within the boundary layer (Lock et al. 2000).

1.4 Thesis Aims

This thesis aims to address the following scientific questions about using Mode-S EHS derived observations:

1. How accurately do observations derived from routine messages exchanged between an aircraft and air-traffic-control represent the state of the atmosphere in terms of the horizontal wind and ambient temperature?
2. What atmospheric phenomena within the boundary layer can be observed using high-frequency observations derived from these routine messages?
3. What benefit does assimilation of these high-frequency observations bring to the Met Office’s convection-permitting numerical weather prediction model?

1.5 Principle Results

The principle new results of this thesis are:

- 1 (a) Mode-S EHS processing reduces the precision of the aircraft’s state vector from 16-bit to 10-bit binary representation. We derive novel error models and demonstrate that the reduced precision of the Mode-S EHS is a significant contributor to errors in the Mode-S EHS derived temperature.
- 1 (b) We use full precision data from research grade instruments, on board the Facility for Atmospheric Airborne Measurements (FAAM), to emulate Mode-S EHS reports and to compare derived observations with the research grade observations. We demonstrate the applicability of the new error models. We show the temperature observation error increases from 1.25 K to 2.5 K between an altitude of 10 km and the surface due to its dependency on Mach number and also Mode-S EHS precision. For the cases studied, the zonal wind error is around 0.50 ms^{-1} and the meridional wind error is 0.25 ms^{-1} . The wind is also subject to systematic errors that are directionally dependent.
- 2 (a) Constructing vertical profiles of temperature and horizontal wind using Mode-S EHS reports from multiple aircraft can reveal meteorological features, e.g., temperature inversion, that may assist operational meteorologists to forecast the onset and duration of hazardous weather that may affect aviation operations.

- 2 (b) The observation error standard deviation of Mode-S EHS observations combined from multiple sources has a similar structure as that shown for the observation error for a single source Mode-S EHS observations, which we showed in our earlier study using the FAAM research aircraft.
- 3 (a) The data assimilation of Mode-S EHS observations is shown to have a neutral impact on the forecasts from the Met Office’s high-resolution convection-permitting NWP model, UKV.
- 3 (b) The observation error standard deviation for Mode-S EHS derived temperature and horizontal wind was estimated using the statistics of observation-minus-background and observation-minus-analysis output from the UKV. It was found that the observation error standard deviation for Mode-S EHS horizontal wind is similar to that used for AMDAR in the current operational version of the UKV but the observation error standard deviation for Mode-S EHS temperature is underestimated. This is consistent with our earlier results, showing that the noise from Mode-S EHS processing makes a significant contribution to the observation error standard deviation.

1.6 Thesis Outline

The rest of this thesis is organised as described in this section.

In chapter 2 we provide background knowledge that will be used throughout this thesis. We review how we observe and model meteorological features of interest: the temperature inversion and the low-level jet (Roach et al. 1976, Brown & Roach 1976, Stull 1988). We introduce the current method of receiving aircraft-based observations (Stickland & Grooters 2005) and describe a new method for obtaining observations based on the aircraft’s Mode-S EHS state vector (de Haan 2011). Using previous studies (Benjamin & Schwartz 1999, Drue et al. 2008, Ballish & Kumar 2008), we provide an overview of the accuracy and precision of aircraft-based observations, assess the level of agreement between them, and their limitations. We cover briefly the trend towards high-resolution convection-permitting NWP models and describe the Met Office implementation of such an NWP model (Clark et al. 2016). We describe the process of data assimilation (Daley 1991, Kalnay 2003) which primes the NWP model for forecasting, and one implementation method: 3-D Variational (3-D Var) Data Assimilation. We compare and contrast previous data assimilation studies that have used Mode-S EHS reports (de Haan & Stoffelen 2012, Lange & Janjic 2016) and Mode-S MRAR reports (Strajnar et al. 2015), and assess their results. We conclude that data assimilation

processing relies upon an accurate representation of the observation and background errors. Misspecified errors can lead to an incorrect analysis and this would affect the subsequent NWP model forecasts. This chapter contains extracts from Mirza et al. (2016, sections 1 and 2).

In chapter 3 we undertake an initial study for utilising Mode-S EHS Observations, which addresses our second thesis question. We assess whether Mode-S EHS reports can be used to identify meteorological features of interest: a temperature inversion and a low-level jet. These features are associated with the formation of fog. The Mode-S EHS reports used in chapter 3 were supplied by National Air Traffic Services (NATS), which provide air navigation services for the United Kingdom. We show how we derive meteorological observations using these Mode-S EHS reports. Using Mode-S EHS reports from aircraft within the vicinity of London Heathrow and London Gatwick airports we construct vertical profiles of temperature and horizontal wind for the period 13th to 15th October 2012. We conclude that these profiles do show the meteorological features but are subject to noise. We show how quantisation error due to reduced precision may account for the observed noise. This chapter contains extracts from Mirza et al. (2016, sections 3.6 and 3.7).

In chapter 4, which addresses our first thesis question, we develop novel error models to quantify the noise due to the reduced precision. We validate these models using in situ observations made by a research aircraft. We conclude that the observation error in the Mode-S EHS derived temperature can be modelled using the statistics of quantisation error, which arises as a result of processing an analogue signal to a digital signal. The work presented in chapter 4 is published in Mirza et al. (2016, sections 3 to 7).

In chapter 5, we describe the synoptic meteorology for the period 2nd to 8th January 2015 used as a case study in later chapters. This period enjoyed calm weather conditions at the start which broke down at the end of the period as cold fronts swept in from the west bringing unsettled weather conditions. We use radiosonde observations and NWP data to show that meteorological features of interest were present: temperature inversions and low-level jets. We also describe the Met Office Mode-S EHS receiver network (Stone & Pearce 2016) and show how these reports are distributed spatially within the vicinity of London Heathrow and London Gatwick airports. The reports collected by this network are used to address our thesis questions which are the subject of chapters 6 and 7.

In chapter 6, which addresses our second and third thesis question, we revisit using Mode-S EHS reports to identify a meteorological feature of interest. The Mode-S EHS reports used in chapter 6 were collected and disseminated using the Met Office

network of ADS-B/Mode-S EHS receivers (Stone & Pearce 2016). We derive meteorological observations using Mode-S EHS reports from aircraft within the vicinity of London Heathrow and London Gatwick airports for the period 3rd January 2015 to 5th January 2015. This period was chosen because fog was a persistent meteorological feature. We construct vertical profiles of aggregated observations for horizontal wind and temperature. We compare these profiles with those obtained from AMDAR and radiosonde. We show that the observation standard deviation of aggregated Mode-S EHS derived temperature is similar to the statistics of quantisation error that we identified in chapter 4.

In chapter 7, which addresses our third thesis question, we evaluate whether assimilation of Mode-S EHS Mach Temperature and horizontal wind can improve the forecasts of a convection-permitting NWP model. For this we use the Met Office Unified Model at its 1.5 km configuration (Tang et al. 2013, Clark et al. 2016), with three dimensional variational data assimilation (Lorenc et al. 2000) using first guess at appropriate time (FGAT) (Lorenc & Rawlins 2005). We use the Desroziers et al. (2005) diagnostic to estimate the observation standard deviation error of AMDAR and Mode-S EHS reports for temperature and horizontal wind. We conclude that Desroziers et al. (2005) diagnosed observation standard deviation error may be characterised by the statistics of quantisation error that we identified in chapters 4 and 6.

In chapter 8 we summarise the work in this thesis. We draw conclusions from the new results seen throughout the thesis and suggest future work that may be carried out.

Appendix A contains the list of abbreviations, definition of terms and mathematical symbols used in this thesis.

1.7 Data sets used in this study

The Mode-S EHS data used in this thesis are obtained from two sources. The first source of data was provided by National Air Traffic Services for October 2012. This data was used to develop the software processing routines and quality control processes. However, this data was not used for data assimilation experiments. This was due to an upgrade of the Met Office numerical weather prediction suite control system. The upgraded suite control system was not backwards compatible to previous versions of the suite. It was also necessary to use the new suite control system so that development for data assimilation of Mode-S EHS reports for operational deployment could be undertaken. The second source of data was provided by the Met Office Mode-S EHS network. The nationwide network of Mode-S EHS receivers became operational in April

2015. However, for this thesis only a sample of data was provided for January 2015 from two receivers located in the South of England. Radiosonde and AMDAR reports were obtained from the Met Office Meteorological Observations Database (MetDB). Finally, in situ observations were obtained from the research aircraft the Facility for Atmospheric Airborne Measurements.

Chapter 2

Review of Meteorological Features, Aircraft-based Observations and Numerical Weather Prediction.

2.1 Introduction

To address the aims of our thesis outlined in section 1.4 (page 3) we need to have an understanding of the weather phenomena we wish to observe (temperature inversions, low-level jets), the current and new methods available to make aircraft based observations, and how the new observations may be used to predict the weather phenomena. This chapter will review each of these areas, providing an introduction and context for the new work in this thesis.

This chapter is organised as follows: in section 2.2 we describe the atmospheric length scale; in sections 2.3 and 2.4 we describe two atmospheric phenomena that we use in our case studies, the temperature inversion and low-level jet; in sections 2.5 to 2.8 we describe the sources for upper air observations and aircraft-based observations used in this thesis; in sections 2.9 to 2.12 we describe the NWP model and the method of data assimilation used in our studies; in section 2.13 we review previous studies for assimilation of aircraft-based observations; we end this chapter with a summary of prior work and the new work in this thesis. We acknowledge that sections 2.6, 2.7, 2.8 and 2.13 in this chapter are extracts from the paper published by Mirza et al. (2016).

2.2 Length Scales of Atmospheric Phenomenon

To study the structure of atmospheric phenomenon, ξ , it is assumed that its rate of change, $\frac{d\xi}{dt}$, is less than the corresponding sampling time t_s , i.e., the time it takes to make measurements of the atmospheric phenomenon (Stull 1988, Section 1.4), so that it appears ‘frozen’ with respect to the measuring system (Taylor 1938). Length scales of ξ are classified according to their length or time scales (Orlanski 1975). Atmospheric phenomena with length scales of the order of 1 m to 4 km have time scales of less than 30 mins, e.g, turbulent eddies, boundary layer convection, micro-bursts, thunderstorms, low-level jets; while those with length scales of the order of 4 km to 40 km have time scales of between 30 min and 24 hours, e.g., land-sea breezes, mountain valley breezes, complex thunderstorms, gravity waves (Orlanski 1975, Fujita 1986).

2.3 Temperature Inversions

In this section we define temperature inversions and describe the atmospheric conditions that give rise to them.

The ambient temperature at the surface is usually higher than the layer of air above it. This is because the influx of solar energy is absorbed mostly at the surface. The layer of air above the surface is heated through convection. Subsequent layers of air are also heated as a result of convection. In addition, as warm air rises it expands and cools (Barry & Chorley 2009, p.22). The effect of these processes cause the ambient temperature, T_A , to decrease as altitude, z , increases. The rate of decrease within the troposphere, the layer of atmosphere between the surface and 11 km, is given by $\Gamma = -\frac{dT_A}{dz}$ (Stull 2000, p. 46) and is called the environmental lapse rate.

The atmospheric conditions for a temperature inversion occur when the environmental lapse rate $\Gamma > 0$. The layer of air above the surface may be warmer than the surface itself or an intermediate layer of air may be warmer than the air above or below. This may arise when there is little vertical mixing in the atmosphere, i.e., the atmosphere is stable. Stable conditions are associated with anticyclonic conditions (high surface pressure), light winds and clear skies at night-time (Roach 1994). The characteristics and lifetime of a temperature inversion depends on the mechanism that gave rise to its formation, radiative cooling at the surface or compression as air descends towards the surface (Roach 1995*a*).

Radiation Inversion. A surface level temperature inversion may arise when the ground cools faster (that is the rate of radiant energy loss is greater) than the layer of air above it. The mechanism behind this cooling leads to the temperature inversion

being called a radiation inversion (Brown & Roach 1976). As the night-time progresses, heat conduction from the surface can create weak convection currents near the surface which may cause the height of the inversion layer to increase.

Subsidence Inversion. Stable conditions may also give rise to an elevated temperature inversion. As air descends from above towards the surface it is compressed, which causes an increase in the local ambient temperature. This results in a layer of air which is warmer than the layers of air above and below it. The mechanism behind this warming leads to such elevated temperature inversions being called subsidence inversion (Barry & Chorley 2009, Ch 9). Near the point of inversion droplet formation may arise leading to a layer of stratus cloud forming. The long-wave radiation emitted at the cloud base warms the air below and as a result suppresses the onset of fog formation at the surface.

Inversion by Advection. This occurs when either a warm (moist) mass of air is advected over a cooler surface or cold mass of (dry) air is advected over a warmer surface (Barry & Chorley 2009, Ch 9). The temperature inversion is present because of the temperature difference between the surface and the air mass being advected over it (Roach 1995*b*).

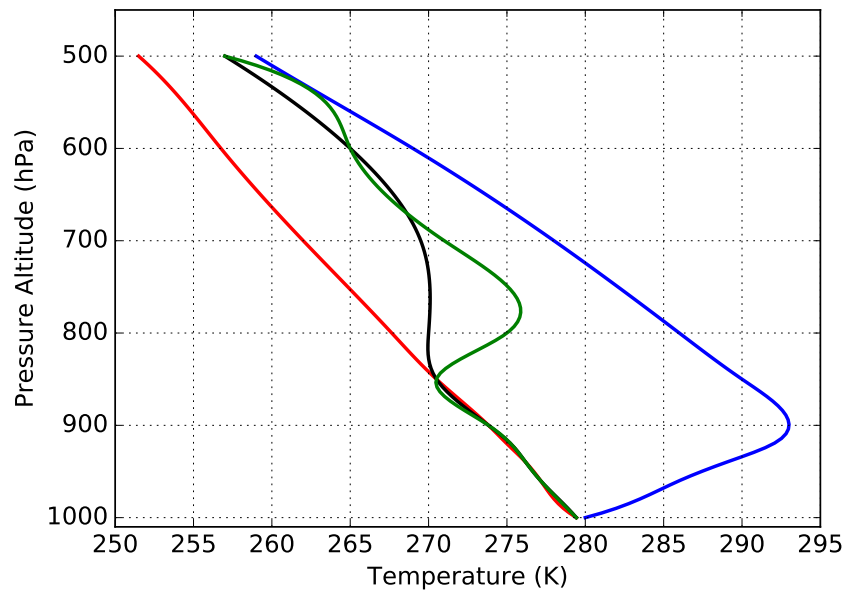


Figure 2-1: Idealised depictions of the temperature profiles for radiation inversion (blue), elevated inversion (green), isothermal region (black) and the expected lapse rate (red).

Figure 2-1 (page 10) shows four idealised lapse rates. The normal lapse rate is shown as the profile with a constant negative gradient. A radiation temperature inversion is

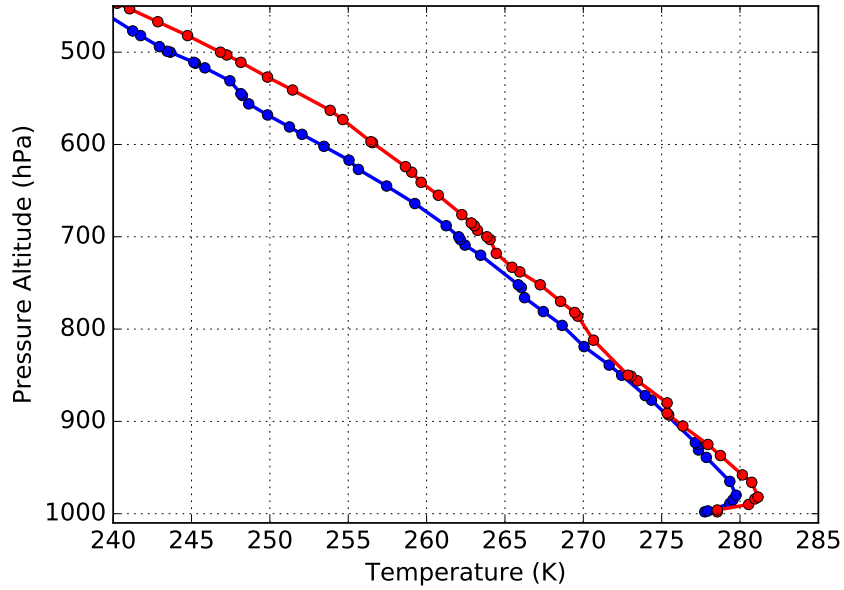


Figure 2-2: Radiosonde temperature profiles for Herstmonceux showing that surface level radiation inversion was present at 0000 UTC on 14th (blue) and 15th (red) October 2012.

characterised with a positive lapse rate from the surface, which continues for a short distance above the surface before turning to a negative lapse rate. The lapse rate for an elevated temperature inversion is similar to that of a radiation inversion except the positive lapse rate originates at a higher altitude. An isothermal region occurs when the lapse rate is undefined and the temperature remains constant for a change in altitude. Figure 2-2 (page 11) shows radiosonde temperature profiles between 0 m and 3000 m for Herstmonceux at 0000 UTC on 14th and 15th October 2012. It is clear that radiation inversions were present at Herstmonceux at these times.

Our characterisation of a temperature inversion follows Kahl (1990) and Andreas et al. (2000). The temperature inversion base, z_b , is the height above the surface where the environmental lapse rate stops decreasing (i.e. $\Gamma > 0$) and the height of the top, z_t , occurs where it begins to decrease (i.e. $\Gamma \leq 0$), where $0 \leq z_b < z_t$. The inversion depth is the vertical distance, $z_d = z_t - z_b$ and the inversion strength is $T_s = T_t - T_b$, where T_t and T_b are the ambient temperatures at z_t and z_b respectively. Thin layers, where $\Gamma < 0$ for a depth of ≤ 100 m which occur within the inversion depth, are ignored. It is assumed that these thin layers are embedded within the stronger inversion.

Temperature inversions are most likely to occur during the early hours of the morning or late at night, and are often the precursor to low visibility conditions and the formation of fog (Roach et al. 1976). The formation of fog has a significant impact

on aviation operations, in particular for the safe conduct of a flight and the rate of arrivals and departures at airports, as low-visibility procedures require greater aircraft separations. Therefore, forecasting the onset, dissipation and location of the conditions that lead to low visibility and fog is important. However, forecasting the conditions of fog depends on the availability of suitable observations (Jacobs et al. 2005, Fowler et al. 2012).

2.4 Low-level Jets

A consequence of the formation of a temperature inversion is the formation of a low-level jet (LLJ), which occurs above the temperature inversion, and is a zone of wind shear (Blackader 1957, Thorpe & Guymer 1977, Stull 1988). Stull describes a low-level jet as ‘*a stream of fast moving air with speeds of 10 ms⁻¹ to 20 ms⁻¹ usually located between 100 m and 300 m above the surface,*’ (Stull 1988, p. 520) but can be found with speeds of up to 30 ms⁻¹ at altitudes of 900 m. Stull (1988, p. 521) defines a low-level jet to occur whenever there is a relative maximum wind speed that is 2 ms⁻¹ faster than the wind speed above, within the lowest 1500 m (approximately 850 hPa). Figure 2-3 (page 13) (adapted from Malcher & Kraus 1983, Fig. 1a) shows the ideal evolution of a low-level jet from the early evening (1800 hours), midnight (0000 hours), early morning (0600 hours) and noon the following day (1200 hours). A low-level jet has formed at an altitude of 390 m by midnight. It is still present at an altitude of 390 m by early morning and it has decayed by noon the following day.

Figure 2-4 (page 14) shows the wind speed profiles between the surface and 1500 m for 0000 UTC on 14th and 15th October 2012 recorded by the radiosonde launched from Herstmonceux. On 14th October, while there is a peak in wind speed at 700 m, this is only 1 ms⁻¹ faster than the wind speeds above, so by Stull’s definition this is not a low-level jet. On the 15th October we suggest that there is a low-level jet at 900 hPa. There is a local wind speed maximum of 11.5 ms⁻¹ at this level and the wind speeds above this level decrease to about 9.0 ms⁻¹.

2.5 In situ Observations

The main source of vertical profiles of temperature and horizontal wind speed below 1500 m is from radiosonde launches. A radiosonde is a small package containing sensors. It is launched using a helium filled balloon. As it rises through the atmosphere it transmits data about the in situ atmospheric pressure, temperature, humidity, the elapsed time since its launch and its location. On the ground the radiosonde data are

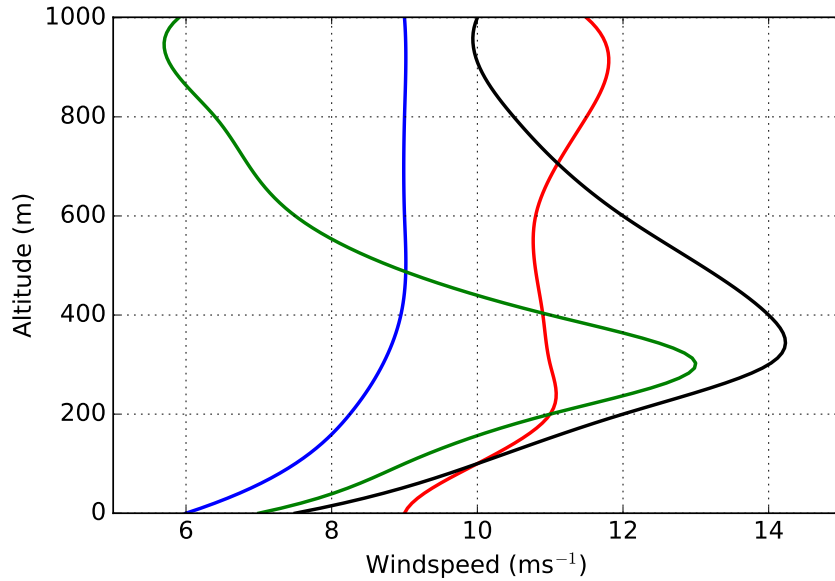


Figure 2-3: Idealised evolution of the wind speed profiles for low-level jet (adapted from Malcher & Kraus 1983, Fig 1a.) at early evening (blue), midnight (green), early morning (black) and noon the following day (red). low-level jet occurs in the region of the atmosphere where there is a local maximum of wind speed that is 2 ms^{-1} greater than the wind speed higher up (Stull 1988, p. 521).

post-processed, the horizontal wind is derived from the tracking data of position and time. Radiosondes are launched from fixed sites that are separated by long distances (approximately 100 km) and at fixed times, usually 0000 UTC and 1200 UTC. Therefore radiosonde observations may not provide sufficient spatial and temporal resolution to capture the evolution of a temperature inversion (Fowler 2010, section 1.2).

In this thesis we will use a case study period for when low visibility conditions were present in the South of England. In chapter 6 (page 109) we will look at the period 3rd January to 5th January 2015. During this period fog affected airport operations at London Heathrow and London Gatwick. The foggy conditions imply that a temperature inversion was present.

2.6 Introduction to Aircraft-based Observations

Aircraft-based observations are another source of in situ observations. The current method of receiving aircraft-based observations commonly used in NWP is from the Aircraft Meteorological Data Relay program (AMDAR) (Stickland & Grooters 2005). AMDAR reports the horizontal wind and ambient temperature obtained from the aircraft's flight management systems (FMS) (Painting 2003). These reports are compiled

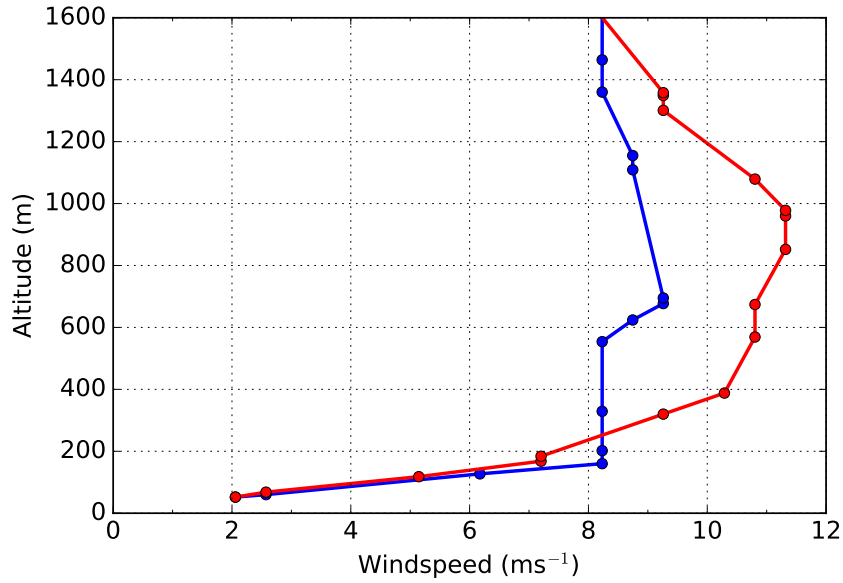


Figure 2-4: Radiosonde windspeed profiles for Herstmonceux showing that at 0000 UTC on 14th October (blue) there is no indication for the presence of a low-level jet at an altitude of 700 m. At 0000 UTC on 15th October (red), a low-level jet appears to be present at altitude of 900 m since there is a local maximum which is 2 ms⁻¹ greater than wind speeds above.

on-board the aircraft and are transmitted to a ground station. The frequency of transmission depends on the phase of flight and whether the aircraft is configured to send a report. By default, during ascent reports are every 6 seconds for the first 90 seconds then every 20 seconds until level flight; during level flight reports are every 3 to 10 minutes; during descent reports are every 60 seconds (Painting 2003, p.32). In Europe this program is managed by E-AMDAR which provides to National Meteorological Services (NMS) only one vertical profile once every three hours from around 100 airports across Europe. The Met Office, the NMS provider for the United Kingdom, obtains one vertical profile once every hour at major airports. In Europe and the UK the reporting frequency of vertical profiles depends on the financial resources made available by the NMSs. This contrasts with Air Traffic Management (ATM) which can interrogate an aircraft's transponder at much higher frequency from a ground station using Secondary Surveillance Radar (SSR), a system which transmits coded messages to an aircraft's transponder and receives coded replies (Boisvert & Orlando 1993, ICAO 2010). Depending on the type of interrogation and transponder, the transponder sends back an aircraft's identification code (MODE-A), altitude information (MODE-C) and more detailed information (Mode-S EHS).

2.7 Mode Selective Enhanced Surveillance

Mode Selective Enhanced Surveillance (Mode-S EHS) is used by Air Traffic Management (ATM) to retrieve routine reports on an aircraft's state vector at a high temporal frequency (every 4 to 12 seconds). The aircraft's state vector consists of true airspeed, magnetic-heading, ground speed, ground heading, altitude and Mach number. Mode-S EHS reports can be used to derive estimates of the ambient air temperature and horizontal wind at the aircraft's location (de Haan 2011). These derived observations have the potential to give weather information on fine spatial and temporal scales. For example high-frequency reporting of vertical profiles of temperature and wind may provide extra information for use in numerical weather prediction (NWP) assimilation and nowcasting (Dance 2004, Rennie et al. 2011, Sun et al. 2014, Simonin et al. 2014, Ballard et al. 2016). Indeed, positive impacts assimilating Mode-S EHS data in regional NWP models have already been seen by several authors (de Haan & Stoffelen 2012, de Haan 2013, Strajnar et al. 2015, Lange & Janjic 2016). These are reviewed in section 2.13 (page 27). To maximize the potential of these data, it is important to understand the error characteristics of the derived observations.

The contents of Mode-S reports depend on what is requested by ATM and this varies from country to country (ICAO 2010). There are three types of reports from which meteorological observations may be obtained:

(a) Mode-S EHS reports contain information on the aircraft's state vector. This vector can be used to derive estimates of the air temperature and horizontal wind at the aircraft's location (Collinson, 2011, Ch. 6; de Haan, 2011).

(b) Mode-S Meteorological Routine Aircraft Reports (MRAR) contain temperature and horizontal wind observations computed by the aircraft's FMS (Strajnar 2012, Strajnar & Trojáková 2015).

(c) Automatic Dependent Surveillance Broadcast (ADS-B) (a sub-system of Mode-S EHS) contain aircraft position and altitude from which a horizontal wind vector (de Leege et al. 2012) and a mean layer temperature (Stone & Kitchen 2015) may be computed.

Whilst Mode-S MRAR provides direct reports of temperature and horizontal wind observations, the regulatory environment does not require aircraft or ATM to make such reports available. (In the United Kingdom, ATM does not poll for MRAR due to the lack of capacity of the communication downlink.) The most common report is the Mode-S EHS aircraft's state vector from which temperature and horizontal wind observations are derived.

To understand the error characteristics of aircraft-based observations previous stud-

ies, reviewed in section 2.8 (page 16), have compared AMDAR reports with observations made using radiosondes or other nearby aircraft (Schwartz & Benjamin 1995, Benjamin & Schwartz 1999, Drue et al. 2008). Similar studies have compared Mode-S EHS (de Haan 2011) and Mode-S MRAR (Strajnar 2012) also with radiosonde and nearby AMDAR reporting aircraft. However, observations are not co-located in time and space. Furthermore, studies by Ballish & Kumar (2008), Drue et al. (2008), de Haan (2011), Jacobs et al. (2014) indicate that aircraft reports have additional error sources that are aircraft-type specific and which affect the temperature and horizontal wind vector reports. While these studies provide useful information about the quality of aircraft-based observations, it is not clear how to partition the errors between the variability due to the aircraft, its instruments, data processing algorithms and the atmosphere.

2.8 Accuracy of Aircraft-based Observations

In this section we review previous studies that assessed the accuracy and precision of aircraft-based observations. We assess the level of agreement between them and summarize their limitations.

A number of studies have been performed to obtain estimates of the accuracy of aircraft-based meteorological reports. This has been done by comparing aircraft-based reports to nearby reports made by radiosonde and other reporting aircraft (Schwartz & Benjamin 1995, Benjamin & Schwartz 1999, Painting 2003, Drue et al. 2008, de Haan 2011, Strajnar 2012) or by comparison to NWP models (Cardinali et al. 2003, Ballish & Kumar 2008, de Haan 2011, de Leege et al. 2012). De Haan (2015) uses a triple collocation method with Doppler radar, sonic detection and ranging (SODAR) and NWP data. Tables 2.1 and 2.2 summarize the results of these studies for root-mean-square-error (RMSE) and mean-bias (MB) respectively, and show fairly consistent results between studies. In particular, De Haan (2011) concludes that the accuracy of Mode-S EHS derived horizontal wind, after pre-processing the aircraft state-vector, is comparable with similar reports from AMDAR but is less accurate when compared with radiosonde. Mode-S EHS derived temperature is less accurate when compared with radiosonde and AMDAR. In addition, the RMSE for temperature is twice as large as that for AMDAR. Strajnar (2012) concludes that the accuracy of Mode-S MRAR directly reported horizontal wind is comparable with similar reports from AMDAR but is less accurate when compared with radiosonde.

De Haan (2011) notes that for two successive Mode-S EHS reports, from a single aircraft and with a time difference of 4 s, the derived observations can exhibit large fluctuations. These fluctuations arise due to the precision of the reported Mach number

and true airspeed of 0.004 and 2 knots respectively. Using these precisions de Haan (2011, p.5) estimates the observation errors between two successive reports for the derived temperature to range between 2 K and 5 K, and for the horizontal wind, estimates errors in the range 0.5 ms^{-1} to 1.5 ms^{-1} . To reduce the effect of these fluctuations a pre-processing method is used.

The de Haan (2011) pre-processing method uses a combination of linear regression and a running average over a time window to smooth the time-series of an aircraft's reports of true airspeed and Mach number. The pre-processing uses a number of consecutive reports and a time window for the linear regression and running average which depends on the phase of flight: for ascents and descents 3 to 4 reports and 10 s while for level flight 12 to 15 reports and 60 s were used. In addition, heading corrections were applied to the aircraft's reported magnetic heading using the 'runway' method de Haan (2011). The runway method uses the 12-month mean difference between the aircraft's reported magnetic heading and the magnetic heading of the runway on which the aircraft touched down. The effect of the pre-processing reduces the difference between successive reports for derived temperature to an estimated 1 K to 2 K, and for the horizontal wind to an estimated 0.25 ms^{-1} to 1.0 ms^{-1} .

A number of other features of aircraft-based observation errors have also been identified. Temperature biases have been found to vary with altitude (Schwartz & Benjamin 1995, Benjamin & Schwartz 1999, Drue et al. 2008, Ballish & Kumar 2008), with errors decreasing as height increases. The large errors near the surface are thought to be due to extra mesoscale variability in the boundary layer and lower troposphere. Schwartz & Benjamin (1995), Drue et al. (2010) also found differences between temperature reports from ascending and descending aircraft, thought to be caused by changes in the aircraft's wing configuration. They may also be due to sensor response time or AMDAR processing of temperature data aboard the aircraft or some combination of the two. There is also evidence for temperature biases that are aircraft-type specific (Ballish & Kumar 2008). Drue et al. (2008) found systematic errors in the wind reports which appear dependent on the aircraft's heading and aircraft type; there are similar findings by de Haan (2011) and Jacobs et al. (2014). The horizontal wind errors are due to a directionally dependent systematic error. De Haan (2013) considered a Mode-S EHS error analysis with respect to NWP and found that heading corrections only affect wind-components transversal to the aircraft's direction of travel. De Haan (2011) introduced a heading correction based on landing aircraft. These values are comparable to the NWP-based corrections (de Haan 2013).

These previous studies have their limitations. For example, there are only one or two radiosonde launches per day, typically at 0000 UTC and 1200 UTC, at limited

Table 2.1: Summary of the results from previous studies on the mean accuracy of aircraft-based observations. The table shows estimates drawn from previous studies for the overall range of the root-mean-square-errors (RMSE) for wind-speed, wind-direction, wind-vector and ambient-temperature. An em-dash (—) symbol indicates the result was not stated.

Study	aircraft-based observations	verified against	horizontal separation (km)	vertical separation (km)	time difference	wind speed RMSE (ms^{-1})	wind direction RMSE ($^{\circ}$)	wind vector RMSE (ms^{-1})	ambient temperature RMSE (K)
Schwartz & Benjamin (1995) de Haan (2011) Strajnar (2012)	AMDAR	Radiosonde	< 25	< 0.030	< 15 mins	2.84	—	4.00	0.59
	Mode-S EHS	Radiosonde	< 20	< 0.030	< 2 mins	1.5 to 2.5	5 to 15	—	0.75 to 1.25
	Mode-S MRAR	Radiosonde	< 25	< 0.100	< 15 mins	3.3	25	—	1.8
Benjamin & Schwartz (1999) Drue et al. (2008)	AMDAR	other nearby AMDAR reports	< 10	< 0.030	< 10 mins	—	—	1.9 to 2.5	0.49 to 0.72
	AMDAR	All AMDAR reports averaged over the hour	—	< 0.050	< 60 mins	—	—	—	0.5 to 0.6
	Mode-S EHS	co-located AMDAR report	—	—	—	1.5 to 2.0	7.5 to 12.5	—	0.5 to 1.5
Strajnar (2012)	Mode-S MRAR	co-located AMDAR report	< 5	< 0.100	< 20 secs	0.8	8	—	0.35
Painting (2003)	AMDAR	—	—	—	—	—	—	2 to 3	0.55 to 0.69
de Haan (2015)	Mode-S	Doppler radar, sodar and HARMONIE 2.5km limited area model (triple collocation)	< 5	—	—	1.1 to 1.5	—	—	—
Cardinali et al. (2003)	AMDAR	ECMWF 40 km Global NWP Model	—	—	—	—	—	2 to 3	1.0 to 1.5
	AMDAR	NCEP Global NWP Model (6 hourly fields)	—	—	—	—	—	—	0.5 to 1.0
Ballish & Kumar (2008)	AMDAR	HIRLAM 11 km Limited Area NWP Model (1 hourly fields)	—	—	—	2.5 to 3.25	12 to 18	—	1.0 to 1.2
	AMDAR	HIRLAM 11 km Limited Area NWP Model (1 hourly fields)	—	—	—	2.5 to 3.4	12 to 20	—	1.0 to 1.7

Table 2.2: Summary of the results from previous studies on mean bias of aircraft-based observations. The table shows estimates drawn from previous studies for the overall range of the mean bias for wind-speed, wind-direction, wind-vector and ambient-temperature. An em-dash (—) symbol indicates the result was not stated.

Study	aircraft-based observations	verified against	horizontal separation (km)	vertical separation (km)	time difference	wind speed bias (ms^{-1})	wind direction bias ($^{\circ}$)	wind vector bias (ms^{-1})	ambient temperature bias (K)
Schwartz & Benjamin (1995)	AMDAR	Radiosonde	< 25	< 0.030	< 15 mins	—	—	—	-0.22
Ballish & Kumar (2008, Fig. 9)	AMDAR	Radiosonde	< 200	< 0.200	< 90 mins	—	—	—	-0.05 to 1.2
Drue et al. (2008)	AMDAR	co-located AMDAR	—	—	< 60 mins	—	—	—	1
Ballish & Kumar (2008, Fig. 3b)	AMDAR	co-located AMDAR	< 150	< 0.008	< 60 mins	—	—	—	-0.6 to 0.5
Drue et al. (2010, Table 1)	AMDAR	(Boundary Layer) Radio Acoustic Weather Radar	—	0.1	15 mins	—	—	2 to 2.5	-2.1 to -0.5
de Haan (2011)	Mode-S EHS	Radiosonde	< 20	< 0.030	< 2 mins	-0.5	0 to 5 $^{\circ}$	—	0 to 0.5
Cardinali et al. (2003)	AMDAR	ECMWF Global NWP Model	< 60	—	—	—	—	-0.25 to 0.20	-0.2 to 0.3
Ballish & Kumar (2008, Tables 3 and 4)	AMDAR	NCEP Global NWP model	—	—	—	—	—	—	-0.99 to 1.16

locations. Therefore, comparisons with co-located radiosondes are very limited in time and space providing only a short time window when aircraft might be close by (as shown in tables 2.1 and 2.2). Direct comparison of Mode-S EHS with AMDAR is limited to those reporting aircraft that participate in the AMDAR programme and which are configured to send reports. In addition, at present, the mapping between Mode-S EHS identifiers and AMDAR identifiers is not straightforward. Not all airlines make aircraft tail numbers available. Thus some additional computational steps are required to co-locate reports using a space-time box but this method of pairing is not robust. This is particularly true in busy areas where Mode-S EHS and AMDAR reports at similar locations and times will not necessarily originate from the same aircraft. The limitations of NWP based studies include the need to take account of uncertainties in the NWP model and observations used, including representativeness errors (Daley 1991, p.12; Waller et al. 2014), NWP forecast errors etc.

Using existing aircraft reports it is difficult to differentiate the contributions to the observation error arising from the aircraft’s sensors, avionics processing and atmospheric variability. The new work in chapter 4 provides an insight into the contribution to the observation error arising from reduced precision in Mode-S EHS reports.

2.9 Numerical Weather Prediction Model Development

During the past two decades the spatial and temporal resolution of numerical models have increased. For example, the Met Office Unified Model (UM) in its global configuration has increased its horizontal and vertical resolution from 90 km and 19 levels in 1992 to 17 km and 70 levels in 2014. Similarly over the same period the limited area model (LAM) configuration of the UM for the United Kingdom has increased resolution from 17 km and 19 levels to 1.5 km and 70 levels in 2010. With the advancement of computational resources the physical representation of the atmosphere has also changed from being hydrostatic to non-hydrostatic, and for the limited area models from parametrized convection (Skamarock & Klemp 2008, Staniforth & Wood 2008) to convection permitting (Clark et al. 2016). Other limited area models have followed similar development paths (table 2.3). Motivation for these higher-resolution convection-permitting models is the need to increase forecast accuracy of severe weather events such as severe thunderstorms and high rainfall rates (Golding et al. 2005, Grahame et al. 2009, Golding et al. 2013) to aid flood forecasting and for the provision of aviation forecasts of wind and temperature within the vicinity of airports.

The trend towards higher resolution limited-area models also requires a similar increase in the number, accuracy and resolution of the observations (Montmerle 2016).

Table 2.3: Horizontal and vertical resolution for a selection of convection permitting numerical weather prediction models.

Model Configuration	Horizontal Resolution (km)	Vertical Resolution (levels)
Met Office Unified Model LAM (UKV) (Lean et al. 2008)	1.5	70
Japan Meteorological Agency Local Forecast Model (JPA-LFM) (Hirahara & Ishimizu 2011, Saito et al. 2006)	2.0	58
Application of Research to Operations at Mesoscale (AROME) (Seity et al. 2011)	2.5	60
Consortium for Small-Scale Modelling (COSMO-DE) (Baldauf et al. 2011)	2.8	50
NOAA/Earth System Research Laboratory High Resolution Rapid Refresh (HRRR) (Benjamin et al. 2016)	3.0	51

Figure 2-5 illustrates this trend with respect to wind and temperature (Kitchen 2012*a*). The red line shows that the spatial resolution of the surface synoptic network has changed little for fifty years. The increase in costs of manned stations has driven the development of automatic weather observing stations. The surface synoptic network in the UK provides observations for use in NWP models with horizontal grid lengths greater than 10 km. The green line shows the development of weather radar systems but these are approaching a limiting resolution (dashed line). However, weather radar only operates effectively when rainfall or other reflective material is present in the atmosphere. For example, the Met Office weather radar network is currently configured to provide observations of reflectivity and Doppler radial velocity of precipitation from which rainfall rates and horizontal wind vectors are derived (Ballard et al. 2012). The blue line shows the development of numerical weather prediction models, from the resolutions of the order of tens of kilometres, to the present day one kilometre, and a projection to sub-kilometre scales (Ballard et al. 2016, Boutle et al. 2016, Hagelin et al. 2014, Golding et al. 2013). However, although horizontal and vertical resolution of the numerical models have increased there are limits to their ability to resolve weather features on the same scale (Dance 2004). Kitchen (2012*a*) suggests that the effective resolution to resolve weather features is of the order of four grid lengths (dashed blue line in fig 2-5). A similar argument may also apply to the spatial distribution of the observation network which is designed largely for synoptic scale weather features. There is an increasing gap between the spatial representation that is supported by the

observation network and the NWP spatial representation (Kitchen 2012*b*). For upper air winds and temperatures it is suggested that observations made by civil aircraft may go some way towards reducing this gap. The use of satellite-based observations may also close this gap. Take for example the Aeolus Earth Explorer, due to be launched during 2017 (Reitebuch et al. 2009). This polar-orbiting satellite will be used to evaluate the capability of a space borne Doppler wind LIDAR (Light Detection And Ranging) to make globally-distributed measurements of vertical wind profiles in the troposphere and lower stratosphere from the near surface to 30 km, with a vertical resolution of between 1 km near the surface and 2 km in the stratosphere. However, there is a long lead time between commissioning satellite systems and use of their observation data in NWP forecast production. Satellite-based observations of wind and temperature offer global coverage but they lack spatial and temporal coverage when compared with aircraft-based observations. For reviews on satellite derived winds see Hernandez-Carrascal & Bormann (2014), Reitebuch (2012), Collard et al. (2011) and Reitebuch et al. (2009).

2.10 Limited Area NWP Model: UKV

The Met Office Unified ModelTM (UM) (Walters et al. 2016) is run routinely for a number of applications. The Global version is run every six hours with a horizontal grid length of 17 km with 70 levels in the vertical, and forecasts out to 7 days (T+168 hrs). A further run is performed three hours later which updates the forecasts out to 2 days (T+48 hrs). The Global model provides the boundary conditions for the limited area models, which have a higher horizontal grid length but shorter forecast ranges. This study used the UKV, a mesoscale limited area version of the UM, as it ran operationally during the period January 2015 - June 2016.

The Met Office limited area NWP model for the United Kingdom, UKV, (Tang et al. 2013) is a configuration of the Unified Model (Davies et al. 2005). The UKV model has a variable grid resolution. Figure 2-6 depicts the domain of the UKV. The green rectangle represents the UKV inner domain at horizontal grid length 1.5 km. The outer domain is represented between the red and grey rectangle at 4 km horizontal grid spacing. The interval between red and green rectangles represents the zone where the resolution is increased smoothly from 4 km to 1.5 km. This smooth transition is to minimise the effect of moving from low-resolution to high-resolution which can cause model errors in representativeness in numerical weather prediction (Tang et al. 2013). There are 70 levels in the vertical from the surface up to 40 km (Tang et al. 2013). The areal coverage of the inner domain is 1096 km in longitude by 1408 km in latitude represented by a 1.5 km grid 744×928. The domain is represented using

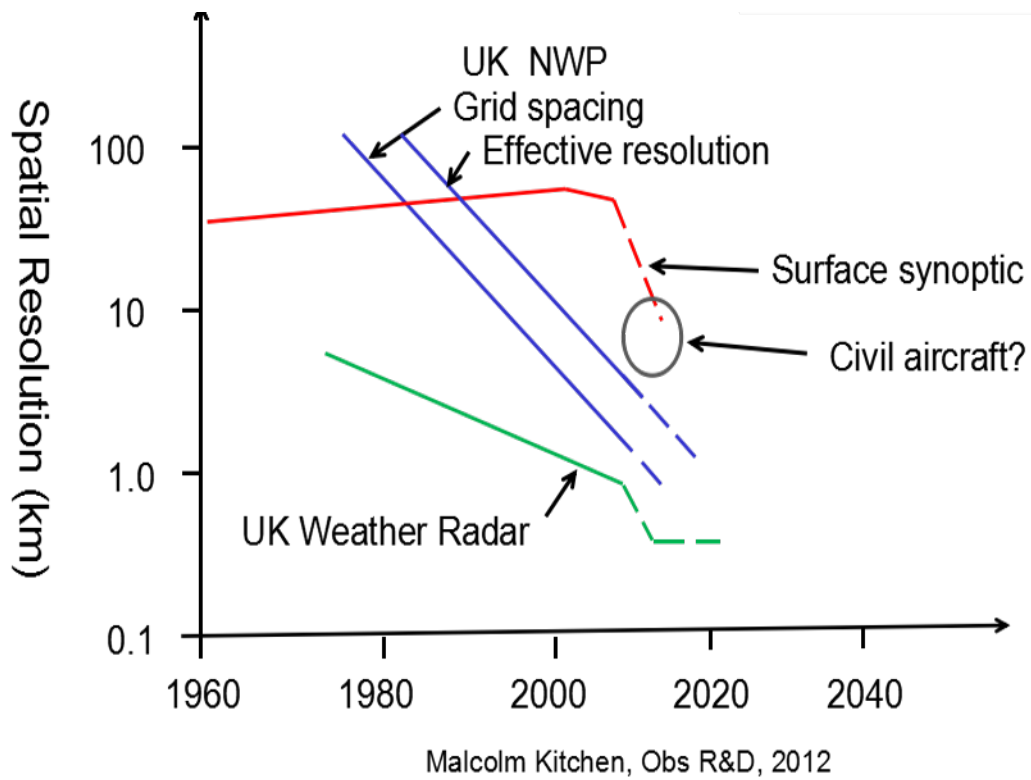


Figure 2-5: Illustration comparing development of spatial representation between the observation network and NWP limited area model for the UK. The solid lines are past and current developments while dashed lines are projected developments. The spatial resolution of the surface network (red) has changed little in the course of time whereas numerical models (blue) appear to have developed, mostly in line with computational resources, (Kitchen 2012a). (Image Crown Copyright, 2012, reproduced under Open Government License 3.0 for public sector information).

spherical co-ordinates and a rotated pole, so that the north pole is placed at 37.5° latitude and 177.5° longitude relative to regular latitude-longitude grid. The effect of this on the UKV domain is that the horizontal grid boxes are as square as possible, i.e., roughly uniform areas. The horizontal grid uses Arakawa C staggering (Arakawa & Lamb 1977) and a terrain-following hybrid-height vertical coordinate with Charney Philips staggering (Lean et al. 2008).

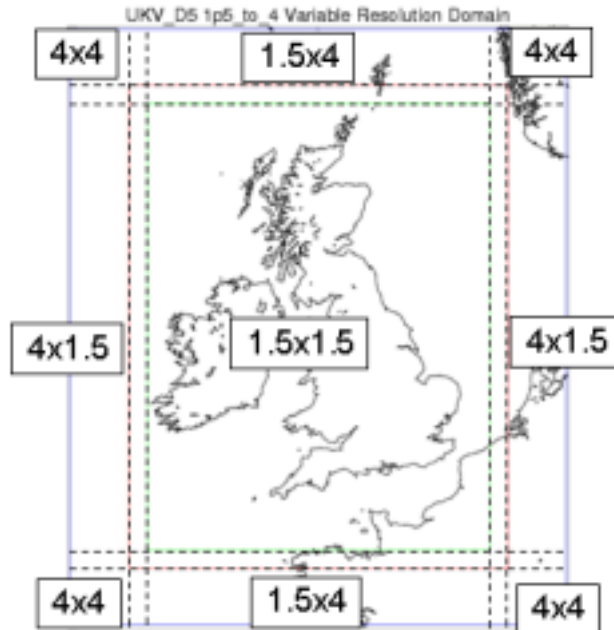


Figure 2-6: Domain of the Met Office UKV Numerical Weather Prediction Model. Image Crown Copyright, 2014, reproduced under Open Government License 3.0 for public sector information.

The UKV is a convection permitting model (Clark et al. 2016, Tang et al. 2013, Lean et al. 2008) with a latent heat nudging scheme (Jones & Macpherson 1997). The NWP model is run eight times per day and generates short range weather forecasts up to 36 hours ahead. The NWP model boundary conditions for the UKV are provided by the Global version of the Unified Model, which are reduced in horizontal scale from 17 km to 4 km. The initial conditions of the NWP forecasting process are obtained from the result of data assimilation (described in section 2.11), using an incremental variational scheme (Renshaw & Francis 2011, Lorenc et al. 2000) to combine recent observations with a previous forecast. The UKV assimilates routinely collected observations (table 2.5) (Ballard et al. 2016) and additional observations that are not assimilated in the Global version of NWP (table 2.4). The data assimilation scheme also uses an adaptive grid (Piccolo & Cullen 2011) in the vertical, which is used to represent boundary layer

Table 2.4: Extra observations used in the data assimilation processing for the Met Office limited area NWP model: 1.5 km UKV, which are not used in the Global NWP model: 17 km Unified Model.

Observation Type	Observation System	Observation Frequency
Surface rain rate	Doppler Radar	1-hourly, 5km resolution
Visibility	Surface synoptic observations (SYNOP)	1-hourly
2 m Temperature and Relative Humidity	Roadside sensors	1-hourly
Radial winds	Doppler radar	3-hourly
Radiances above low cloud	Spinning Enhanced Visible and Infrared Imager (SEVIRI) - channel 5	—
High-resolution Atmospheric Motion Wind Vectors	Meteosat Second Generation satellite.	—
Cloud fraction profiles for cloud tops	GeoCloud satellite imagery	3-hourly, 5km resolution
Cloud fraction profiles for cloud base	SYNOP reports.	3-hourly

features, such as temperature inversions.

2.11 Data Assimilation

Data assimilation is a process that uses sophisticated mathematical methods to combine current knowledge of the atmospheric state obtained from a vector of observation measurements, $\mathbf{y}_o \in \mathbb{R}^p$, and from a modelled NWP state, $\mathbf{x}_b \in \mathbb{R}^n$, e.g., a previous forecast. The result of the process is the best representation of the modelled state of the atmosphere, $\mathbf{x}_a \in \mathbb{R}^n$, at some time t (Daley 1991, Talagrand 1997, Kalnay 2003, Frehlich 2011). This process also takes into account errors in observations and in the modelled NWP state. We note that the number of available observations is often less than the number of available model state parameters, i.e., $p < n$.

We compare observations to the model by calculating, $\mathbf{H}(\mathbf{x})$, where $\mathbf{H} : \mathbb{R}^n \rightarrow \mathbb{R}^p$ is the observation operator that performs the necessary steps to interpolate and transform the model’s state vector in NWP model space to be the equivalent observation vector in observation space. Thus we can write,

$$\mathbf{y}_o = \mathbf{H}(\mathbf{x}) + \epsilon_o. \quad (2.1)$$

The error in the observation, $\epsilon_{\mathbf{o}}$, arises from several sources: the instrument itself; any processing steps done on the instrument's measurement to obtain the required observation; the formulation of the observation operator; and the mismatch in scale (space and time) between what the instrument can measure and what the NWP model can represent.

We assume that observation measurements are unbiased and uncorrelated (Kalnay 2003, pp.153-154) so that we can define the observation error covariance matrix, \mathbf{R} , as

$$\mathbf{R} = E[\epsilon_{\mathbf{o}}\epsilon_{\mathbf{o}}^T], \quad (2.2)$$

where E is the expectation operator and $\mathbf{R} \in \mathbb{R}^{p \times p}$

Similarly we define the truth in the model space, $\mathbf{x}_{\mathbf{t}}$, to be the exact representation of the atmosphere which is unknown. We estimate the true NWP model state as,

$$\mathbf{x}_{\mathbf{a}} = \mathbf{x}_{\mathbf{t}} + \epsilon_{\mathbf{a}} \quad (2.3)$$

and

$$\mathbf{x}_{\mathbf{b}} = \mathbf{x}_{\mathbf{t}} + \epsilon_{\mathbf{b}} \quad (2.4)$$

where $\epsilon_{\mathbf{a}}$ is the error in the analysis (after data assimilation) and $\epsilon_{\mathbf{b}}$ is the error in the the background (before data assimilation) of these NWP model states. We assume that the estimated errors in the model states are unbiased so that we can define the background error covariance matrix, \mathbf{B} , as

$$\mathbf{B} = E[\epsilon_{\mathbf{b}}\epsilon_{\mathbf{b}}^T], \quad (2.5)$$

where $\mathbf{B} \in \mathbb{R}^{n \times n}$. The background state errors may be due to inaccurate representation of physical processes, and errors in spatial representation and temporal evolution of the NWP model (Bannister 2008).

Data assimilation may be expressed as a correction term added to the known model state (Kalnay 2003, p. 15, eq. 1.4.1),

$$\mathbf{x}_{\mathbf{a}} = \mathbf{x}_{\mathbf{b}} + \mathbf{K}(\mathbf{y}_{\mathbf{o}} - \mathbf{H}(\mathbf{x}_{\mathbf{b}})), \quad (2.6)$$

where the gain factor, $\mathbf{K} \in \mathbb{R}^{n \times p}$, is used to weight the difference between the measured and the modelled observations.

2.12 3-D Variational Data Assimilation

One method of data assimilation processing is Three-dimensional Variational Data Assimilation (3-D Var). This method defines a cost function, J , as the sum of the squared errors between the observations and the model state, \mathbf{x} , in observation space J_o , and those between the background state and the model state, in the model's space J_b , (Lorenc 1986, Courtier et al. 1998),

$$J = J_o + J_b. \quad (2.7)$$

The squared errors are given by the respective terms in the sum,

$$J(\mathbf{x}) = \frac{1}{2}(\mathbf{y} - \mathbf{H}(\mathbf{x}))^T \mathbf{R}^{-1}(\mathbf{y} - \mathbf{H}(\mathbf{x})) + \frac{1}{2}(\mathbf{x} - \mathbf{x}_b)^T \mathbf{B}^{-1}(\mathbf{x} - \mathbf{x}_b), \quad (2.8)$$

and are scaled by the covariance of the observation errors, \mathbf{R} , and the background errors, \mathbf{B} . The analysis state is the value, $\mathbf{x} = \mathbf{x}_a$, that minimises the cost function, eq (2.8). We assume initially that the background and observation errors are mutually uncorrelated and the errors are randomly distributed so that they can be characterised by using a Gaussian distribution (Kalnay 2003, ch 5.). With this assumption Lorenc (1986) showed that eqs. (2.6) and (2.8) are equivalent if the gain factor, \mathbf{K} , is expressed in terms of the error covariances,

$$\mathbf{K} = \mathbf{B}\mathbf{H}^T (\mathbf{H}\mathbf{B}\mathbf{H}^T + \mathbf{R})^{-1}, \quad (2.9)$$

thus we can express eq. (2.6) in the conventional form (Kalnay 2003, ch 5.) as,

$$\mathbf{x}_a = \mathbf{x}_b + \mathbf{B}\mathbf{H}^T (\mathbf{H}\mathbf{B}\mathbf{H}^T + \mathbf{R})^{-1} (\mathbf{y} - \mathbf{H}(\mathbf{x}_b)). \quad (2.10)$$

To obtain the best estimate of the atmospheric state, \mathbf{x}_a , requires that the error characteristics of the background state and observations to be well known.

2.13 Data Assimilation of Aircraft-based Observations

In this section we review the data assimilation studies using Mode-S EHS reports by de Haan & Stoffelen (2010), Lange & Janjic (2016) and Mode-S MRAR reports by Strajnar et al. (2015). These studies have shown that NWP model forecasts with lead times of 3-hours to 6-hours ahead for horizontal wind and ambient temperature can benefit from assimilating Mode-S EHS derived observations. However, assimilation of AMDAR alone results in better forecasts for forecasts up to six hours. The direct

comparison of the results of these studies is difficult.

Experiments conducted by Lange & Janjic (2016), Strajnar et al. (2015), de Haan & Stoffelen (2010) all used different sets of observations, different NWP models are used which affects the background forecast, and observation error standard deviations used to characterise the aircraft-based observations differ. All these may affect the quality of the resulting NWP analysis. The assimilated observations used in each of these studies are listed in table (page 29). The main properties of the NWP models and configuration of the data assimilation systems used in these studies are summarised in table 2.6 (page 30). For easier comparison later, we also include the configuration of our own experiments described in chapter 7.

Apart from the differences in NWP models used, de Haan & Stoffelen (2010) and Lange & Janjic (2016) used Mode-S EHS observations that were pre-processed using the method described by de Haan (2011) (section 2.8, page 16). In the corresponding data assimilation experiments the Mode-S EHS observations were thinned spatially. De Haan & Stoffelen (2010) thinned the Mode-S EHS reports to around 5% of the total number 1.5×10^6 per day collected around Schipol airport, i.e., 75000 per day. However, Lange & Janjic (2016) found that up to 50% of the average 184559 reports per day, i.e., of the order 90,000 per day, could be used before there was no additional benefit to the subsequent forecasts.

Strajnar et al. (2015) used Mode-S MRAR temperature and winds, which have been shown to be of similar quality to AMDAR reports. Mode-S MRAR temperature do not suffer from the precision errors that affect the Mach Temperature derived from Mode-S EHS. The horizontal winds are not corrected for heading errors as described by de Haan (2011) but the MRAR reports are smoothed using the same method as de Haan & Stoffelen (2010). Strajnar et al. (2015) found it necessary to spatially thin the MRAR reports horizontally to one report every 25 km. It is estimated that around 5000 MRAR reports per day were available for data assimilation (Strajnar et al. 2015, Fig. 4).

In all these studies the observation error standard deviation for Mode-S EHS and Mode-S MRAR horizontal wind was assumed to be the same as for AMDAR. The observation error standard deviation for Mode-S MRAR temperature was also assumed to be the same as for AMDAR (Strajnar et al. 2015). However, for Mode-S EHS temperature the observation error standard deviation was assumed to be larger by a factor of up to 1.5 times the AMDAR (de Haan 2011). This is discussed further in section 7.3.3 (page 159).

We conclude from these studies that, for Mode-S EHS observations, some method to smooth the reports is required and heading corrections should be applied. To use

Table 2.5: Observations Assimilated in each NWP Model used to evaluate Mode-S EHS observations. A ‘No’ indicates that the observation type is not used. A ‘Yes’ indicates the observation type is used or, where information is available, H indicates the hourly time frequency of the reports used.

Observations	HIRLAM-X11	ALADIN	COSMO-KENDA	UKV
Pressure (P) at surface	1 H	Yes	1 H	1 H
Temperature (T) at 2 m	No	Yes	No	1 H
Humidity (Q) at 2 m	No	Yes	No	1 H
Surface Visibility (V)	No	No	No	1 H
Wind Vector (W) at 10 m	No	Yes	1 H	1 H
Radiosonde (W, T, Q)	6 H	Yes	12 H	12 H
AMDAR (W, T)	1 H	Yes	Yes	1 H
Air Reports (AIREP) (W, T)	No	No	No	Yes
SHIP	No	No	No	No
BUOY	No	No	No	No
Wind Profiler	No	Yes	0.5 H	1 H
Doppler Radial Wind	No	No	No	3 H
Satellite Radiances	No	Yes	No	Yes
Atmospheric Motion Vectors	No	Yes	No	Yes

these observations in data assimilation consideration should be given to the observations density. For the assumed observation error standard deviation then we expect this to be the same for Mode-S EHS and AMDAR horizontal winds. For Mode-S EHS temperature we expect the observation error to be larger than that assumed for AMDAR.

2.14 Summary

We have reviewed the atmospheric conditions that give rise to temperature inversions and low-level jets, and how these meteorological features can be observed using vertical profiles of temperature and horizontal wind. We have reviewed how we obtain observations of temperature and horizontal wind from aircraft and from routine messages, Mode-S EHS, exchanged between an aircraft and air-traffic control. The accuracy of these observations are found to vary depending on the source of the observation. Measurements made by the aircraft being more accurate than those derived from routine messages.

In summary, surface weather features such as fog and mist are most likely to form when atmospheric conditions near the surface are: stable, possess high humidity, low horizontal wind speed, there is little vertical mixing of the air and temperature inver-

Table 2.6: Configuration of the NWP Models used for Data Assimilation of Mode-S EHS Observations. The time period used for Mode-S EHS observations is given relative to the assimilation time, a negative value indicates the period before and a positive value is the period after the analysis time.

NWP Model	HIRLAM-X11 De Haan & Stoffelen (2010)	ALADIN Strajnar et al. (2015)	COSMO-KENDA Lange & Janjic (2016)	UKV Used in Chapter 7
Domain	Netherlands	Slovenia	Germany	United Kingdom
Vertical Levels	40	87	50	70
Horizontal Grid Length (km)	11	4.4	2.8	1.5
Convection Permitting	No	Yes	Yes	Yes
Data Assimilation Scheme	3-D Var	3-D Var	Ensemble	3-D Var
Assimilation Analysis Cycling	1-hourly	3-hourly	1-hourly	3-hourly
Assimilation horizontal grid length (km)	not specified	not specified	8	3
Assimilation vertical levels	not specified	not specified	30	70
Mode-S EHS Observations used (minutes)	-10	-90 to +90	-60	-30 to +30

sions are present within the boundary layer (Roach et al. 1976, Brown & Roach 1976). Surface level inversions are most likely to arise under clear skies as a result of greater heat loss through radiation. A consequence of the formation of a temperature inversion is the formation of a low-level jet, which would be above the temperature inversion, and would be a zone of wind shear.

We have reviewed that the current NWP model development is in the realm of kilometre-scale horizontal grid lengths, with a trend towards using convection-permitting limited area models and sub-kilometre scales. We have suggested that these developments require observations at a higher spatial and temporal resolution than currently used.

We have outlined the method of 3-D Var data assimilation, which provides the initial NWP model state for weather forecasting. This method has been used to assimilate aircraft-based observations obtained from AMDAR, Mode-S EHS and Mode-S MRAR. These studies suggest that forecast errors of wind and temperature are reduced when AMDAR and Mode-S EHS are assimilated but that this benefit persists for the first two to three hour forecasts. These data assimilation experiments assume that the errors in the observations are random and are uncorrelated. All these studies smoothed and thinned the Mode-S EHS reports prior to their assimilation, since too many Mode-S EHS reports can distort the NWP analysis. Thinning schemes differ, from random selection to spatial separation of reports.

The analysis fields output by the data assimilation processing rely upon an accurate representation of the observation and background errors. Misspecified errors can lead to an incorrect analysis and this would affect the subsequent NWP forecasts. For the studies by de Haan & Stoffelen (2012), Strajnar et al. (2015) and Lange & Janjic (2016) the observation error standard deviation for Mode-S EHS and Mode-S MRAR horizontal wind are the same as those used for AMDAR. But the observation error standard deviation for Mode-S EHS temperature is at least 1.5 times greater than that used for AMDAR.

The new work in this thesis overcomes some of the limitations of the study by de Haan (2011). De Haan (2011) estimates the observation error for Mode-S EHS wind and temperature by comparing the differences between two successive Mode-S EHS derived observations. We develop novel error models to characterise the observation error standard deviation for Mode-S EHS derived observations based on our knowledge of Mode-S EHS processing (chapter 3). We validate our novel error models using in situ observations obtained from a research aircraft (chapter 4), so meteorological observations and Mode-S EHS reports are co-located in time and space. (No previous study estimating Mode-S EHS errors have been able to use co-located observations.) In

this new work, we also analyse the effects of the data processing by the aircrafts avionics and the measured atmospheric variability for their contribution to the accuracy and precision of the Mode-S EHS derived observations.

De Haan (2011) also observed that the Mode-S EHS derived temperature can exhibit large fluctuations especially at low altitude, due to the precision of the Mach number. He reports using only one method to reduce the fluctuations in Mode-S EHS reports of Mach number and true airspeed. In our new work, we investigate the use of four methods (chapter 6) to reduce these fluctuations. We compare their effect with our error model for Mode-S EHS derived temperature (chapters 3 and 4). In our new work, we also show that by smoothing and aggregating Mode-S EHS derived observations (chapter 6) within the vicinity of an airport's terminal manoeuvring area then meteorological features, such as temperature inversions (section 2.3, page 10), are identifiable.

Previous studies by de Haan & Stoffelen (2012), Strajnar et al. (2015) and Lange & Janjic (2016) have assimilated Mode-S observations into NWP models, with horizontal grid lengths of 11 km, 4.4 km and 2.8 km respectively. In our new work, we use the Met Office's convection-permitting high-resolution limited area NWP model, the UKV (chapter 7), which uses a horizontal grid of 1.5 km, the highest horizontal grid length so far used to assimilate Mode-S EHS observations. Using the results of chapters 3, 4 and 6, we assess the benefit of using Mode-S EHS observations in the UKV at its 1.5 km horizontal grid length configuration. We also provide a new validation of our results from chapter 4 by diagnosing the observation error variance using the observation-minus-background and observation-minus-analysis values output by the UKV NWP model (Desroziers et al. 2005).

Chapter 3

Initial Study on Utilising Mode-S EHS Observations.

3.1 Introduction

In this chapter we introduce sources of Mode-S EHS data and the concepts that will be used to process these data. We introduce these data sources and concepts by applying them to an initial case study. We do this to develop our understanding of the processing of the Mode-S EHS reports, and the characteristics and utility of Mode-S EHS derived meteorological observations. From this initial case study we will show the effects of Mode-S EHS processing in more detail in chapter 4, and the utility of the derived meteorological observations for operational meteorology in chapter 6 and for numerical weather prediction in chapter 7. Sections 3.4 and 3.5 in this chapter are extracts from the paper published by Mirza et al. (2016).

We begin our initial study by exploring our first two thesis questions (section 1.4, page 3) which we summarise as follows:

1. How accurately do observations derived from routine messages exchanged between an aircraft and air-traffic-control represent the “state” of the atmosphere?
2. What atmospheric phenomena within the boundary layer can be observed from using high-frequency observations derived from these routine messages?

To address these questions we, initially, use data obtained from National Air Traffic Services (NATS) (which we describe later in section 3.2). However, during the course of this initial study the Met Office developed and deployed its own capability to collect Mode-S EHS reports (which we describe in section 5.5). The main benefit of using the Met Office network is the reduced cost of collecting the data.

We are interested in weather phenomena affecting operations in the vicinity of airports of the London Terminal Manoeuvring Area (LTMA), namely London Heathrow and London Gatwick. We will discuss one occurrence of a temperature inversion (section 2.3, page 9) and an associated low-level jet (section 2.4, page 12). These weather phenomena are identified from vertical profiles of the horizontal wind and ambient temperature.

We construct these vertical profiles from the collected Mode-S EHS reports. In section 3.3 we describe the domain used to collect and select Mode-S EHS reports. We use the Mode-S EHS data provided by NATS to derive temperature and horizontal wind observations. In section 3.6 we apply a box-average method to aggregate these observations to form vertical profiles of the mean horizontal wind and ambient temperature.

As will be shown, the results of the case study suggest that Mode-S EHS derived observations may have utility for operational meteorology. We also show that the profiles exhibit fluctuations which may be related to the reduced precision of the aircraft's state vector. The reduced precision is a consequence of Mode-S EHS processing aboard the aircraft. We believe that the reduced precision is a significant source of error for Mode-S EHS derived observations. We show that this error can be described by the statistics of quantisation error which arises when an analogue signal is converted to a digital signal (section 3.9). Characterising this error is an important consideration for data assimilation of Mode-S EHS derived observations.

3.2 National Air Traffic Services Secondary Surveillance Radar Mode-Select

Tracking and range detection radar is a surveillance network operated by an air navigation service provider. In the UK this service is provided by National Air Traffic Services (NATS). There are two forms of surveillance: primary and secondary. Primary surveillance radar is operational within the terminal manoeuvring area of an airfield or airport. It uses reflected radio signals which provide information on range, azimuth and elevation of detected objects. Secondary surveillance radar (SSR), which we described in section 2.7, is operational within a flight information region. NATS currently operate around twenty secondary surveillance radars with coverage for the flight information regions "Scottish" and "London" (figure 3-1a). In essence, when an SSR detects a new object it sends a sequence of radio signals to obtain the object's state vector (section 2.7, page 15). It is from these responses that meteorological observations of temperature and horizontal wind can be derived (de Haan 2011). We show

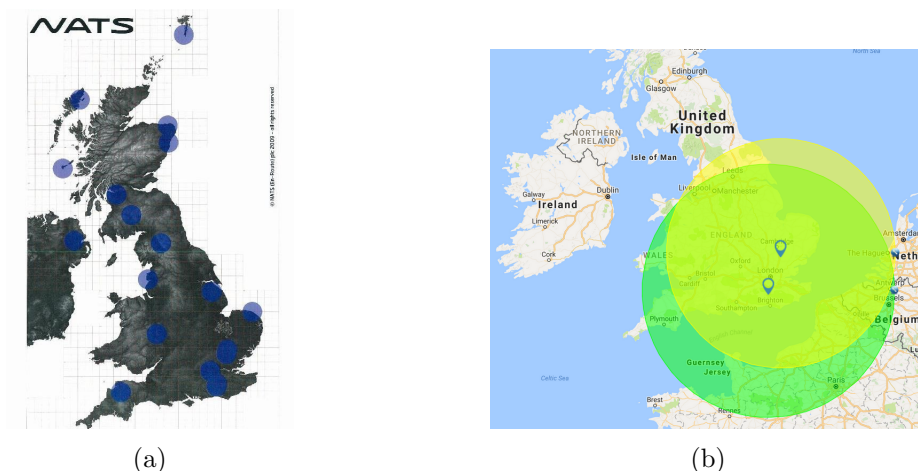


Figure 3-1: (a) Location of NATS SSRs (blue circles) within the United Kingdom (©NATS 2009, reproduced by permission). (b) SSRs at Debdon (yellow circle, radius = 270 km) and Peas Pottage (Green circle, radius = 330 km). The radius of each circle indicates the approximate maximum detection range of the SSR at high altitude. The detection range decreases with altitude. (Map data ©2017 GeoBasis-DE/BKG, ©2017 Google, ©2017 Inst Geogr. Nacional, reproduced under licence for non commercial use.)

how these are derived in sections 3.4 and 3.5.

At the start of this research project NATS supplied the Met Office with a sample of Mode-S EHS data from their archive. The NATS archive only contained data from their secondary surveillance radars located at Peas Pottage and Debdon, shown in fig 3-1b. These radar sites provide coverage for the busiest air traffic routes and airports in the United Kingdom. NATS use this archive for research and development of their air navigation services. Moreover, there is no regulatory requirement for NATS to retain air traffic management data after 30 days (Civil Aviation Authority 2014, Part C, Section 3: SUR 10). Thus while SSR coverage within the United Kingdom is nationwide, the extended archive of SSR coverage is mostly limited to the two SSRs.

3.3 Airport Domains

Mode-S EHS reports for the case studies discussed in section 3.7, and later in chapter 6, are those which are received within two domains depicted in figure 3-2. The domains are centred around London Heathrow and London Gatwick. Each domain is a 3-D column, its height between 0 m and 3000 m above mean sea level, and horizontal dimensions being 80 km East-West and 40 km North-South, with the airport centred within the domain at the surface. These horizontal and vertical dimensions are

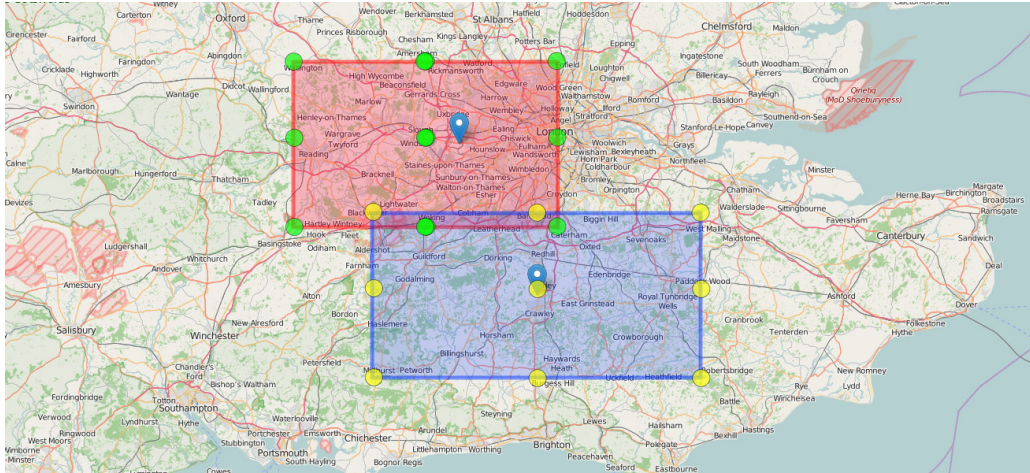


Figure 3-2: Horizontal domains for London Heathrow (top) and London Gatwick (bottom) with the airports at the centre of the domain. From the centre, the domain extends approximately 20 km North, 20 km South, 40 km East and 40 km West. The Heathrow domain is curtailed on its eastern edge so as to remove air traffic within the approach to London City Airport. Green and yellow dots show the locations for the NWP UKV one-dimensional vertical profiles. (Background map ©OpenStreetMap contributors, reproduced under licence Creative Commons Attribution-ShareAlike 2.0.)

based on the orientation of the runway. For London Heathrow we use runway 09R/27L and for London Gatwick we use runway 08R/26L so as to favour Mode-S EHS reports from aircraft departing or arriving at these airports. In addition the vertical dimension is chosen so as to capture meteorological phenomena occurring within the lower atmosphere, i.e., boundary layer.

London Heathrow Airport (EGLL) is situated approximately 21 km west of the city of London. To the north and south it is surrounded by suburban housing, business premises and mixed-use open land (Civil Aviation Authority 2015a). To the east there are suburban housing and business premises and to the west three large reservoirs, mixed-use open land, housing and business premises. The airport has two runways: runway 09L/27R to the north, which is 3,901 m long, and runway 09R/27L to the south, which is 3,660 m long. The rate of departures and arrivals at London Heathrow tends to be uniform and more or less constant throughout its operating hours (0600-2330). The two parallel runways provide a traffic flow rate of an average of 75 aircraft arriving or departing per hour.

London Gatwick Airport (EGKK) is located approximately 45 km south of London and about 3 km north of Crawley. It is situated in mostly lightly populated countryside with nearby towns of Crawley and Horley (Civil Aviation Authority 2015b). The airport has one main runway, designated runway 08R/26L, which is 3,316 m long. There is

also one standby runway, runway 08L/26R, that can be used if the main runway is out of operation. The airport operates over the same operating hours as Heathrow but has only a single main runway, which provides a traffic flow rate on average of 55 aircraft arriving and departing per hour. Furthermore, the traffic pattern differs from London Heathrow, with two peak periods of high traffic density, the first mid-morning and the second mid-afternoon. Therefore for routine airport operations we can expect a more variable hourly rate of reports of Mode-S EHS reports from Gatwick compared with a near constant hourly rate from Heathrow.

While traffic flow patterns are influenced by the prevailing meteorological conditions on the day, in general, aircraft will take-off and land into a headwind to maximise lift during take-off and maximise deceleration upon landing (Civil Aviation Authority 2015*a*). In the UK the prevailing winds are south-westerly, so at most airports aircraft land from the east and depart to the west (westerly operations) about 70-80% of the time.

3.4 Deriving the Ambient Air-temperature from Mode-S EHS Reports of Mach Number and True Airspeed

Following the method of de Haan (2011) the ambient air-temperature is derived from Mode-S EHS reports of Mach number and airspeed. The Mach number is defined as the ratio of the aircraft's airspeed V_A , and the local speed-of-sound, A , (Houghton & Carpenter 2003) so that

$$M = \frac{V_A}{A}. \quad (3.1)$$

The magnitude of the local speed-of-sound is related to the local ambient temperature and is given by (Collinson 2011, pp. 390-392),

$$A = \sqrt{\gamma R_a T_A}, \quad (3.2)$$

where γ is the ratio of the specific heats for dry air at constant volume and constant pressure; R_a is the characteristic gas constant for dry air; and T_A is defined as the local ambient temperature in Kelvin.

Using equation (3.2) we can relate the local ambient temperature to the Mach number and airspeed as follows,

$$A = A_0 \sqrt{\frac{T_A}{T_0}} = \frac{V_A}{M}, \quad (3.3)$$

where the speed-of-sound $A_0 = 340.294 \text{ ms}^{-1}$ and the ambient temperature $T_0 =$

288.15 K. These are reference values defined at mean-sea-level pressure under international standard atmosphere conditions ISA (ICAO 1993). So the ambient temperature can be recovered from the Mode-S EHS reports as

$$T_A = \frac{T_0}{A_0^2} \left[\frac{V_A}{M} \right]^2. \quad (3.4)$$

It is assumed that the recovered ambient temperature does not contain effects of heating due to air compression within the housing of the temperature sensor or cooling due to evaporation of moisture from the temperature sensing element (Lawson & Cooper 1990, Woodfield & Hayne 1965). It is expected that the FMS processing removes these effects.

3.5 Deriving the Horizontal Wind Vector from the Mode-S EHS Message

In this section we show how the horizontal wind vector is derived from the Mode-S EHS message. We define the aircraft's air-vector, \mathbf{V}_A , as the speed of the aircraft relative to the surrounding air, V_A , and its horizontal orientation in space, θ_A . (In aviation terms these are the aircraft's 'true airspeed' and 'true heading.')

We also define the aircraft's ground-vector, \mathbf{V}_G , as its ground speed, V_G , and ground heading, θ_G . These are the aircraft's speed and track projected onto the Earth's surface. (In aviation terms these are the aircraft's 'ground speed' and 'true-track angle.')

We now show how the wind vector is derived. The horizontal wind-vector, \mathbf{V}_W , is the vector difference between the aircraft's ground-vector and the aircraft's air-vector, i.e., $\mathbf{V}_G - \mathbf{V}_A$ (Painting 2003, p. 11).

The horizontal wind-vector, \mathbf{V}_W , is resolved into orthogonal components: a zonal component (West-East), U , and a meridional component (South-North), V . These are obtained by resolving the corresponding components of the air-vector, \mathbf{V}_A , and ground-vector, \mathbf{V}_G , along the South-North and West-East axes, so that,

$$U = V_G \cos\left(\frac{\pi}{2} - \theta_G\right) - V_A \cos\left(\frac{\pi}{2} - \theta_A\right), \quad (3.5)$$

and

$$V = V_G \sin\left(\frac{\pi}{2} - \theta_G\right) - V_A \sin\left(\frac{\pi}{2} - \theta_A\right). \quad (3.6)$$

For these equations, the unit of angular measure for θ_G and θ_A is radians, although the Mode-S EHS reports use angular degrees. (The angle $\pi/2$ radians is equivalent to 90° .) Using these wind components the wind speed and wind direction are determined.

It is assumed that the horizontal wind-vector lies within a 2-D horizontal plane which is parallel to a tangent plane drawn at the Earth’s surface at the aircraft’s latitude and longitude. Any vertical component to the wind-vector is assumed negligible compared to the horizontal components.

3.6 Aggregated Observations

In this section we describe how we form aggregated observations to represent the mean meteorological conditions. Mode-S EHS reports are frequent but, as shown by de Haan (2011), they are noisy. De Haan (2011) reduces the effect of noise by smoothing the time series of reports of individual aircraft. This involves identifying all reports for an individual aircraft and its current phase of flight. This is a non-trivial problem since the aircraft state vector provides no information as to whether the aircraft is ascending or descending or when it has completed one journey (from take-off to touch-down). Given the high density of Mode-S EHS we propose a simpler method, to obtain a representative value by aggregating observations from multiple aircraft.

We distinguish our method of ‘aggregated observation’ from the ‘super-observation’ cell (Lorenz 1981, Berger et al. 2004). A Super-observation cell, O_{so} , is formed by the linear combination of an NWP background model value, b_o , representing the cell’s observation, and the mean of the weighted difference between NWP background model value at the location of the observation, b_i , and the actual in situ observations, o_i , within the cell,

$$O_{so} = b_o + \frac{1}{N} \sum_{i=1}^N w_i(o_i - b_i), \quad (3.7)$$

where N is the number of observation-background pairs and w_i is the weighting applied to each pair.

The super-observation cell can be scaled to represent spatial scales that are larger than the spatial scales of the in situ observations, e.g., the spatial scale of the NWP model has a 1.5 km horizontal grid spacing while the in situ within the super-observation cell may have spatial scales that are smaller. This method of super-observation has been used to assimilate satellite-based observations (Berger et al. 2004) and Doppler radar radial wind (Simonin et al. 2014). However, over a small area, an aggregated observation and super-observation would be equivalent if the background model value in eq. (3.7) does not vary across the small area cell such that $b_o - \frac{1}{N} \sum_{i=1}^N w_i b_i \approx 0$. Our method of ‘aggregated observation’ does not include the use of a background NWP model. We choose to use our method of ‘aggregated observation’ so that we can investigate its observation error.

An aggregated observation is formed to represent the mean meteorological conditions for a horizontal layer of thickness, Δh m, which is centred around an airport. The horizontal layer has dimensions l km in the East-West direction and b km in the North-South direction. The curvature of the Earth's surface across this domain is considered minimal¹. A vertical column of height, H m, is made up of a sequence of horizontal layers. The number of layers is given by,

$$N = \frac{H}{\Delta h}, \quad (3.8)$$

and the altitude of the mid-point of the layer, L , is given by,

$$h_L = \left(L + \frac{1}{2}\right) \times \Delta h, \quad (3.9)$$

where L is the layer number, starting from zero and counting upward.

An aggregated-observation is the arithmetic mean of the derived observations in layer L , received during the time period ΔT ,

$$\langle O_L \rangle = \frac{1}{N_L} \sum_{i=1}^{N_L} O_{i,L}, \quad (3.10)$$

where $O_{i,L}$ is the i^{th} derived observation in layer L , and N_L is the number of observations in layer L .

Observations are derived using reports from aircraft within layer L . For a single aircraft it is assumed initially that errors in the reports of the aircraft's state vector follow a Gaussian distribution with a mean bias of zero and with standard deviations of 0.6 K for temperature and 3.5 ms⁻¹ for the horizontal wind components (as in Painting (2003)). Errors in reports from different aircraft-types within a layer are assumed uncorrelated (Drue et al. 2008). These initial assumptions seem reasonable within the terminal area of an airport. Arrivals and departures occur on time-scales of minutes; aircraft wake categories (small, medium, large and very large) and different aircraft types (Airbus, Boeing, BAe, etc.) are managed so as to optimise traffic flow rates through an airport. For arrivals and departures, aircraft are sequenced with separations ranging from 6 km to 12 km depending on the aircraft wake category.

Aggregated reports use all available data to create a representative value, which also reduces the volume of data to be processed at later stages. The method improves

¹The horizontal distance, d , to the horizon is given by $d \approx \sqrt{2R_e h}$, where R_e is the radius of the Earth, and h is the height above mean sea level. For a height of 300 m above mean sea level, Earth radius of 6372 km, the horizontal distance to the horizon is 62 km.

the representativeness of the observation by reducing unbiased random errors (Taylor 1982, Ch. 4 and 5) that may arise within reports from a single aircraft. However, this technique will not identify any systematic correlated error, if this is present and can be determined.

3.7 Derived Vertical Profiles for Horizontal Wind and Temperature

In this section we address the second thesis question, what meteorological phenomena can be detected using observations derived from Mode-S EHS reports. For example the presence and duration of temperature inversions and low-level wind shear within the vicinity of London Heathrow and London Gatwick airports can adversely affect the operations of ATM. Timely identification of these weather phenomena can mitigate their effects. These weather phenomena are identified from vertical profiles of wind and temperature.

Using a sample of Mode-S EHS reports we derive vertical profiles of temperature and horizontal wind. The reports were supplied by NATS from their archive for the period 13th to 15th October 2012 and consist of the state vectors (defined in section 2.7) of all aircraft within the vicinity of the airport domains. The aggregated profiles generated are for the London Heathrow and London Gatwick domains shown in figure 3-2.

3.7.1 Meteorological Conditions for the period 13th to 15th October 2012

The weather regime for October 2012 was mostly unsettled but there were some brief periods of settled weather with mild and damp conditions (Eden 2012). On the 13th October 2012, a low pressure system was just north of Scotland which brought rain, which eased overnight as the low moved further north. In central and southern England, clearing skies, falling temperatures and light winds allowed mist and fog to form. The Met Office analysis charts for 0000 and 1200 UTC on the 14th October (Met Office 2012), figure 3-3, show for this period the low pressure regions moving from west to east in Scotland and a ridge of high pressure over the southern regions of the United Kingdom. Thus most parts of England and Wales had long clear spells overnight, allowing temperatures to fall close to, or just below, freezing quite widely. As temperatures dropped, mist and fog formed again, mainly across southern parts of England and Wales. Through the morning, the overnight fog was slow to clear in some parts of

southern and south-western England. Most other places had a dry day with some sunshine. Through the evening, clear spells across central and southern parts of England again allowed temperatures to fall. On the 15th October, it was a cooler night in those parts of the country where it remained dry and clear, with an air frost forming in rural parts of south-east England. Some mist and fog also developed overnight, but this soon cleared once the sun had risen. Many places saw sunny spells during the day. The weather regime changed from calm to unsettled conditions as a band of rain pushed into Cornwall during the second half of the afternoon of the 15th October. It continued northwards and eastwards across south-west England and Wales, into the Midlands and Northern Ireland during the evening, and then into northern England and southern Scotland overnight. This rain was fairly heavy in places (Met Office 2012). The effect of this change in weather type reduced the occurrence of low visibility conditions due to mist and fog.

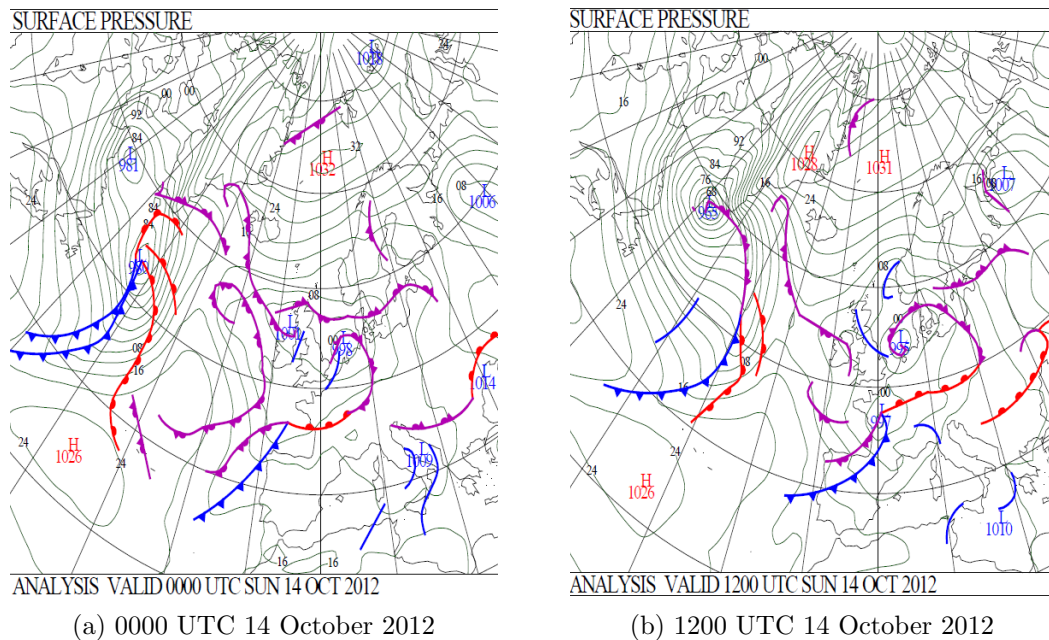
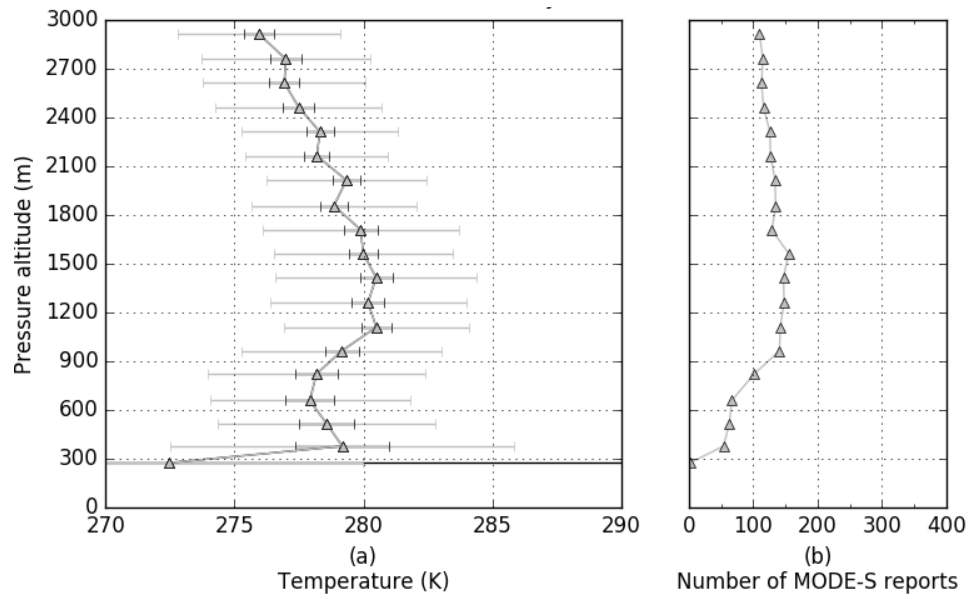
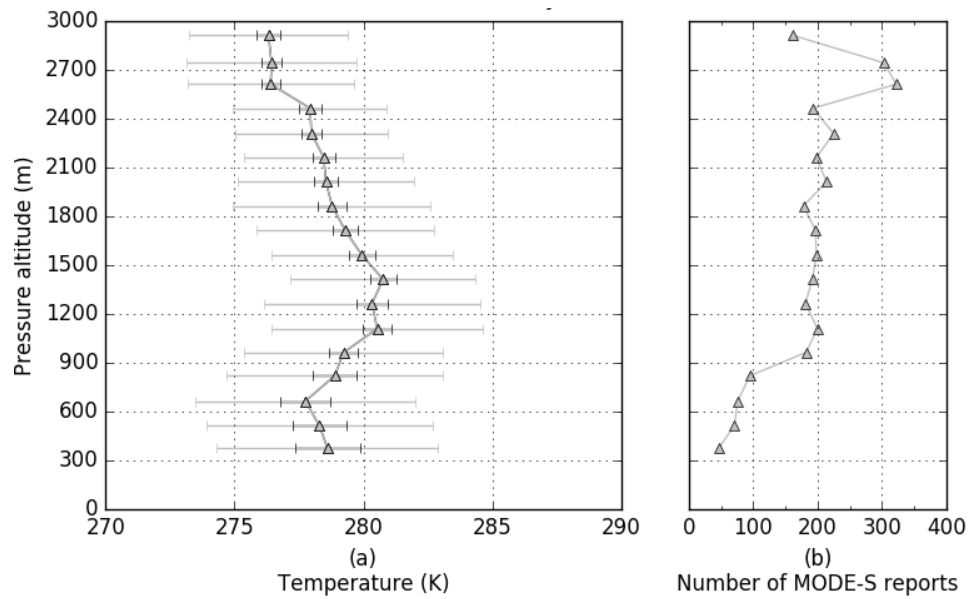


Figure 3-3: Met Office Analysis Charts for NATS case study day 14th October 2012 (Met Office 2012). Images are Crown Copyright and reproduced under the Open Government Licence for public sector information (<https://www.nationalarchives.gov.uk/doc/open-government-licence>, last accessed 29th August 2016.)

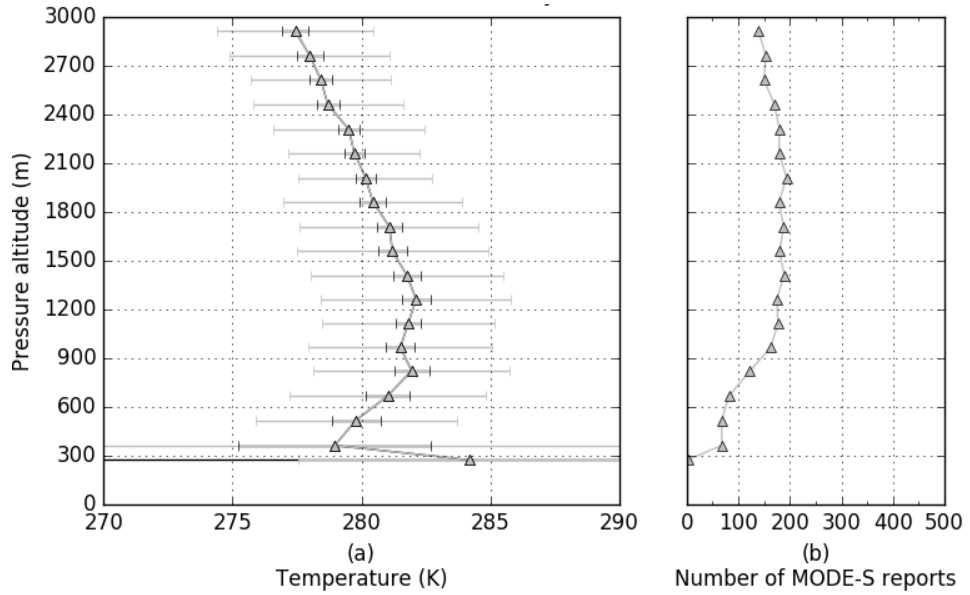


(a) 0600 UTC 14th October 2012

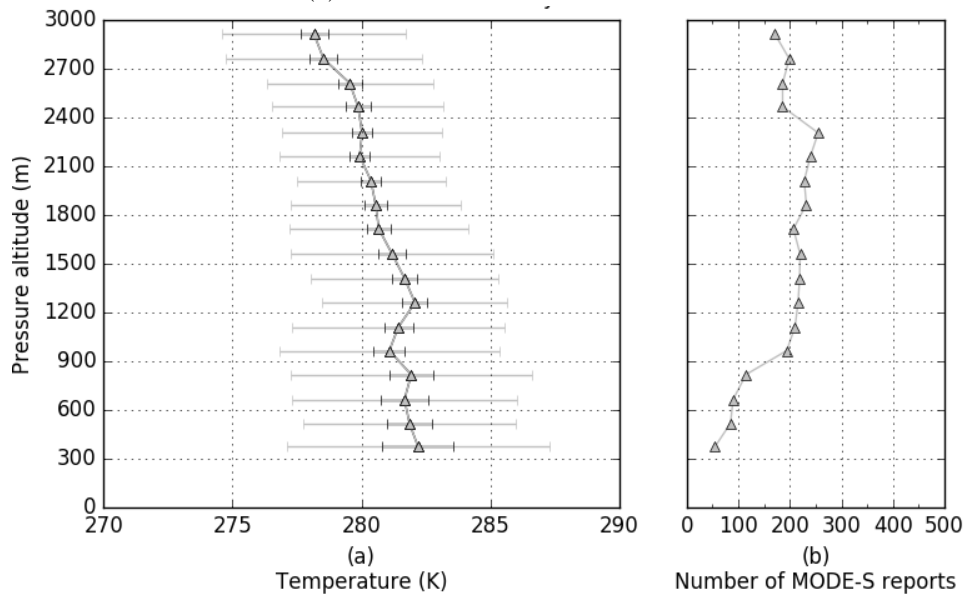


(b) 0900 UTC 14th October 2012

Figure 3-4: Each panel in this figure shows (i) aggregated Mode-S EHS temperature profiles for the London Heathrow domain. Reports used are ± 30 minutes of the validity time, with the mean profile centred at the validity time. (ii) The number of reports used for each altitude bin shown on the adjacent plot. For plotting purposes each aggregated report is plotted at the mean altitude of the reports within the altitude bin. The error bars are for the standard deviation (grey) and the 95% confidence limits for the mean (black), assuming a Student-t distribution based on the number of reports.

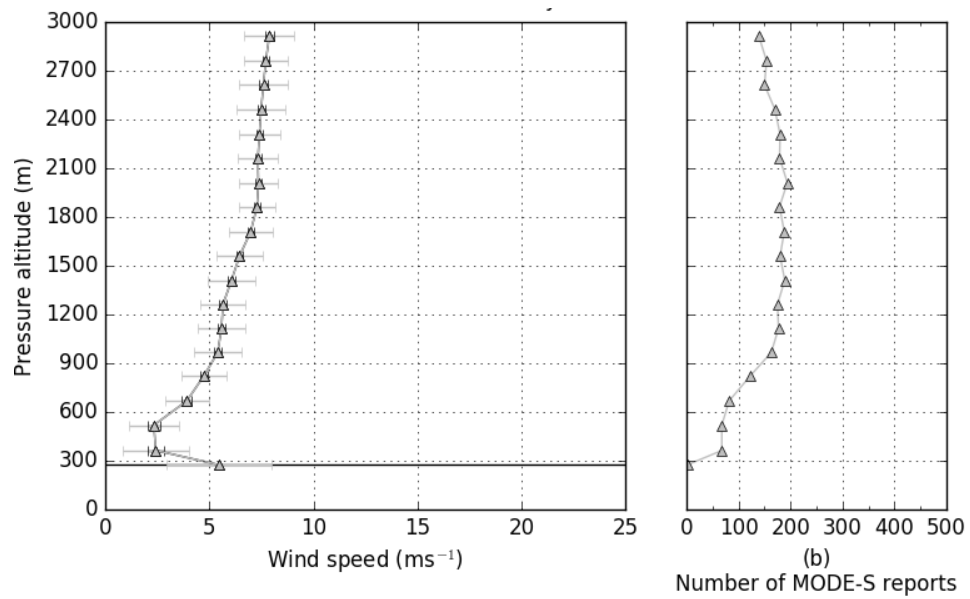


(c) 0600 UTC 15 October 2012.

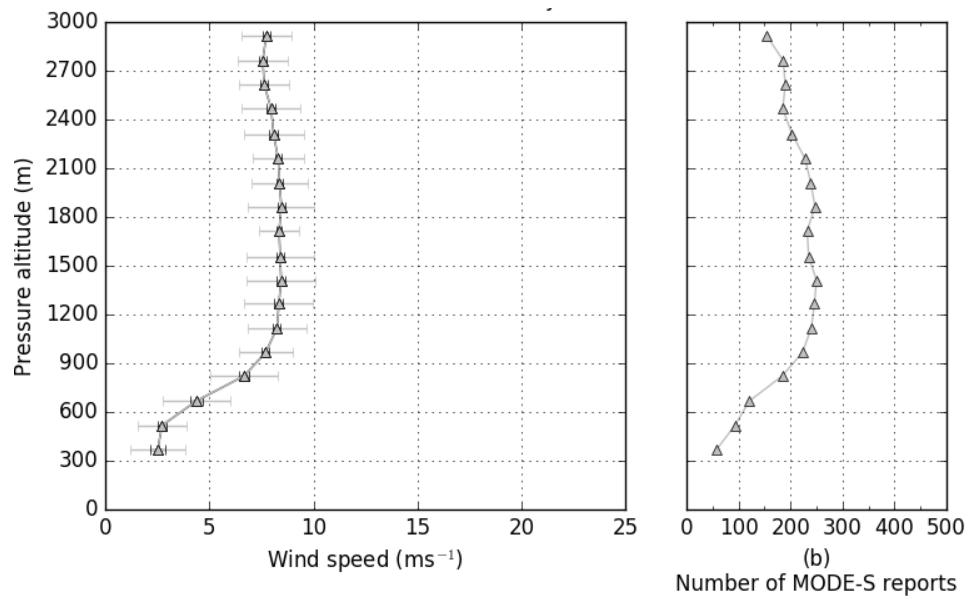


(d) 0900 UTC 15 October 2012

Figure 3-4: continued from page 43

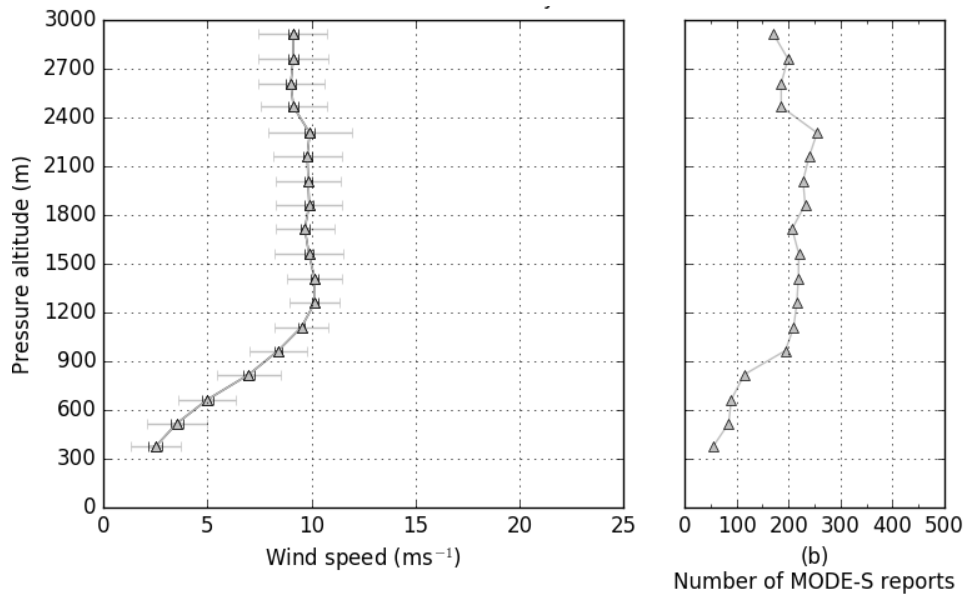


(a) 0600 UTC 15th October 2012

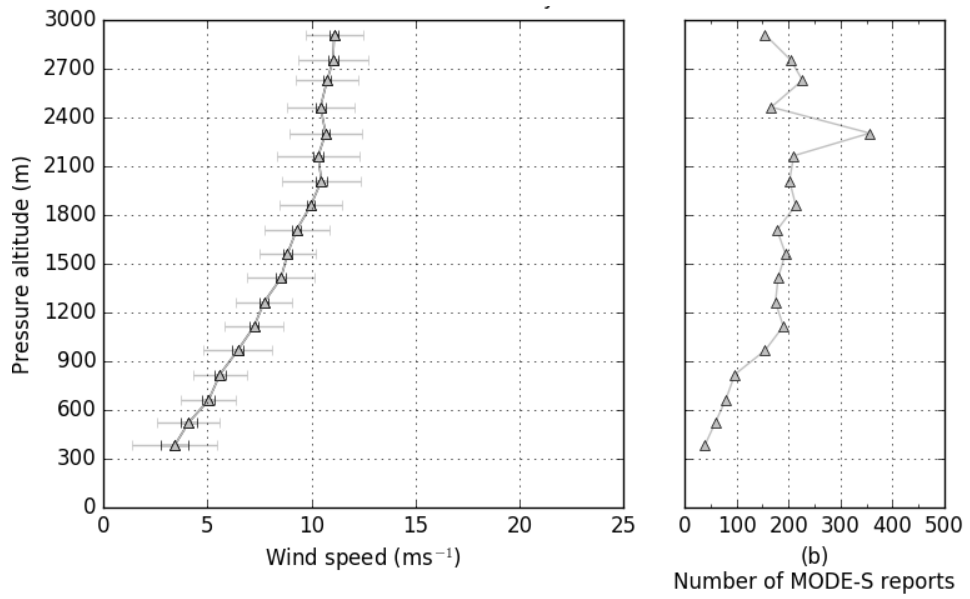


(b) 0700 UTC 15th October 2012

Figure 3-5: The legend is the same as for figure 3-4 except showing vertical profiles of the aggregated reports for horizontal mean wind speed.



(c) 0900 UTC 15th October 2012



(d) 1000 UTC 15th October 2012

Figure 3-5: continued from page 45

3.7.2 Case Study: 14th and 15th October 2012, Aggregated Observations

Since fog was present in the south-east of England, we use the aggregated Mode-S EHS reports to determine whether meteorological features such as the temperature inversion and low-level jet can be discriminated.

Figure 3-4 shows four panels (a), (b), (c) and (d). In each panel there is shown (i) a temperature profile constructed using aggregated Mode-S EHS reports and (ii) the number of reports used at each altitude bin. The four panels represent four time periods or snapshots of the vertical temperature profile at 0600 UTC and 0900 UTC on 14th October 2012 and 15th October 2012 for the London Heathrow domain. There are two error bars depicted for each aggregated observation. The first is the standard deviation (grey) which represents the variability of the Mode-S reports used to compute the aggregated observation. The second is the 95% confidence limits for the mean (black), assuming a Student-t distribution based on the number of reports. This represents the confidence in the aggregated observation, the fewer the reports the greater the estimated uncertainty, e.g., the lowest report as shown in figure 3-4a.

As discussed in section 2.3, one of the conditions associated with the formation of fog and mist is the presence of a temperature inversion. In the southeast of England and conditions were clear and calm. The 0000 UTC Herstmonceux radiosonde report on the 14th October indicates that there was a surface level temperature inversion present between 50 m and 500 m (figure 2-2, page 11). For the Heathrow domain, figure 3-4a indicates that for 0600 UTC there is an elevated temperature inversion between 500 m and 1200 m, and figure 3-4b indicates that by 0900 UTC the meteorological conditions persisted such that the elevated temperature inversion is still present. If the surface level inversion seen in the radiosonde measurement (figure 2-2) was widespread then it is likely it had become elevated by the early hours of the morning. The continuing calm conditions may explain why the overnight mist and fog was slow to clear on 14th October 2012 in some parts of southern and south-western England. The 0000 UTC Herstmonceux radiosonde report on the 15th October (figure 2-2) also shows a surface level temperature inversion present between 50 m and 300 m. Similarly, figure 3-4c suggests that for 0600 UTC there is a low-level temperature inversion between 300 m and 1200 m; again it is suggested that the inversion may have become elevated. By mid morning, 0900 UTC, the vertical profile in figure 3-4d shows signs that the inversion had started to dissipate as the weather regime become more unsettled.

Figure 3-5 shows the time series for the hourly mean vertical profile of wind speed between 0600 UTC and 1000 UTC 15th October 2012. The mean profile is constructed using the same method as for the temperature profile. This time series shows the

possible evolution of a low-level jet, which is a phenomenon associated with the presence of a temperature inversion (section 2.4, page 12.). We see at 0600 UTC (fig 3-5a) that winds are light for the whole altitude range. At 0700 UTC (fig 3-5b) the wind speed increases at levels above 750 m. The increased wind speed at low level is sustained at 0900 UTC (fig 3-5c) but by 1000 UTC (fig 3-5d) begins to break down. This appears consistent with the breakdown of the temperature inversion around the same time.

We make the following observations about figures 3-4 and 3-5. The number of reports decreases sharply below 900 m and there are no aggregated observations below 300 m. This may be due to a decrease in polling by the SSR or that there is no direct line of sight between the aircraft and the SSR operated by NATS. The standard deviation for the aggregated temperature observation is large $\approx \pm 3$ K, this indicates that there is a high degree of variability in the data used. There appear to be fluctuations or discrete step changes in the temperature profiles, which become larger when the number of reports used to compute the aggregated observations is less than 200. Similar features are evident in the aggregated observations for wind speed although to a lesser degree. In the next section we consider whether the increased fluctuations may be due to the Mode-S EHS processing.

3.8 Preliminary Analysis of Mode-S EHS Processing

In this section we take a closer look at the effect of Mode-S EHS processing on the true airspeed and Mach number, and the subsequent effects on the derived temperature.

Figure 3-6 shows a time series plot of the Mode-S EHS reported true airspeed and Mach number. The airspeed is shown in the unit of knots since this is the unit for such reports. The aircraft was on a descent path to London Heathrow, hence the airspeed shows a decrease for the time period. The figure also shows the derived temperature, which shows an increase over the period which would be consistent with the aircraft descent. However, it is clear that the temperature appears to vary by order of 10 K, even over short periods of time (< 15 s). Such variability is unlikely to be due to the variations in the ambient air temperature. Closer inspection shows that the temperature variation is due to step changes in either the true airspeed or Mach number. For example, between 06:36:30 and 06:37:00 UTC, the plots show that the Mach number is constant but there is a step change in the true airspeed. This causes a step change in the derived temperature. A similar effect on the derived temperature may be seen for step changes in Mach number when the airspeed is constant.

Figure 3-7 shows data that were obtained from a research aircraft used for atmospheric studies, which we conducted and are described more fully in chapter 4. The

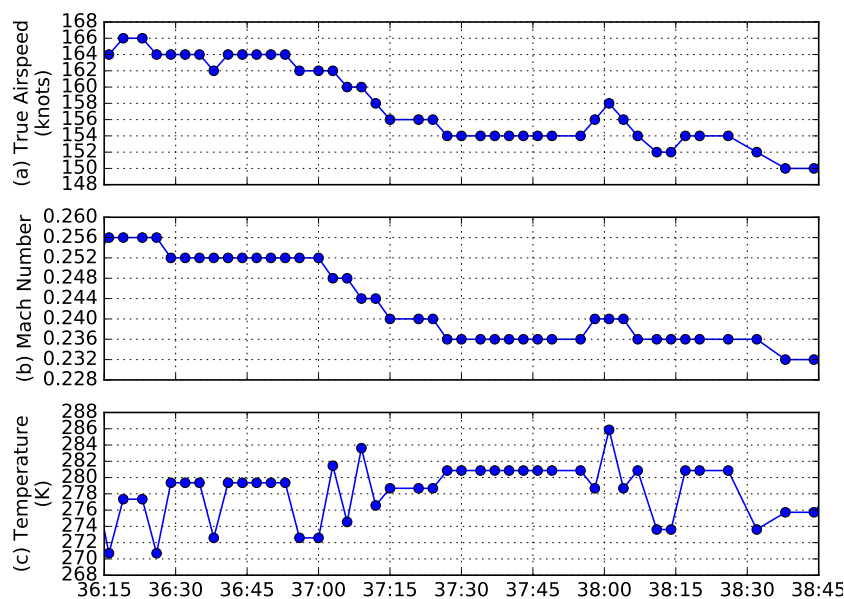


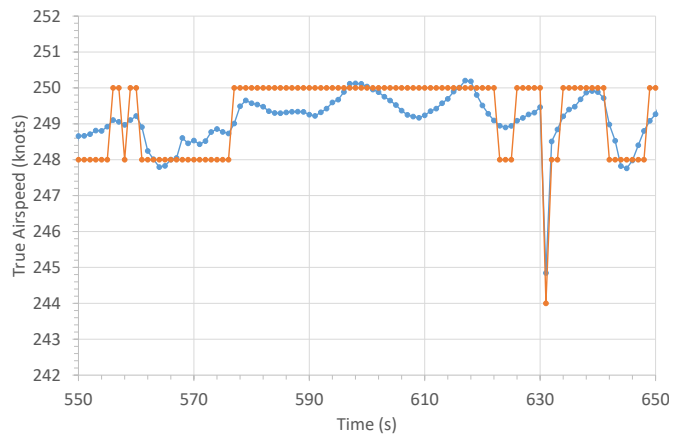
Figure 3-6: Time series plot of aircraft with Mode-S address AB4FAE. Plots are for (a) Mode-S EHS true airspeed, (b) Mode-S EHS Mach number and (c) Mode-S EHS derived temperature. Data obtained from NATS for 14th October 2012, the horizontal axis is for time of day from 06:36:15 to 06:38:45 UTC.

plots show a time series of (a) true airspeed, (b) Mach number and (c) temperature respectively. The time series show two traces, the blue trace show the reference (REF) data that could be available to the aircraft’s flight management system (FMS) and the orange trace shows the corresponding Mode-S EHS report.

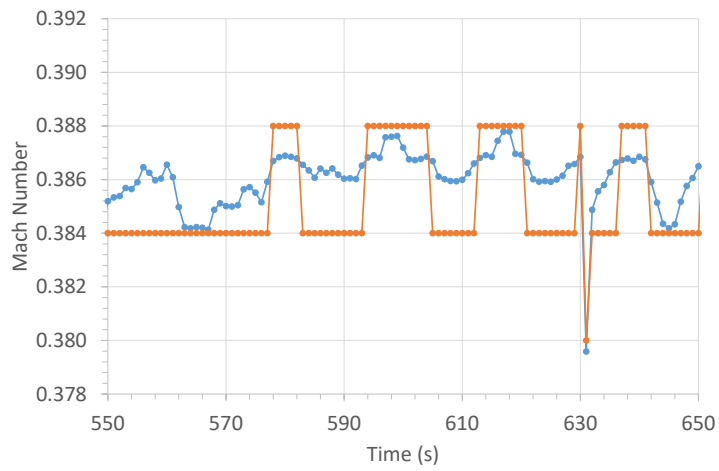
In figure 3-7a we see that there are periods where Mode-S EHS airspeed (orange) remains constant while the REF airspeed (blue) is varying. The apparent constant airspeed is the result of Mode-S EHS processing which rounds-up or rounds-down the REF airspeed to a multiple of 2 knots. A similar effect is seen in figure 3-7b, where the REF Mach number is rounded to some multiple of 0.004. We note also that the changes in Mode-S EHS reports of airspeed and Mach number are not synchronised in time.

Figure 3-7c shows the time series for the REF temperature (blue) and the corresponding Mode-S EHS temperature (orange). The REF temperature is a measured value. The Mode-S EHS temperature is computed using eq. (3.4) (page 38) and the data shown in figures 3-7a and 3-7b. We see that over the time period shown the REF temperature variation is of the order of 1 K, and for most of the time period it is a little above 275 K. By contrast for the same time period the Mode-S EHS derived temperature shows much greater variation both in time and magnitude.

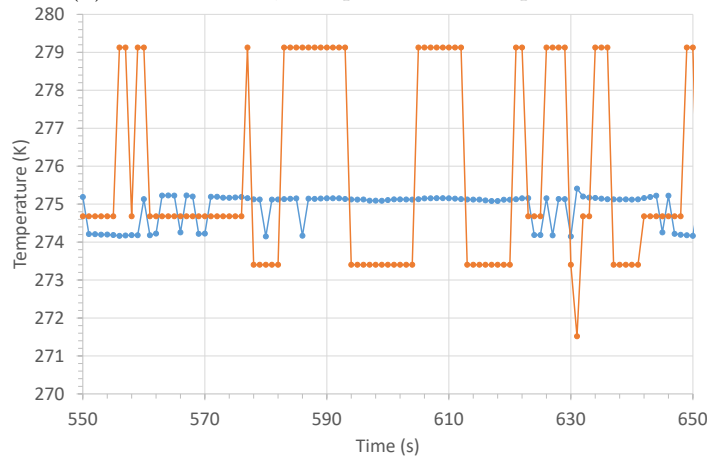
When we compare the time series in Mode-S EHS temperature with the correspond-



(a) True airspeed, the quantisation step is 2 knots.



(b) Mach number, the quantisation step is 0.004.



(c) Measured temperature v Mode-S EHS derived temperature.

Figure 3-7: Plots of the time-varying continuous signal (blue) and its ADC signal (orange) for (a) true airspeed and (b) Mach number. Plot (c) shows how the temperature derived from the digitised values in (a) and (b) varies when compared with the in situ measured temperature.

ing variation in Mode-S true airspeed and Mach number we see that the asynchronous variation in the latter two parameters gives rise to the variation in time in the former. For example, between 550 s and 570 s the Mode-S EHS Mach number is constant but the Mode-S EHS airspeed changes which causes the Mode-S EHS temperature to change also. For the first change at 556 s there has been no change in the REF temperature while at 560 s the temperature changes by 1 K. Between 590 s and 620 s we see that the Mode-S EHS airspeed is constant at 250 knots while the Mode-S EHS Mach number varies between 0.384 and 0.388. It is this variation that gives rise to the variation in the Mode-S EHS temperature. During this period of time the REF temperature shows only a small variation around 275 K.

Figure 3-7 shows clearly that the variation in Mode-S EHS temperature is dominated by the effects of Mode-S EHS processing, which involves rounding and truncating the REF data used to generate its reports. The difference between Mode-S EHS and REF data is known as quantisation error. If the observed Mode-S EHS variation is dominated by this type of error then it may be possible to model the error using the statistics of quantisation error. We suggest that fluctuations shown by de Haan (2011) are also due to quantisation error.

3.9 Quantisation Error

In this section we describe how quantisation error, ΔQ , arises when a Mode-S EHS transponder processes a time-varying analogue waveform, $C(t)$, into a digital waveform, $Z_m(t)$. This process is referred to as analogue-to-digital conversion (ADC), where the waveform is an electrical voltage. We suggest that it is the effect of this processing that gives rise to the oscillations observed in the Mode-S EHS observations shown in figures 3-6 (page 49) and 3-7 (page 50). A detailed discussion on ADC is beyond the scope of this project (see Begueret et al. (2008) or Pelgrom (2017, Ch. 8) for a description). However, a part of the process is described.

There are three steps for the Mode-S EHS processing:

(a) The first step is the conversion from an analogue waveform, $C(t)$, to a sampled waveform $S(t_k)$,

$$S(t_k) = C(t) I_k \text{ for sample } k = 1, 2, 3, \dots, \quad (3.11)$$

where t_s is the time between samples. The term I_k is an indicator function given by,

$$I_k = \begin{cases} 0 & \text{for } t - kt_s \neq 0 \\ 1 & \text{for } t - kt_s = 0. \end{cases} \quad (3.12)$$

(b) The sampled waveform is passed through to a flash ADC where it is converted

to a binary number. The flash ADC is an electronic circuit composed of a series of state comparators. The output of a state comparator is a binary value. For further details on the ‘flash’ ADC and state comparators see Horowitz & Hill (2015, Ch. 13) or Pelgrom (2017, Ch. 8) .

Mathematically, the ADC binary encoding of the sample $S(t_k)$ is in terms of the ADCs quantisation step size, ϵ , which is given by (Pelgrom 2017, p. 92),

$$\epsilon = \frac{|S_{max}|}{2^n}, \quad (3.13)$$

where $|S_{max}|$ is the maximum amplitude of the continuous-time waveform, $|C(t)|$, and n is the number of binary bits used by the ADC. The ADC process causes the sample $S(t_k)$ to be rounded-up or rounded-down by up to $\pm 0.5\epsilon$. (Note that if $|S_{max}| < |C(t)|$ then this results in distortion of the digital waveform called clipping, i.e., when $|C(t)| > |S_{max}|$ then $S(t_k) = |S_{max}|$. However, ADCs are usually designed to avoid this problem.) The ADC converts the sample $S(t_k)$ to binary form $Z_n(t_k)$ (Pelgrom 2017, p. 92),

$$Z_n(t_k) = \sum_{p=0}^n b_p 2^p \epsilon, \quad (3.14)$$

where b_p is an indicator that represents the state of the ADC at the binary bit position p ,

$$b_p = \begin{cases} 1 & \text{ADC state 'on'} \\ 0 & \text{ADC state 'off.'} \end{cases} \quad (3.15)$$

(c) The final step in the Mode-S EHS processing is truncation, which reduces the number of bits from n to m . This step uses the first m higher-order terms from $Z_n(t_k)$ so the truncated value is,

$$Z_m(t_k) = \sum_{p=n-m}^n b_p 2^p \epsilon, \quad (3.16)$$

where $m < n$.

The quantisation error is then the difference between the analogue input value and the digitised output value (Widrow et al. 1996, Bennett 1948),

$$\Delta Q = C(t) - Z_m(t), \quad (3.17)$$

where $Z_m(t) = Z_m(t_k)$ for $kt_s < t < (k+1)t_s$, i.e., $Z_m(t)$ remains constant until the next sample is taken (this step is called ‘sample and hold’).

The distribution of ΔQ is finite and can be represented as a continuous uniform

distribution on the interval $[a, b]$ (Widrow et al. 1996),

$$F(\Delta Q) = \begin{cases} \frac{1}{b-a} & a < \Delta Q < b \\ 0 & \text{elsewhere} \end{cases} \quad (3.18)$$

the mean and variance of its distribution are given by Walpole et al. (2011, Ch 6) as,

$$E(\Delta Q) = \frac{b+a}{2} \quad (3.19)$$

and

$$Var(\Delta Q) = \frac{(b-a)^2}{12} \quad (3.20)$$

respectively. When $a = -\frac{1}{2}\epsilon$ and $b = \frac{1}{2}\epsilon$ then the mean $E(\Delta Q) = 0$ and the standard deviation of quantisation error is given by,

$$\sigma = \sqrt{Var(\Delta Q)} = \sqrt{\left(\frac{\epsilon^2}{12}\right)} = \frac{\epsilon}{\sqrt{12}}. \quad (3.21)$$

We hypothesize that it is the quantisation effect from ADC used by the Mode-S EHS processor that causes the step changes observed in the Mach number and true airspeed, as shown in figures 3-6 (page 49) and 3-7 (page 50). Furthermore, we suggest that this variability can be expressed as a contribution to observation error using the standard deviation of quantisation error.

3.10 Summary

In this chapter we have described how NATS use a network of SSRs to actively interrogate individual aircraft to request Mode-S EHS reports of the aircraft's state vector. We have used a sample of Mode-S EHS data from the NATS archive to construct vertical profiles of temperature and wind speed. We create these profiles by aggregating the Mode-S EHS reports into altitude bins within a defined region around London Heathrow airport. We have used these profiles to identify the occurrence of meteorological features, the temperature inversion and the low-level jet. We suggest that these may provide information that may be useful for operational meteorological forecasting and for numerical weather prediction. However, we note that quality of the observations requires further investigation. We suggest that quantisation error is a major contributor to the estimation of error in the aggregated observations and which affects the quality, and therefore, the utility of the resulting derived observations.

We use the knowledge and understanding gained from this initial study to motivate

the studies in the rest of this thesis. In chapter 4 we address our first thesis question about the accuracy of the measurements for horizontal wind and ambient temperature. We use the standard deviation of quantisation error to develop and validate error models for the Mode-S EHS observations. We use reports collected by the Met Office Mode-S EHS receiver network described in chapter 5 to address our second thesis question in chapter 6, what atmospheric phenomena within the boundary layer can be observed from using observations derived from these routine messages. For this question we construct vertical profiles for ambient temperature, and we show that quantisation is still a dominant source of error. In chapter 7 we address the third thesis question on the benefit that assimilation of these high frequency observations brings to the Met Office UKV numerical weather predictions. We suggest that the quantisation error remains a significant source for the observation error used in data assimilation.

Chapter 4

Comparison of Aircraft Derived Observations with in situ Research Aircraft Measurements.

We acknowledge that sections 4.2 to 4.9 inclusive are extracts from the paper published by Mirza et al. (2016).

4.1 Introduction

This chapter investigates the errors of Mode-S EHS derived observations resulting from the limited precision of the transmitted aircraft state vector. We do this using *in situ* recordings made with research-grade high precision instruments aboard the Facility for Atmospheric Airborne Measurements (FAAM BAe-146) (Smith & Gratton 2004). Unfortunately the FAAM aircraft does not have a Mode-S transponder so we emulate the processing of the aircraft's state vector, using the in situ research observations, so as to generate Mode-S EHS type reports. We then derive the temperature and wind and compare with the actual *in situ* observations. We also derive novel error models based on a consideration of Mode-S EHS processing and validate these models using the *in situ* observations.

This chapter is organized as follows: in section 4.2 we describe the FAAM aircraft, the data parameters available from its avionics systems and how we emulate Mode-S EHS reports using data recorded by the FAAM BAe-146. Section 4.3 describes the instruments used to obtain the in situ observations and details the six case studies to be examined. We evaluate one case study in detail and describe the methodology used for the analysis. Section 4.4 defines our notation and metrics for our quality assessment

of the derived temperature, section 4.5, and horizontal wind, sections 4.6 and 4.7. We derive and apply our error models for the Mode-S EHS processing. Section 4.8 presents the results for all of the cases studied, which suggest that the observation error standard deviation for temperature increases from 2 K at 10,000 m to 4.5 K near the surface, an order of magnitude greater than AMDAR's 0.4 K (Painting 2003). For the cases studied, the observation error standard deviation for horizontal wind is up to 0.5 ms^{-1} compared with AMDAR's 2 to 3 ms^{-1} (Painting 2003). These results are shown to be due to the reduced precision of the aircraft state vector that results from Mode-S EHS processing. Section 4.9 summarizes the findings of this work and concludes that horizontal wind derived from Mode-S EHS observations may have practical applications for high-resolution NWP, while derived temperatures may be aggregated from multiple aircraft to provide useful information. However, this requires further investigation to assess how to minimize their errors. Finally, in light of the findings in this chapter, we note that direct reports of higher precision data would be preferable.

4.2 Facility for Atmospheric Airborne Measurements (FAAM BAe-146)

The Facility for Atmospheric Airborne Measurements (FAAM) BAe-146 (Smith & Gratton 2004) is a research aircraft operated by the United Kingdom's National Centre for Atmospheric Science (NCAS). It is a modified BAe 146-301. This facility provides an aircraft measurement platform for use by the UK atmospheric research community on campaigns throughout the world. The aircraft carries research-grade instruments to make measurements for a particular campaign. These data are recorded every second while the aircraft is in flight and at 32-bit floating point precision. Note this is not intended to indicate the precision of the actual research instrument. Two parameters, pressure altitude and indicated airspeed, are recorded from the flight management system via a network interface card that uses the Aeronautical Radio Incorporated (ARINC) 429 Standard.

4.2.1 Aeronautical Radio Incorporated (ARINC) 429 Standard

A network protocol is used to transfer data between aircraft subsystems. The network protocol used aboard the FAAM is the Aeronautical Radio Incorporated (ARINC) 429 standard (AEEC 2004; Spitzer 2006, Ch. 2). The network protocol defines how data are transferred in the form of data packets. An ARINC 429 data packet is a 32-bit binary number, of which 20 bits are available for representing data; label information

to indicate the content of the data packet uses 8 bits; the remaining bits are available to indicate the validity and quality of the data in the packet. The actual number of bits used to represent data is determined by consensus among the original equipment manufacturers, then published as an aeronautical standard. If this number is less than 20 bits then the unused bits may be re-purposed, for example to store data to a higher level of binary precision during computation. From the ARINC-429 standard, the data range, number of bits, and the data increment that are relevant for meteorological reporting are listed in table 4.1. (The network protocol will be aircraft-type specific, for example, newer aircraft may use the later edition of the standard, ARINC 629. An ARINC 629 data packet has 16 bits available for representing data.)

The data used for the aircraft state-vector are represented using an n -bit binary counter, where n is the maximum number of bits. The data increment or quantisation step, ϵ , is the decimal value of the least significant bit (LSB). This is defined using eq. (3.13),

$$\epsilon = d/2^n,$$

where d is the numerical range of the reported parameter and 2^n is the range of the counter expressed as a decimal integer. The precision of the data is taken to be $\pm 0.5 \times \epsilon$. For example, the ARINC-429 label 205 is for Mach number, M , and its numerical range is defined as $0 \leq M < 4.096$. The binary counter used to represent this range is of length 16 bits, which provides a decimal integer range from 0 to 2^{16} . The value of the LSB is then $\epsilon = 4.096/2^{16} = 0.00006250$. Thus the ARINC-429 Mach number precision is taken to be ± 0.00003125 . For examples of how data can be represented using an n -bit binary counter see Begueret et al. (2008).

4.2.2 The Mode-S EHS Message Format

The Mode-S EHS message format (EUROCAE 2008) is used by the Mode-S EHS transponder to transfer data between aircraft subsystems and ground-based subsystems and is part of the secondary surveillance radar system (Boisvert & Orlando 1993). The precision of the data contained in a Mode-S EHS message is lower than that of the ARINC-429 data packet. Table 4.1 shows that most of the parameters relevant for meteorological reporting are reduced from 16 bit to 10 bit representation. Using eq. (3.13), the Mode-S EHS Mach number precision is taken to be ± 0.002 .

A Mode-S EHS transponder reports an aircraft's state vector using the reduced precision parameters listed in table 4.1. These reports are retrieved by a secondary surveillance radar network operated by ATM. The maximum rate at which these reports are requested is determined to some extent by the rotation rate of the secondary radar;

Table 4.1: Aircraft state parameters relevant for meteorological reporting using the ARINC-429 standard (AEEC 2004) and for transmission by Mode-S EHS (EUROCAE 2008). These data are expressed using an n-bit binary counter, where n is the number of bits. The data increment is the decimal value of the least significant bit (LSB). This is defined as the range of the reported parameter divided by the numerical range of the n-bit binary counter. The precision is taken to be $\pm 1/2 \times \text{LSB}$. For example, the Mach number for Mode-S EHS is rounded to three decimal places with a precision of $\pm 1/2 \times 0.004$ (ICAO 2012). Precisions for latitude, longitude and barometric pressure altitude are stated simply as expected precisions because of the complex algorithms used to encode and decode these data. Number of bits include an extra bit to represent numerical ranges with negative values.

Parameter	Symbol	Units	Mode-S EHS			ARINC-429			Comment	
			Numerical Range, d	Number of bits, n	Data increment of LSB, ϵ	Numerical Range, d	Number of bits, n	Data increment of LSB, ϵ		Label
Roll angle	θ_R	degrees	± 90	10	0.175	± 180	15	0.01	325	Rotation of the aircraft about its longitudinal axis which runs from the nose to the tail. Clockwise rotation is positive.
True track angle (ground heading)	θ_G	degrees	± 180	11	0.175	± 180	16	0.0055	313	Aircraft's direction of travel along the Earth's surface reported in degrees clockwise from true north.
Ground speed	V_G	knots	0 to 2046	10	2	0 to 4096	15	0.125	312	Speed of the aircraft with respect to the Earth's surface.
Magnetic heading	θ_{mag}	degrees	± 180	10	0.175	± 180	16	0.0055	320	Direction of the aircraft's longitudinal axis in reported in degrees clockwise from magnetic north.
True airspeed	V_A	knots	0 to 2046	10	2	0 to 2048	15	0.0625	210	Speed of the aircraft with respect to the air.
Mach number	M	—	0 to 4.096	10	0.004	0 to 4.096	16	0.0000625	205	Ratio of the aircraft's true airspeed to the local speed of sound.
Latitude	ϕ	degrees	± 180	20	0.00034	± 180	21	0.000172	310	Geographic position at the Earth's surface. Accuracy when airborne is equivalent to 5 metres.
Longitude	λ	degrees	± 180	20	0.00034	± 180	21	0.000172	311	Geographic position at the Earth's surface. Accuracy when airborne is equivalent to 5 metres.
Barometric pressure altitude	H	feet	-1000 to 126752	15	4	0 to 131702	17	1	203	Vertical height above mean sea level under ideal conditions. Accuracy depends on phase of flight.
Time	t	seconds	-	-	0.2	1	20	1×10^{-6}	140	Universal Coordinated Time (UTC).
Static Temperature	T_S	Celsius	± 128	11	0.125	0 to 512	11	0.25	213	Meteorological Routine Aircraft Report.
Wind speed	V_{ws}	knots	0 to 511	9	1	0 to 256	8	1	315	Meteorological Routine Aircraft Report.
Wind direction (true)	θ_{wd}	degrees	0 to 360	8	1.41	± 180	13	0.05	316	Meteorological Routine Aircraft Report.

typically every 4 to 12 seconds. However, other factors may reduce the number of reports received, e.g., distance from the radar, air-traffic density and radio interference. Nevertheless, the number of reports received is (usually) sufficient to enable ATM to perform their function of maintaining safe separation between aircraft. The parameters for the aircraft's state vector are stored within the Mode-S EHS transponder on the aircraft and updated, typically, every 1.3 seconds (ICAO 2012).

4.2.3 Emulation of Mode-S EHS messages

The FAAM aircraft is not equipped with a Mode-S EHS transponder. Thus for this study Mode-S EHS reports for the aircraft's state vector were instead emulated using data recorded by the FAAM aircraft, although the actual transmission of the Mode-S EHS message was not emulated.

The parameters for the aircraft's state vector are drawn from the FAAM's recorded data. The Mode-S EHS ground-direction, ground speed, magnetic-heading, latitude, longitude and time-of-report are obtained from the FAAM's global positioning system (GPS) and inertial navigation system (INS) (Woolley 2008*a*, Applanix 2006). The pressure altitude was obtained from the aircraft's FMS. The Mach number, M , is calculated post-flight using the equation (Collinson 2011, pp. 392-395),

$$\frac{Q}{P_S} = (1 + 0.2M^2)^{\frac{7}{2}} - 1, \quad (4.1)$$

where Q (hPa) is the pitot-static pressure difference and P_S (hPa) the static pressure, obtained from the FAAM's turbulence probe (Woolley 2014*a*). The true airspeed was obtained by the following method: A pitot-static pressure difference was measured by the turbulence probe, from which a Mach number was obtained. This, along with the de-iced temperature measurement, was used to compute the true airspeed. Full precision data are used in these computations. More details about these sensors are given in section 4.3.

Before being passed to a process that generates the Mode-S EHS message format, each parameter is converted from 32 bits floating point representation to 16 bits unsigned integer. This requires the Mach number to be expressed in the unit of milli-Machs. The directional parameters are recast as follows:

- (i) The data range of the ground heading, θ_G , is changed to $0^\circ \leq F(\theta_G) < 360^\circ$, where

$$F(\theta_G) = \begin{cases} \theta_G & : 0^\circ \leq \theta_G < 180^\circ \\ \theta_G + 360^\circ & : -180^\circ \leq \theta_G < 0^\circ. \end{cases} \quad (4.2)$$

Table 4.2: Algorithm for Mode-S EHS processing. The middle column of the table contains the general algorithm for Mode-S EHS processing. The right-hand column illustrates the Mode-S EHS processing for an input value representing the ARINC Mach number, using the appropriate parameters given in table 4.1.

Step Number	Algorithm	Example calculation for Mach number
0	The input values are the data, I_{32} , the data increment, ϵ and the data range d .	The input values, expressed in the unit of milliMachs, are the Mach number, $I_{32} = 541$, the data increment is $\epsilon = 4$, the data range, $d = 4096$
1	Compute the decimal value of the least significant bit, $LSB = d/2^{16}$.	$LSB = 4096/2^{16} = 0.0625$
2	Express the input data as a 16 bit unsigned binary value, $I_{16} = I_{32}/LSB$.	0010000111010000
3	Express the precision as a 16 bit unsigned binary value, $P_{16} = 0.5 \times \epsilon/LSB$.	0000000000100000
4	Round-up the input data by computing the sum, $I_{16} + P_{16}$.	0010000111110000
5	Truncate the result to the first ten bits, where \wedge is the logical ‘‘AND’’ operator, $I_{10} = (I_{16} + P_{16}) \wedge (1111111111000000)$	0010000111000000
6	Convert I_{10} to a decimal value	$I_{10} = 8640$
7	Compute the result, $R = I_{10} \times LSB$.	$R = 8640 \times 0.0625$
8	Return the result,	$R = 540$ milliMachs

- (ii) The input true heading, θ_A , is converted to magnetic-heading, θ_{mag} , using the 2010 World Magnetic Model (Maus et al. 2010), so that its data range is $0^\circ \leq F(\theta_{mag}) < 360^\circ$, where

$$F(\theta_{mag}) = \begin{cases} \theta_{mag} & : 0^\circ \leq \theta_{mag} < 180^\circ \\ \theta_{mag} + 360^\circ & : -180^\circ \leq \theta_{mag} < 0^\circ. \end{cases} \quad (4.3)$$

(The conversion between true heading and magnetic-heading is discussed further in subsection 4.2.4.)

The algorithm used to convert the aircraft state parameters to the corresponding Mode-S EHS bit-level precision is given in table 4.2. The algorithm is illustrated using an example computation for the Mode-S EHS Mach number. The effect of the algorithm is to round-up or round-down the input value by an amount such that the result is a multiple of the LSB for Mode-S EHS. (A similar algorithm is used for converting FAAM’s core data to the corresponding ARINC-429 bit level precision.)

4.2.4 Aircraft True Heading

In order to compute the horizontal wind-vector, the aircraft’s true heading, θ_A , is required. This is the direction of the aircraft’s longitudinal axis measured clockwise from

Geographic North. However, the Mode-S EHS report contains the aircraft’s magnetic-heading, θ_{mag} , which is the angle measured clockwise from Magnetic North. Geographic North and Magnetic North are not coincident and their separation varies over time and by location. In addition, the aircraft’s true heading may be subject to instrument error that depends on the type of heading-reference system being used for navigation (Mullally & Anderson 2011, Jacobs et al. 2014). Thus, the aircraft’s true heading, θ_A , is the sum of these components:

$$\theta_A = \theta_{mag} + \theta_{var} + \theta_{dev}, \quad (4.4)$$

where θ_{var} , called the magnetic variation, takes account of the angular difference between Geographic and Magnetic North; and θ_{dev} , called the magnetic deviation (or the compass error), takes account of the remaining sources of error which include instrument errors in the heading reference system.

An aircraft’s FMS applies the corrections for θ_{var} and θ_{dev} . The magnetic variation, θ_{var} , is obtained from a look-up table based on the World Magnetic Model (WMM) (Maus et al. 2010). The WMM models the estimated variations in the Earth’s magnetic field and is updated every five years. The aircraft’s magnetic deviation, θ_{dev} , is obtained from calibration of the heading reference system against a reliable reference source, usually a high-precision gyroscope (Civil Aviation Authority 2013), and programmed into the FMS as a look-up table. (It should be noted that a FMS may be using outdated versions of the WMM (Nakamura 2013, Weinstein 2009) and compass calibrations are only required to be performed once every two to three years (Civil Aviation Authority 2013).)

The FAAM INS reports true heading, θ_A . We assume that the INS is calibrated so that the magnetic deviation, θ_{dev} , is approximately zero. This is because the tables for magnetic deviation were unavailable. So for the purpose of this study the magnetic-heading is emulated as, $\theta_{mag} = \theta_A - \theta_{var}$.

4.3 Meteorological Research Measurements

The observation and reference data used in this study were recorded during the Convective Precipitation Experiment (COPE) which took place during the summer of 2013 (Leon et al. 2015). The project’s goal was to study the evolution of convective conditions within regions of the United Kingdom. In addition to data obtained during the COPE campaign, aircraft data were also obtained during scheduled flights for maintenance and instrument tests; including one flight for calibrating the International Sub-Millimetre Airborne Radiometer (Moyna et al. 2010). Table 4.3 lists the six flights

used for this study along with a short description of each flight. A total of 21.7 hours of flight data were recorded for six flights of which 12.2 hours passed quality control processing. The weather conditions for these flights are described by Eden (2013*a,b*).

Reference (REF) measurements of the horizontal components of the wind (U_{REF} , V_{REF}) are obtained from the aircraft's five-port pressure sensor located in the nose-cone of the aircraft. The centre port measures the static pressure. The wind-vector components are then determined by the pressure differential recorded by the remaining four sensors. The methodology is described by Brown (2004*a*) and Nicholls (1980). The method makes use of the aircraft's ground vector, as measured by the inertial navigation system. Corrections are made for the rotation of the aircraft around its pitch axis, which is an imaginary line that runs from wing-tip to wing-tip; and its yaw-axis, which is an imaginary line that runs vertically through the aircraft; both lines have their origin at the aircraft's centre of gravity.

Temperature is recorded by two Rosemount type 102B hot-wire thermometers located at the front starboard side of the aircraft's main body. One thermometer is heated to prevent icing. These thermometers record the total-air-temperature (Woolley 2009, Stickney et al. 1994), which is the sum of the ambient temperature and the heating effect due to air being compressed in the sensor's housing. The measurement of the temperature is done by two sensors; one sensor has its housing heated to prevent icing while the other's housing is not heated. During post-flight processing two ambient temperatures are recovered which are referred to as the de-iced temperature, where the effect of the heated housing is removed, and the non-de-iced temperature (Woolley 2008*b*). The de-iced temperature is used as the reference temperature. The aircraft's geographic position is recorded by an INS/GPS receiver. Reference time is taken from the INS/GPS receiver and is measured as the elapsed number of UTC seconds since the start of the day. In addition to these measured parameters, we use the aircraft's recorded pressure altitude and indicated airspeed which are obtained from the aircraft's FMS.

Once the aircraft has returned to its base of operations, the FAAM measurements are post-processed to produce data at 1 Hz and are corrected for known instrument biases. The indicated air speed and pressure altitude are used as first-guess values for calibration when deriving the meteorological measurements for the horizontal and vertical winds, and ambient temperature. The expected accuracies of aircraft state parameters after post processing are shown in table 4.4. The expected accuracies for the U_{REF} and V_{REF} obtained from the turbulence probe are assumed to be $\pm 0.2 \text{ ms}^{-1}$. This assumption is based on the experiments carried out by Tjernstram & Friehe (1991) that used a similar turbulence probe on a Sabreliner 40A.

Table 4.3: Brief description of the six flights studied in chapter 4. All flights took place within the United Kingdom between June and August 2013. Weather conditions for these cases are described by Eden (2013*a, b*)

Date	Flight No.(f)	Description of flight
25 Jun	B783	Departure from Cranfield Airport, United Kingdom (UK) . Flight over East Anglia and nearby coast. Descent from cruising altitude 6000 m to low-level 300 m. Followed by three staged ascents with level flights at 1500 m, 2100 m and 2400 m, each lasting 15 minutes. Ascent to 8200 m followed by a descent to 600 m. Followed by a staged descent back to Cranfield Airport. Region of flight: 0.4°E to 2.4°E and 52.2°N to 53.4°N
04 Jul	B785	Departure from Exeter Airport, UK, flying westerly to Irish sea North of Cornwall. Maintained steady altitude circling in a North-South trajectory at 4600 m for an hour followed by an East-West trajectory at 7600 m for an hour. This was followed by staged descents from 9100 m, 7600 m, 6100 m, 3050 m, 300 m, each stage lasting around ten minutes. The low level stage at 300 m lasting around one hour with trajectories west-east over Cornwall followed by south-north over Devon. Flight returned back to Exeter Airport. Region of flight: 7.0°W to 3.5°W and 50.0°N to 51.5°N
11 Jul	B787	Departure from Exeter Airport flying north to Bristol Channel. On arriving performing East-West trajectories over the Irish Sea north of Cornwall. Staged ascents 300 m, 3000 m, 6000 m, 9800 m, each phase lasting around 45minutes. Followed by staged descents from 9800 m, 3000 m, 2400 m, each phase lasting around 30 minutes. Followed by staged descent to Exeter Airport. Region of flight: 7.0°W to 3.5°W and 50.0°N to 51.5°N
25 Jul	B789	Departure from Exeter Airport to Cornwall on arrival flying trajectories south-west to north-east. Staged ascents from 500 m to 3000 m incrementally at 150 m, each stage lasting approximately 5 minutes. Followed by an ascent to 3600 m and descent to 300 m before a staged return to Exeter airport. Region of flight: 5.0°W to 4.0°W and 50.0°N to 51.5°N
28 Jul	B790	Departure from Exeter airport arriving central Cornwall in the region between Truro, Bodmin and St Austell. On arrival executing North-South, East-West trajectories. Staged ascents from 300 m, 120 0m, 2700 m, 3300 m, 3800 m, each phase lasting approximately between 20 to 30 minutes. Final ascent to 4500 m before returning to Cranfield airport. Region of flight: 5.0°W to 4.0°W and 50.0°N to 51.2°N
29 Jul	B791	Departure from Exeter airport arriving Cornwall. On arrival executing south-west to north-east trajectories. Staged ascents from 300 m, 1500 m, 1000 m, 2700 m, 3500 m, 3800 m, 4100 m, 3800 m, each phase lasting approximately between 15 to 30 minutes. Final descent to 300 m then ascent to 3 km before returning to Cranfield airport. Region of flight: 6.0°W to 4.0°W and 49.8°N to 51.2°N

Table 4.4: Accuracy of FAAM Aircraft Parameters (Woolley 2014*b*)

Parameter	Instrument accuracy (for one standard deviation)
GPS/INS True heading	$\pm 0.02^\circ$
Horizontal Position	± 5 m
Altitude above mean sea level	± 7 m
Ground speed	± 0.07 ms ⁻¹
Total air temperature (non de-iced)	± 0.3 K
Total air temperature (de-iced)	± 0.3 K
Static Pressure (Corrected)	± 2 hPa
True airspeed (Corrected)	± 0.4 ms ⁻¹

Table 4.5: Acceptance criteria used for filtering the FAAM aircraft data.

Parameter	Threshold	Comment
true airspeed	$25 \text{ ms}^{-1} < V_A \leq 300 \text{ ms}^{-1}$	Gross error range check
magnetic-heading	$0^\circ < \theta_{mag} \leq 360^\circ$	Aircraft heading with respect to magnetic North
ground speed	$25 \text{ ms}^{-1} < V_G \leq 425 \text{ ms}^{-1}$	Gross error range check
ground heading	$0^\circ < \theta_G \leq 360^\circ$	ground heading with respect to geographic North
(Ground - Magnetic) Heading	$ \theta_G - \theta_{mag} < 45^\circ$	Gross error range check
Mach Number	$0.000 < M \leq 0.85$	Gross error range check
Roll Angle	$\leq \pm 1.5^\circ$	threshold for stable level flight

4.4 Notation and Metrics

For discussion of the results the notation listed in table 4.6 is used to maintain the distinction between the derived and reference values. An estimate of the unbiased sample standard deviation, σ , is obtained from the metrics of the mean bias (MB) and root mean square error (RMSE) (Wilks 2011, Jolliffe & Stephenson 2012) using (Ross 2009, p.271),

$$RMSE^2 = MB^2 + \sigma^2, \quad (4.5)$$

where

$$MB = \frac{1}{N_f} \sum_{i=1}^{N_f} (o_i - r_i), \quad (4.6)$$

Table 4.6: Notation for observations and measurements.

Symbol	Label	Comment
T_{REF}	Reference Temperature	The reference observations are the FAAM's measurements of the static ambient temperature measured by the de-iced sensor
U_{REF} and V_{REF}	Reference Horizontal Wind Components	The reference wind components derived from the FAAM's turbulence probe.
U_{ARINC} and V_{ARINC}	ARINC Horizontal Wind Components	The winds calculated using ARINC precision data and using eqs. (3.5) and (3.6) (page 38).
U_{Mode-S} and V_{Mode-S}	Mode-S EHS Horizontal Wind Components	The winds calculated using Mode-S EHS precision data and using eqs. (3.5) and (3.6) (page 38).
T_{MACH}	Mach Temperature	The static ambient temperature derived from the emulated Mode-S EHS report using eq. (3.4)(page 38)

and

$$RMSE = \sqrt{\frac{1}{N_f} \sum_{i=1}^{N_f} (o_i - r_i)^2}. \quad (4.7)$$

The term o_i is the i^{th} Mode-S EHS derived observation, i.e., T_{MACH} , U_{Mode-S} or V_{Mode-S} , and the term r_i is the corresponding REF observation matched by position and time, i.e., T_{REF} , U_{REF} or V_{REF} . The term N_f is the number of observation and reference pairs that passed the quality control criteria given in table 4.5. The uncertainty in the standard deviation is estimated by (Taylor 1982, pp.294-298),

$$\delta\sigma = \frac{\sigma}{\sqrt{2(N_f - 1)}}. \quad (4.8)$$

For comparing results we define a box-average. The pressure-altitude is divided into bins of height 0.3 km from the surface to 10 km. The Mode-S EHS reports, Mode-S EHS derived observation and corresponding REF observation are sorted into the bins. For each bin, σ , $\delta\sigma$, MB and RMSE are computed and each result assigned to the centre of each bin. In addition, the mean values of Mode-S EHS reports are computed and the result assigned to the centre of the bin. The results assigned to the centre of

each bin are referred to as the box-average.

4.5 Quality of Derived Mach Temperature

In this section we analyse the vertical profile of the temperature difference $T_{MACH} - T_{REF}$. An error model is derived to estimate the observed differences and we suggest that the differences are dominated by the effect of Mode-S EHS processing. We also use the error model to estimate the precision of the derived temperature, ΔT , for three levels of Mode-S EHS data precision.

4.5.1 Differences in T_{MACH} and T_{REF}

Figure 4-1(a) is the vertical profile of T_{REF} for the whole flight recorded by the FAAM de-iced temperature sensor. At the start of the flight there was a low level temperature inversion which had dissipated by the end of the flight. This can be seen as the two intercepts at the surface. Figure 4-1(b) is the vertical profile of T_{MACH} computed using eq. (3.4) (page 38). This profile shows the effects of Mode-S EHS processing. Firstly a distinct temperature inversion cannot be seen in the figure due to the spread in the data. Restricting the data plotted to the early part of the flight indicates this feature is still detectable in the derived measurements (not shown). Secondly, there is an apparent double profile between 7 km and 9 km; it was found that the reduced precision of the Mach number causes T_{MACH} to oscillate between two values resulting in the double profile. Figure 4-1(c) is the temperature difference profile $T_{MACH} - T_{REF}$. The magnitude of the differences range from 6 K near the surface to 3 K at high altitude. (The grey profile is discussed in section 4.5.2.) Figure 4-1(d) depicts the distribution of these differences as a histogram, for the whole flight. The distribution appears to be approximately symmetric and uni-modal in form, with a sample mean 0.029 K and a sample standard deviation 2.14 K.

4.5.2 Estimated Error in T_{MACH}

We use the method of error propagation analysis (Taylor 1982) on eq. (3.4) (page 38) which leads to the estimated Mach temperature error, ΔT , being given by,

$$\Delta T = \pm \frac{T_0}{A_0^2} \frac{2V_A}{M^2} \sqrt{\left(\Delta V_A^2 + \frac{V_A^2}{M^2} \Delta M^2 \right)}, \quad (4.9)$$

where ΔV_A is the true airspeed precision and ΔM is the Mach number precision. These precisions may be represented as the instrument's scale division, data increment or the

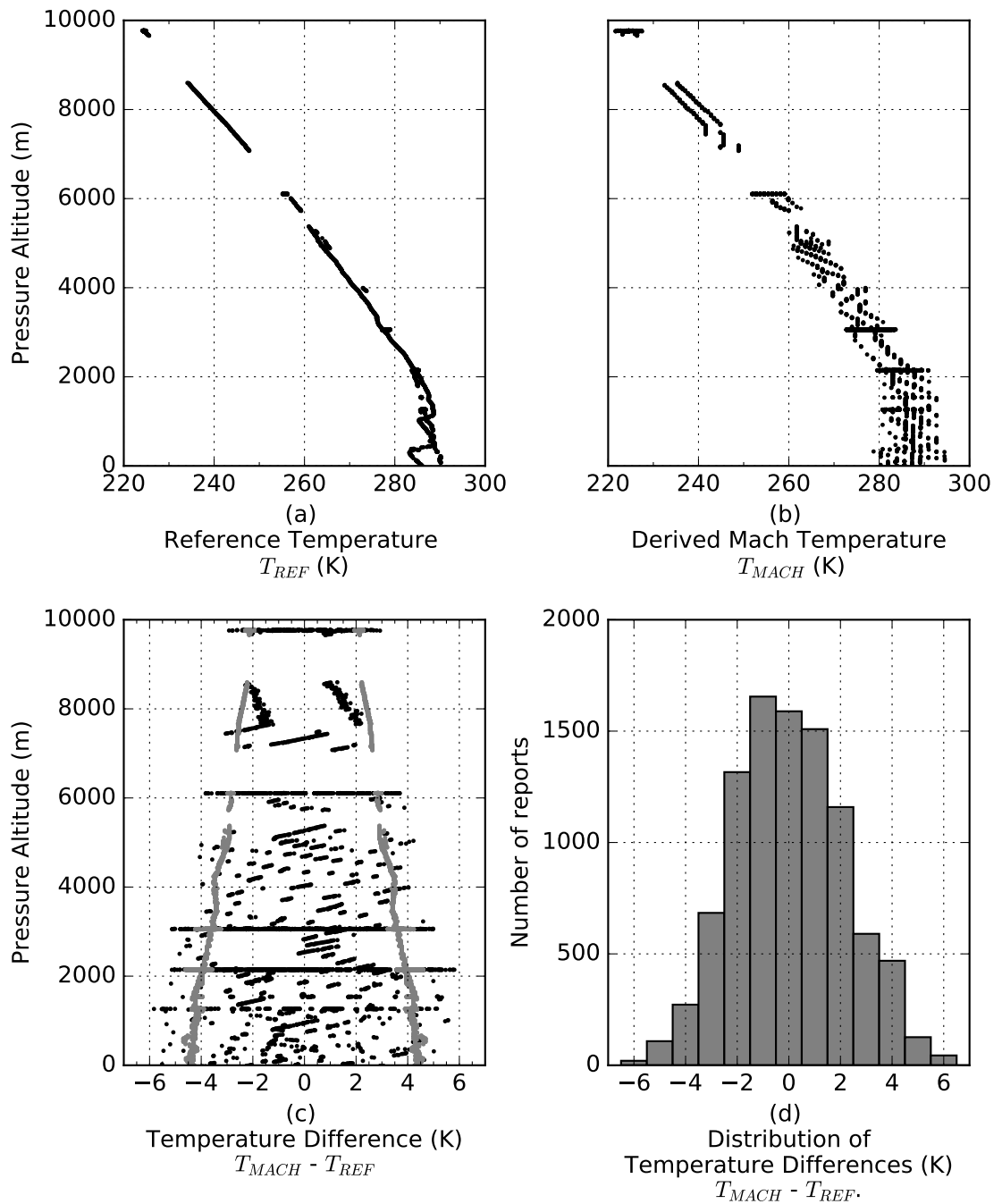


Figure 4-1: Flight B787 (11th July 2013) (a) Vertical profile of reference temperature T_{REF} . (b) Vertical profile of derived Mach temperature, T_{MACH} . The stripe effect is the result of the reduced precision of the input data. (c) Vertical profile of temperature difference $T_{MACH} - T_{REF}$ (black). The estimated maximum error profile for Mach temperature (grey) (see also figure 4-2(a)). (d) Histogram of temperature differences using a centred bin width of 1 K.

standard deviation obtained from a sequence of measurements (Taylor 1982). For Mode-S EHS reports the data increment for true airspeed is 2 knots (1.03 ms^{-1}) and for Mach number it is 0.004 (ICAO 2012). We use in situ measurements of temperature and an error model for Mode-S EHS processing to validate estimates of temperature error given by eq. (4.9), and suggest the source of the observed error estimates.

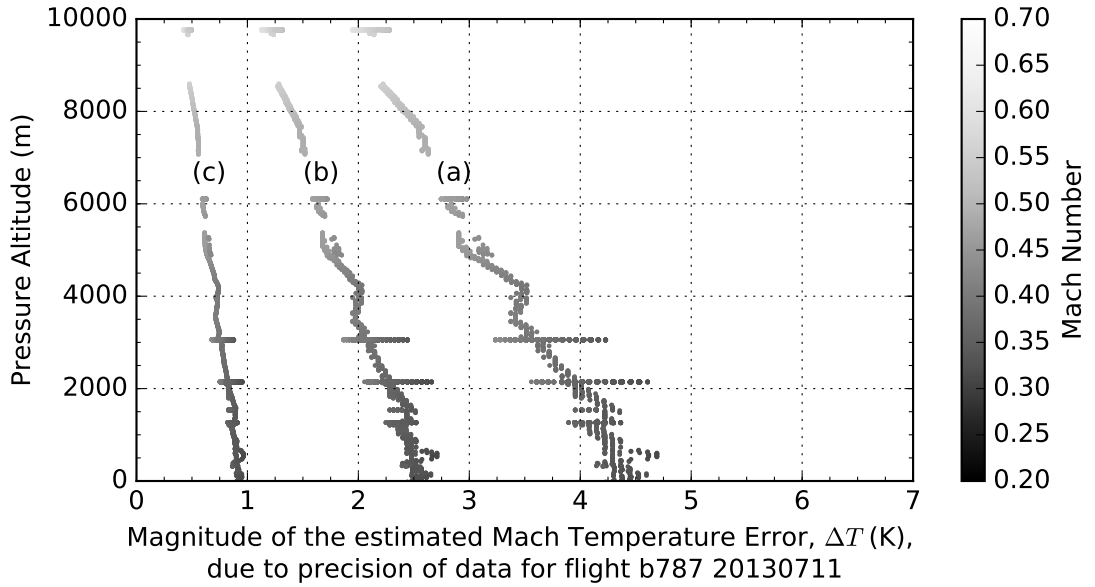
The true airspeed and Mach number from FAAM flight B787 are used to generate the corresponding emulated Mode-S EHS reports. In figure 4-2, profile (a) shows the estimated ΔT when the precision of the Mode-S EHS reported true airspeed is taken to be $\Delta V_A = 0.5 \times 2$ knots and Mach number is taken to be $\Delta M = 0.5 \times 0.004$. It is clear that the magnitude of the estimated error increases from 2.0 K to 4.5 K as the aircraft's altitude decreases. Profile (a) assumes a fixed error value (ΔV_A , ΔM) for each report of true airspeed and Mach number so the estimated temperature error (ΔT) represents a maximum value. However, due to the binary representation of the data, there is a contribution to the error which arises from the process of rounding and truncation called the quantisation error (Widrow et al. 1996). In section 3.9 (page 51) we discussed the digitization of an analogue signal. We noted that the quantization error may be uniformly distributed between $\pm 0.5\epsilon$, where ϵ is the magnitude of the data increment or quantisation step. The quantization error has a mean of zero and a standard deviation given by (Widrow et al. 1996),

$$\sigma = \frac{\epsilon}{2\sqrt{3}}.$$

If we use the standard deviation given by eq. (3.21) (page 53) as a measure of precision due to quantisation (Taylor 1982, Chapter 5) then for the true airspeed, $\Delta V_A = 2/\sqrt{12}$ knots and for the Mach number, $\Delta M = 0.004/\sqrt{12}$. Figure 4-2 profile (b) shows that the magnitude of the estimated error due to quantisation is approximately half that shown in profile (a), and increases from 1.25 K to 2.5 K as the aircraft's altitude decreases. A sensitivity analysis on the magnitude and standard deviation due to quantisation error was performed to seek desirable values for data increments for Mach number and true airspeed. This was done by increasing the number of bits for the Mode-S EHS reports of Mach number and true airspeed.

The sensitivity analysis indicates that to achieve ΔT at around 1 K near the surface, shown in figure 4-2 profile (c), then we require that the true airspeed precision to be $\Delta V_A = 1/\sqrt{12}$ knots and the Mach number precision to be $\Delta M = 0.001/\sqrt{12}$. However, it should be noted that the uncertainty profiles given in figure 4-2 are due to effects of quantisation error and do not consider other sources of error (Painting 2003).

We use the quantisation error model for the precision (eq. (3.21)) to analyse and



(a) Maximum Error, (b) Quantisation Error, (c) Ideal Quantisation Error.

Figure 4-2: This plot shows the vertical profile of the estimated error in the Mach temperature, ΔT , (using eq. (4.9)) derived from the emulated Mode-S EHS reports of true airspeed and Mach number for flight B787 on 2013-07-11. Gaps in the vertical profile indicate where data were removed as a result of quality control processing. The striped effect, most visible in profile (a), is the result of numerical rounding and truncation required for Mode-S EHS reporting precisions. Profile (a) shows the variation of ΔT with pressure altitude assuming precisions of the reported true airspeed is $\Delta V_A = 1$ knot (0.51444 ms^{-1}) and Mach number is $\Delta M = 0.002$. Profile (b) is the variation of ΔT assuming precisions arise from the standard deviation of quantisation error (using eq. (3.21)), $\Delta V_A = 2/\sqrt{12}$ knots and $\Delta M = 0.004/\sqrt{12}$. Profile (c) is the result of a sensitivity analysis to achieve an estimated temperature error of 1 K near the surface assuming the precisions for standard deviation of quantisation error are $\Delta V_A = 1/\sqrt{12}$ knots and $\Delta M = 0.001/\sqrt{12}$. The colour of the line and side-bar indicates the Mach number range for when the BAe-146 is in flight. Number of reports = 9541.

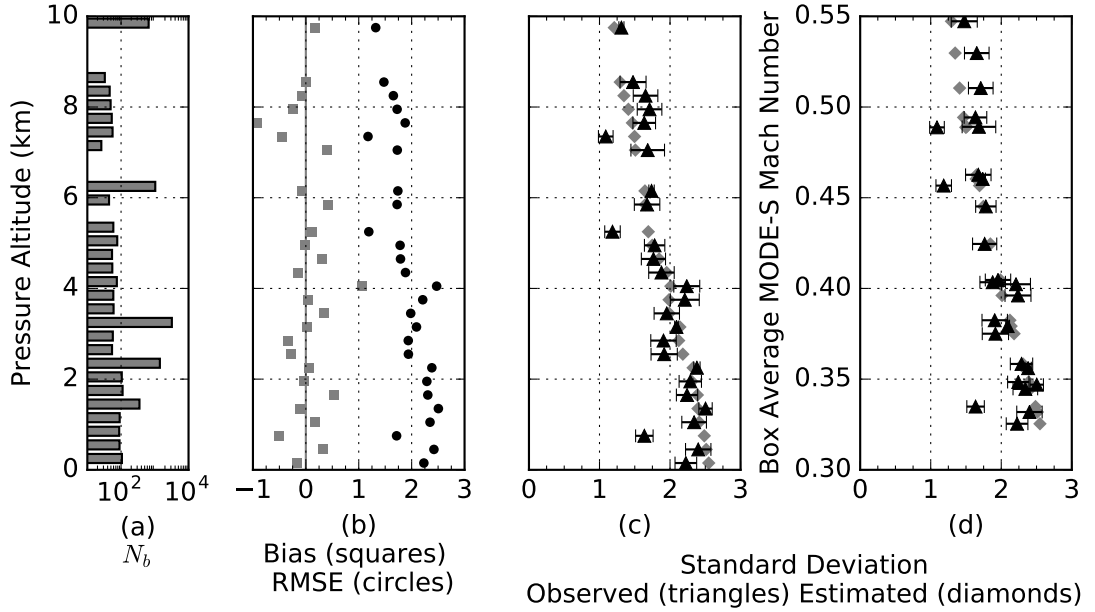


Figure 4-3: Flight B787 (11th July 2013). Box average statistics for temperature. Results binned by altitude, with bin heights at 0.3 km intervals. Plot (a) is the number of reports per altitude bin, N_b , expressed using a \log_{10} scale. Plot (b) vertical profile of temperature difference ($T_{MACH} - T_{REF}$) mean bias (MB) (squares) and RMSE (circles). Zero is marked by the vertical line. Plot (c) Vertical profile of the box-average observed σ (triangles) (using eqs. (4.5) and (4.8)) and the box-average ΔT (diamonds) due to the quantisation error (using eqs. (4.9) and (3.21)). Plot (d) depicts the results of plot (c) against the box-average M reported by Mode-S EHS.

characterize the error in T_{MACH} (given by eq. (4.9)) when compared with T_{REF} .

Figure 4-3 depicts box-average statistics for temperature differences $T_{MACH} - T_{REF}$. The data are binned into pressure altitude intervals of height 0.3 km. Figure 4-3 (a) is the number of reports per altitude bin, N_b , expressed using a \log_{10} scale. Figure 4-3 (b) depicts the vertical profile of the MB (squares) and RMSE (circles) for each pressure altitude bin. The box-average MB ranges between -1 K and 1 K but is often close to zero. This is expected since the difference $T_{MACH} - T_{REF}$ should on average be close to zero (compare with figure 4-1(c)). The box-average RMSE is greatest near the surface and decreases with altitude, with a total range of 1.2 - 2.5 K. (For comparison, for the whole flight the MB is 0.25 K and the RMSE is 2.06 K.) Figure 4-3 (c) depicts the vertical profile of the box-average ΔT (diamonds), computed using eq. (4.9), with precisions given by eq. (3.21) (page 53) for true airspeed $\epsilon = 2$ knots and for Mach number $\epsilon = 0.004$. Also depicted is the vertical profile of the box-average standard

deviation (triangles) computed using eq. (4.5), with the uncertainty estimated using eq. (4.8). Apart from a few outliers, the trend of the box-average standard deviation appears to correspond well with the box-average ΔT profile. These results suggest that quantisation error in the Mach number and airspeed makes a stronger contribution to the error in T_{MACH} , and illustrates the effect of Mode-S EHS processing. Figure 4-3 (d) depicts the results from (c) plotted against the box-average Mode-S EHS Mach number; since for reasons of flight safety the control of the aircraft is often by reference to Mach number rather than true airspeed if the aircraft is at high speed, high altitude or for airborne separation. The reported Mach number is computed under the prevailing atmospheric pressure conditions (eq. (4.1)) whereas the reported pressure altitude is referenced to a static mean-sea-level pressure under ISA conditions. Thus this may afford a more suitable representation for data assimilation of Mach Temperature. This result still suggests that there is a significant contribution to the error in T_{MACH} due to quantisation error.

4.6 Quality of Derived Horizontal-Wind Vector

Figure 4-4 (page 72) depicts the vertical profile of the horizontal wind components: fig 4-4(a) zonal U_{REF} and fig 4-4(c) meridional V_{REF} obtained from the FAAM's turbulence probe, while fig 4-4(b) zonal U_{Mode-S} and fig 4-4(d) meridional V_{Mode-S} are the wind components obtained from applying the wind vector eqs. (4.10) and (4.11). The vertical striping effect in figures 4-4(b) and (d) may be due to the reduced precision of the Mode-S EHS reports of true airspeed, magnetic-heading, ground speed and ground heading. The striping effect is more pronounced in the zonal wind component possibly because the flight trajectory and wind direction are mostly in this direction. To assess the effect of Mode-S EHS processing it is useful to compare the output Mode-S EHS data with the input ARINC data. This affords insight into partitioning errors that can be attributed to data processing and to other sources of error for the wind components.

In figure 4-5 (page 73), the zonal U_{ARINC} and meridional V_{ARINC} wind components are obtained using data with ARINC precision and are compared with the reference observations. To facilitate plotting and for ease of comparison, outliers greater than 3σ from μ , where μ is the mean value and σ is the standard deviation, were removed from the plots but were not removed from the computation of the results, see table 4.7 for details.

Figure 4-5(a) depicts the vertical profile difference $U_{ARINC} - U_{REF}$ and figure 4-5(d) depicts the vertical profile difference $V_{ARINC} - V_{REF}$. The trajectory for this flight was mostly East-West with a more North-South trajectory at the start of the flight.

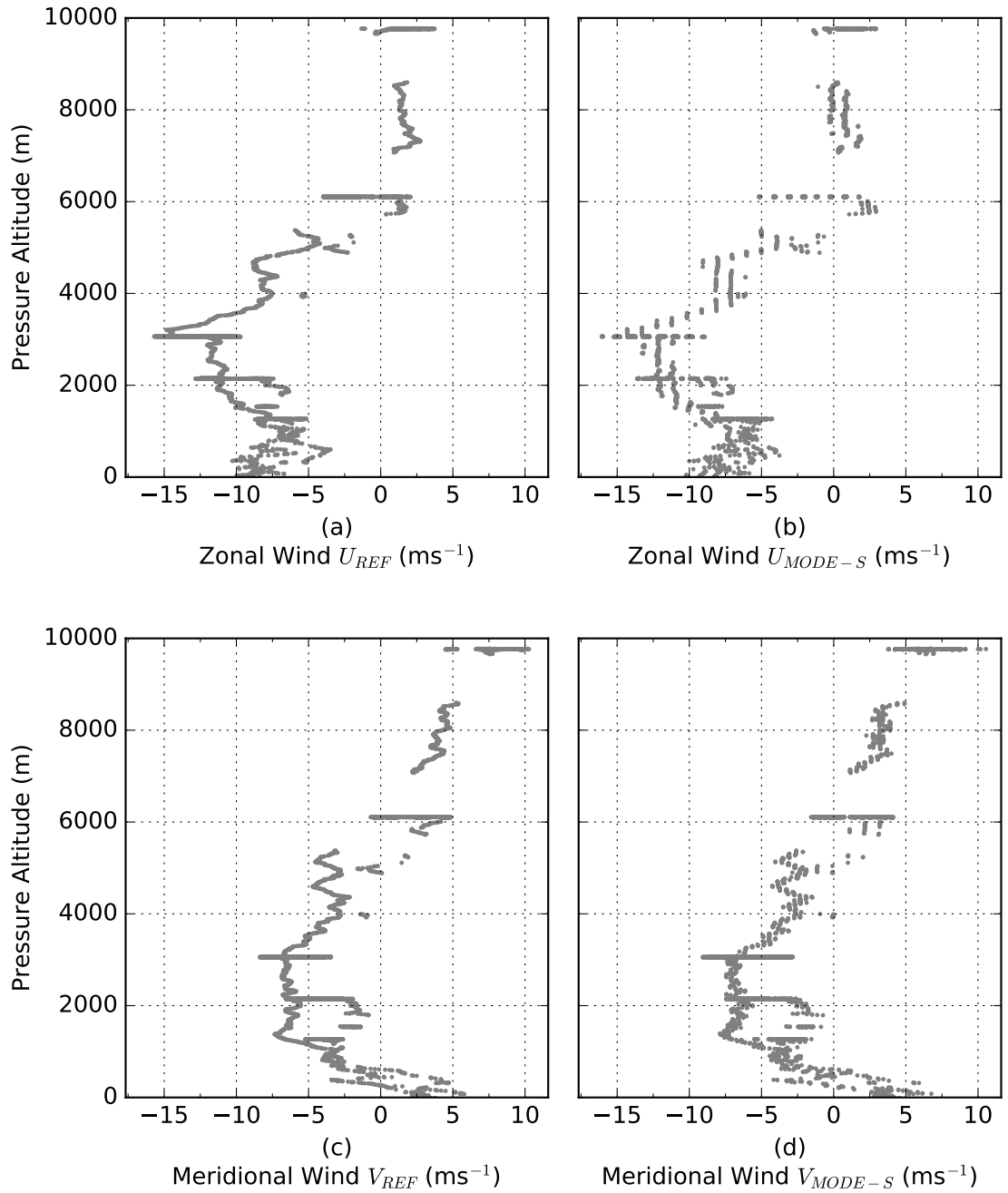


Figure 4-4: Flight B787 (11th July 2013) vertical profiles of the reference components (a) zonal U_{REF} and (c) meridional V_{REF} . Vertical profile of derived components (b) zonal U_{Mode-S} and (d) meridional V_{Mode-S} . The stripe effect visible in (b) and (d) is due to the reduced precision of the input data to the wind vector eqs. (4.10) and (4.11). This is more pronounced in the zonal component since the majority of the flight was in this direction.

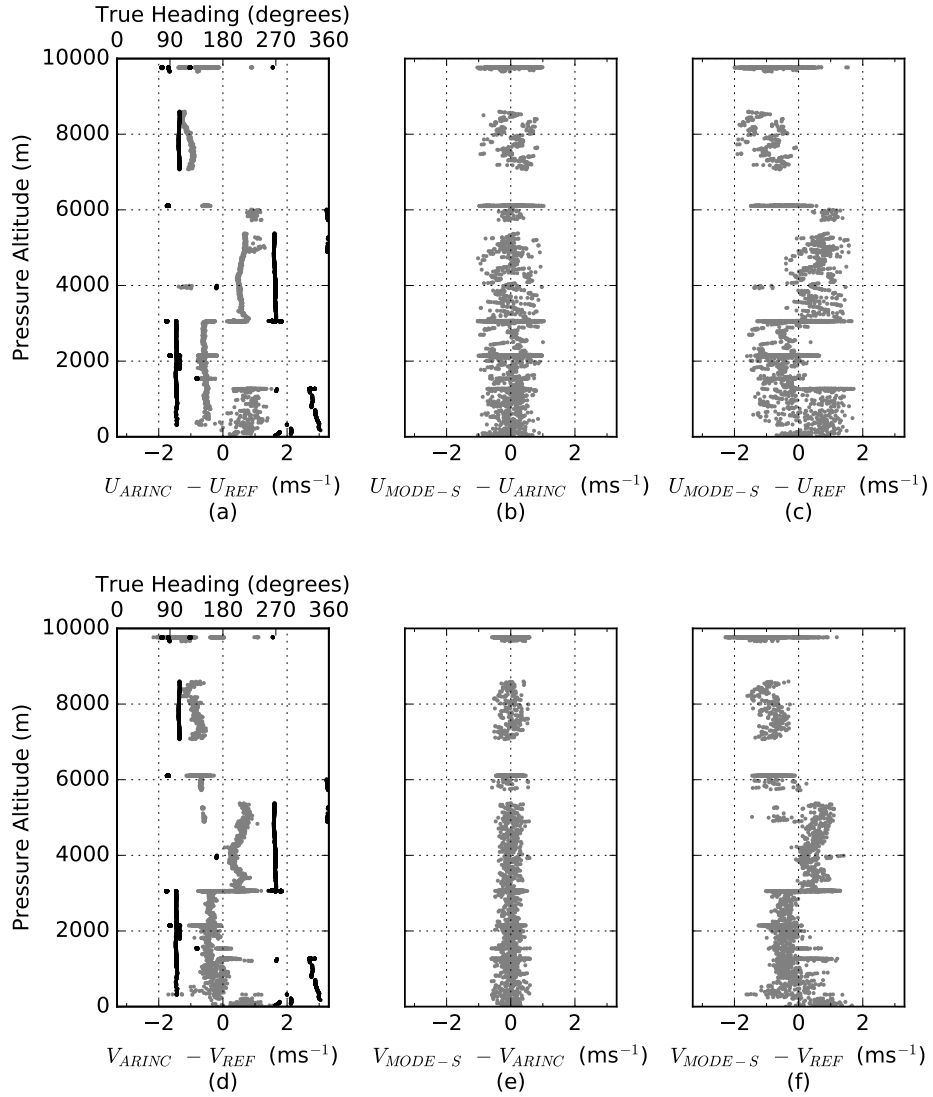


Figure 4-5: Flight B787 (11th July 2013) Vertical difference profiles of the zonal (U) and meridional (V) wind components obtained using eqs. (4.10) and (4.11). The difference between the input ARINC and REF observations are shown as the grey line in plots (a) $U_{ARINC} - U_{REF}$ and (d) $V_{ARINC} - V_{REF}$. These plots also depict the aircraft's true heading shown as the black lines referenced to the upper scale. The difference between the input ARINC and output Mode-S EHS are shown in plots (b) $U_{Mode-S} - U_{ARINC}$ and (e) $V_{Mode-S} - V_{ARINC}$. The difference between the output Mode-S EHS and REF observations are shown plots (c) $U_{Mode-S} - U_{REF}$ and (f) $V_{Mode-S} - V_{REF}$. The REF observations are derived from the FAAM's turbulence probe. To facilitate plotting, outliers greater than 3σ from μ are not displayed, see table 4.7 for details.

Table 4.7: Outliers not displayed in plots for horizontal wind (ms^{-1}), shown in figure 4-5, when the magnitude of the plotted value is greater than 3σ from μ .

Figure	μ	3σ	Min value	Max value	Number of outliers
4-5(a)	-0.077	1.1518	-1.384	1.510	0
4-5(b)	0.077	1.213	-1.042	1.031	0
4-5(c)	-0.068	1.932	-1.996	1.714	6
4-5(d)	-0.100	2.164	-2.165	2.240	37
4-5(e)	-0.001	0.599	-0.601	0.597	99
4-5(f)	-0.095	2.247	-2.278	2.330	31

The differences appear to occupy four zones. In figure 4-5(a) between the altitude ranges 0 m to 1 km and 3 km to 6 km the difference is positive while between 1 km to 3 km and above 6 km the difference is negative. Similar differences are seen in figure 4-5(d). In both plots the magnitude of the difference is of the order $\pm 1 \text{ ms}^{-1}$. There appears also to be a directional bias which affects both wind components in the same way. Recall that the reference winds and ARINC precision winds are computed using different input data (except for the ground vector), and different calculation methods (see sections 4.2.3 and 4.3). A key difference appears to be the aircraft's heading. Directional errors relating to an aircraft's navigation are suggested by Drue et al. (2008), de Haan (2011) and Jacobs et al. (2014).

Figure 4-5(b) depicts the difference $U_{Mode-S} - U_{ARINC}$ and figure 4-5(e) depicts the difference $V_{Mode-S} - V_{ARINC}$. Thus these figures show the effect of Mode-S EHS processing. For the zonal wind the differences are typically within $\pm 1 \text{ ms}^{-1}$ and for the meridional wind the differences are typically within $\pm 0.5 \text{ ms}^{-1}$. Possible causes that may explain why the magnitude of the meridional wind differences are smaller when compared to the zonal wind differences are: a strong zonal component to the wind direction when compared with the meridional component (figures 4-4(a) and (c)); this particular flight was mostly in the zonal direction. The wind differences appear evenly distributed when compared figures 4-5(a) and (d) respectively, this suggests that there is no directional bias due to Mode-S EHS processing. This is expected since the output Mode-S EHS data are just the input ARINC data rounded then truncated. Figure 4-5(c) depicts the difference $U_{Mode-S} - U_{REF}$. It is clear from this plot that the magnitude of the differences is of the same order as that shown in figures 4-5(b). Also, two effects can be separated, firstly the directional bias seen in figure 4-5(a) is replicated and secondly the spread of the data seen in figure 4-5(b) is superimposed. Similar results are seen for $V_{Mode-S} - V_{REF}$ in figure 4-5(f). However, these results do not make it clear as to the source of the directional bias, that is whether this is solely due to the heading reference system that provides the true heading, contamination

affecting the turbulence probe’s pressure ports, e.g., ice particles, or some combination of the two. There is no record in the post flight report regarding contamination of the pressure ports.

These results indicate that error arising from Mode-S EHS processing makes a stronger contribution to the total observational error. In the next section an error model is used to account for some of the observed differences, and is also used to characterize the differences due to Mode-S EHS processing.

4.7 Estimated Error in the Derived Horizontal-Wind Vector

Following the method of analysis used for the Mach temperature error (section 4.5.2, page 66), we apply the propagation-of-error method (Taylor 1982) to eqs. (3.5) and (3.6) (page 38), and we obtain an error equation for the zonal and meridional wind components,

$$\begin{aligned} \Delta U^2 = & (\sin(\theta_G)\Delta V_G)^2 + (V_G \cos(\theta_G)\Delta\theta_G)^2 + \\ & (-\sin(\theta_A)\Delta V_A)^2 + (-V_A \cos(\theta_A)\Delta\theta_A)^2 \end{aligned} \quad (4.10)$$

and

$$\begin{aligned} \Delta V^2 = & (\cos(\theta_G)\Delta V_G)^2 + (-V_G \sin(\theta_G)\Delta\theta_G)^2 + \\ & (-\cos(\theta_A)\Delta V_A)^2 + (V_A \sin(\theta_A)\Delta\theta_A)^2, \end{aligned} \quad (4.11)$$

where ΔV_G and ΔV_A are the precision errors in the ground speed and true airspeed in ms^{-1} ; and $\Delta\theta_G$ and $\Delta\theta_A$ are the precision errors in the ground heading and true heading respectively in radians. We have chosen to carry out the error analysis in the frame of reference of the earth, since the zonal and meridional wind are the variables used in the observation operator for aircraft winds in the UK Met Office assimilation system. However, an alternative, complementary, approach would be to carry out the analysis in the frame of the aircraft, and consider along-track and transverse components of the wind errors (Drue et al. 2010, de Haan 2013, Jacobs et al. 2014). This approach would result in a rotated form of eqs. (4.10) and (4.11).

We use the wind components error model (eqs. (4.10) and (4.11)) to characterize the error in the zonal and meridional wind for the case study flight B787. For this flight calm conditions prevailed such that for most of the flight the mean true airspeed was 250 knots with the magnitude of the differences for speed and direction were (true

airspeed - ground speed) ≤ 25 knots and (true heading - ground heading) $\leq 5^\circ$. We use the data increments of $\epsilon = 2$ knots for the ground speed and for true airspeed and a data increment of $\epsilon = 0.175^\circ$ for the ground heading and true heading, respectively (table 4.1, page 58). These data increments are used to compute precisions for the quantisation error given by eq. (3.21) (page 53).

It can be seen from eqs. (4.10) and (4.11) that the component wind error depends on three factors: the precision of the parameter, the directions and the speeds. For this case study flight, we consider each of these factors in turn.

1. **Dependency on precisions:** The main contributors to the wind component errors are the precisions of the true airspeed and ground speed. The magnitude of the precision due to quantisation error for airspeeds is 0.297 ms^{-1} and for the directions is 0.000882 radians (or equivalently 0.05°). The contribution from the precision in direction is airspeed dependent. In figure 4-6(a) the flight direction in the region labelled (v) changes from North (0°) to North-West (315°). This has the effect of increasing the zonal wind error as the contribution due to precision of speeds is increased. At the same time, the meridional wind error decreases with respect to the precision in speed, 4-6(b). The contribution due to the precision in direction remains small, particularly at low altitudes where airspeeds are lower.
2. **Dependency on directions:** When the aircraft headings are near the cardinal compass points 90° or 270° then the main contribution to the zonal wind error, ΔU , is mostly due to the precision in the speeds. In figure 4-6(a), the region labelled (ii) the aircraft true heading is due West while for regions labelled (i) and (iii) it is due East. For these flight directions, 4-6(a) depicts the magnitude of the estimated error for the zonal wind component which is constant with altitude (0.40 ms^{-1}). By contrast the contribution to the meridional wind error, ΔV , is smaller, shown in figure 4-6(b). We expect to see periodic variations in the magnitude of the wind component error. Thus when the aircraft headings are near the cardinal compass points 0° and 180° we observe the reverse case. In figure 4-6(b), when the the aircraft true heading is due North (region labelled (iv)) the meridional wind component is constant with altitude (0.40 ms^{-1}) and the corresponding zonal wind component error is smaller, as shown in figure 4-6(a) region (iv). These results are consistent with de Haan (2013) who found airspeed corrections were most effective on the component of the wind parallel to the air vector, and heading corrections most effective on the transversal wind component.
3. **Dependency on speeds:** As noted earlier there is the contribution to the error

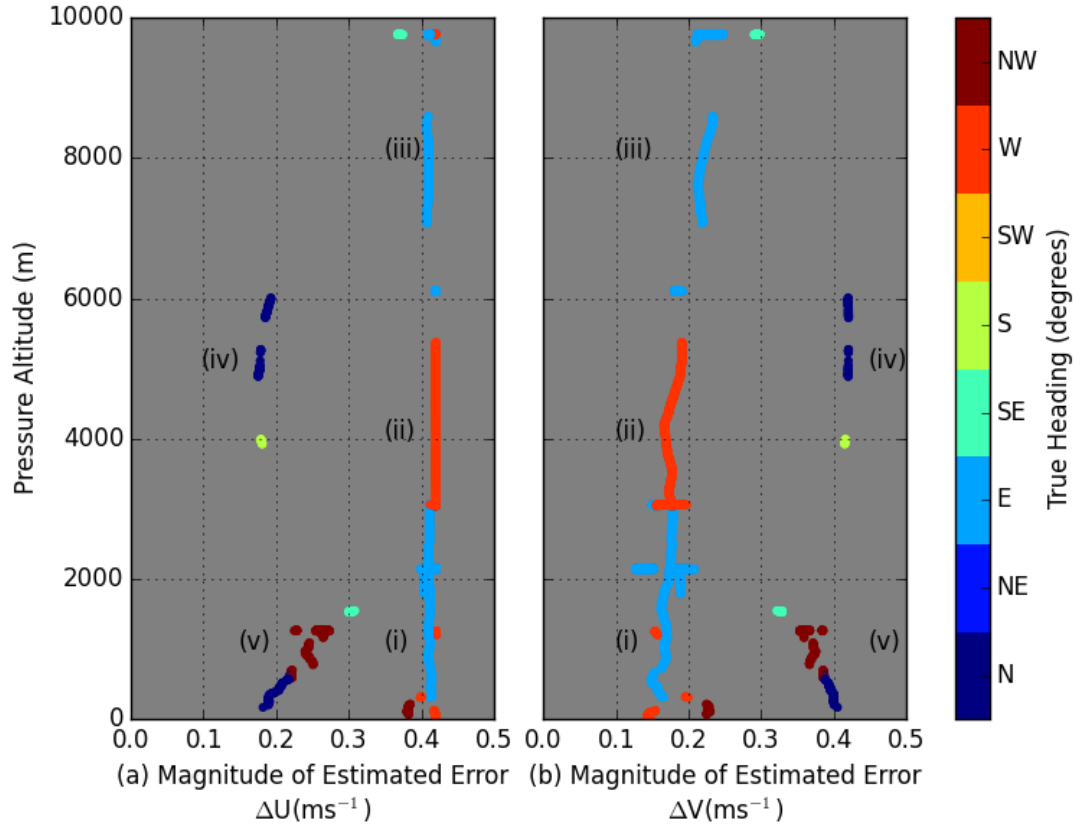


Figure 4-6: Flight B787 (11th July 2013). Vertical profiles for the estimated error for the zonal, ΔU (eq. (4.10)) and meridional, ΔV (eq. (4.11)), wind components. The precision of the input data are given by the standard deviation for quantisation error, headings $\Delta\theta_G = \Delta\theta_A = 0.00305/\sqrt{12}$ radians (which is equivalent to 0.05°) and speeds $\Delta V_G = \Delta V_A = 1.0289/\sqrt{12}$ ms^{-1} . The sidebar indicates the general direction of the aircraft, with true headings binned into 45° regions centred around the cardinal compass points. Regions (i) to (v) in the plot indicate the general direction of the aircraft's true heading: (i) and (iii) East, (ii) West, (iv) North and (v) North-West.

due to the precision in the headings which in general is small but in eqs. (4.10) and (4.11) there are cross terms in speed and direction. We can see that the contribution to the error due to the precision of the headings depends also on the magnitude of the airspeed. When the speeds reach the order of 100 ms^{-1} or more then the error due to the precision in direction becomes significant (100×0.000882), particularly at the cardinal compass points where the periodic terms are at a maximum. The airspeed varies with altitude, with speeds of 50 ms^{-1} near the surface and 250 ms^{-1} at 10 km. Since airspeed increases with altitude so does the contribution to the zonal and meridional wind errors due to the precision in direction. An example of this error is shown in figure 4-6(b). For regions (i), (ii) and (iii) we see the main contribution to the meridional error is from the precision in direction which is airspeed dependent.

Under the calm conditions of this flight the magnitude of the estimated error in zonal and meridional wind components, due to quantisation errors in the speeds and directions, varies periodically between 0.15 ms^{-1} and 0.40 ms^{-1} . However, we have no data for these estimated errors in wind conditions with a higher range of wind speeds.

For the wind components in this case study we use the same analysis method as used for the mean temperature profiles in section 4.5.1. The wind component profiles are depicted in figures 4-7 and 4-8. The MB are depicted as squares, the RMSE as circles, the diamonds are the box-average of the estimated wind component error due to quantisation, and the triangles are the box-average standard deviation from applying eq. (4.5). The uncertainty in the standard deviation is calculated using eq. (4.8). The number of reports used to compute the box average is depicted as log plots adjacent to each plot. We first consider the effect of Mode-S EHS processing, then compare the Mode-S EHS processed results with in situ observations.

Figure 4-7 depicts the effect of Mode-S EHS processing on the box-average standard deviation. Figures 4-7 (a) and (c) show that the MB is near zero for the zonal and meridional wind direction. The deviations from zero MB are possibly due to sampling not being representative leading to positive and negative biases. These data are at one second intervals. The side bar in the figure shows the number of records available for each altitude bin. There are two regions (7 km and 10 km) where the number of data points is less than 30. For the remaining non-level-flight regions the number of data points ranges between 45 and 111 data points; level flight regions contain 1000+ data points. Some of the occurrences of a non-zero bias also arise when the Mode-S EHS rounding results in a greater difference in one or other of the input data components. For example, when the differences between the input and output ground speeds are greater than the corresponding input and output for the true airspeed. This

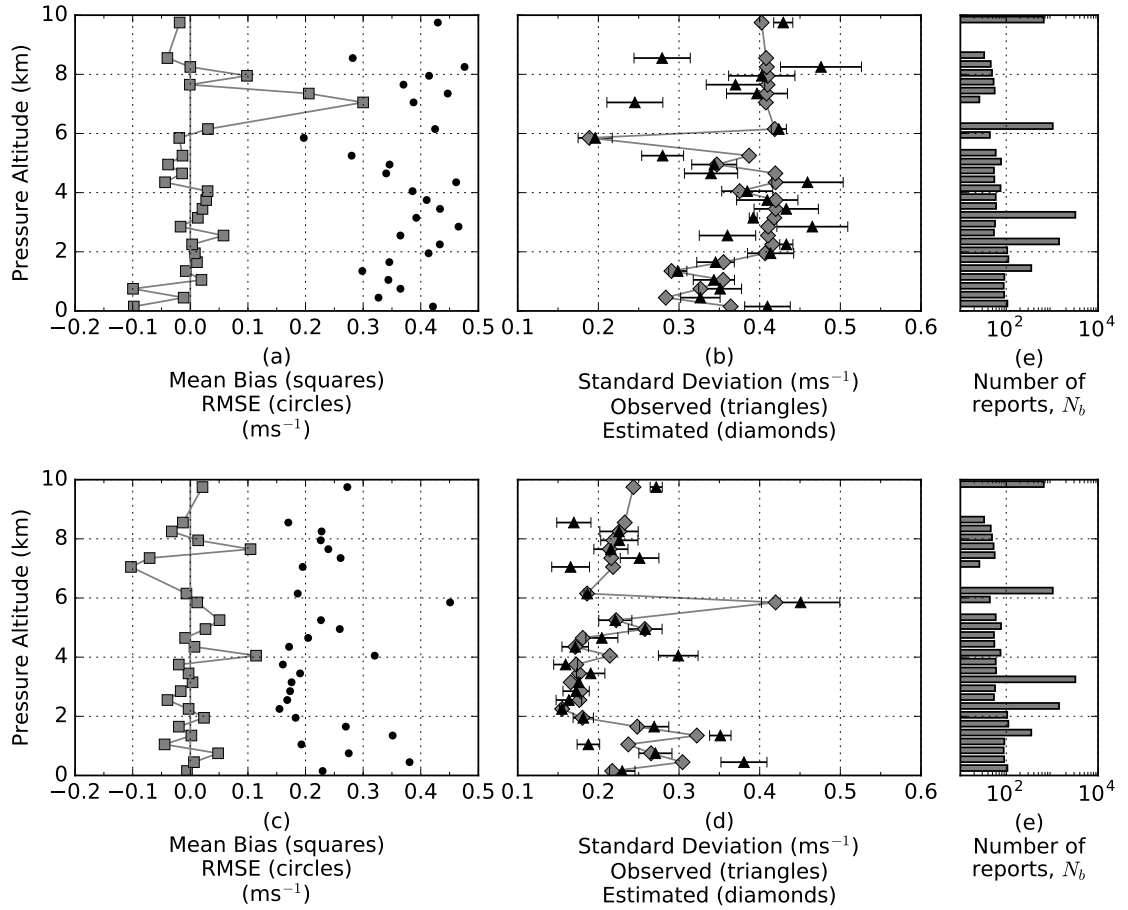


Figure 4-7: Flight B787 (11th July 2013) Box-average statistics for the effect of Mode-S EHS processing on the zonal (U) and meridional (V) wind components. Results binned by altitude, with bin heights at 0.3 km intervals. Plots (a) and (c) depict for the zonal and meridional winds respectively, vertical profiles of the mean bias (squares) and RMSE (circles). Zero is marked by the vertical line. Plots (b) and (d) depict for the zonal and meridional winds respectively, the vertical profiles of the box-average observed σ (triangles) using eq. (4.5) and box-average estimated component wind speed error (diamonds) due to the quantisation error using eqs. (4.10) and (4.11). Plot (e) depicts the number of reports per altitude bin, N_b , expressed using a \log_{10} scale. This distribution is the same for each wind component.

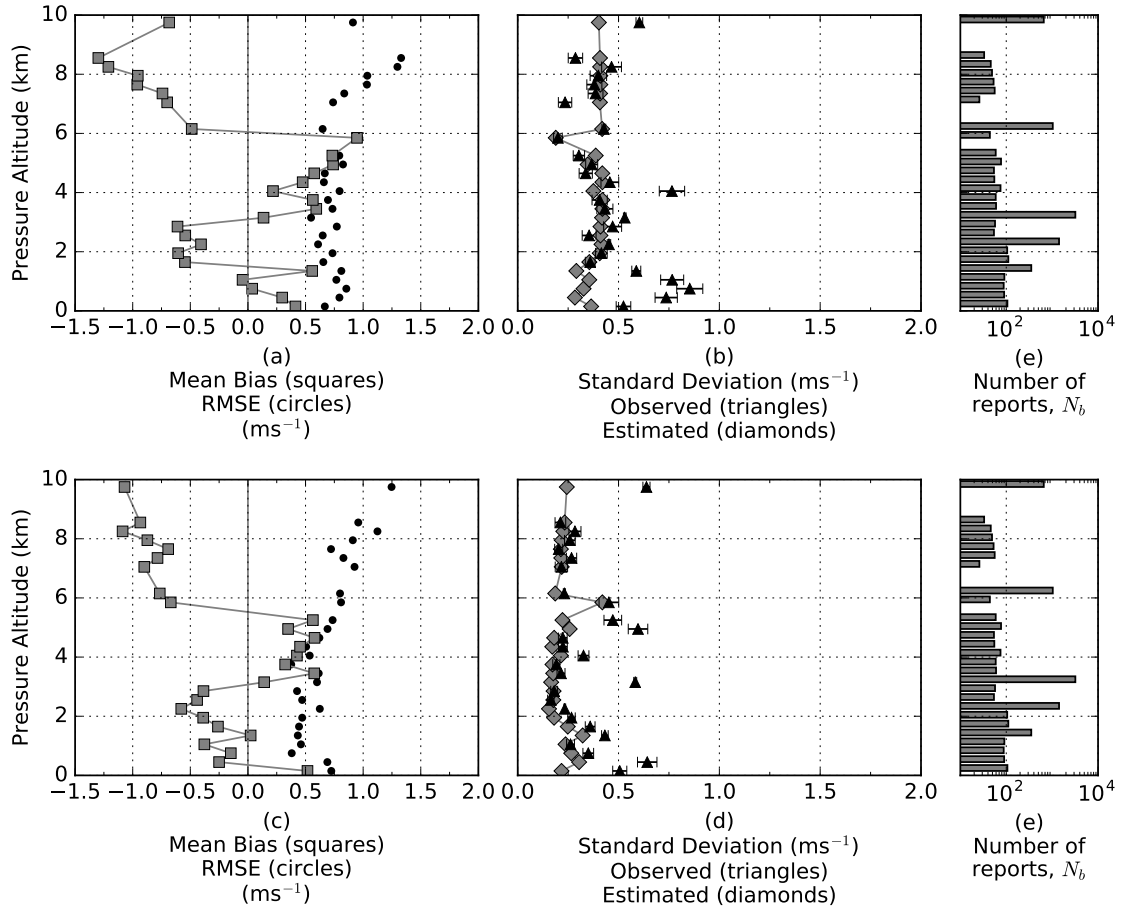


Figure 4-8: Flight B787 (11th July 2013) Box-average statistics comparing Mode-S EHS processed with measured (REF) zonal (U) and meridional (V) wind components. Results binned by altitude, with bin heights at 0.3 km intervals. The REF observations are from the FAAM’s turbulence probe, located at the nose of the aircraft. Plots (a) and (c) depict for the zonal and meridional winds respectively, vertical profiles of the mean bias (squares) and RMSE (circles). Zero is marked by the vertical line. Plots (b) and (d) depict for the zonal and meridional winds respectively, the vertical profiles of the box-average observed σ (triangles) using eq. (4.5) and box-average estimated component wind speed error (diamonds) due to the quantisation error using eqs. (4.10) and (4.11). Plot (e) depicts the number of reports per altitude bin, N_b , expressed using a \log_{10} scale. This distribution is the same for each wind component.

occurs for the lowest data point in figure 4-7(a) at 150 m. These differences that arise from the Mode-S EHS processing are reflected in the RMSE. Figures 4-7 (b) and (d) depict the observed sample standard deviation (triangles) for each altitude bin obtained by applying eq. (4.5). The uncertainty for the standard deviation is given by eq. (4.8). The estimated wind component errors (diamonds) are given by eqs. (4.10) and (4.11). These assume that the precision of the input data is represented entirely by the standard deviation due to quantisation error given by eq. (3.21). There is good correspondence between the box-averaged observed and expected standard deviations, although there is a small amount of variability. In figures 4-7 (b) and (d) a single point stands out at 5.7 km. For the zonal wind the standard deviation is 0.21 ms^{-1} whereas for the meridional wind the standard deviation is 0.45 ms^{-1} these are consistent with expected standard deviations (shown in figure 4-6). Examination of the time-series data for these data points indicate that the aircraft was heading North. The apparent rapid change in the magnitude of the standard deviation is artificial: it occurs due to quality control procedures, removing an aircraft manoeuvre. Just below the 5.7 km level the aircraft trajectory is West-East whilst just above the 5.7 km level the trajectory is East-West. These points indicate that the quality control processing may require further refinement. Figure 4-7 (e) depicts the number of reports per altitude bin, N_b , expressed using a \log_{10} scale. This distribution is the same for each wind component.

Figure 4-8 compares the Mode-S EHS processed derived zonal and meridional wind components with corresponding in situ reference observations. In figures 4-8 (a) and (c) the MB ranges between -1.00 ms^{-1} and $+1.00 \text{ ms}^{-1}$. It is notable that between the altitudes 3 km to 6 km the bias is positive whilst the aircraft trajectory is West-East. Above and below these altitudes the bias is negative whilst the aircraft trajectory is East-West. We suggest that this change in the wind bias may be due to a bias in the heading reference system, although a bias in the turbulence probe measurements cannot be ruled out. This bias pattern does not appear to affect the Mode-S EHS processing (figure 4-7). The RMSE varies between 0.50 ms^{-1} to 0.80 ms^{-1} , with a significant increase to 1.30 ms^{-1} above 6 km which appears to coincide with an increase in the magnitude of the MB. Figures 4-8 (b) and (d) depicts the box-average standard deviation (triangles) and the box-averaged expected error (diamonds). There is less correspondence between the box-averaged observed and expected standard deviations. We observe that some fraction of the quantisation error still persists. The periodic behaviour of the standard deviation is illustrated by the two points at 5.7 km (as mentioned above). There is more variation especially at the lower altitudes, which may be related to a directional bias (discussed earlier in section 4.6 (page 71)). It is difficult to isolate the directional error since there are no reference data that can be used to

quantify the directional error in the aircraft’s heading reference system. There may be fine-scale variability being recorded by the turbulence probe, which is more sensitive to such variations. Furthermore, the fine-scale variability would be too weak to affect the aircraft’s inertia. Figure 4-8 (e) depicts the number of reports per altitude bin, N_b , expressed using a \log_{10} scale. This distribution is the same for each wind component.

These differences aside, the results depicted in figures 4-7 and 4-8 suggest that quantisation error in the aircraft’s headings and speeds contributes to the total error in the computed Mode-S EHS wind components.

4.8 Results Obtained for All Cases

In this section the error equations for temperature and horizontal wind components are applied to all cases listed in table 4.3 (page 63) using the analysis steps described in sections 4.5 (page 66) and 4.6 (page 71). The precisions for the input data are taken to be the standard deviations for quantisation error given by eq. (3.21) expressed in SI units. So $\Delta M=(0.004/\sqrt{12})$, $\Delta V_A=\Delta V_G=(1.03/\sqrt{12}) \text{ ms}^{-1}$ and $\Delta\theta_A=\Delta\theta_G=(0.00305/\sqrt{12})$ radians (or equivalently 0.05°). The vertical profiles of the box-averaged estimated errors are compared with the box-averaged standard deviation obtained from the MB and RMSE. We first present the results for the estimated temperature error then the results for the estimated error in the horizontal wind components.

Figure 4-9 (page 83) depicts the vertical profile for the box-averages of the Mode-S EHS derived temperatures. Figure 4-9 (a) is the number of reports per altitude bin, N_b , expressed using a \log_{10} scale. Figure 4-9 (b) shows that the overall MB is near zero, there is less variability in these results when compared with figure 4-3 (page 70) which may be directionally dependent. The RMSE varies from 2.5 K near the surface, decreasing smoothly with altitude to 1.25 K at 10 km. Figure 4-9 (c) shows that the observed standard deviation (triangles) correlates well with the estimated Mach temperature error using the error model given by eq. (4.9) (similar to profile (b) in figure 4-2). Figure 4-9 (d) expresses the standard deviation results against Mode-S EHS Mach number, which may be a more useful representation for data assimilation, and which also shows good agreement between standard deviations from the observed and quantisation errors. We conclude from this analysis that the estimated error in the derived Mode-S EHS temperature can be represented by standard deviation of quantisation error for M and V_A that results from Mode-S EHS processing. This estimated error does not include other sources of error such as the instrument error. For this result to be valid we require that the magnitude of the instrument error is smaller than the standard deviation of quantisation error.

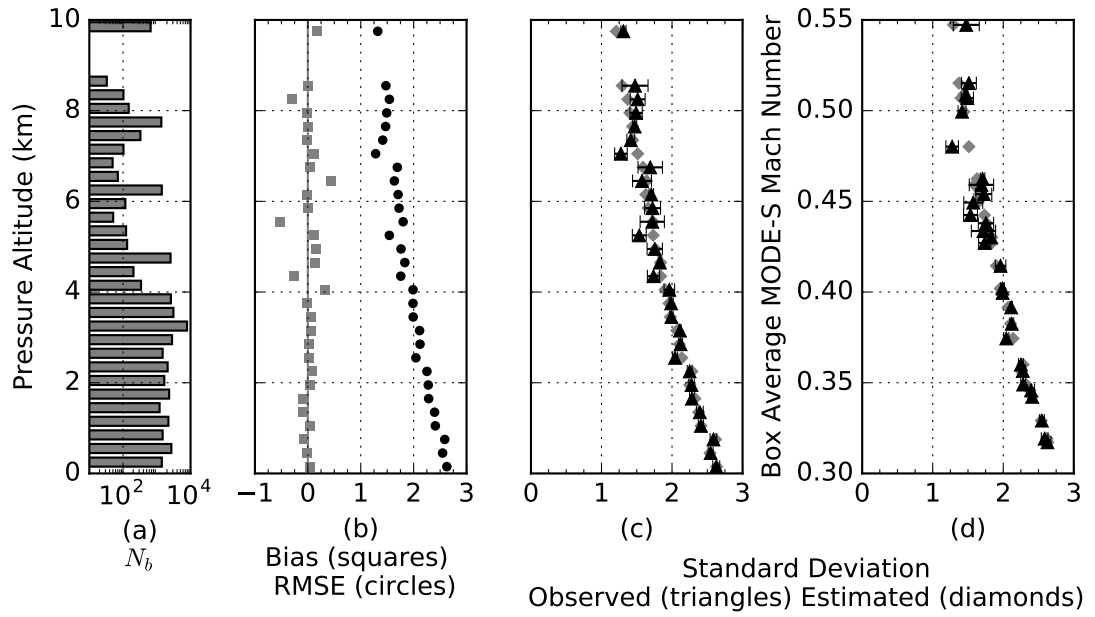


Figure 4-9: For all case studies listed in table 4.3. Box-average statistics for temperature. Results binned by altitude, with bin heights at 0.3 km intervals. Plot (a) is the number of reports per altitude bin, N_b , expressed using a \log_{10} scale. Plot (b) vertical profile of temperature difference ($T_{MACH} - T_{REF}$) mean bias (MB) (squares) and RMSE (circles). Zero is marked by the vertical line. Plot (c) Vertical profile of the box-average observed σ (triangles) (using eqs. (4.5) and (4.8)) and the box-average estimated ΔT (diamonds) due to the quantisation error (using eqs (4.9) and (3.21)). Plot (d) depicts the results of (c) against the box-average M reported by Mode-S EHS.

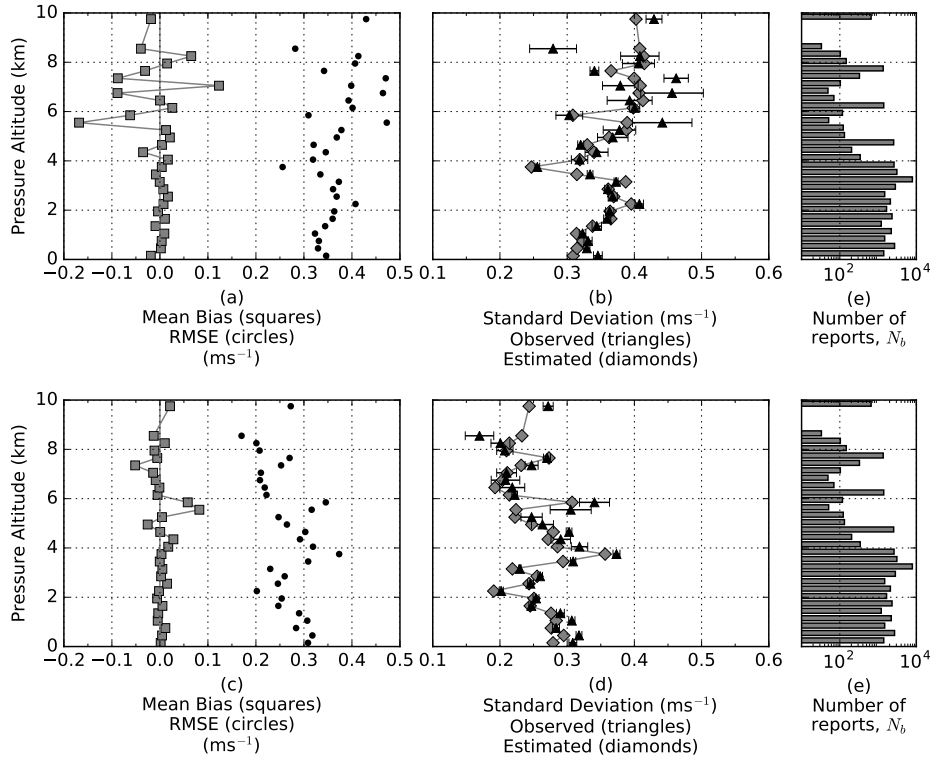


Figure 4-10: For all case studies (table 4.3). Box-average statistics for the effect of Mode-S EHS processing on the zonal (U) and meridional (V) wind components. Results binned by altitude, with bin heights at 0.3 km intervals. Plots (a) and (c) depict for the zonal and meridional winds respectively, vertical profiles of the mean bias (squares) and RMSE (circles). Zero is marked by the vertical line. Plots (b) and (d) depict for the zonal and meridional winds respectively, the vertical profiles of the box-average observed σ (triangles) using eq. (4.5) and box-average estimated component wind speed error (diamonds) due to the quantisation error using eqs. (4.10) and (4.11). Plots (e) depicts the number of reports per altitude bin, N_b , expressed using a \log_{10} scale. This distribution is the same for each wind component.

Figure 4-10 (page 84) depicts the effect of Mode-S EHS processing for the zonal and meridional wind components. The vertical profiles are for the box-averaged MB (squares) and RMSE (circles), figures 4-10 (a) and (c). For the Mode-S EHS processing the MB is near zero for both the zonal and meridional wind below 4 km altitude. Above 4 km the zonal wind bias varies between -0.18 ms^{-1} and 0.12 ms^{-1} . This variation may be due to the non-uniform sampling distribution above this level when compared to those below this level. Examination of the distribution of differences between the aircraft state vector at ARINC precision (before processing) and Mode-S EHS precision (after processing) shows that these are mostly uniform below 4 km and non-uniform above. The difference in variability between the zonal and meridional components may be due to flight trajectories, being mostly East-West above 4 km, indicating a directional bias. The increase in the RMSE for the zonal wind may also be due to the non-uniform sampling distribution. Similar conclusions may be drawn for the meridional wind. The MB and RMSE are used to compute the box-average σ , depicted as the triangles in figures 4-10(b) and 4-10(d). The vertical profile of σ shows good agreement with the estimated error (diamonds), given by eqs. (4.10) and (4.11) (page 75), when precisions for speeds and directions are represented as the standard deviation due to quantisation. The minima in the estimated zonal wind σ at 4 km and 6 km of 0.25 ms^{-1} and 0.30 ms^{-1} , and the corresponding maxima in the meridional wind of 0.35 ms^{-1} and 0.30 ms^{-1} are most likely to be due to the aircraft's trajectory changing direction. This behaviour is suggested by figure 4-6 (page 77), as discussed in section 4.6 (page 71). Figure 4-10 (e) depicts the number of reports per altitude bin, N_b , expressed using a \log_{10} scale. This distribution is the same for each wind component.

Figure 4-11 compares the Mode-S EHS processed derived zonal and meridional wind components with corresponding in situ reference observations. In figures 4-11 (a) and (c) the MB below 4 km is near zero. Above this level, for the zonal wind the MB ranges between -1.4 ms^{-1} to 2.0 ms^{-1} while for the meridional wind the MB ranges from 0.25 ms^{-1} to -1.0 ms^{-1} . This variability is thought to be related to a directional bias discussed earlier in section 4.6 (page 71). Figures 4-11 (b) and (d) depicts the box-average standard deviation (triangles) and the box-averaged expected error (diamonds). It is clear that there is less correspondence between the observed standard deviation with respect to the measured wind components and the expected error due to Mode-S EHS processing. This suggests that there are additional sources of error, such as instrument error, or fine-scale variability being recorded by the turbulence probe (which is more sensitive to such variations) and which are too weak to affect the aircraft's inertia. Figure 4-11 (e) depicts the number of reports per altitude bin, N_b ,

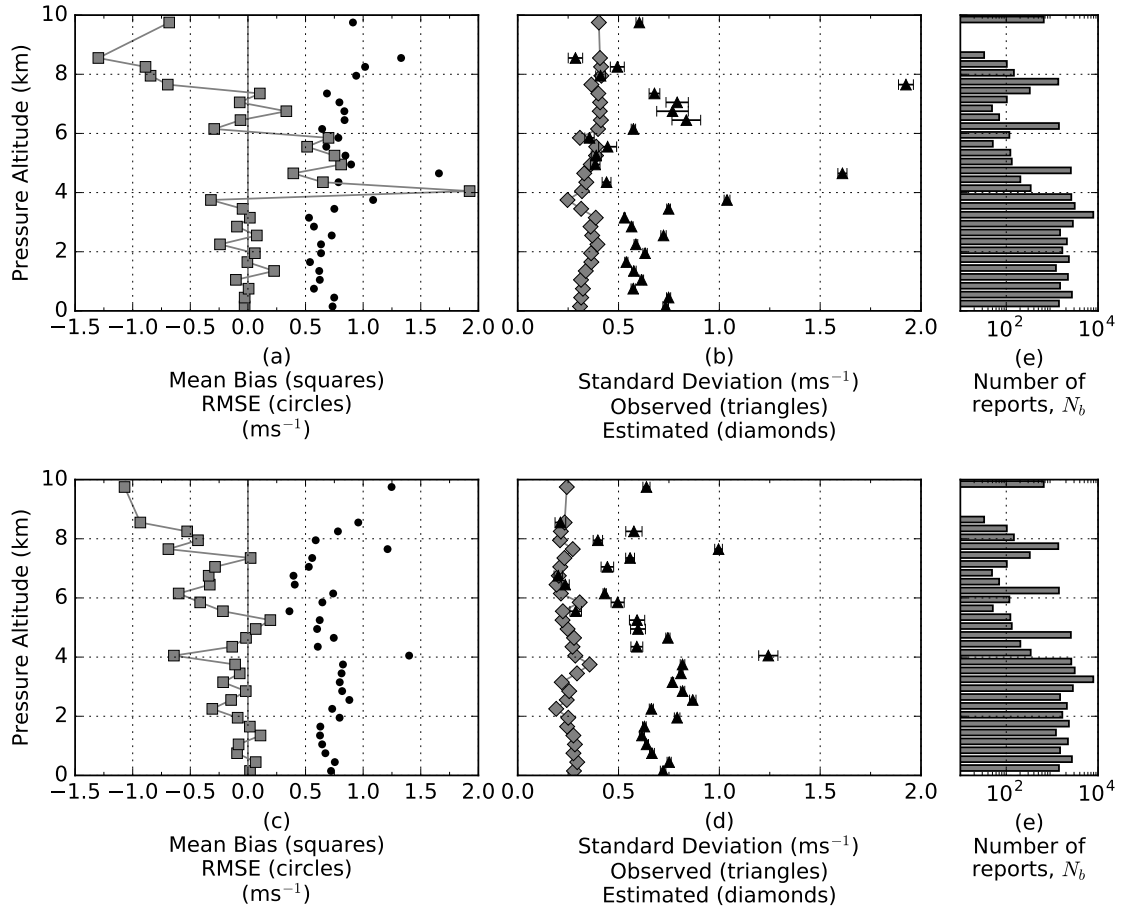


Figure 4-11: For all case studies (table 4.3). Box-average statistics comparing Mode-S EHS processed with measured (REF) zonal (U) and meridional (V) wind components. Results binned by altitude, with bin heights at 0.3 km intervals. The REF observations are from the FAAM's turbulence probe, located at the nose of the aircraft. Plots (a) and (c) depict for the zonal and meridional winds respectively, vertical profiles of the mean bias (squares) and RMSE (circles). Zero is marked by the vertical line. Plots (b) and (d) depict for the zonal and meridional winds respectively, the vertical profiles of the box-average observed σ (triangles) using eq. (4.5) and box-average estimated component wind speed error (diamonds) due to the quantisation error using eqs. (4.10) and (4.11). Plots (e) depicts the number of reports per altitude bin, N_b , expressed using a \log_{10} scale. This distribution is the same for each wind component.

expressed using a \log_{10} scale. This distribution is the same for each wind component.

We conclude from this analysis that the estimated error in the derived Mode-S EHS horizontal wind includes a component that can be represented by the standard deviation of quantisation error that results from Mode-S EHS processing. The majority of the case studies involved trajectories that were mainly East-West in direction. Therefore the case studies do not provide a uniform distribution of headings and wind-vector. Figure 4-12(a) depicts the distribution of differences for the zonal ($U_{Mode-S} - U_{REF}$) and figure 4-12(b) meridional ($V_{Mode-S} - V_{REF}$) wind components. The range of differences are shown in grey while the MB is shown by the black circles. The MB is computed over bin-widths of 5° intervals. Figure 4-12 (c) depicts the distribution of the number of records used to compute the MB expressed as a log plot. This shows that the sampling is not uniform in direction. For uniform distribution we would expect the MB for the wind component difference to be near zero. However, figures 4-12 (a) and (b) show that there is a directionally-based bias. It is not clear where the systematic error arises, whether it is due to the heading reference system (Drue et al. 2008, de Haan 2011, Jacobs et al. 2014), or to an instrument sensor error, or a combination of the two. It is known that the turbulence probe can become contaminated with aerosols and ice particles during the flight but there are no reports of such contamination for these case-study flights. Quantifying the directionally dependent error remains an area of active investigation.

4.9 Summary and Conclusions

This chapter studies uncertainty in the derived observations obtained from Mode-S EHS, with a focus on errors due to reduced precision. The source of the research data is a research aircraft, BAe-146 FAAM, which has an atypical mode of operation when compared with commercial aircraft. For example, the flight trajectories tend to be short and within a limited area; the ascents and descents are steeper and may occur at any time during the flight; and the research aircraft often sets out to operate in atmospheric conditions that commercial aircraft would ordinarily avoid or not encounter. Furthermore, the BAe-146 FAAM is not equipped with a Mode-S EHS transponder. Mode-S EHS data used for reporting the aircraft's state vector were emulated using avionics data recorded aboard the aircraft. The emulated Mode-S EHS reports were used to derive meteorological observations for temperature and horizontal wind components. The derived observations were compared with reference observations made in situ using research grade instruments. The effect of the Mode-S EHS processing is to reduce the precision of the aircraft's state vector from 16 binary-bits to 10 binary-bits.

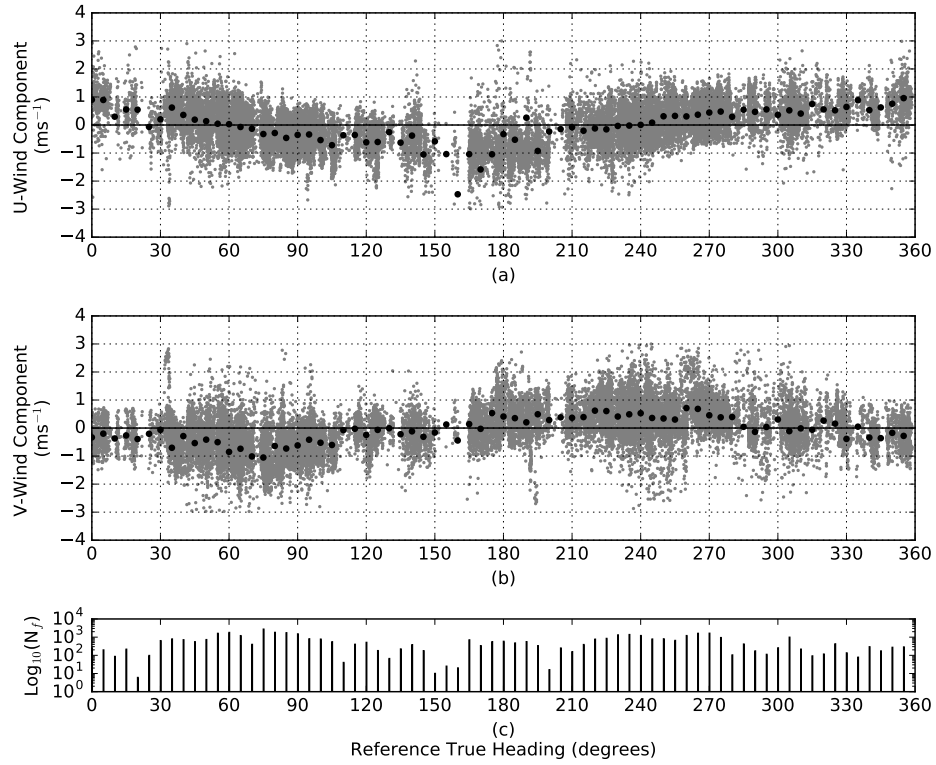


Figure 4-12: For all case studies. These plots suggest that there is a systematic error related to the aircraft's heading. Plot (a) depicts the zonal wind difference ($U_{Mode-S} - U_{REF}$) (grey). Plot (b) depicts the meridional wind difference ($V_{Mode-S} - V_{REF}$) (grey). The black circles depict the mean bias binned at 5° intervals. The number of reports per bin-intervals is depicted in plot (c) as $\log_{10}(N_f)$. Outliers are not shown where these are greater than three times the standard deviation, σ , from the mean μ . Maximum and minimum values stated but not shown. Indicated also are number of outliers removed and the total number of records. Outliers are retained for statistical results. For all records, nrecs=42792, for plot (a) $\mu=-0.028$, $3\sigma=2.71$, min=-15.72, max=14.64, outliers=289, and for plot (b) $\mu=-0.118$, $3\sigma=2.36$, min=-8.50, max=4.66, outliers=77

Error models were used to quantify the estimated error in the derived observations arising from Mode-S EHS processing. However, no account was taken of processing either by the flight management system or the transponder itself since these details were unavailable.

An error model was used to estimate the Mach temperature error, ΔT . It was found that ΔT varies according to the magnitude of the precisions for true airspeed and Mach number. When the precisions were represented using the standard deviation for quantisation error then ΔT varied from 2.5 K to 1.25 K for the pressure altitude range 0 km to 10 km, with a near linear trend between the two points. However, this result excludes other sources of error, e.g., instrument error due to calibration drift, noise and response times, which are expected to be small when compared to the quantisation error. We note that there are likely to be temporal correlations in our data for observation errors. However, this is also the case for actual Mode-S EHS data sampled by secondary surveillance radar. Quantization errors are not white noise because of the rounding processes involved in reducing the precision. Heading errors also result in systematic errors. It is important to bear this in mind for data assimilation. Further work is required to quantify the effects of error correlations.

An error model was also used to estimate the error in the horizontal wind components. The precisions of the speeds and directions were represented using the standard deviation for quantisation error. It was found that the magnitude of the estimated error for zonal wind varied from 0.25 ms^{-1} to 0.40 ms^{-1} , while the estimated error of the meridional wind was almost constant by altitude with a magnitude near 0.25 ms^{-1} . However, these results are not fully representative for all aircraft flight directions. It was also suggested that the differences in the wind components may be affected by a systematic error that is directionally dependent. The magnitude of the errors are smaller when compared with previous studies discussed in section 2.8 (page 16) since we were investigating the precision error and not looking for a true estimate of the actual observation error inherent in the FAAM data itself.

When suitable correction schemes are used, the derived horizontal wind and temperatures (above a certain height) have already been shown to be useful in data assimilation for regional numerical weather prediction (de Haan & Stoffelen 2012, Strajnar et al. 2015, Lange & Janjic 2016). Similarly, Mach temperature reports may offer further useful information in the boundary layer when aggregated from multiple aircraft. However, these previous studies assume an observation error standard deviation that is based on that used for AMDAR. We use aggregated Mode-S EHS reports in chapter 6. It is expected that any uncorrelated random error would be reduced; however, we show that the results of this study indicate that quantisation error remains a dominant

source of error.

The results of this study will be used in chapter 7 where we perform data assimilation experiments using Mode-S EHS derived observations. Quantifying the statistical error due to Mode-S EHS processing may assist with data-assimilation of the derived observations. For example, the total observational error may be partitioned between the variability due to the aircraft's trajectory, its instruments, processing algorithms and the representative error for the measurement due to temporal and spatial sampling (Daley 1991).

Chapter 5

Synoptic Meteorology and Distribution of Aircraft Observations for Case Studies.

5.1 Introduction

In chapter 4 we addressed our first thesis question on the accuracy of the observations derived from Mode-S EHS reports. We found that the observation error for Mach temperature and horizontal wind may be modelled by assuming that the dominant error is from the Mode-S EHS processing.

In chapter 3, for our initial investigation on using Mode-S EHS reports, we used archived data supplied by NATS. During the course of our research the Met Office installed its own network of Mode-S EHS receivers. The main difference between the NATS network and Met Office network is that the latter is passive. The Met Office network cannot actively request Mode-S EHS reports. It is dependent on the configuration of the NATS network for requesting Mode-S EHS reports. We use data collected by the Met Office network to answer our second and third thesis questions (section 1.4).

- 2 What atmospheric phenomena within the boundary layer can be observed from using high-frequency observations derived from these routine messages?
- 3 What benefit does assimilation of these high frequency observations bring to the Met Office UKV numerical weather predictions?

In this chapter we describe the synoptic meteorology, the source of our Mode-S EHS reports and the distribution of aircraft observations that will be used to address these

thesis questions, which we cover in chapters 6 and 7 respectively.

In section 5.2 we describe the synoptic meteorology for the case study period 2nd to 8th January 2015 using surface based reports and surface pressure analysis charts. We describe the atmospheric state using available radiosonde reports in section 5.3 and in section 5.4 we use forecasts from the Met Office 1.5 km NWP model. In section 5.5 we describe the Met Office Mode-S EHS receiver network. In sections 5.6 and 5.7 we describe the distribution of aircraft and the observations collected using the Met Office network for the airport domains London Heathrow and London Gatwick. Section 5.8 summarises this chapter.

5.2 Summary of Meteorological Conditions 2nd to 8th January 2015

In this section we describe the meteorological conditions for the case study period between 2nd January and 8th January 2015. We do this using a combination of analysis and significant weather charts. The analysis charts, figure 5-1 (page 94), show the surface pressure pattern using isobars (lines of equal pressure) and indicate areas of high (H) and low pressure (L) along with their central pressure value. Isobars are represented by solid lines. High pressure is usually associated with settled weather while low pressure is normally associated with unsettled weather. Weather fronts are also shown and are determined from surface based observations of the 1.5 m temperature, humidity and the 10 m horizontal wind. Significant weather charts, figure 5-2 (page 96), are a record of weather types observed near a synoptic reporting weather station, e.g., heavy rain, thunderstorms, snow, fog, ice. Symbols are used to indicate the weather type and its observed intensity. These charts are produced four times daily (Met Office 2011).

Figure 5-1a shows the Met Office analysis chart for 3rd January 2015 valid at 1200 UTC. There is a low pressure system to the south of England, and several frontal systems are present over England: occluded fronts (solid triangles and semi-circles) where warm-air is being lifted above cool-air and a layer of subsiding-air above the surface (open semi-circles) (Barry & Chorley 2009, Ch 9). The analysis chart shows that a ridge of high pressure is developing to the west of the United Kingdom. Figure 5-2a shows that the significant weather in the Southeast for this period (symbols shown in table 5.1) was mostly precipitation, full cloud cover and light surface winds from the south to southeast.

Figure 5-1b shows the analysis chart for 3rd January 2015 valid at 1800 UTC. The low pressure system has moved off to the East and is being replaced with the developing

high pressure region. The significant weather chart (fig 5-2b) for this time indicates that for the Southeast, surface winds were light and variable in direction, regions of mist had formed whilst some areas had intermittent light rain. Overall, as the high pressure developed, cloud cover dissipated to leave clear sky conditions.

Figure 5-1c shows the analysis chart for 4th January 2015 valid at 0000 UTC. Here we observe that the high pressure region is well established over the United Kingdom. The significant weather chart (fig 5-2c) for this time indicates that for the Southeast significant regions were affected by fog and mist.

Figure 5-1d shows the analysis chart for 4th January 2015 valid at 1200 UTC. The high pressure remains and stable conditions persist. The significant weather chart (fig 5-2d) for this time indicates that for the Southeast, mist and fog remain as the main weather features.

The period 4th to 5th January 2015, fog and mist persisted for much of the Southeast of England. The analysis charts from 1800 UTC 6th to 1200 UTC 8th January 2015 (Prichard 2015) show that a low pressure system located near Iceland brought strong south westerly winds and unsettled conditions to the North-East of England, Wales and Scotland, while calmer conditions persisted in eastern and southern England - where the Mode-S EHS reports are mostly concentrated, for this period.

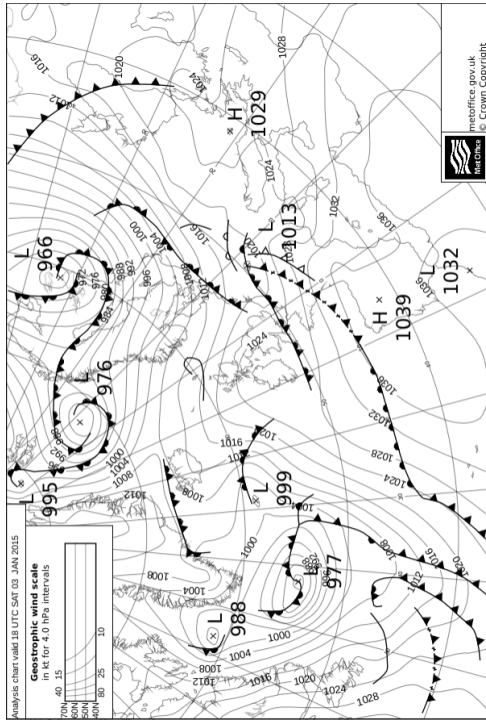
5.3 Meteorological Observations: Radiosondes

In this section we show the meteorological features that are present using upper air observations that are closest to the airport domains.

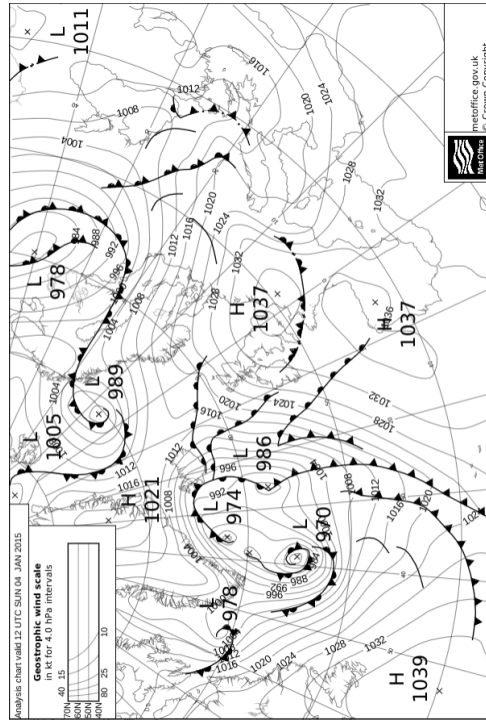
Upper air observations are obtained from Herstmonceux radiosonde station which is the nearest station to Heathrow and Gatwick airports. The data were retrieved from the Met Office meteorological database. A radiosonde is launched twice a day to correspond with the synoptic reporting times 0000 UTC and 1200 UTC. During adverse weather conditions such as low visibility and fog, additional radiosondes may be launched on demand by weather forecasters. The radiosonde's sensor is the Vaisala RS92 which reports the following observations with their precision stated within the brackets: ambient temperature (± 0.5 K), horizontal wind-speed (± 0.15 ms⁻¹) and horizontal wind-direction ($\pm 2^\circ$).

Figure 5-3 (page 97) shows the vertical profiles available for the 3rd and 4th January 2015. There was an additional radiosonde ascent for 0600 UTC on 4th January 2015.

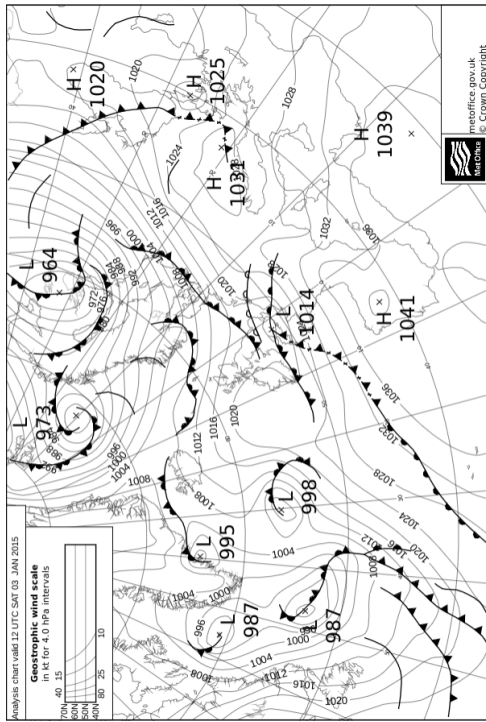
Figure 5-3a depicts the temperature profiles for 0000 UTC (red) and 1200 UTC (black) on 3rd January 2015. The 0000 UTC profile shows that there is a surface (low) level temperature inversion between 0 m and 250 m and by 1200 UTC is still present



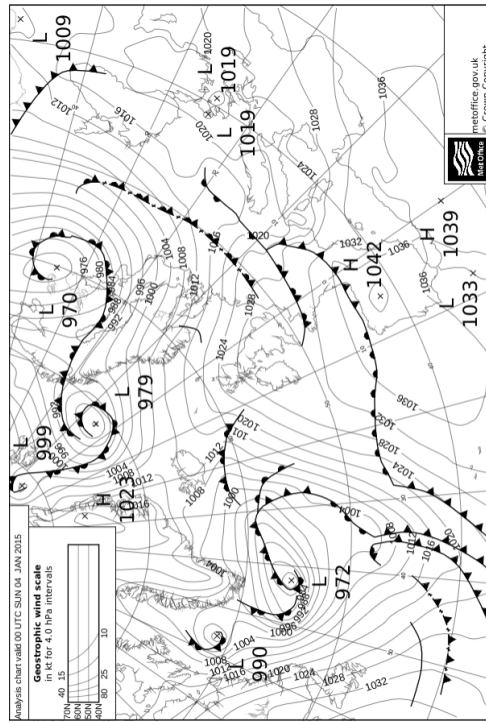
(b)



(d)




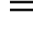
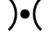





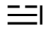

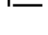
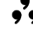






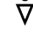




(a)



(c)

Figure 5-1: Met Office surface analysis charts for (a) 1200 UTC 3rd January 2015, (b) 1800 UTC 3rd January 2015, (c) 0000 UTC 4th January 2015, (d) 1200 UTC 4th January 2015 (Met Office 2015a). This sequence depicts the evolution of a region of high pressure that is advected from north-west to the south-east of the United Kingdom, resulting in calm conditions. Crown Copyright public sector information reproduced under the Open Government Licence (<https://www.nationalarchives.gov.uk/doc/open-government-licence>, last accessed 29/08/2016).

Table 5.1: World Meteorological Organisation present weather symbols reported from weather stations which may be manned or automatic. (Images at <https://github.com/OGCMetOceanDWG/WorldWeatherSymbols>, last accessed 9/12/2015, licensed under Creative Commons License 3.)

Symbol	Description
	Haze
	Mist
	Precipitation, reaching the ground or the surface of the sea, but distant > 5 km from the station
	Drizzle (not freezing) or snow grains not falling as shower(s)
	Rain (not freezing) not falling as shower(s)
	Shower(s) of rain
	Shower(s) of snow, or of rain and snow
	Fog or ice fog
	Fog or ice fog, sky visible, has become thinner during the last hour
	Fog or ice fog, sky invisible, no appreciable change during the last hour
	Fog or ice fog, sky invisible, has become thicker during the last hour
	Drizzle, not freezing, continuous, moderate at time of observation
	Drizzle and rain, slight
	drizzle and rain, moderate or heavy
	Rain, not freezing, intermittent, slight at time of observation
	Rain, not freezing, continuous, slight at time of observation
	Rain, not freezing, continuous, moderate at time of observation
	Rain, not freezing, continuous, heavy at time of observation
	Rain shower(s), slight
	Rain shower(s), moderate or heavy
	Haze or,smoke, or dust in suspension in the air, visibility ≥ 1 km
	Precipitation, slight or moderate
	Intermittent precipitation

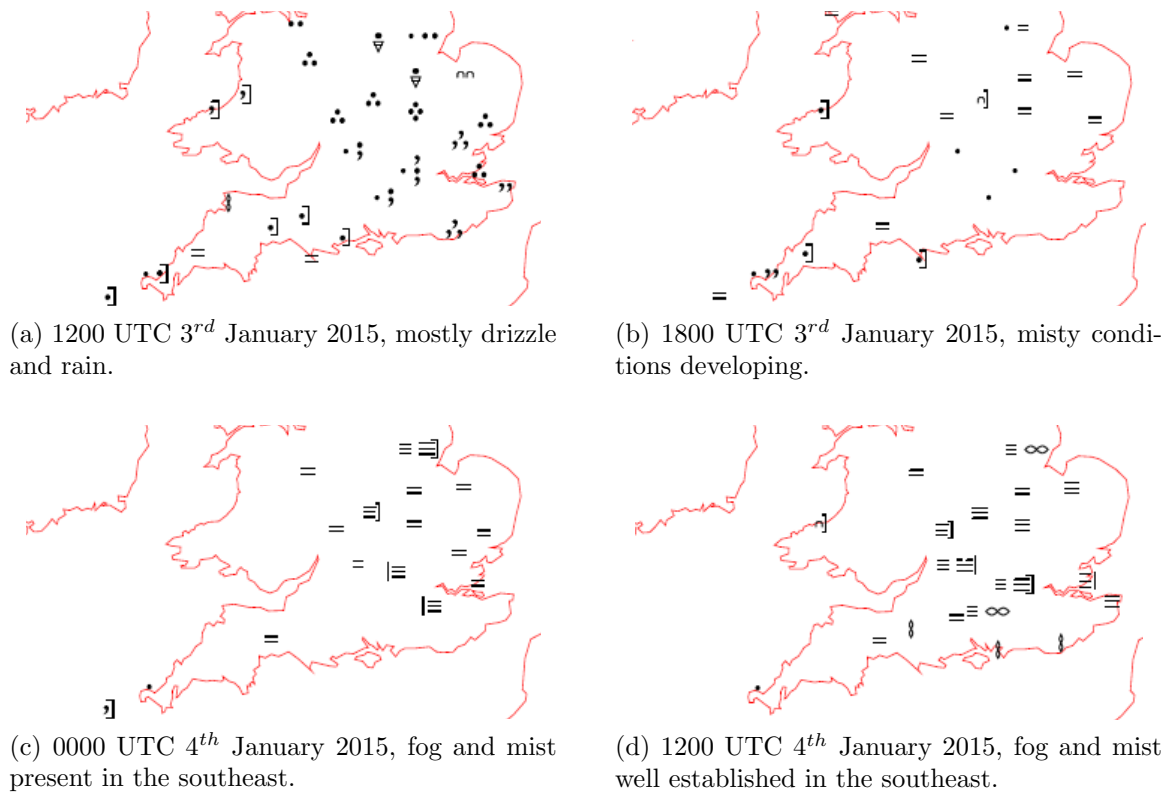


Figure 5-2: This sequence of significant weather charts shows the change in weather type resulting from a high pressure that is advected from north-west to the south-east of the United Kingdom during this period (Met Office 2015a). Symbols are listed in table 5.1. Crown Copyright public sector information reproduced under the Open Government Licence (<https://www.nationalarchives.gov.uk/doc/open-government-licence>, last accessed 29/08/2016).

but it is not a significant feature. This is due to the passage of weather fronts with warm air and precipitation.

Figure 5-3b depicts the temperature profiles for 0000 UTC (red), 0600 UTC (blue) and 1200 UTC (black) on 4th January 2015. By 0000 UTC (red) on 4th January 2015 the temperature inversion is re-established at 250 m. At 0600 UTC (blue) the temperature inversion appears to have risen to between 500 m and 1000 m and is a weak inversion. Sunrise on this day was around 8.00 am so it is unlikely that this weakening is due to daytime heating but may instead be due to weak convection at the surface. The elevated temperature inversion present at 2000 m is likely due to warming that results from subsidence of the upper air. At 1200 UTC (black) the low-level temperature inversion is re-established, with the subsidence inversion appearing

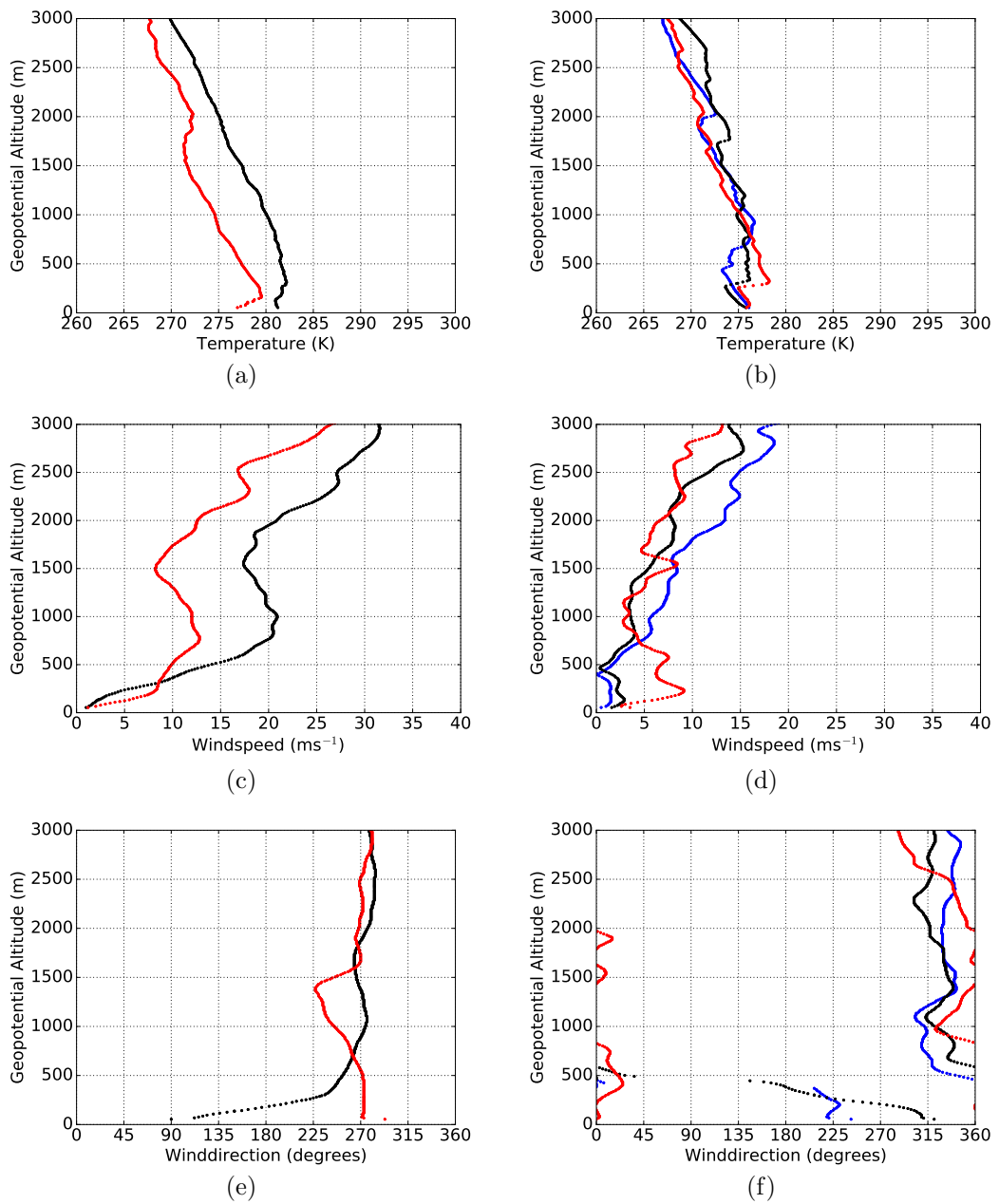


Figure 5-3: Radiosonde Herstmonceux, vertical profiles for 2015-01-03 (a) temperature (c) wind speed (e) wind direction and for 2015-01-04 (b) temperature (d) wind speed (f) wind direction. Validity times are for 0000 UTC (red), 0600 UTC (blue) and 1200 UTC (black) (Met Office 2015*b*).

lower down at 1750 m.

Figure 5-3c depicts the wind speed profiles for 0000 UTC (red) and 1200 UTC (black) on 3rd January 2015. The 0000 UTC profile shows that there is a low-level jet (see section 2.4, page 12) between 750 m and 1500 m, which is still present by 1200 UTC with increased magnitude. Figure 5-3d depicts the wind speed profiles for 0000 UTC (red), 0600 UTC (blue) and 1200 UTC (black) on 4th January 2015. By 0000 UTC the magnitude of the low level wind shear has reduced and thereafter calmer conditions begin to prevail at levels below 1000 m. At 0600 UTC and 1200 UTC calm conditions prevail near the surface (0 m to 500 m) with a steady increase in wind speed above this level.) Figure 5-3f shows that by 0600 UTC and 1200 UTC below 500 m wind direction is highly variable. This variability may be due to oscillations of the radiosonde sensor package since the magnitudes of the windspeeds are low for this period.

Figure 5-4 shows the track of Herstmonceux 0600 UTC radiosonde, launched at 0530Z on 4th January 2015. Figure 5-4a shows that the radiosonde headed in a southerly direction. It indicates that the prevailing wind direction is from the North. Figure 5-4b shows the direction of travel of the radiosonde for the altitude range 0 m to 3000 m and that air mass sampled is south of London Heathrow and London Gatwick.

5.4 Numerical Weather Prediction Data: UKV

In this section we show meteorological features using NWP data that are used to represent the atmospheric state for the airport domains.

Figure 5-5 (page 100) shows temperature profiles valid at 0600 UTC from the Met Office's NWP limited area model the UKV (which is described in section 2.10 (page 22) based on analysis at 0300 UTC on 4th January 2015 for (a) London Heathrow (EGLL) and (b) London Gatwick (EGKK) domains (these are defined in section 3.3 (page 35). The UKV NWP data have been bi-linearly interpolated in the horizontal to 1-D columns at 9 locations within the airport domain. These profiles are chosen to sample the mesoscale temperature variability of the model within the airport domain. Using these 1-D temperature profiles, a mean temperature profile can be computed for the centre of the airport, with the mesoscale variability being represented by the standard deviation of the sample.

In figure 5-5a the NWP vertical profiles show that low-level temperature inversions are forecast to be present within the London Heathrow domain. The bases of the inversions are at or near the surface in the north-west to just above the surface in the south-east of the domain. The tops of the inversions appear to be between 500 m to 1000 m. Similarly, figure 5-5b shows for the sample of locations in the EGKK domain

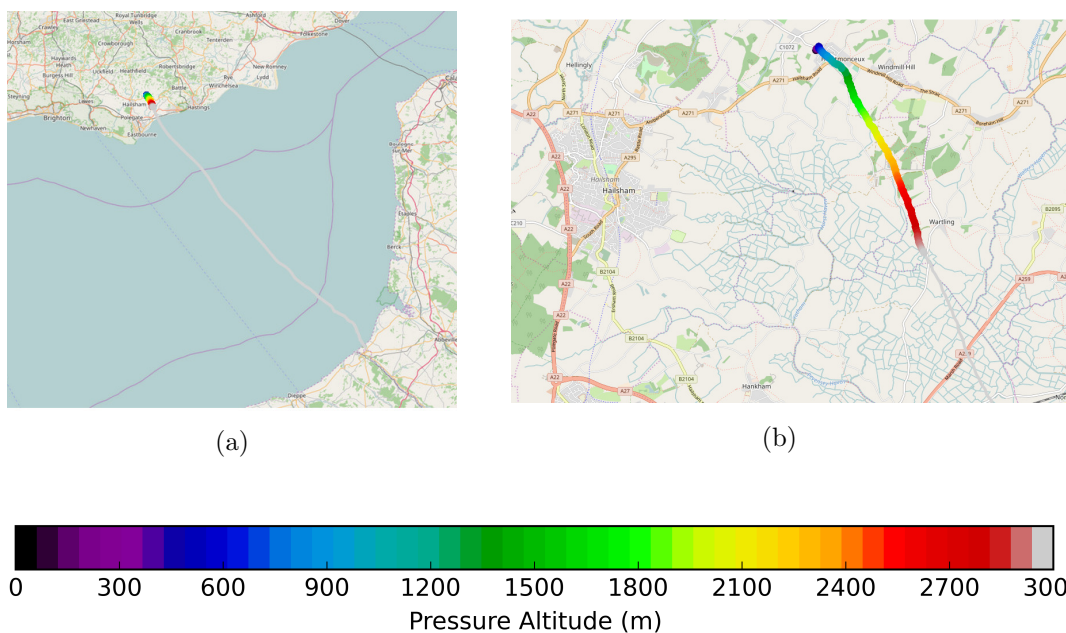


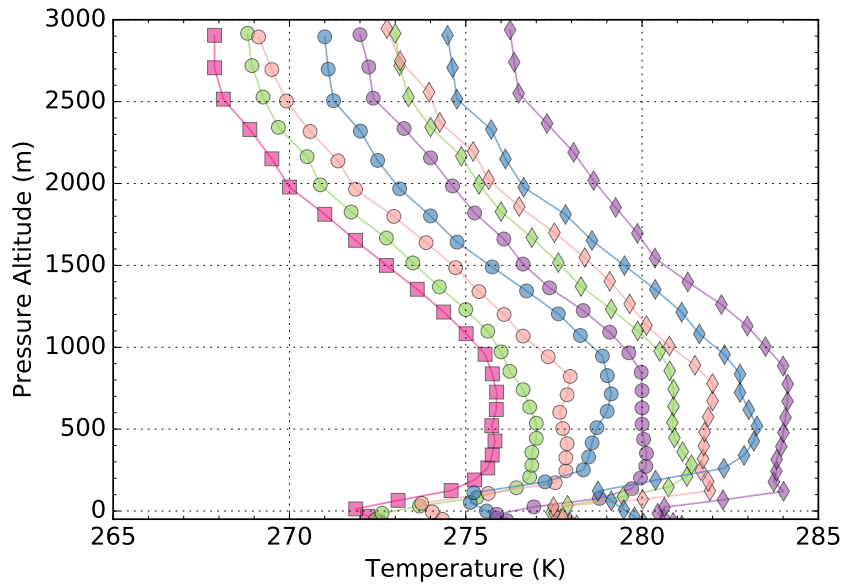
Figure 5-4: (a) The track of Herstmonceux 0600 UTC radiosonde, launched at 0530Z on 4th January 2015. Track shows the radiosonde was heading southwards (bearing 152° N), away from the airport domains, total distance travelled 120 km. (b) Track of radiosonde for altitude range 0 m to 3000 m, distance travelled 5 km. Each report is colour coded by pressure altitude (colour bar), grey indicates altitude is ≥ 3000 m.

that low-level temperature inversions are also forecast to be present. The bases of the inversions are all above the surface at around 200 m. The tops of the inversions appear to be between 400 m to 500 m. The depth of the inversion at EGLL is greater than that at EGKK. Above 1000 m at EGLL and 500 m at EGKK the temperature lapse rate follows the expected rate of change $\frac{\Delta T}{\Delta z} < 0$ (see discussion on temperature inversion in section 2.3, page 9).

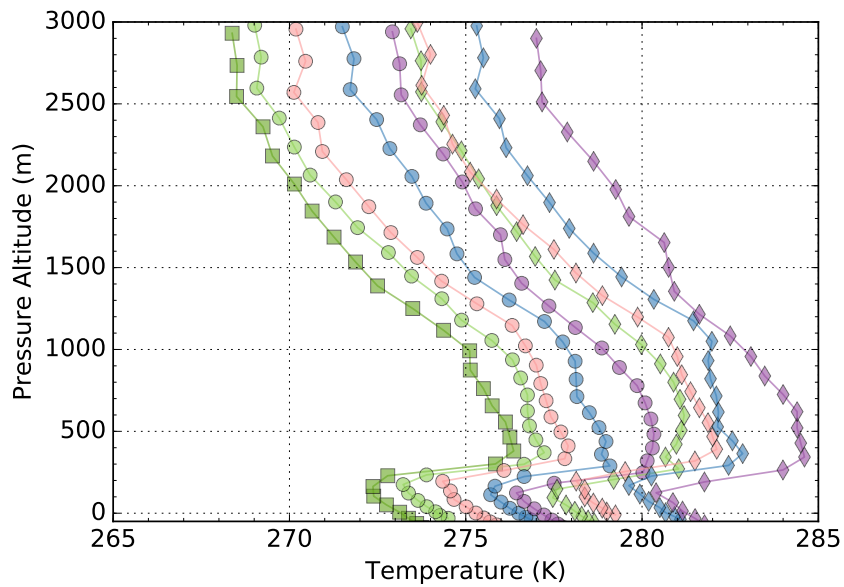
5.5 Met Office Mode-S EHS Receiver Network

In this section we describe the new source of Mode-S EHS reports which are used for the case studies in chapters 6 and 7.

The Met Office Mode-S EHS receiver network consists of five receivers. Table 5.2 (page 103) lists the five locations (Stone & Pearce 2016, Table 1). Four of the five receivers are co-located with Met Office operational Doppler radar sites. The network as a whole has been operating since March 2015. However, for the case study period only the receiver at Thurnham was available.



(a)



(b)

Figure 5-5: 1-D column temperature profiles valid at 0600 UTC from the Met Office NWP UKV analysis at 0300 UTC 4th January 2015 for (a) London Heathrow (EGLL) and (b) London Gatwick (EGKK) domains. The profile with large squares is centred at the airport, the circles are the profiles at the domain's cardinal compass points North (N) (light green), East (E) (pink), South (S) (blue), West (W) (purple) and the small diamonds are at Northwest (NW) (light green), Northeast (NE) (pink), Southeast (SE) (blue), Southwest (SW) (purple). To show the detail in each profile a constant is added to the temperature reports at the cardinal compass points (N+1, E+2, S+3, W+4, NW+5, NE+6, SE+7, SW+8).

The Mode-S EHS receiver consists of a 1090 MHz tuned antenna mounted atop the radar tower and connected to an in-line amplifier. The receiver intercepts down-linked Mode-S EHS encoded messages (ICAO 2012, Table A-2-83) which are decoded on-site before being transmitted to the Met Office in Exeter. The Met Office Mode-S EHS receivers are passive so are not capable of requesting Mode-S EHS encoded messages. The down-linked messages are mostly polled for by secondary surveillance radars operated by NATS (described in section 3.2) but smaller regional airports may also operate such radars independently. Therefore only reports that have been actively polled for by air traffic services are collected and processed by the Met Office receiver network.

Figure 5-6 (page 102) depicts the coverage of the Met Office network for the receipt of Mode-S EHS reports received between 21st May 2015 to 31st June 2015 inclusive (Stone & Pearce 2016, fig 2(a)). The figure shows that low-level reports are received for airports located in the Southeast and the Northwest of England, and the east coast of Ireland. The lowest altitude for which Mode-S EHS reports are received depends on the line-of-sight between the aircraft and the Mode-S receiver. The current network may not be optimal since the receivers are located at sites chosen for meteorological monitoring rather than for collection of aircraft reports. Thus coverage at the lower altitudes may be incomplete around some commercial airports. The Mode-S EHS reports are collated on-site then transmitted in batches every 10 minutes to a central processing facility located at the Met Office, Exeter, where the data are then passed through a quality control process.

Quality control consists of two stages (Stone & Pearce 2016). The first is a gross error check which removes reports considered erroneous. This is followed by checks to remove duplicate reports received by different receivers (see table 5.3). The second stage is an aircraft specific true heading correction similar to the NWP methods suggested by de Haan (2011) and Mulally & Anderson (2011). The NWP model used is the Met Office limited area model the UKV (Tang et al. 2013). The UKV wind vector, the aircraft's reported ground vector and true airspeed are used to compute an estimate of the aircraft's true heading. The true heading correction for each aircraft is defined to be the mean difference between the reported heading and the estimated heading, where differences are computed from the previous seven days of UKV NWP forecasts. Using the aircraft's derived heading correction, a wind vector and Mach temperature are computed using eqs. (3.5), (3.6) and (3.4) (page 38). (The methods for these computations are discussed in sections 3.4 and 3.5.)

The results along with the original Mode-S EHS reports and additional meta data, such as the aircraft's Mode-S address and receiver location, are stored in the Met

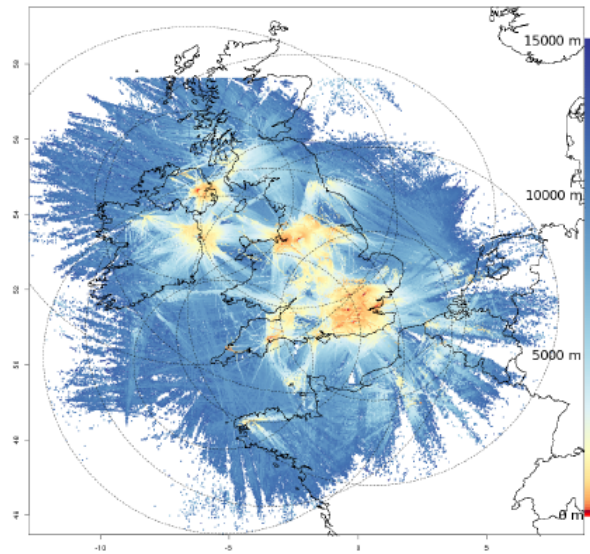


Figure 5-6: Spatial coverage of the Met Office Mode-S EHS receiver network. Colours indicate the lowest observation altitude within a 0.0125 longitude/latitude box (as determined from the Global Navigation Satellite System (GNSS)). Reports received between 21st May 2015 to 31st June 2015 inclusive. Image ©Met Office, 2015, reproduced under Open Government Licence (Stone & Pearce 2016, Fig 2).

Office’s Meteorological Database (MetDB).

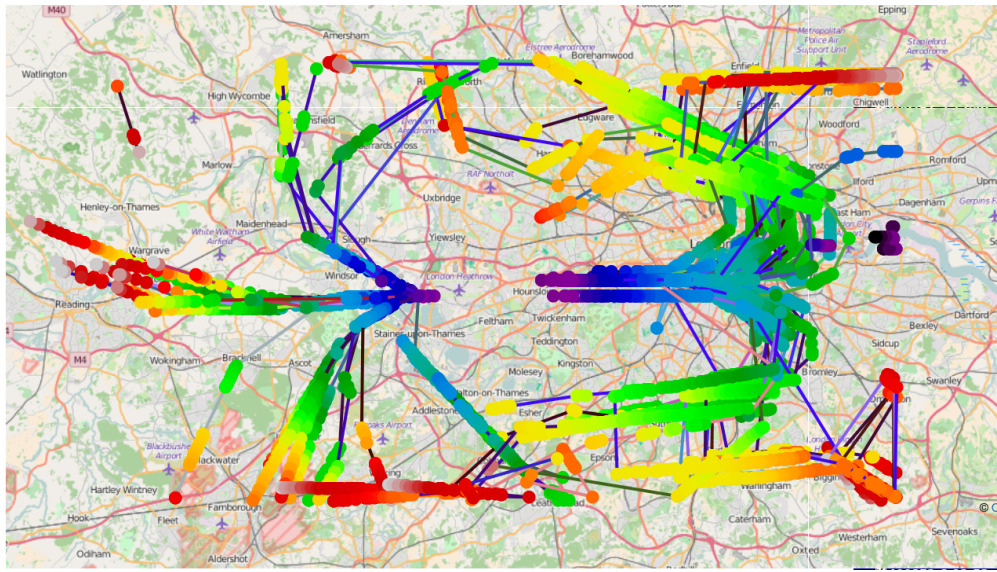
5.6 Geographic Distribution of Aircraft

In this section we show an example of the horizontal and vertical distribution of aircraft within the airport domains, which are defined in section 3.3 (page 35). The distribution is for a one hour period. This is used in chapter 6 for constructing vertical profiles of the mean temperature and mean horizontal wind for the airport domain.

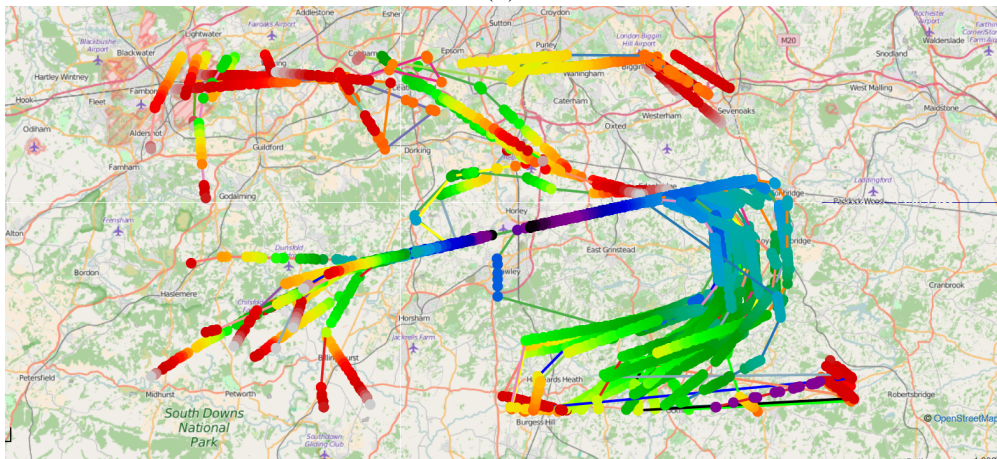
Figures 5-7a and 5-7b (page 104) show the spatial distribution of aircraft within the London Heathrow and London Gatwick domains on 4th January 2015 between 1200 to 1300 UTC. Each coloured dot represents a Mode-S EHS report and the colour of the dot indicates the pressure altitude. The colour bar provides the scale for the reported pressure altitude, the scale increment is 10 metres. The reported positions show that there were few Mode-S EHS reports below 300 m at London Heathrow during this period. By contrast, for the same period at London Gatwick there are more aircraft reporting Mode-S EHS below 300 m, especially for aircraft arriving. The difference may be due to the line-of-sight between the airport’s runway and the Mode-S EHS receiver. Such is the precision of modern aircraft navigation systems that aircraft tracks are

Table 5.2: Mode-S EHS receiver locations for the Met Office network, and the nearest airport with its ICAO identifier in brackets. Table adapted from (Stone & Pearce 2016, Table 1)

Site ID	Location	Expected number of observations per day	Site Description
EXT	Exeter, Met Office HQ	400000	Tuned antenna, 2 m from the top of a metal 10 m mast. Site is 3 km west of Exeter International Airport (EGTE)
RAD1	Thurnham, Met Office Radar Site	1600000	Tuned antenna on a radar tower, mounted so the top of the antenna is below the bottom of the radar dome. Site is 60 km north east of London Gatwick Airport (EGKK)
RAD2	Preddanack, Met Office Radar Site	500000	Tuned antenna on a radar tower, mounted so the top of the antenna is below the bottom of the radar dome. Site is in the far south west of Great Britain.
RAD3	Caster Bay, Met Office Radar Site	600000	Tuned antenna on a radar tower, mounted so the top of the antenna is below the bottom of the radar dome. Site is in Northern Ireland, 20 km south west of Belfast International Airport (EGAA)
RAD4	Hamelton Hill, Met Office Radar Site	1400000	Tuned antenna on a radar tower, mounted so the top of the antenna is below the bottom of the radar dome. Site is in North West England, 40 km, north of Manchester Airport (EGCC)



(a)



(b)

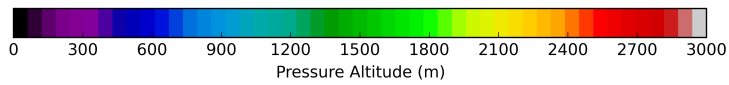


Figure 5-7: Spatial distribution of aircraft 4th January 2015, 1200 to 1300 UTC. (a) London Heathrow domain (b) London Gatwick domain. Aircraft departures are heading west and arrivals are from the east. The coloured dots indicates Mode-S EHS reports and the pressure altitude of the report. Colour bar is for the pressure altitude in the range 0 m to 3000 m in increments of 10 m (Background map ©OpenStreetMap contributors, reproduced under licence Creative Commons Attribution-ShareAlike 2.0.)

Table 5.3: Quality control parameters used by the Met Office Mode-S EHS gross error check. The asterisk (*) indicates the conditions used to remove manoeuvring aircraft. (Stone & Pearce 2016, Table 3)

Parameter	Quality Control Thresholds
True airspeed (knots)	$75 < V_A < 550$
Indicated airspeed (knots)	$100 < V_I < 550$
Difference between the calculated and reported ground track angle	$< 5^\circ$
Difference between the calculated and reported ground speed	$< 5^\circ$
Maximum time between the four required Mode-S reports	$< 10 \text{ s}$
Roll angle*	$< 2^\circ$
Difference between the last and current reported heading*	$< 20^\circ$
Difference between the aircraft heading and reported ground track angle*	$< 20^\circ$

overlaid giving the appearance of only a few tracks.

London Heathrow has two parallel runways which allows simultaneous arrivals and departures. Aircraft departures are on the left-side of the figure and arrivals are on the right-side of the figure. There were 43 aircraft arrivals, at approximately 90 s intervals, and 32 aircraft departures, at approximately 120 s intervals.

London Gatwick differs from London Heathrow. It has only one runway; consequently the traffic mix differs. The runway usage alternates, with aircraft arriving from the East followed by aircraft departures take-off towards the west. There were 24 departures and 22 arrivals. The average time separation between aircraft is 78 s.

The arrival and departure rate at this time of day, along with the precision of the navigation suggests that aircraft derived observations may be able to capture the mesoscale variability in temperature and horizontal wind within the vicinity of each airport. The spatial distribution of the reports suggest that the shape of the sampling domain could be described using an inverted cone or pyramid, with its apex centred at the airport and its base covering the approach and departure routes at 3000 m.

5.7 Aircraft-based Observations

In this section we describe the aircraft-based observations that are available for the case studies discussed in chapter 7. All aircraft based observation reports are retrieved from the Met Office meteorological database.

Figure 5-8 shows the time-series of the available AMDAR and Mode-S EHS reports for the period 2nd to 8th January 2015. There is a diurnal variation in the number of available observations which is consistent with the regulated operating hours of UK airports. The plot also shows that the number of Mode-S EHS reports is at least 100-times the number of AMDAR reports. This time-series profile is a typical distribution of these type of reports.

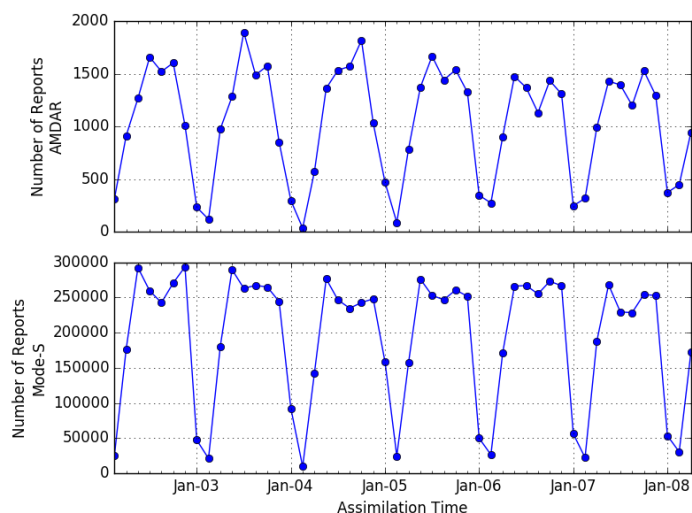


Figure 5-8: Typical number of AMDAR and Mode-S EHS reports available for the period 0300 UTC 2nd to 0600 UTC 8th January 2015. Data shown is for temperature, the number of reports for wind is of the same order.

The geographic distribution of the reports for AMDAR and Mode-S EHS is shown in figure 5-9. In figure 5-9a the AMDAR reports are distributed unevenly across the whole of the UKV domain, they are mostly concentrated along the main air traffic routes. They appear to emanate from three centres: the South-east and North-west England, and Central Scotland. The greatest concentration is in the South-east. The rate of AMDAR reporting is configured at the time of flight (see section 3.1). In contrast, the distribution of Mode-S reports shown in fig. 5-9b are concentrated in the South of England. This is expected as the reports are collected using the Met Office receiver network (see section 5.5) which had only two receivers in operation (Thurnham and Exeter) at the time of data assimilation trial. The lower density of AMDAR reports is due to the number of suitable equipped aircraft in the participating airline fleet and the cost constraints for aircraft communication charges.

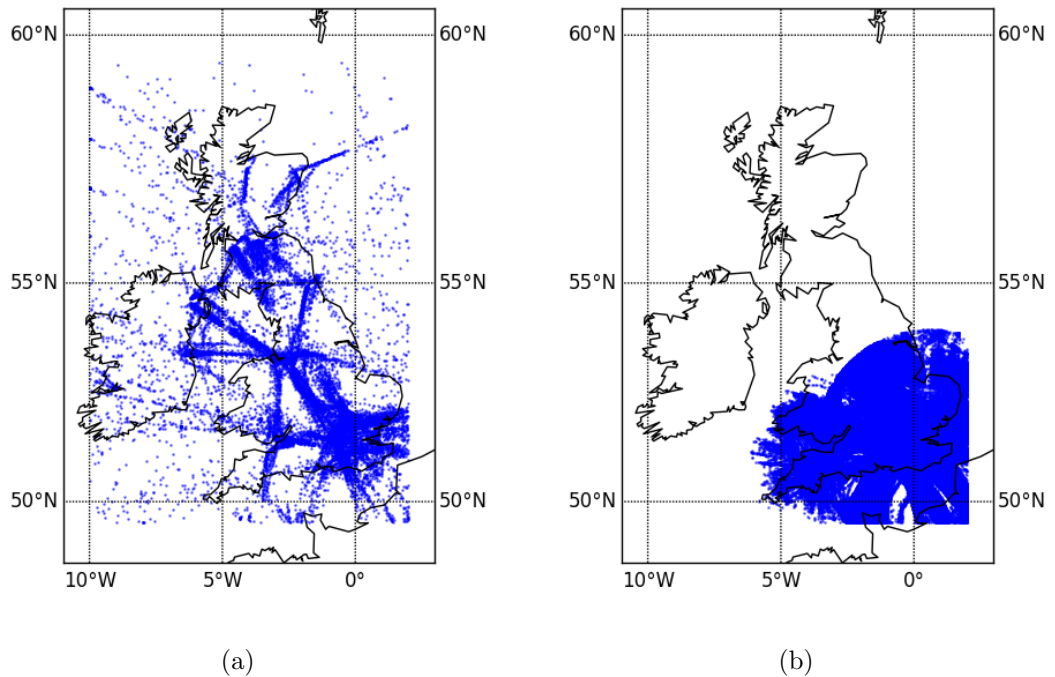


Figure 5-9: Geographic distribution of observations (a) AMDAR (b) MODES for the period 0300 UTC 2nd January 2015 to 0600 UTC 8th January 2015. Each blue dot represents a single report. Total number of reports for AMDAR is 18,384 and for Mode-S EHS is 589,120.

5.8 Summary

In this chapter we have described the synoptic meteorology for the 2nd to 8th January 2015. Briefly, this period enjoyed calm weather conditions at the start which broke down at the end of the period as cold fronts swept in from the west bring unsettled weather conditions. The calm period was notable for the presence of fog which persisted for two days. Using observations from Herstmonceux radiosonde, we have shown that meteorological features of interest were present: temperature inversions and low-level jet. Similarly, using NWP data for the airport domains, London Heathrow and London Gatwick we have shown that temperature inversions were forecast. We have described the Met Office Mode-S EHS receiver network and shown how these reports are distributed spatially for the airport domains. The reports collected by this network will be used to address our two thesis questions which are the subject of chapters 6 and 7.

With the knowledge gained in this chapter, in chapter 6 we aim to determine

whether meteorological features shown to be present using radiosonde observation data and NWP data can be shown to be present using Mode-S EHS reports.

Chapter 6

Meteorological Information Contained in Mode-S EHS Derived Observations.

6.1 Introduction

In this chapter we address our second thesis question: what atmospheric phenomena within the boundary layer can be observed from using high-frequency observations derived from Mode-S EHS messages. For our preliminary study in section 3.7.2 (page 47) we used Mode-S EHS reports supplied by NATS. Using these reports we constructed vertical profiles of derived temperature and horizontal wind. With the results from this preliminary study we suggested that meteorological features such as temperature inversions could be identified.

In chapter 4 we investigated the first thesis question on the accuracy of the observations derived from Mode-S EHS reports. We concluded that the precision of the reported air vector and Mach number leads to a significant source of error in the derived meteorological observations. The source of the error is due to the increase in quantisation error that results from the reduced precision.

In this chapter we investigate further the second thesis question by using the high-frequency observations derived from the routine collection of Mode-S EHS reports from multiple aircraft. However, in this investigation we use Mode-S EHS reports collected using the Met Office Mode-S EHS receiver network (described in section 5.5, page 99). Moreover, we also investigate the effect of quantisation error on the spatial and temporal averaging of these reports. We conclude that the effects of quantisation remains a significant source of error. Furthermore, this becomes the dominant source

of error below 1000 m as the density of reports decreases and because the temperature calculation is more sensitive at lower Mach numbers.

Air traffic density in the UK is greatest within the vicinity of London Heathrow and London Gatwick. The use of two SSRs (fig 3-1b, page 35) to monitor air traffic also provide higher frequency of reporting Mode-S EHS. Using these reports, it is possible to construct vertical profiles of temperature at more frequent intervals in space and time than is currently available from radiosonde and AMDAR. We validate these profiles qualitatively against available AMDAR and radiosonde reports. The benefit of Mode-S EHS is its low cost and more frequent reporting. This may provide additional weather information at airport locations, e.g., temporal evolution of temperature inversions that may provide an indication for the onset and duration of conditions leading to adverse weather, e.g., fog and low visibility, that would affect airport operations.

In this chapter we use a case study period to evaluate the use of aggregated Mode-S EHS reports for locating temperature inversions within the boundary layer. In section 2.3 (page 9) we described the meteorological conditions that give rise to temperature inversions. In section 5.2 (page 92) we described the meteorological conditions for our case study period 3rd to 5th January 2015, during which low visibility occurred.

In section 6.2 we review our method of constructing temperature profiles to find the most practical horizontal layer depth to use for our method aggregation, which we used in section 3.7.2 (page 47) to construct vertical temperature profiles within the vicinity of an airport. In section 6.4 we make qualitative comparisons between our constructed vertical profiles of temperature and the nearest available temperature observations from AMDAR and radiosonde and with NWP forecast temperature profiles. We note from the previous section that there large fluctuations in the aggregated temperature, especially at altitudes below 1000 m. Therefore in section 6.5 we describe four methods to smooth the fluctuations in Mode-S EHS reports for Mach number and true airspeed. Before we apply the low-pass-filters, we need to construct the aircraft's trajectory which we discuss in section 6.6. These trajectories show that the Mach number and airspeed change asynchronously, so in sections 6.7 and 6.8 we investigate the effect of the asynchronous changes using the low precision the Mach number and true airspeed on the Mach temperature. Then in section 6.9 we apply and evaluate the use of the low-pass-filters for smoothing the asynchronous changes in the Mode-S EHS reports of Mach number and True Airspeed for individual aircraft. We then re-construct the vertical profiles of Mach Temperature. In section 6.10 we use the error model for Mach Temperature, developed in section 4.5 (page 66), to estimate the uncertainty in the smoothed aggregated Mach Temperature. We conclude this chapter in section 6.11 with our finding that quantisation error remains a strong source of error for the

smoothed aggregated observations.

6.2 Constructing Temperature Profiles using Mode-S EHS Reports

We wish to estimate the depth of a horizontal layer in which to form aggregated observations (section 3.6, page 39). The aggregated observations should provide sufficient vertical resolution so as to identify the depth of a temperature inversion (section 2.3, page 9) or the peak wind speed of a low-level jet (section 2.4, page 12), and contain a sufficient number of reports from different aircraft to minimise uncorrelated random errors. We will call this depth the altitude bin width.

In figures 6-1 and 6-2 we show temperature profiles constructed from aggregated Mode-S EHS reports for the London Heathrow domain on 4th January 2015 with a validity time of 0600 UTC. The aggregation of observations is described in section 3.6 (page 39). There are other profiles shown which will be discussed in section 6.4 (page 118). We also show for Mode-S EHS temperature profiles the effect of changing the width of the altitude bin used to aggregate the observations: 150 m (fig 6-1), 300 m (fig 6-2a), and 75 m (fig 6-2b). The Mode-S EHS observation for each altitude bin is the aggregate of the derived temperature reports that are ± 30 minutes of the validity time. The constructed mean profile is centred at the validity time. We choose the time period ± 30 minutes of the validity time to correspond with ascent time for the radiosonde temperature profile. For plotting purposes each aggregated Mode-S EHS observation is plotted at the mean altitude of the reports within the altitude bin. The error bars for the Mode-S EHS observation are for the standard deviation (grey) and the 95% confidence limits for the mean (black) of the derived temperature reports used within the altitude bin. In computing the 95% confidence limits we use the Student-t distribution (Hoel 1984, Chapters 5 and 11) with the degrees of freedom ($N-1$) where N is the number of reports in the altitude bin. We use the Student-t distribution because the uni-modal distribution of reports within each altitude bin becomes less certain at levels below 1000 m, due to the drop in the number of reports, and the observation mean and standard deviation is estimated. Furthermore, we assume that the errors in the Mach number and true airspeed, used to derive the temperature, follow a uniform distribution. However, the distribution of resulting Mach temperature error appears to be uni-modal. This is evident when inspecting the distribution of temperature reports at altitudes above 600 m, for example see figure 6-3.

In figure 6-3 we show the corresponding distribution of temperatures within each altitude bin for the first eight bins: 75 m (fig 6-3a), 150 m (fig 6-3b) and 300 m (fig

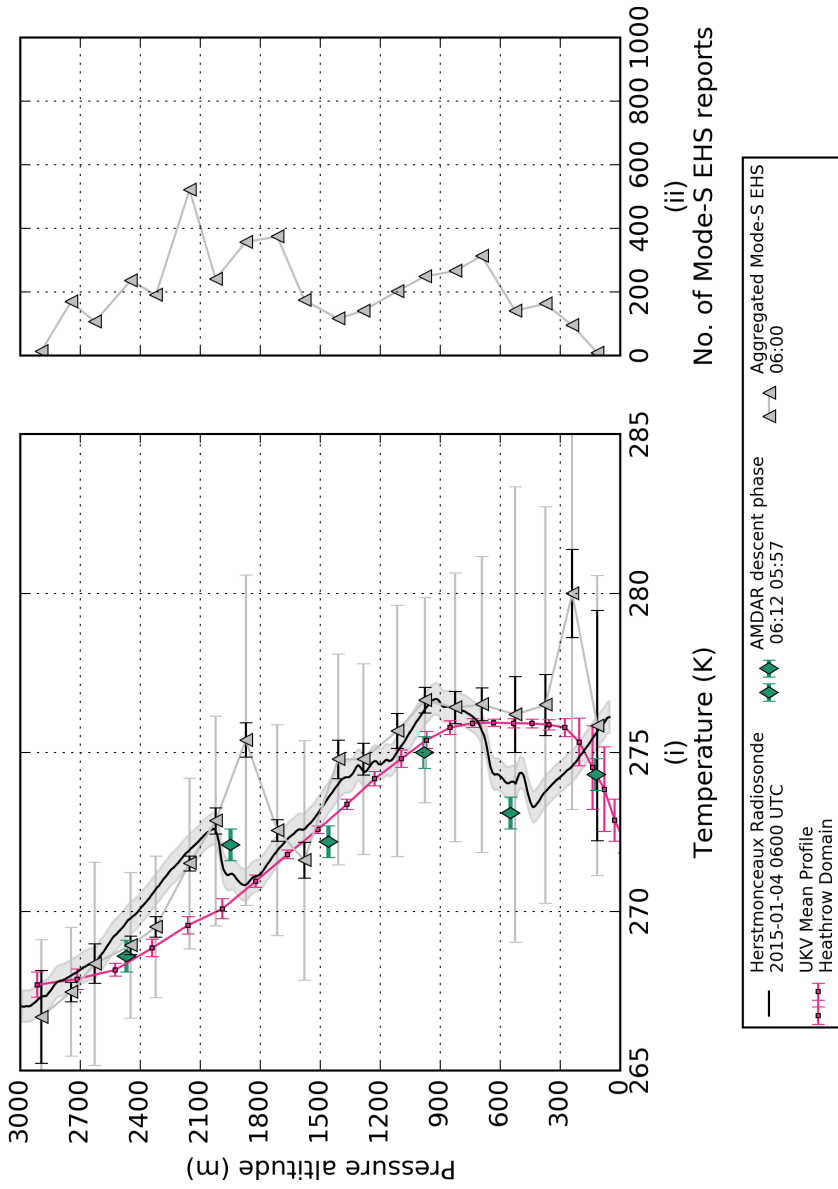
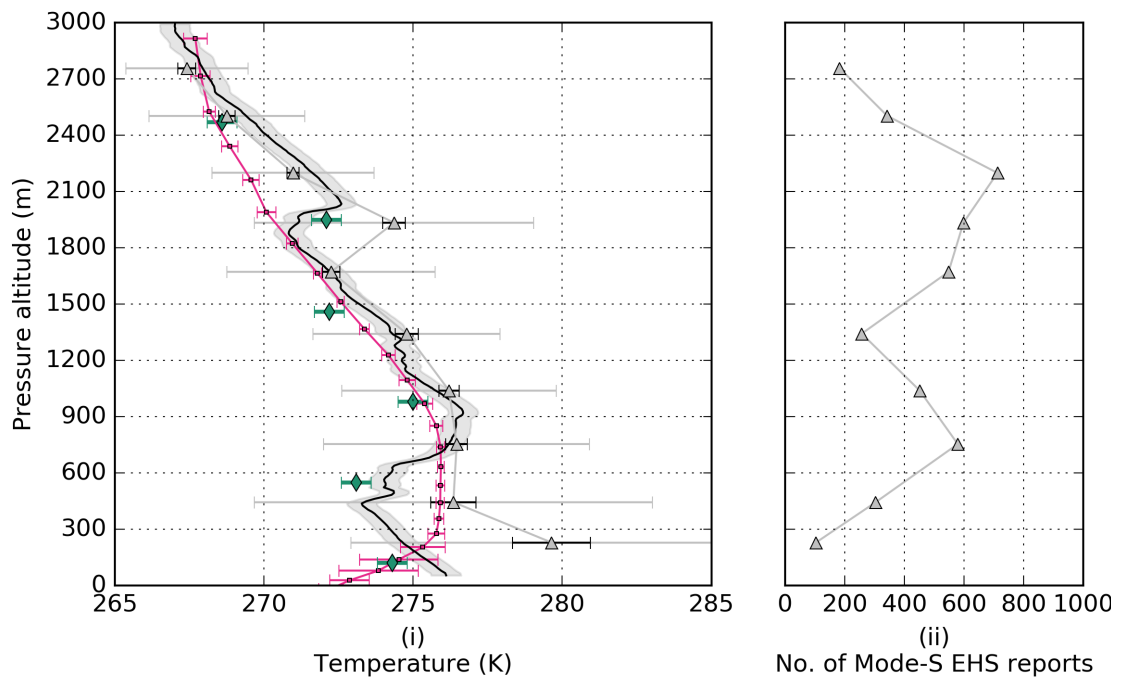
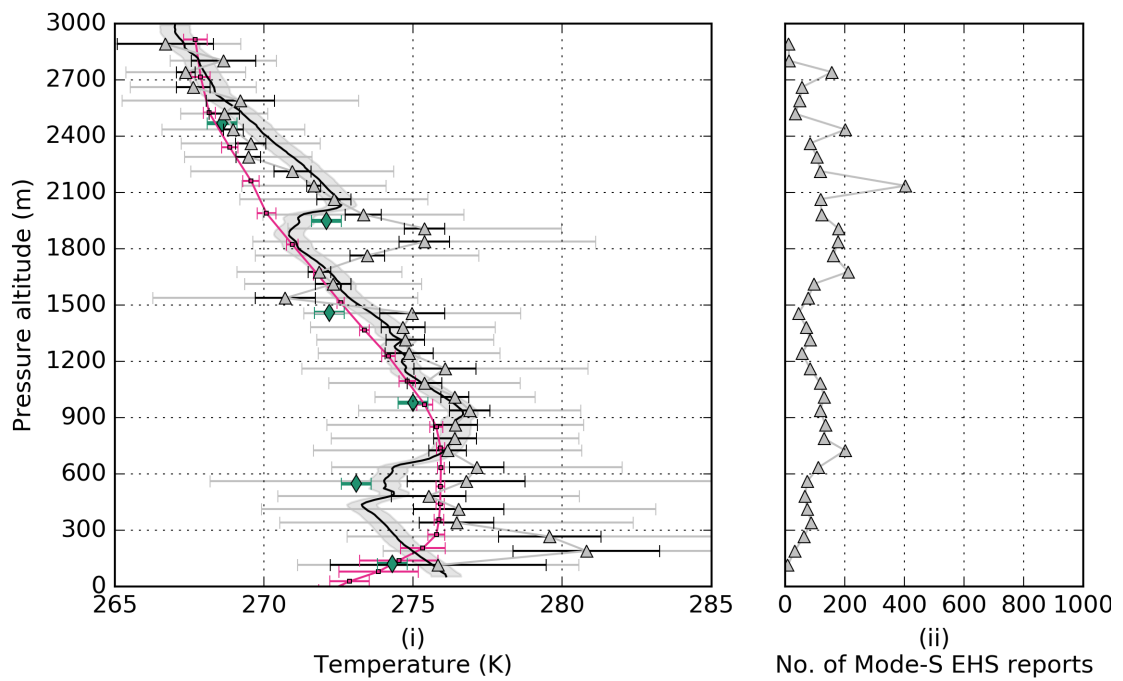


Figure 6-1: (i) Temperature reports for London Heathrow domain for the validity period 0530 to 0630 UTC on 4th January 2015. Aggregated Mode-S EHS Mach temperature profile (triangles), with the mean profile centred at the validity time 0600 UTC. The error bars are for the standard deviation (grey) and the 95% confidence limits for the mean (black). Herstmonceux 0600 UTC radiosonde temperature profile (black) estimated accuracy is ± 0.5 K (shaded region). Mean temperature 1-D vertical profile (magenta) from the Met Office UKV 4th January 2015 03Z UKV valid at 0600 UTC, error bars indicate the 95% confidence limits of the mean. AMDAR reports (diamonds), the error bars are for the estimated accuracy (± 0.5 K). (ii) The number of Mode-S EHS reports used to compute the aggregated observation.



(a) Altitude bin width 300 m.



(b) Altitude bin width 75 m.

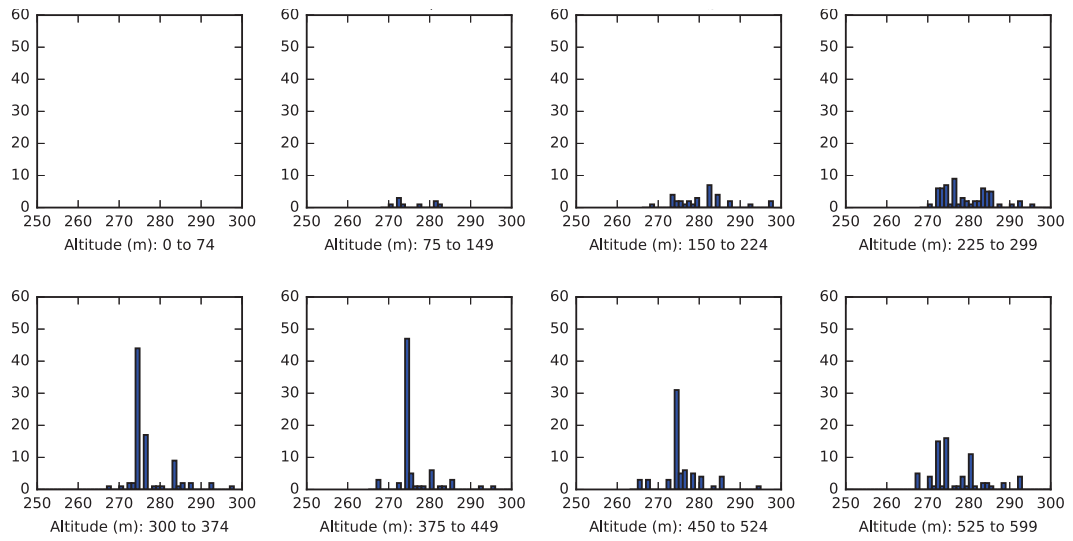
Figure 6-2: This plot shows aggregated Mode-S EHS Mach temperature profiles (triangles) for London Heathrow domain using different altitude bin widths (a) 300 m and (b) 75 m. Plot legend is the same as in figure 6-1.

6-3c). (Table 6.1, page 116, tabulates for each altitude bin width the number of reports, the mean Mach Temperature, \bar{T}_{Mach} , the standard deviation, σ , standard error of the mean σ_e and the mean of the estimated Mach Temperature Error.) As can be seen from these distributions the narrower the altitude bin the fewer Mode-S EHS reports it contains. This results in a spread of temperature reports across a finite range. So for the smaller altitude bin there is no apparent central tendency for a single temperature report that can be considered as representative of the prevailing ambient temperature.

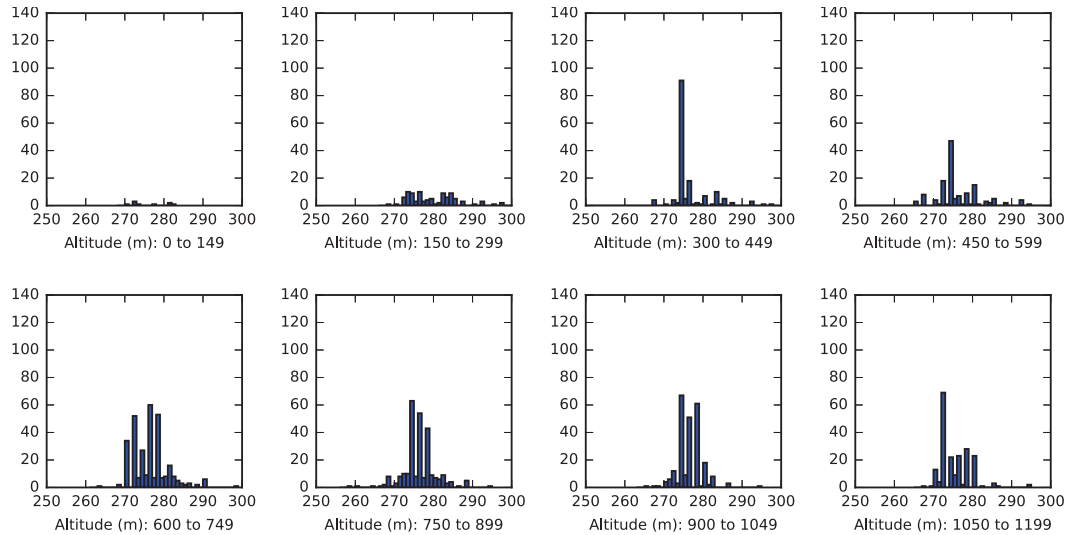
A balance needs to be struck between the width of the altitude bin, the number of reports it contains and the subsequent confidence in the result. Figure 6-2a shows the aggregated Mode-S EHS temperature profile for the altitude bin width 300 m. This has the advantage of containing a large number of Mode-S EHS reports, of the order 500 reports in altitude bins above 600 m. A large number of reports provides a more uni-modal distribution such as shown in figure 6-3c and higher confidence in the computed mean. However, the disadvantage of this altitude bin width is that it is not suitable for resolving sharp or rapid changes in temperature such as those near the surface.

Figure 6-2b shows the aggregated Mode-S EHS temperature profile for the altitude bin width 75 m. The effect of reducing the altitude-bin width is to reduce the number of Mode-S EHS reports that can be used to compute the aggregated observation. A lower number of reports provides distributions which appear bi-modal, non-uniform or skewed such as shown in figure 6-3a and it is less clear what the mean of the distribution should be. We note that some of the distributions appear to have two peaks. This may be due to the derived temperature oscillating between two values such as seen in the FAAM temperature profile shown in figure 4-1b (page 67). We have suggested that this oscillation may be an artefact arising from the low precision of the Mach number. The advantage of the smaller altitude bin width is to increase the vertical resolution of the temperature profile. This affords the facility to resolve sharp or rapid changes in the temperature gradients. However, this does cause an increase in the uncertainty in the mean value, especially at low levels where the number of available reports tail off toward zero.

Figure 6-1 shows the aggregated Mode-S EHS temperature profile for the altitude bin width 150 m. This appears to be a suitable compromise between the number of reports available to compute a reliable mean value; the distribution of the reports is mostly uni-modal above 500 m, and there is less variation in the means along the profile. This altitude bin width affords the facility to resolve reasonably rapid changes in the temperature gradient above 500 m. Thus we choose to use an altitude bin width of 150 m. We acknowledge that this altitude bin width may not be suitable for identifying temperature gradients below 500 m. This is because below 500 m the mean derived



(a) Distribution when altitude bin is 75 m. Altitude range 0 m to 600 m.



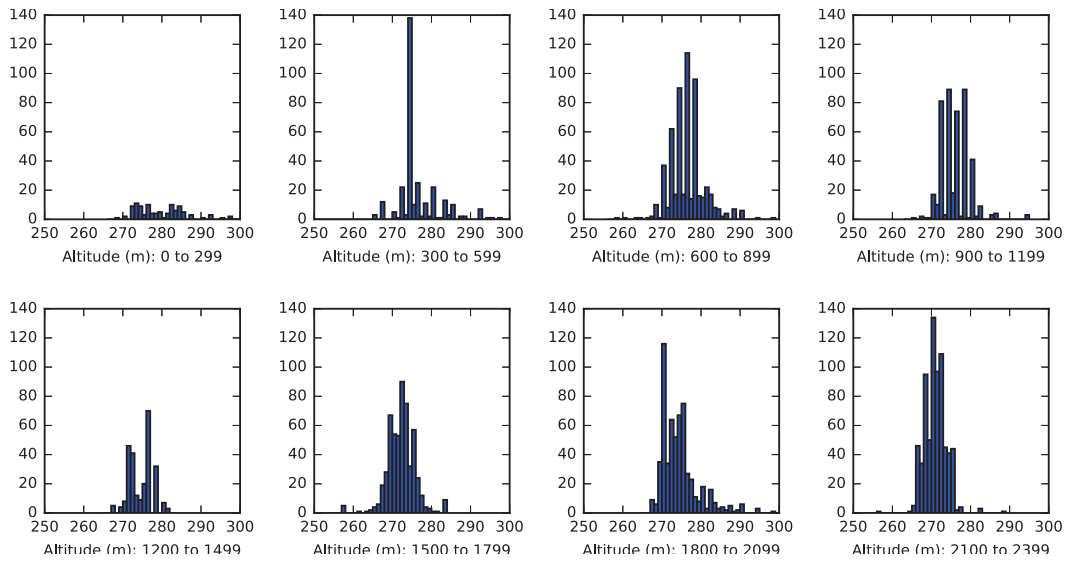
(b) Distribution when altitude bin is 150 m. Altitude range 0 m to 1200 m.

Figure 6-3: Distribution of Mach Temperatures for different altitude bins. London Heathrow Domain, 05:30 to 06:30 UTC, 4th January 2015. For each plot, y-axis is Number of reports, x-axis is Mach Temperature (K) where bin-width = 1 K. In panel (a) there are no reports below 75 m.

temperature becomes less certain, as shown by the histogram distributions in figure 6-3.

Table 6.1: Statistics for histogram distributions shown in figure 6-3

Altitude Range (m)	N_R	\bar{T}_{Mach}	σ	σ_e	MachT Error
Altitude Bin Width 75 m (see figure 6-3a)					
0	74	0	-	-	-
75	149	9	275.84	4.71	1.57
150	224	32	280.81	6.82	1.21
225	299	63	279.58	6.80	0.86
300	374	88	276.46	5.92	0.63
375	449	75	276.53	6.61	0.76
450	524	66	275.52	5.06	0.62
525	599	75	276.78	8.59	0.99
Altitude Bin Width 150 m (see figure 6-3b)					
0	149	9	275.84	4.71	1.57
150	299	95	280.00	6.79	0.70
300	449	163	276.49	6.23	0.49
450	599	141	276.19	7.16	0.60
600	749	313	276.51	4.65	0.26
750	899	266	276.41	4.22	0.26
900	1049	249	276.64	3.22	0.20
1050	1199	202	275.67	3.95	0.28
Altitude Bin Width 300 m (see figure 6-3c)					
0	299	104	279.64	6.72	0.66
300	599	304	276.35	6.67	0.38
600	899	579	276.46	4.46	0.19
900	1199	451	276.21	3.60	0.17
1200	1499	257	274.79	3.13	0.20
1500	1799	548	272.25	3.49	0.15
1800	2099	598	274.36	4.69	0.19
2100	2399	712	270.98	2.71	0.10



(c) Distribution when altitude bin is 300 m. Altitude range 0 m to 2400 m.

Figure 6-3: Figure continued from page 115.

6.3 Time and Length Scales of Aircraft-based Observations

In section 2.2 we introduced the concept of a time and length scale that can be associated with an atmospheric phenomenon. The length scale of an atmospheric phenomenon that can be studied using aircraft-based observations is determined by its horizontal sampling length. This is defined as the distance travelled by the aircraft during the sampling time. The distance travelled by the aircraft is a function of its true airspeed and the sampling time of its reporting or its measuring instruments (Lenschow & Stankov 1986; Sharman & Lane 2016, p. 99).

For single Mode-S EHS observations we can expect the horizontal sampling length scale to be a function of the aircraft's true airspeed and the average time between Mode-S EHS reports, this is illustrated in figure 6-4. The aircraft's true airspeed will also be function of its altitude above the surface, so the horizontal sampling length will also vary by altitude (not shown). The length scales shown in figure 6-4 correspond to mesoscale atmospheric phenomena such as deep convection, short gravity waves and clear air turbulence (Orlanski 1975, Fig 1).

For aggregated Mode-S EHS observations the horizontal sampling length is fixed by the horizontal spatial extent and time period over which the observations are aggregated and the vertical resolution is fixed by the altitude bin width. Aggregation

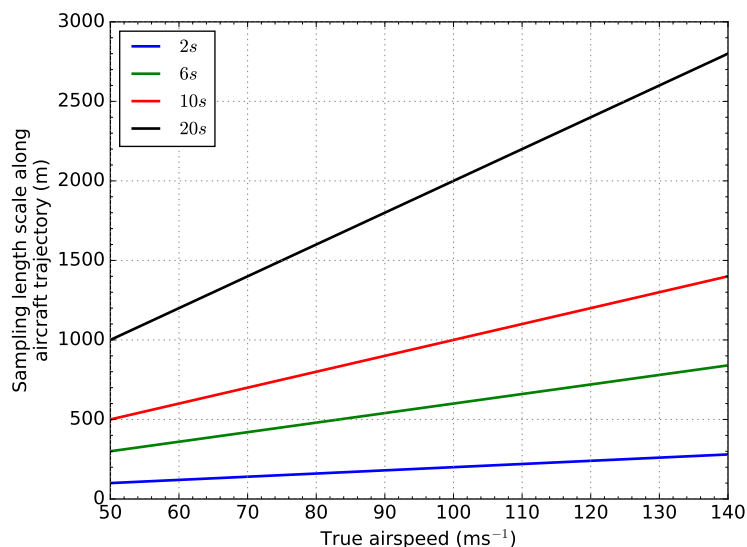


Figure 6-4: Horizontal sampling length scale along the aircraft’s trajectory. The sampling time is given in the legend.

of observations averages out smaller scale variations that may be detected by a time series of single observations. For our case study our aggregated observations used a horizontal spatial extent of 80 km, a time period of one hour and a vertical resolution of 150 m. The horizontal length scale is comparable to that of meteorological phenomena such as the nocturnal low-level jet, mesoscale convective systems and weather fronts (Orlanski 1975, Fig 1). We have shown in figure 6-1 that the vertical resolution is still sufficient to resolve temperature inversions, even after the horizontal averaging.

6.4 Derived Mode-S EHS Temperature Profiles

We consider whether the density of observations available from Mode-S EHS is sufficient to capture weather phenomena such as temperature inversions. We use Mode-S EHS reports of Mach number and true airspeed to derive Mach Temperature using eq. (3.4) (page 38). To use as much of the observational data as possible we aggregate the Mode-S EHS observations to form mean profiles for temperature (section 3.7.2, page 47). We assume the averaged observations to have a smaller error than an individual observation, which can be approximately 10 K. The standard error of the mean scales by $1/\sqrt{N}$, where N is the number of reports and if the random errors are uncorrelated (Hoel 1984, Ch 5 and Ch 10). We assume further that the resulting mean profiles are representative of the meteorological conditions for the airport’s domain. We compare these profiles with corresponding UKV NWP mean 1-D profiles and observations from

AMDAR or Radiosondes where these are available.

In Figure 6-1 (page 112) the left panel shows four vertical profiles for temperature for the Heathrow domain:

1. the Mode-S EHS temperature profile (triangles) for the validity time 0600 UTC. The profile was constructed using aggregated Mode-S EHS reports received ± 30 minutes of the validity time using altitude bins of 150 m. The aggregated report is centred at the mean altitude of the reports within the bin. The Mode-S EHS temperature error bars are for the standard deviation (grey) of the reports in the altitude bin and the 95% confidence limits for the mean (black). The right panel shows the number of Mode-S EHS reports used to compute the aggregated observation for each altitude bin.
2. the Herstmonceux 0600 UTC radiosonde temperature profile (black) with the accuracy (± 0.5 K) represented by the shaded region. The radiosonde was launched at 0515 UTC, headed due south of its launch site at Herstmonceux (fig 5-4, page 99), and reached an altitude of 3000 m at 0524 UTC. Position and temperature reports were made every 2 s. The region of the atmosphere sampled by the radiosonde is not contained within the Heathrow domain.
3. The mean forecast temperature profile for the Heathrow domain (magenta) with the validity time 0600 UTC. This is from the Met Office UKV NWP model run on 4th January 2015 0300 UTC. The mean temperature profile is computed by using 1-D column profiles at the nine points indicated in figure 3-2 (page 36). The error bars indicate the 95% confidence limits of the mean. The standard deviation (not shown) at each point shows that at this time there is little variation (< 0.5 K) in the temperature across the domain between 300 m and 3000 m and below 300 m the standard deviation is around 1.5 K. A study by Ingleby & Edwards (2015) estimated the average UKV NWP model error, when compared against high-resolution radiosonde reports, to be 0.75 K for this altitude range.
4. For the validity period 0600 UTC ± 30 minutes there is one AMDAR profile (aircraft identifier AFZA63). The error bars are for the estimated accuracy AMDAR temperature reports (± 0.5 K).

For the identification of useful meteorological information we use the radiosonde temperature profile as our reference, even though it is outside of the Heathrow domain. The 0600 UTC observations from the radiosonde and AMDAR would not have been available for data assimilation for the UKV forecast, which was generated 3-hours earlier.

In figure 6-1 (page 112) the radiosonde report indicates the presence of two temperature inversions: a low level temperature inversion between 500 m to 900 m, reported at 0516 UTC, and an elevated temperature inversion between 1800 m to 2000 m, reported at 0520 UTC. The AMDAR reports, reported between 0557 UTC to 0612 UTC, are broadly in agreement with the radiosonde. However, there is a clear difference between the direct observations and the UKV NWP forecast.

The UKV NWP forecast places the low level inversion between the surface and 300 m and does not forecast the elevated inversion. The radiosonde and AMDAR reports would be received after the UKV NWP data assimilation observations processing time, 0130 to 0419 UTC, thus these observations were not included in the UKV NWP assimilation. Therefore the UKV NWP forecast will not have taken into account the existence and the location of the temperature inversions shown by these observations since there are no other source of upper air temperature observations during the observations processing time. The observed temperature inversions are not shown in the UKV NWP forecasts at 0300, 0400 and 0500 UTC. We note that the absence of the elevated temperature inversion at around 2000 m, that is recorded in the radiosonde report, would be important for the subsequent forecasts. An upper level inversion in effect caps vertical movement and dispersion of atmospheric aerosols, this may affect the forecast conditions for solar insolation and the formation of fog and cloud (Fowler et al. 2012).

The Mode-S EHS aggregated reports are largely in agreement with the radiosonde and AMDAR between 700 m up to 1800 m and 2000 m to 3000 m. Between 1800 m and 2000 m the reports indicate the presence of an elevated temperature inversion in a similar region as that shown by the radiosonde and AMDAR reports, and which is not represented by the UKV NWP forecast. However, the magnitude of the inversion suggested by the Mode-S EHS aggregated report differs significantly from the radiosonde and AMDAR reports. Below 700 m the Mode-S EHS aggregated report is in more agreement with the UKV NWP forecast. However, the direct comparison is difficult since time and spatial scales differ.

The radiosonde and AMDAR reports are essentially instantaneous values, reporting on a time scale of seconds to minutes. The aggregated Mode-S EHS observation uses all available Mode-S EHS reports over a large spatial domain (see figure 3-2, page 36) with a mean time of 2 s between reports. The aggregated observation is an average over the hour thus representing the mean conditions in time, so some variability will be lost due to the averaging process. For the mean reporting time, the horizontal spatial sampling scale is on average around 250 m (see figure 6-4, page 118). We find some agreement between the aggregated Mode-S EHS observation and the UKV

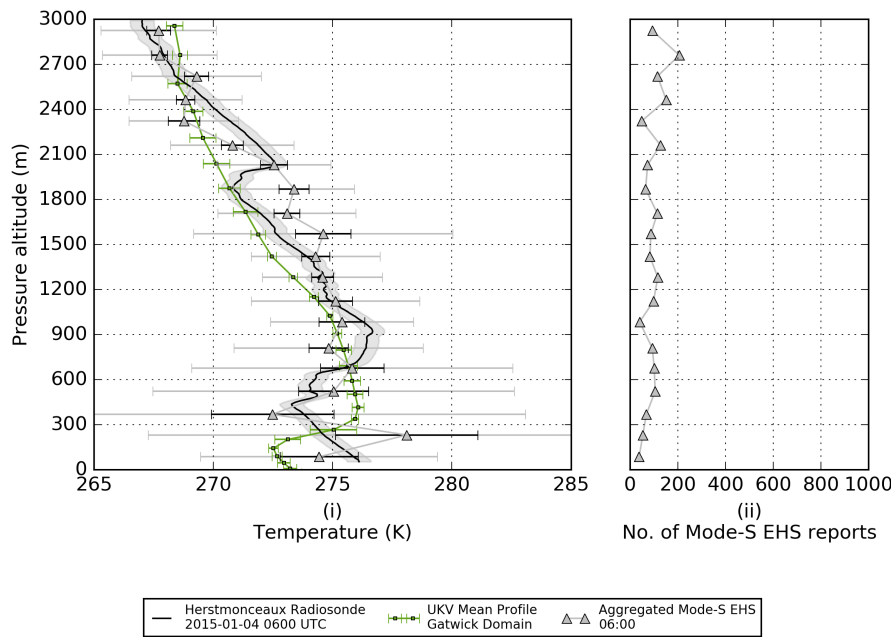
NWP because the latter also represents the mean conditions over the hour, although its spatial sampling scale is 1500 m. However, we still find some differences. For example, at 300 m the Mode-S EHS profile shows significant departure from the UKV NWP mean profile. This departure is a persistent feature for all hourly aggregated Mode-S EHS observations between 0600 and 1500 UTC when compared to the corresponding hourly UKV NWP forecasts.

Examination of the hourly profiles from this data set for the period 0600 UTC to 1500 UTC show that the low level Mach Temperature varied between a minimum of 277.8 K (4.6°C) ± 2.2 K at 0900 UTC and a maximum of 281.7 K (8.7°C) ± 2.5 K at 0700 UTC. The low level UKV NWP mean temperature varied between a minimum of 271.76 K (-1.39°C) ± 0.33 K at 0900 UTC and maximum of 276.74 K (3.59°C) ± 0.15 K at 1500 UTC. The surface observation reports from Heathrow airport show that at 0550 UTC the 2 m temperature was 272 ± 1 K, and which varied from 272 ± 1 K to 276 ± 1 K for the same period. The surface observations from the Met Office synoptic weather reporting stations within 25 km of Heathrow show that the 2 m temperature was between 271 ± 0.5 K and 273 ± 0.5 K at 0600 UTC, and which varied from 271 ± 0.5 K to 276 ± 0.5 K for the same period.

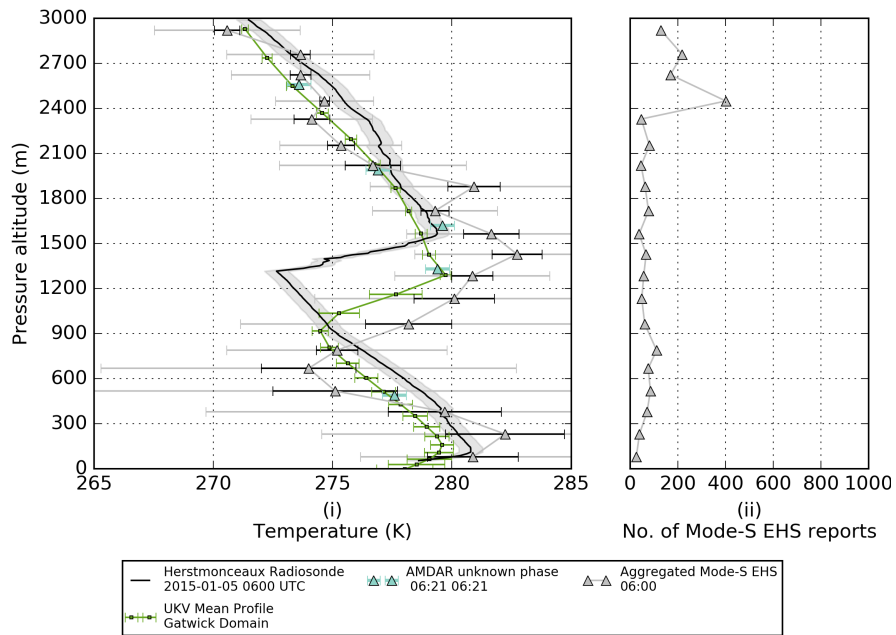
It is clear that the low level Mode S EHS Mach Temperature is reporting warmer conditions than is indicated by the AMDAR reports and UKV NWP forecasts. The temperature difference between them is of the order of 5 K . It is uncertain whether this difference is due to atmospheric variability from low-level turbulence that affects the aircraft sensors or an artefact that results from the Mode-S EHS processing.

It is clear that the Mode-S EHS aggregated reports show a degree of variability, represented by the standard deviation, which is not seen in the other profiles, especially at levels below 1000 m. As discussed earlier (section 6.7) we suggest that this variability is dominated by the precision of the data used to derive the temperature, since the atmospheric conditions do not appear to vary greatly over the hour, as indicated by the radiosonde and AMDAR reports. Nonetheless the vertical profile formed from the Mode-S EHS aggregated reports may provide additional information about the vertical temperature profile that is not represented by the other observations from radiosonde and AMDAR.

Figures 6-5 and 6-6 show plots for vertical temperature profiles at different times for London Gatwick and London Heathrow domains. The processing and labelling for these plots is the same as that used in figure 6-1 (page 112). Each plot shows the aggregated Mode-S EHS Mach Temperature (triangles) with the number of Mode-S EHS reports used for each altitude bin shown by the adjacent plot. Where available, other in situ temperature observations are also shown: radiosonde (black) and AMDAR (coloured

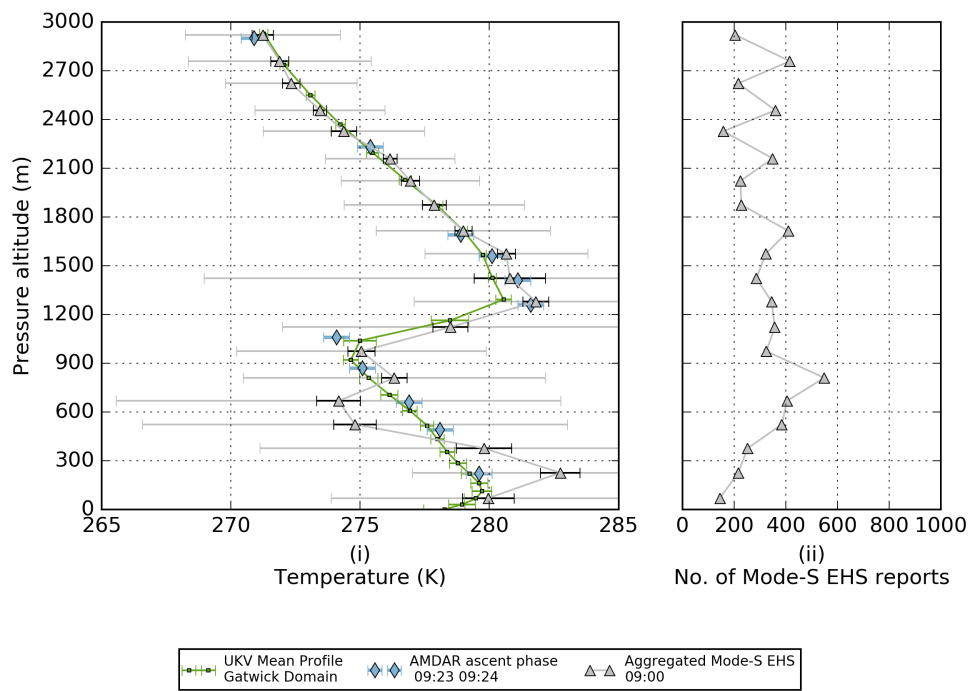


(a) London Gatwick 2015-01-04

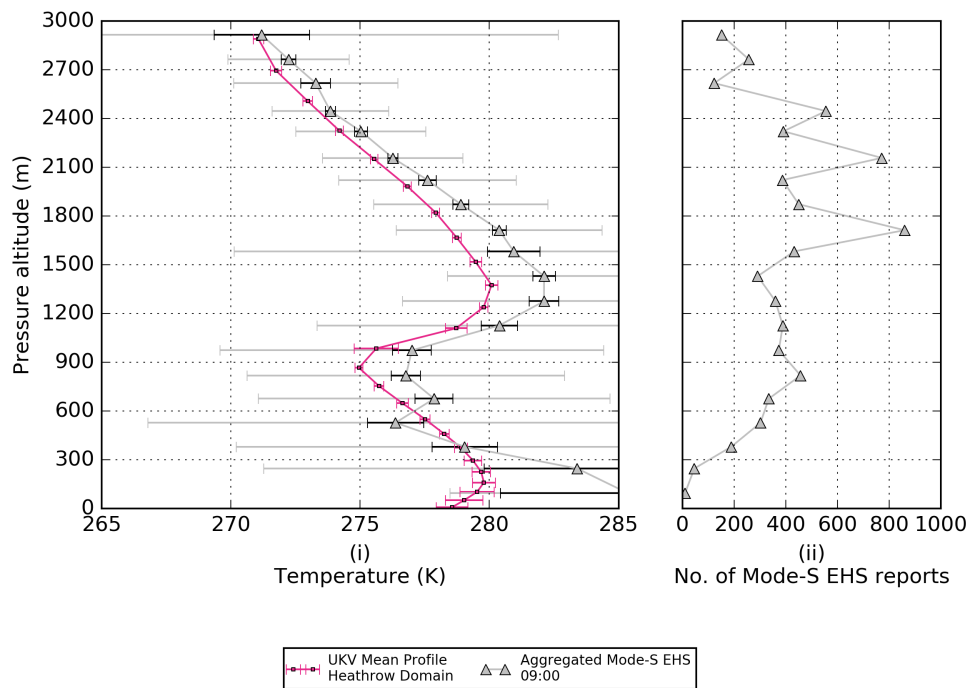


(b) London Gatwick 2015-01-05

Figure 6-5: London Gatwick at 0600 UTC for two days. (i) Mode-S EHS aggregated Mach Temperature vertical profiles (triangles), radiosonde (black) and mean UKV NWP (green) temperature profiles. (ii) The number of Mode-S EHS reports used for each altitude bin. See fig 6-1 for further plot details.



(a) London Gatwick



(b) London Heathrow

Figure 6-6: Mode-S EHS aggregated Mach Temperature vertical profiles (triangles) for London Gatwick and London Heathrow domains at 0900 UTC 5th January 2015. See fig 6-1 for further plot details.

points). The mean NWP forecast temperature profile (magenta/green) is from the UKV NWP model run at 0300 UTC on each day.

Figure 6-5a shows the 0600 UTC vertical temperature profile for London Gatwick domain. As already shown in figure 6-1 (page 112) the radiosonde report indicates a low level temperature inversion between 500 m and 1000 m. The UKV NWP temperature profile indicates the presence of a low level temperature inversion between 200 m and 400 m. There being no radiosonde or AMDAR observations for this time the Mach Temperature reports between 0 m and 450 m also suggest the presence of the low level temperature inversion. The Mach Temperature profile between 900 m and 2100 m indicates warmer temperatures when compared to the UKV profile, with a possible isothermal region between 900 m and 1500 m but no indication of an elevated temperature inversion between 1800 m and 2100 m, as shown by the radiosonde report. The uncertainty in the Mach Temperature reports at levels above 900 m does not rule out the presence of an elevated inversion. Below 900 m the uncertainty in the Mach Temperature increases and this is consistent with the effect of the reduced availability of the Mode-S EHS reports below 900 m, as shown in 6-5a panel (ii). So while the Mach Temperature reports between 0 m and 450 m indicate the presence of a low level temperature inversion it cannot be ruled out that the aggregated report is being affected by noise, which originates from the reduced precision of the Mode-S EHS reports for Mach number and true airspeed.

Figure 6-5b shows the vertical temperature profile for London Gatwick domain at 0600 UTC on 2015-01-05. Observations are from an 0600 UTC Herstmonceux radiosonde report (black) and five reports from an aircraft reporting AMDAR (coloured dots). (From the AMDAR time parameter it was not possible to determine whether these reports were from an aircraft ascent or descent.) We use the 2015-01-05 0300 UTC UKV NWP forecast to generate the 1-D profile temperature profile (green). The radiosonde and aircraft-based observations were not used to generate the UKV NWP forecast since they were received after the cut-off time, 0419 UTC, for accepting observations. It is clear from the radiosonde report that there is a strong elevated temperature inversion (for magnitude of the inversion see section 2.3) present between 1300 m and 1600 m and a low level temperature inversion between 0 m and 100 m. Similarly the UKV NWP forecast with validity time 0600 UTC shows the low level temperature inversion but forecasts the elevated temperature inversion between 900 m to 1300 m. The strength of the inversion is shallower when compared with the radiosonde. The AMDAR reports are largely in agreement with the UKV profile, except at 1600 m where this report is in agreement with the top of the inversion as recorded by the radiosonde report. The Mach Temperature profile is suggestive of the low level temperature inver-

sion but there is a large uncertainty. The elevated inversion is shown to be stronger and lower down in the atmosphere. (The uncertainty in the vertical position is small since at low levels the precision of the reported pressure altitude is ± 8 m, and the number of reports is around 50, so the standard error in the mean pressure altitude is of the order 1 m.) The number of reports available is significantly lower than that obtained for Heathrow. This difference is likely to be due to the lower traffic density at London Gatwick at this time of day.

Figure 6-6a shows the vertical temperature profile for London Gatwick domain three hours later at 0900 UTC on 2015-01-05. There are ten observations available from an ascending aircraft reporting AMDAR (coloured dots). The UKV NWP temperature profile (green) is the forecast mean of the 1-D profiles for validity time 0900 UTC obtained from the UKV NWP output at 0300 UTC. There is no radiosonde report for this time period. The UKV NWP forecast shows that there are elevated and low level temperature inversions. The AMDAR reports are mostly in agreement with UKV profile, the difference is small. At this time the number of Mode-S EHS reports is an order of magnitude greater than that for the same location at 0600 UTC. The resulting Mach Temperature vertical profile above 1000 m appears much more well defined when compared to the UKV profile. The increase in the number of Mode-S EHS reports between the surface and 1000 m does not appear to have improved the accuracy of the Mode-S EHS Mach Temperature profile. The magnitude of the difference between the Mach Temperature profile and the UKV profile is of a similar order as that shown three-hours earlier in figure 6-5b, where the magnitude of difference is around 2 K to 3 K. We suggest that changes of this order of magnitude are due to the Mode-S EHS precision error. A similar conclusion is drawn when comparing the Mode-S EHS Mach Temperature profile against the available AMDAR reports.

Figure 6-6b shows the vertical temperature profile for the London Heathrow domain at 0900 UTC on 2015-01-05. There are no observations from radiosonde or AMDAR at this time. There is no radiosonde report because these are normally available only at 0000 UTC and 1200 UTC unless additional launches are requested by the National Weather Service. The absence of AMDAR reports may be because there were either no suitably equipped aircraft or that any AMDAR reporting aircraft had its reporting managed by an optimisation reporting process (Carlberg 2012). The UKV NWP temperature profile (green) is the forecast mean of the 1-D profiles for validity time 0900 UTC obtained from the UKV NWP output at 0300 UTC. The UKV NWP forecast shows elevated and low level temperature inversions, so the atmospheric conditions are similar at Heathrow and Gatwick. Above 1500 m the number of Mode-S EHS reports available around Heathrow is greater than that available around Gatwick, this is likely

due to the different traffic patterns between the two domains, as well the line of the sight of the receiver unit. The Mach Temperature vertical profile above 1000 m appears well defined when compared to the UKV profile, if marginally warmer. Again, we note that above 1000 m the number of Mode-S EHS reports is of the order 400+. Despite the larger number of reports used for computing the aggregated observation the standard deviation remains high. There is a sharp increase in the Mach Temperature below 300 m when compared against the UKV, again, we suggest the changes of this order of magnitude are due to the Mode-S EHS precision error.

We conclude that qualitatively it appears that vertical temperature profiles constructed from aggregated Mode-S EHS reports could be used to identify temperature inversions. When constructed over the hour during the course of the day these profiles would provide additional information about the atmospheric state that may otherwise not be observed. However, there are significant limitations to this method due to the level of noise apparent in the data. We suggest in the first instance that Mode-S EHS processing is a significant source of the resulting temperature differences, as is suggested by the results from chapter 4 (page 55). In the remainder of this chapter we investigate the use of low-pass filters to reduce the effect of the quantisation error introduced by the Mode-S EHS processing. We note also that the higher range of Mach Temperatures at low levels may include a bias which may be the result of the difference in the number of aircraft ascents or descents used in computing the aggregated Mach Temperature.

6.5 Low-pass-filters

In this section we describe four low-pass-filters: block-window average (Flyvbjerg & Petersen 1989, Schmelling 1995), moving centred average (Brockwell & Davis 2002, Section 1.5), linear regression (Walpole et al. 2011, Ch 11) and exponential moving average (Wright 1986). These low-pass-filters are designed to smooth out rapid changes, i.e., high frequency components, in the Modes-S EHS reports for Mach number and true airspeed which are used to compute the Mach Temperature. The low-pass-filter replaces a group of adjacent reports, the validation window, by their filter value.

For each low-pass-filter we use the following notation: for one Modes-S EHS report type, N is the total number of reports in the time-series of an aircraft track; t_k is the time assigned to an individual report, x_k ; where k is the time index, ranging between 1 and N ; $2m + 1$ is the number of reports used to compute the average which contains the Mode-S EHS reports, where m is an integer value used to set the number of reports used by the low-pass-filter; $X_{\bar{t}}$ is the computed value of the Mode-S EHS report after applying the low-pass-filter, with validity time, \bar{t} .

A quality threshold is used. This is based on the time difference between two successive Mode-S EHS reports, δt . Where δt is greater than a maximum time difference δt_{max} then $X_{\bar{t}}$ is set to a missing data indicator. The value of δt_{max} ensures that the data used in the low-pass-filter are closely related in time and space. To estimate a value for δt_{max} , we compute the standard deviation of all time differences along all aircraft tracks identified for the day. We then round the standard deviation to the nearest integer value and assign this to δt_{max} . We do this because we expect fewer Mode-S EHS reports along an aircraft trajectory than are actually available in principle. This is due to quality control processing of Mode-S EHS reports (see table 5.3, page 105) .

6.5.1 Block-window average

The block-window average method creates a time-series of Mode-S EHS reports using the average of a validation window. The time-series is split into a sequence of blocks then the average of each block is computed. In computing the average no report is used more than once. The new filtered time-series is given by,

$$X_{\bar{t}} = \frac{1}{2m+1} \sum_{j=-m}^{+m} x_{k+j} \quad \text{for } k = m+1, 3m+2, 5m+3, \dots, \left\lfloor \frac{N}{2m+1} \right\rfloor (2m+1) - m, \quad (6.1)$$

and the validity time, \bar{t} , is given by,

$$\bar{t} = \frac{1}{2m+1} \sum_{j=-m}^{+m} t_{k+j}, \quad (6.2)$$

where $\left\lfloor \frac{N}{2m+1} \right\rfloor$ is the number of blocks of data of size $2m+1$ in the dataset. The operator $\lfloor x \rfloor$, gives the greatest integer that is less than or equal to x (Oldham et al. 2010, p.68).

This method is simple to implement but is not robust. It is still susceptible to large variations since all the reports within the validity window are equally weighted. Gaps in the time-series may arise because the time-difference between the reports used fail the quality control criteria.

6.5.2 Moving centred average

This is a straightforward method of computing a value over a short validity window. The method weights each report equally, so reports at the start of the validity window are treated to be of the same importance as those reports at the end of the validity

window. The new time-series is given by,

$$X_{\bar{t}} = \frac{1}{2m+1} \sum_{j=-m}^{+m} x_{k+j} \quad \text{for } k = m+1, m+2, m+3, \dots, N-m, \quad (6.3)$$

with the validity time given by eq. (6.2).

However, this method is not robust since it can be affected by large outliers and fluctuations in the new time-series may lag behind that seen in the original time-series, although the magnitude of the variations is reduced. Outliers may be the result of some random process or larger than expected values of Mach Temperature which appear inconsistent with the prevailing atmospheric conditions. However, filtering out these outliers is a subjective process without using corroborating observations, such as similar reports from nearby aircraft. The size of the validity window may result in the fluctuations of the output time-series lagging behind that observed in the input time-series.

6.5.3 Linear regression

This uses the least squares regression method to compute a local rate of change, which is assumed to be linear over the period for the reports $2m+1$. This is a statistical method that minimises the differences between a control variable and predicted values. The new time-series is given by,

$$X_{\bar{t}} = \alpha \bar{t} + \beta, \quad (6.4)$$

where the validity time is given by eq. (6.2) and the local constant, β , is given by

$$\beta = \bar{x} - \alpha \bar{t}, \quad (6.5)$$

where the mean value over the validity window is given by,

$$\bar{x} = \frac{1}{2m+1} \sum_{j=-m}^{+m} x_{k+j}, \quad (6.6)$$

and the local rate of change, α , (i.e., the gradient) is given by,

$$\alpha = \frac{\sum_{j=-m}^{+m} (x_{k+j} - \bar{x})(t_{k+j} - \bar{t})}{\sum_{j=-m}^{+m} (t_{k+j} - \bar{t})^2}, \quad (6.7)$$

for $k = m+1, m+2, m+3, \dots, N-m$.

Unlike the moving centred average this method is more responsive to variations in the time-series. The mean values obtained from fitting a straight line to the data

locally are used to create the new time-series.

6.5.4 Exponential Moving Average

The exponential smoothing method is similar to the moving centred average except observations are weighted according to their position in time. The current observation is weighted more than the observations made earlier in the time-window. The simple exponential moving average (Brown 2004*b*, Ch. 7) assumes observations are available at regular time intervals. However, since the Mode-S EHS reports used to construct aircraft trajectories may be at irregular time intervals and there may be missing data, the ((Wright 1986); (Kim & Huh 2011, Ch. 6)) method is used, which extends the method to irregular time intervals. The new time-series is given by,

$$X_{t_k} = (1 - V_k)X_{t_{k-1}} + V_k x_{t_k}, \quad (6.8)$$

where

$$V_k = \frac{V_{k-1}}{b_k + V_{k-1}} \quad (6.9)$$

and

$$b_k = (1 - a)^{(t_k - t_{k-1})}, \quad (6.10)$$

for $k = 2, 3, 4, \dots, N$, and $0 \leq a < 1$.

The value a is a smoothing parameter which determines the proportion of the new information to be added to the running average. The initial value of weighting function, V_1 , is equal to one. The larger the value of the smoothing factor, V_k , the less weight is given to the running average. The smoothing factor is a function of the time separation between the current report and the running average. This method is more sensitive to the variations in the time-series whilst maintaining a link to the overall trend in the time-series, so suppresses rapid changes (i.e., high frequency components).

6.6 Time-series of Mode-S EHS Derived Mach Temperature

In this section we describe our method to construct a time-series of Mach Temperature reports for an aircraft. The time-series consists of Mode-S EHS reports that can be assigned to an aircraft that was present in the airport domain for a chosen day. We do this so that we can apply our low-pass-filter to each aircraft's reports. We apply this method to obtain time-series reports for all aircraft.

Aircraft tracks are constructed for each day using Mode-S EHS reports, collected

by the Met Office receiver network (described in section 5.5, page 99), which were retrieved from the Met Office Meteorological Database (MetDB). This is done using the time-series of an aircraft's identifier which is the ModeS EHS transponder's six character hexadecimal address, hereafter called the 'ip' address. To identify a track, two conditions must be fulfilled for each ip address (1) three or more Mode-S EHS responses are required and (2) the end of a track is marked by a gap in the time-series of at least thirty minutes between two successive reports for each Mode-S EHS address. (Thirty minutes is the expected turnaround time between arrival and departure of the same aircraft operated by a low-cost airline.) Small gaps in the aircraft track can arise when data is missing or was filtered out as part of the quality control processing applied before the data were stored in the MetDB.

Each track is allocated an identifier as 'ip_trk_no' where 'trk_no' is the track number allocated to each of the aircraft's time-series of reports identified on the chosen day. Having established an identifiable track, the following aircraft reports which can be attributed to the ip address are assigned to the track's time-series: time of report, geographic position, pressure altitude, Mach number, true airspeed and derived Mach Temperature. Figure 6-7 (page 132) depicts the time-series of aircraft track attributes that were present for the period 0530 to 0630 UTC in the London Heathrow domain on 4th January 2015. This time period is selected as it corresponds to that of the radiosonde launched at Herstmonceux.

In figure 6-7 the tracks of the pressure altitude report show that between 0530 and 0550 UTC only two aircraft were descending into Heathrow. From 0550 to 0630 UTC nearly all the tracks are showing aircraft are descending. This is typical for London Heathrow as the early morning flights are mostly transatlantic or transcontinental arrivals. However, these time-series also include two tracks for ascending aircraft. At 0549 UTC the track 4C041_1 appears to show that the aircraft was descending then starts to ascend. This is probably a missed approach, which indicates that the pilot encountered a problem during the landing procedure and decided to abort the landing. At 0618 UTC the track 4951CE_1 shows that the aircraft was ascending. At 0622 UTC the track 89402A_1 shows the aircraft was in level flight at approximately 3000 m, this is likely to be an aircraft just leaving the holding stack to start its descent into the airport. The segments of aircraft tracks which are outside this time period are not shown and their data are not used. A closer inspection of the time-series shows that it is similar to that shown in figure 3-6(a) and 3-6(b) (page 49), which indicates that the Mach number and true airspeed appear smooth and free from large deviations. However, the time-series for the derived Mach Temperature shows significant variability (figure 6-7), similar to that shown in figure 3-6(c). It is unlikely that this variability is

due to the prevailing atmospheric ambient air temperature.

Figures 6-9 and 6-10 show the time-series of aircraft tracks as vertical profiles, where time is replaced with pressure altitude. The vertical profiles are for the Mach number, true airspeed and derived Mach Temperature. Figure 6-9c shows pressure altitude against the elapsed time of the aircraft's track, indicating whether an aircraft is ascending or descending. The aggregated observations (described in section 3.6, page 39) for Mach Number, true airspeed and Mach Temperature are shown as the black points with error bars. The error bars are the standard deviations of the reports within the altitude bin. The altitude bin height is 150 m. Each aggregated observation is plotted at the mean pressure altitude of all reports within the altitude bin. These profiles show which parts of an aircraft's track would be available for computing the aggregated observation.

In figures 6-9a and 6-9b there are three aircraft profiles which appear to depart significantly from the profile formed from the aggregated observations (black points). Aircraft 4C041_1 (green stars) performed a missed approach manoeuvre, i.e., it descended but did not touch down on the runway it instead ascended. The profile 4951CE_1 (green dots) corresponds to an aircraft take-off from the runway. The profile 40688B_1 (grey squares) corresponds to an aircraft entering the domain at a lower altitude, with upper part of its descent not being within the domain. All the other aircraft for this time period are descending and so are decelerating. The rates of acceleration and deceleration differ due to speed controls imposed for reasons of air traffic management and regulatory restrictions.

Aircraft arriving at an airport will be directed onto a standard arrival trajectory. While on the approach to land aircraft would be expected to maintain target airspeeds for each leg of the descent profile. The descent profile consists of three segments: the outer leg, the base leg and the final approach. The outer leg altitude range is 3000 m to 2000 m with target speed of 114 ms^{-1} . The base leg altitude range is 2000 m to 1000 m with target speed of 92 ms^{-1} . The final approach altitude range is 1000 m to 300 m with target speed of 82 ms^{-1} . Between 300 m and the aircraft landing there is no speed control beyond that required to maintain airborne safety (Civil Aviation Authority 2016). There will be some variability around these target speeds depending on aircraft type, prevailing weather conditions and air traffic density. Target airspeeds are used to control aircraft airborne separation and to maintain a steady rate of arrivals to the runway.

The use of target airspeeds suggests that descent profiles would all be similar in character. This can be seen in profiles for Mach number (fig 6-9a) and true airspeed (fig 6-9b). Figure 6-10 shows the derived Mach Temperature profile for each aircraft track.

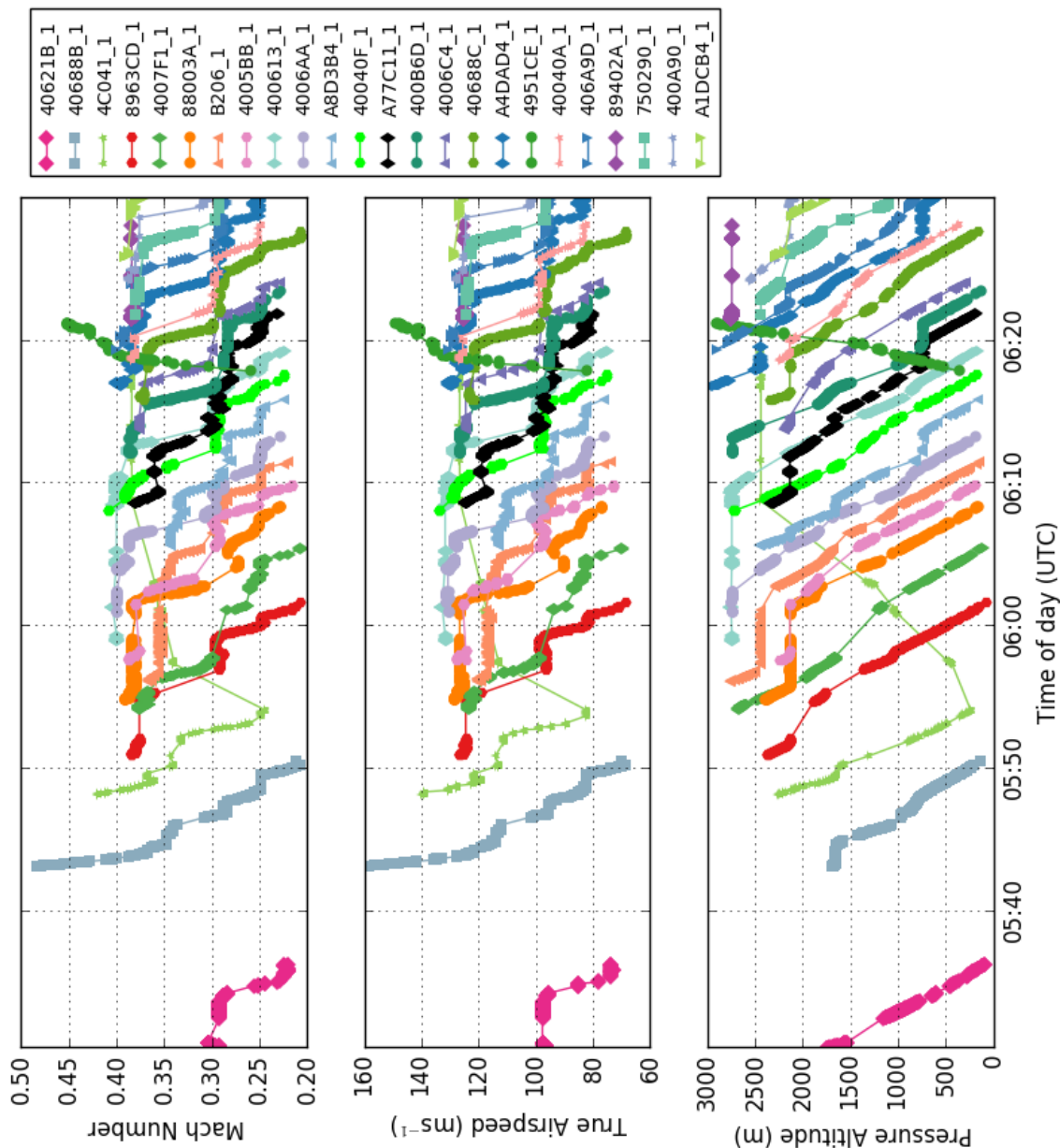


Figure 6-7: This plot depicts the time-series of aircraft tracks that were present for the period 0530 to 0630 UTC in the London Heathrow domain on 4th January 2015. From the top to the bottom, the panels are for the time-series of the Mach number, true airspeed and pressure altitude. The adjacent legend lists the aircraft's track identifier which takes the form ip_trk_no where ip is the Mode-S EHS transponder hexadecimal address and trk_no is the track number allocated to the aircraft's track identified on the day.

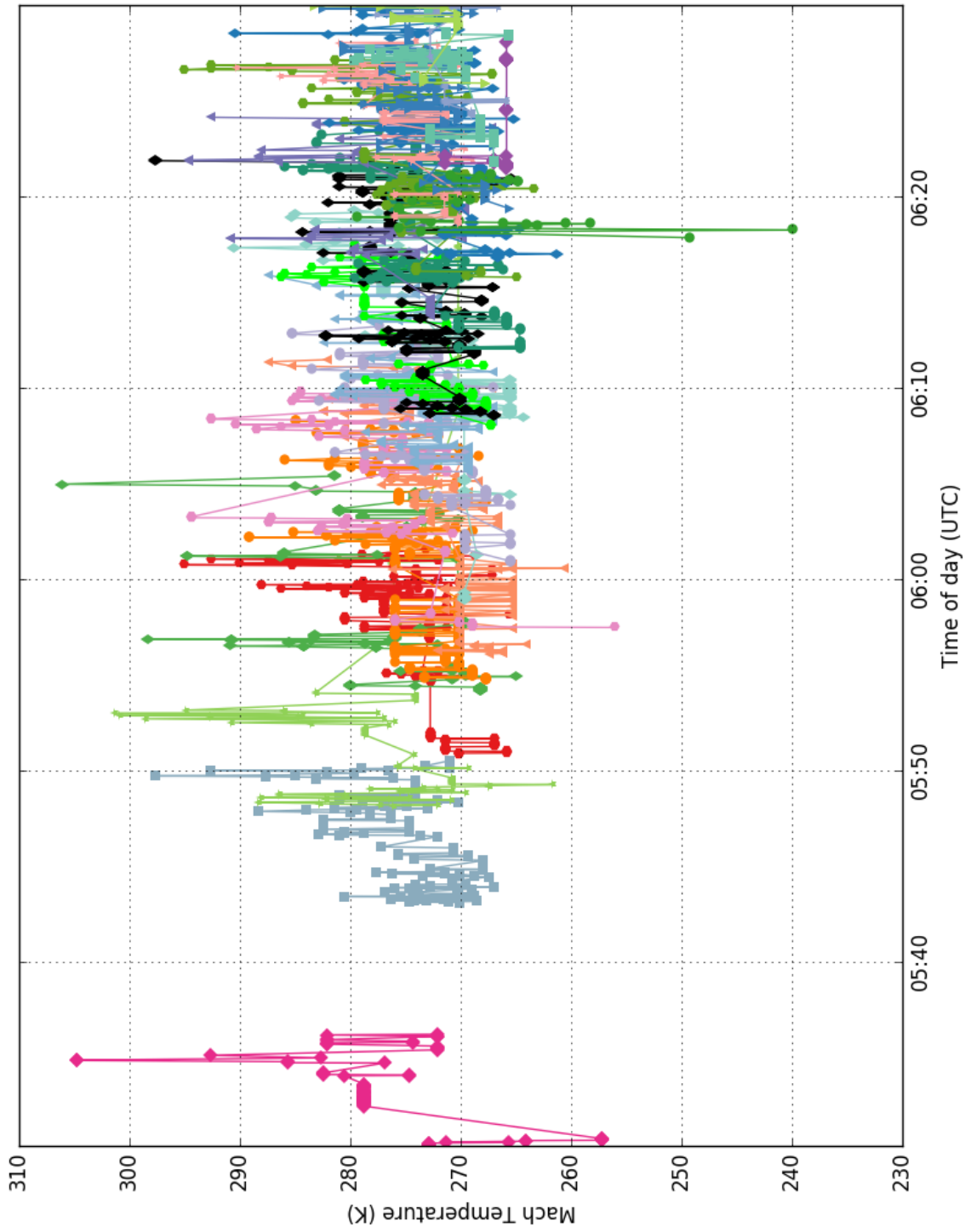


Figure 6-8: Time-series plot of derived temperature for aircraft that were present for the period 0530 to 0630 UTC in the London Heathrow domain on 4th January 2015. See figure 6-7 for plot details and key to symbols.

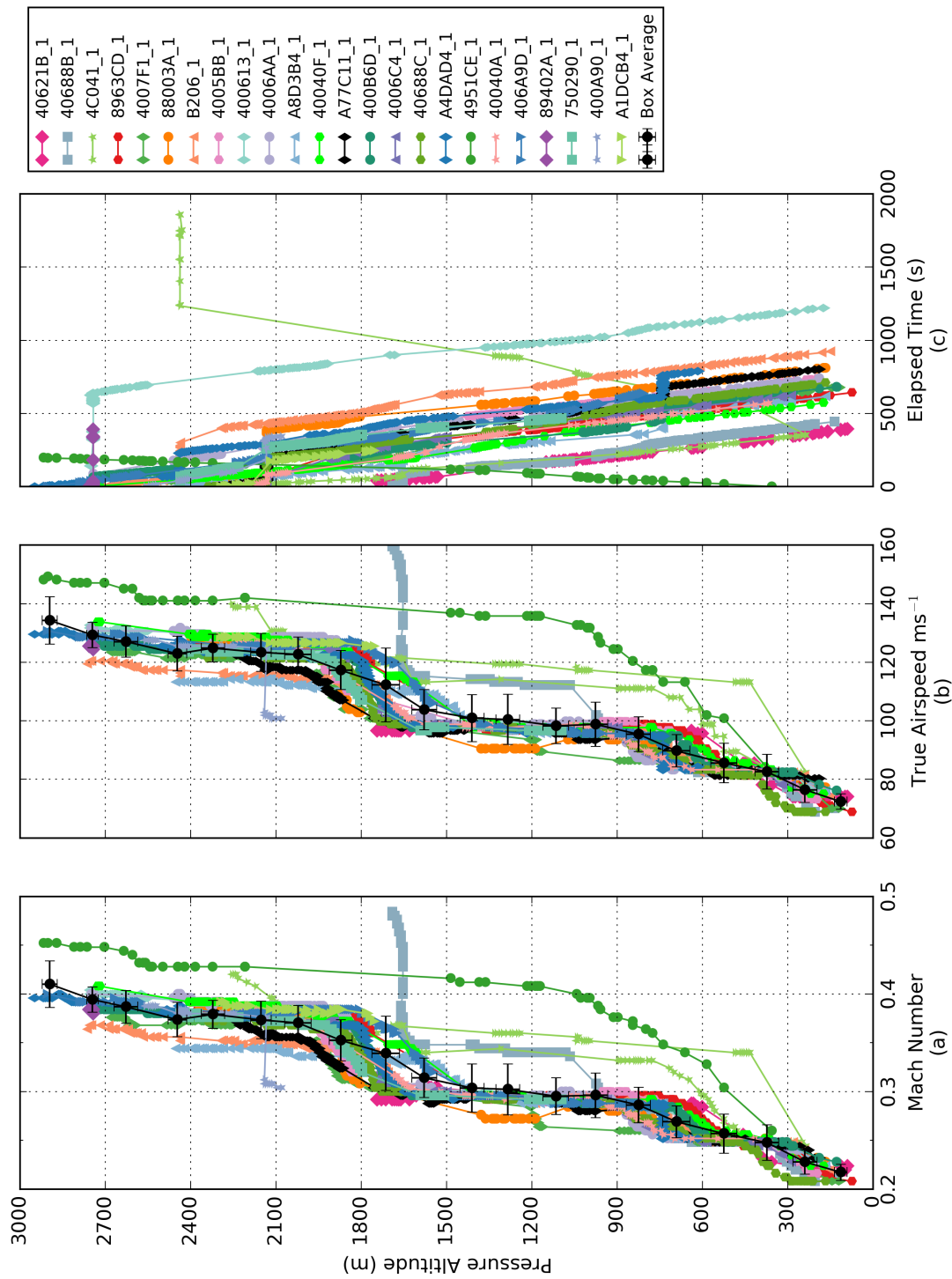


Figure 6-9: This plot depicts the time-series of aircraft tracks as vertical profiles for the period 0530 to 0630 UTC in the London Heathrow domain on 4th January 2015. From left to right, the panels are the vertical profiles for Mach number, true airspeed and pressure altitude. The adjacent legend lists the aircraft's track identifier. In addition to the aircraft tracks are the box averaged Mach number and true airspeed shown as the black points. The altitude bin width is 150 m. The mean report is plotted at the mean pressure altitude for all reports within the altitude bin. The error bars are the standard deviations of the reports in the altitude bin in each direction.

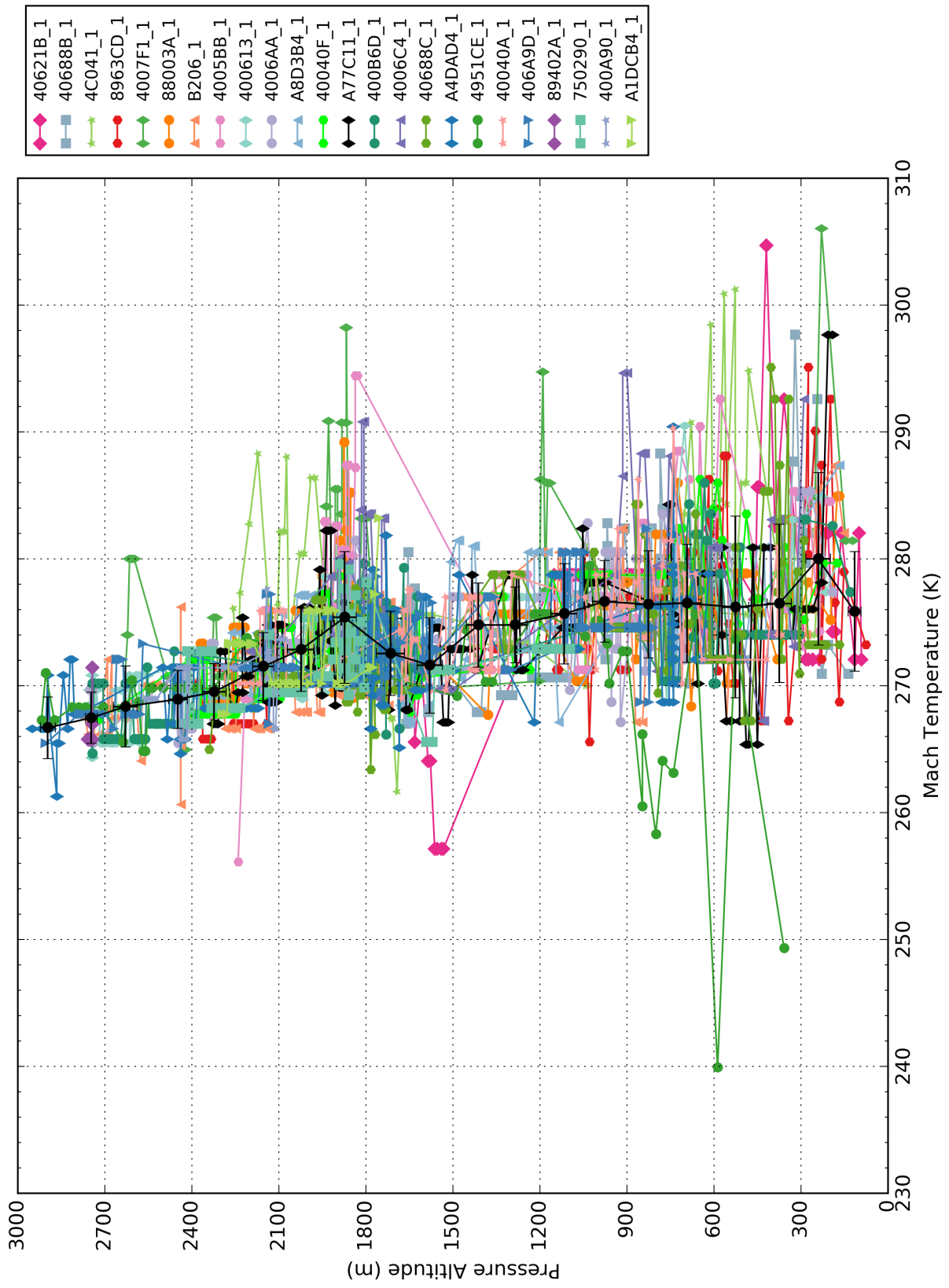


Figure 6-10: The panel shows the vertical profiles for derived Mach Temperature. The box averaged derived Mach Temperature is shown as the black points. Plot details are the same as in figure 6-9.

There is a large amount of variability in the individual Mach Temperature profiles. In the altitude range 1800 m to 2100 m the Mach temperature reports range between 260 K and 300 K, while below 900 m the reports vary between 240 K and 305 K. It is unlikely that the ambient temperature would exhibit this degree of variability.

If the fluctuations in the Mach Temperatures for individual aircraft are due to unbiased random processes then the expectation is that on computing the aggregated observation then random noise will be diminished by being averaged out. However, we note from our previous study in section 4.5.2 (page 66) that Mach Temperature error does vary by altitude, with variability increasing at lower altitudes, as shown in figure 4-2 4-2. Figure 4-1 suggests that Mach Temperature variability from a single aircraft could range ± 6 K about the actual ambient temperature. While it is expected that Mach Temperature would be increasing during a descent, since ambient temperature increases, we suggest that this variability arises from an increase in the quantisation error for descending aircraft at lower altitudes. This may be the result of pilot or FMS use of controls to maintain target airspeeds.

6.7 Variation in Mode-S EHS Derived Mach Temperature

In this section we further examine the effects of quantisation error and air speed controls used during ascents and descents on the variation of Mach Temperature. For the case study day we estimate a plausible range of ambient temperatures based on the mean 1.5 m screen temperature at London Heathrow and the ISA Lapse rate. The range of screen temperatures for period 0020 UTC to 2350 UTC at Heathrow Airport was -1.2°C to 2.9°C , with the mean for the day being 1.4°C . This was obtained from the observations at the airport which are reported every thirty minutes. If we assume the ISA Lapse rate is $\Gamma = -6.49^{\circ}\text{C km}^{-1}$ then the temperature at 3000 m would be -18.0°C . Thus, within the London Heathrow domain, for the time of year, it seems unlikely that ambient temperatures would exceed a range $\pm 25^{\circ}\text{C}$ along a vertical profile between the surface and 3000 m. We use a larger range of temperatures to take account of any temperature inversions that may be present since the ISA Lapse rate assumes temperature decreases linearly with altitude.

Figure 6-11 shows a scatter plot of the reports of True Airspeed v Mach number for all aircraft ascents from the London Heathrow domain on 4th January 2015. The histogram plots show the distribution of true airspeeds and Mach number. A colour is assigned to the derived Mach Temperature. A temperature range of $\pm 25^{\circ}\text{C}$ is used and where temperatures are less than the minimum these are coloured grey and those that exceed the maximum are coloured black. The scatter plot is used to identify whether

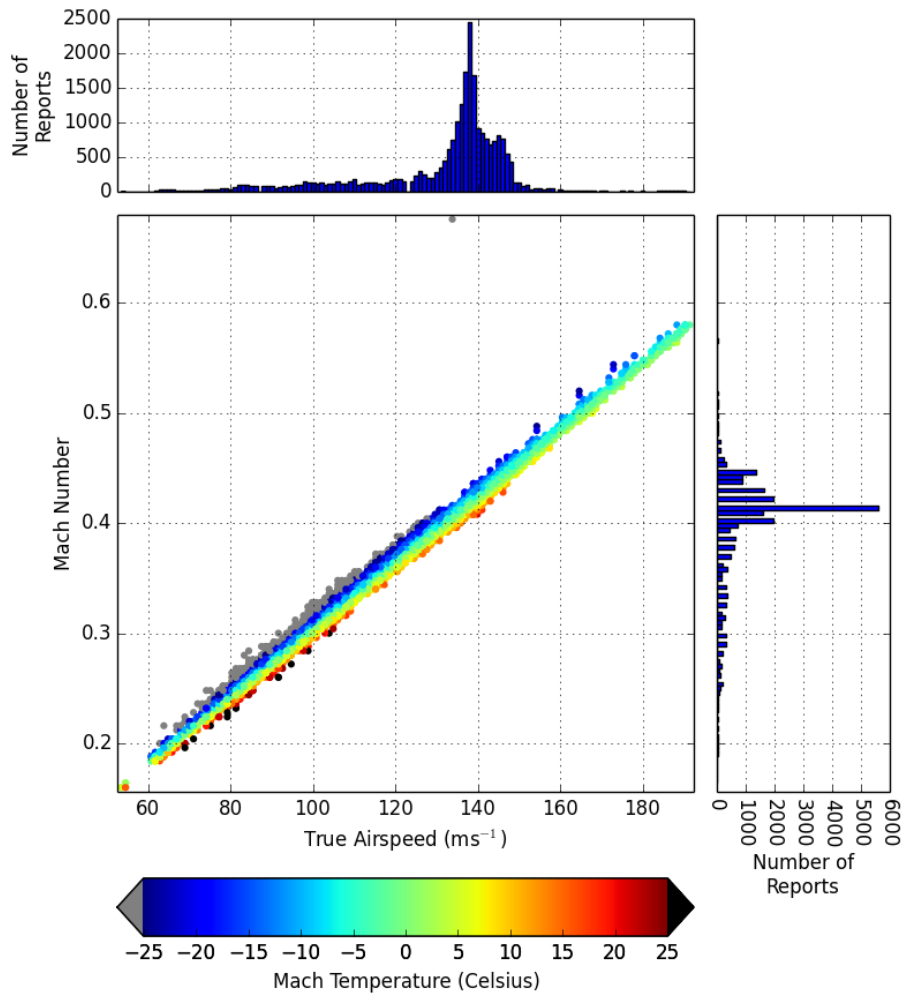


Figure 6-11: This figure shows a scatter plot of True Airspeed v Mach number with the histograms showing the corresponding distributions. This is for for all aircraft ascents within the London Heathrow domain on 4th January 2015. Each point is coloured by the magnitude of the derived Mach Temperature; outliers are coloured grey ($<-25^{\circ}\text{C}$) and black ($>-25^{\circ}\text{C}$). For ease of interpretation we use the Celsius temperature scale.

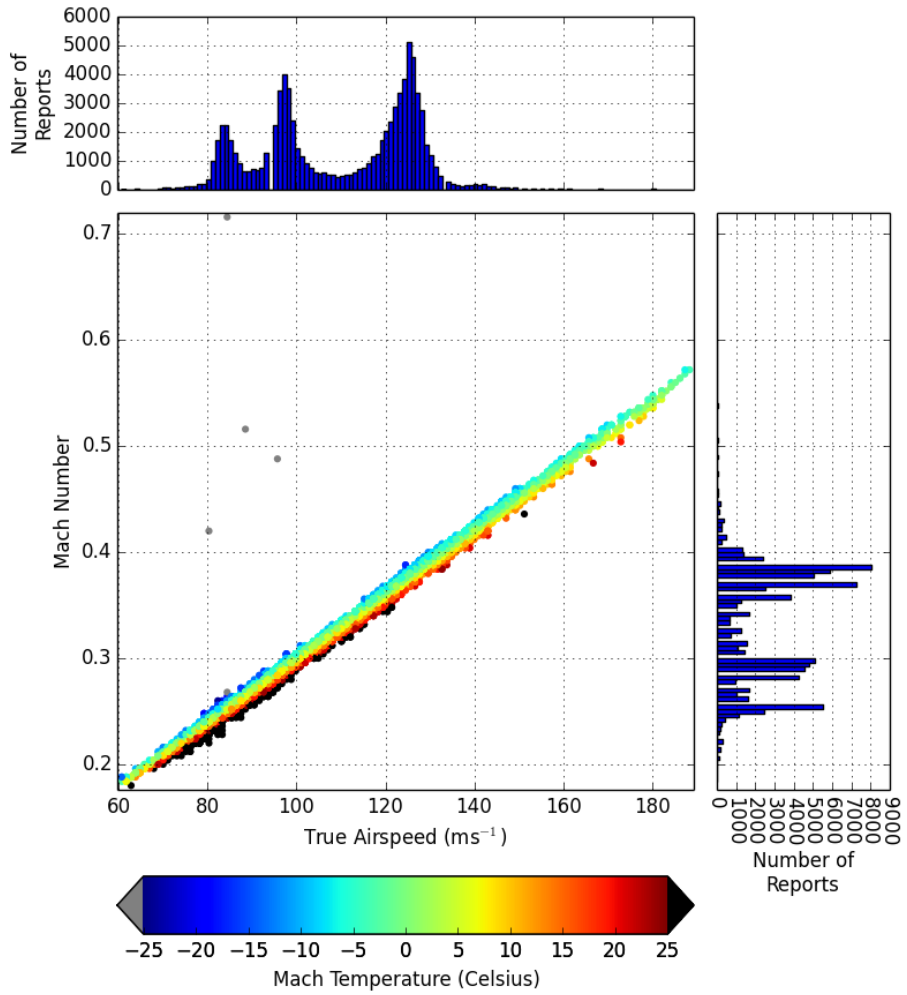


Figure 6-12: Scatter plot of True Airspeed v Mach number for all aircraft descents. Keys to plots are the same as for figure 6-11.

large variation in temperatures, as seen in the Mach Temperature profiles in figure 6-10, are due to outliers or random fluctuations in the range of True Airspeeds and Mach Numbers. Figure 6-12 is for all aircraft descents with the key to the plots being the same as in figure 6-11.

In figure 6-11 the histogram for true airspeeds shows a single peak at approximately 140 ms^{-1} (270 knots) which is consistent for aircraft ascents on standard departure routes (Civil Aviation Authority 2016). The long tail to the left of the peak value is where aircraft are accelerating for take-off, from a standing start. The shorter tail to the right of the peak value is due to aircraft following their standard departure route, where the range of aircraft speeds is directed by ATM. The decrease in the number of reports occurs as these aircraft leave the London Heathrow domain. The scatter plot shows one or two reports that exceed the minimum threshold for Mach Temperature but on the whole there appear to be no extreme values of Mach number or true airspeed which on their own would result in erroneous derived temperatures. However, it is noticeable that there are a higher number of Mach Temperatures near the minimum temperature threshold (coloured grey) for true airspeeds in the range 60 to 120 ms^{-1} .

Figure 6-12 shows three peaks in the histogram of true airspeeds which correspond to the target true airspeeds that aircraft need to maintain during the three phases of descent. These may vary according to aircraft-type, prevailing weather conditions and by instruction from ATC. The three peaks are also reflected in the Mach number. The scatter plot shows there are outliers that exceed the minimum Mach Temperature threshold (grey dots). But as noted for ascents, there appear to be no extreme values of Mach number or true airspeed. It is noticeable that there are a higher number of Mach Temperatures near the maximum threshold (coloured black) for true airspeeds in the range 60 ms^{-1} to 120 ms^{-1} . The variation in the Mach temperature may be due to temperature variation in the atmosphere since aircraft spend more time on a descent track when compared with an ascent track; however, this is unlikely on the day in question.

These scatter plots do not suggest that random fluctuations in the range of true airspeeds and Mach numbers are a significant source of the observed temperature variation. If this were so then we would expect to see much more scatter in the dataset. Instead there may be a more systematic process leading to an apparent warm bias in Mach Temperatures for descents and cool bias for ascents. Similar results were also found for the 3rd January 2015 (not shown) and for the same period at London Gatwick domain (not shown).

6.8 Mach Temperature Differences

We have noted the wide variation in temperature reports especially at low levels. We suggest that this wide variation is due to the quantisation effects arising from the reduced precision of the Mach number and true airspeed. We described the quantisation effect in section 3.9 (page 51) and in section 4.5 (page 66) we have shown that this may account for the variability of the derived Mach Temperature for a single aircraft. To show the effect of the reduced precision of the reports we compute the Mach Temperature using eq. (3.4) for a selected range of Mach numbers and true airspeed that correspond approximately to an aircraft's descent profile. We show the change in the magnitude of the Mach Temperature that results from step changes in (a) the Mach number for constant true airspeed and (b) the true airspeed for constant Mach number.

We use the target true airspeeds for each leg of a descent which are 114 ms^{-1} , 92 ms^{-1} and 82 ms^{-1} , and estimate the corresponding Mach numbers from figure 6-12. For each of these true airspeeds we compute the change in Mach Temperature for discrete changes in Mach number at constant true airspeed and for discrete changes in true airspeed at constant Mach number. The change in Mach number is in increments of 0.004 and changes in true airspeed is in increments of 1 ms^{-1} (2 knots), these being their reported precisions (section 4.2.3, page 59).

Table 6.2 shows that for discrete single step changes in Mach number at constant airspeed can give an apparent change in Mach temperature of between from 6.78 K to 8.99 K at constant true airspeed. For discrete changes in true airspeed at constant Mach number, Mach Temperature changes range from 4.87 K to 6.31 K. Thus deviations in Mach Temperature $> 6 \text{ K}$ are most likely due to step changes in the Mach number. For the stable atmospheric conditions present on the case study day we would expect air temperature to vary smoothly, i.e., no large rapid fluctuations ($> 1\text{K}$) over short altitude ranges ($> 150 \text{ m}$).

These step changes may arise during an aircraft's descent as a result of small changes made by either the FMS or Pilot which cause the aircraft to accelerate or decelerate in order to maintain its target airspeed. These small changes are magnified as a result of the reduced precision resulting from Mode-S EHS processing. We would expect to see similar fluctuations in derived Mach Temperature for aircraft ascents, as they are accelerating.

Table 6.2: The change in Mach Temperature is computed for discrete changes in Mach number at constant true airspeed, and for discrete changes in true airspeed at constant Mach number. Using eq. (3.4) Mach Temperature is computed for the Mach number and true airspeed which would correspond to three legs of an aircraft's descent profile. The change in Mach number is in increments of 0.004 and changes in true airspeed is in increments of 1 ms^{-1} (2 knots) these being their reported precisions. We tabulate the change in Mach Temperature for each incremental change.

Apparent change in Temperature at constant true airspeed				Apparent change in Temperature at constant Mach number			
Mach No	True Airspeed ms^{-1}	Mach Temperature K	Difference K	Mach No	True Airspeed ms^{-1}	Mach Temperature K	Difference K
0.244	82.00	281.03		0.252	80.00	250.78	
0.248	82.00	272.04	-8.99	0.252	81.00	257.09	6.31
0.252	82.00	263.47	-8.57	0.252	82.00	263.47	6.38
0.256	82.00	255.30	-8.17	0.252	83.00	269.94	6.47
0.260	82.00	247.51	-7.79	0.252	84.00	276.48	6.54
0.284	95.00	278.43		0.292	93.00	252.41	
0.288	95.00	270.75	-7.68	0.292	94.00	257.87	5.46
0.292	95.00	263.39	-7.36	0.292	95.00	263.39	5.52
0.296	95.00	256.31	-7.08	0.292	96.00	268.96	5.57
0.300	95.00	249.52	-6.79	0.292	97.00	274.59	5.63
0.372	140.0	352.44		0.380	138.0	328.17	
0.376	140.0	344.98	-7.46	0.380	139.0	332.94	4.77
0.380	140.0	337.75	-7.22	0.380	140.0	337.75	4.81
0.384	140.0	330.75	-7.00	0.380	141.0	342.60	4.85
0.388	140.0	323.97	-6.78	0.380	142.0	347.47	4.87

6.9 Temporal smoothing using low-pass-filters

In this section we apply four methods that perform the function of a low-pass-filter (described in section 6.5, page 126) to a sample of the data for the London Heathrow domain. As demonstrated in section 6.8 (page 140) we suggest that the observed variation in the Mach Temperature is due largely to Mode-S EHS processing and the effects of control adjustments of an aircraft along its trajectory rather than large variations in the actual ambient temperature. The precision of the Mode-S EHS reports is such that it is difficult to model the aircraft's control movements. So employing methods such as a Kalman Filter (Kalman 1960) (or its variants) may not be feasible since lack of precision in the data makes it difficult to create a realistic predictive model. For example, we cannot discount the possibility that the variation in Mach Temperature is due to some atmospheric phenomenon such as wind-shear, disturbing the air around the pitot static sensor, which is used to compute the true airspeed. So instead we assume that a fraction of the control movement is due to random events effecting the aircraft's trajectory over a short time scale, for example, turbulence, which cause variations in true airspeed - this being equivalent to a high-frequency signal. The effect of the Mode-S EHS processing is to amplify this high-frequency signal. It is suggested that these high-frequency components can be smoothed by the use of a low-pass filter based on averaging methods.

6.9.1 Applying low-pass-filters to time-series of Mode-S EHS Reports

The low-pass-filters are applied to the time-series of Mode-S EHS reports of each aircraft trajectory and the result of the low-pass-filter is used to generate a new aircraft report. The time-series of new reports is used to create a low pass filtered aircraft trajectory. The Mach Temperature report is recomputed using the Mach number and True Airspeed from the low pass filtered trajectory. For all methods except the exponential method, the time, position (latitude and longitude) and pressure altitude of the low pass filtered trajectory is the mean of these quantities from the selected block of reports. The low pass filtered trajectory may contain fewer reports than the original trajectory, this is especially so for the block-average filter. For the exponential smoothing a slightly different approach is used. Each report in the aircraft's trajectory is replaced by the exponentially weighted average of the running average and the current report. The low pass filtered trajectory therefore contains the same number of reports.

For the block-average (eq. (6.1)), moving average (eq. (6.3)) and linear regression filters (eq. (6.4), page 127) the size of the validity window is set for $m = 2$. This provides five reports within the window, i.e., where each filtered report has two reports

either side, which are used to compute the mean value, except at the start and end of the time-series. For the exponential smoothing (eq. (6.8)), we use a smoothing factor $a = 0.2$ as this weights the running average higher. A smoothing factor of $a = 0.8$ would weight the current observation higher than the running average thus reducing the effect of smoothing out high frequency components. The weighting function is initialised with the time difference $t_k - t_{k-1} = 1$ s. This weighting factor was selected so that when the time separation between reports is 4 s, the expected rate of rotation of the Secondary Surveillance Radar, then the exponential smoothing will weight the running average and the current observation equally.

The quality threshold, δt_{max} , uses the standard deviation for the time difference between successive Mode-S EHS reports along an aircraft track. For the selected day all tracks are used to compute the standard deviation. The result is rounded to the nearest whole second. For the London Heathrow domain this is 6 s.

6.9.2 The Effect of Applying low-pass-filters to time-series of Mode-S EHS Reports

In this section we show the effects of applying the low-pass-filters discussed in section 6.5. The main effect of Centred Moving Average (CMA), Local Linear Regression (LIN) and Exponential Smoothing at Irregular Times (IRR) filters is to reduce the variance of the Mach Temperature distributions at each altitude bin. This is the desired effect as it shows that the impact of the high-frequency components is being diminished. The effect of applying the Block Average (BA) filter to Mach temperature is negligible for the most part.

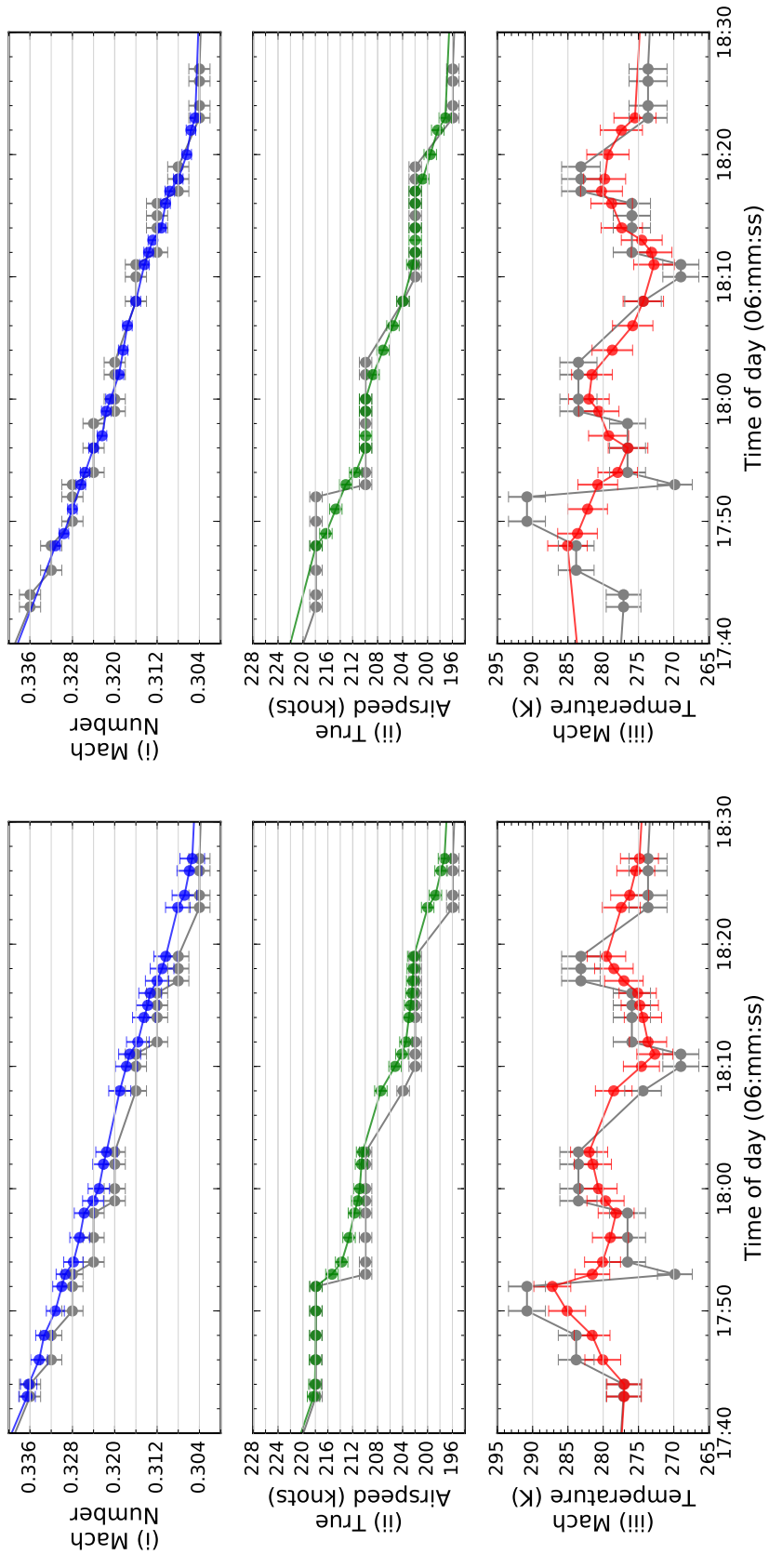
The low-pass-filters described in section 6.5 are applied to all aircraft tracks shown in figure 6-7. To illustrate the effect of applying the low-pass-filters we use a short time-series segment (one minute) from one aircraft track extracted from figure 6-7. The Mode-S EHS reports for the aircraft track 4006C4_1 are shown in figure 6-13. Each panel in figure 6-13 shows the original reports of (i) Mach number, (ii) true airspeed and computed (iii) Mach Temperature (black circles). We note that the time-series shows that there are short periods where the Mach number appears constant and that there are step changes in its magnitude as the aircraft descends. Similar periods of constant values and step changes are seen for true airspeed. It is clear that there are times when the airspeed is constant whilst the Mach number undergoes small step changes and vice-versa. All the low-pass-filters in effect smooth the transition between the step changes in Mach number and true airspeed by interpolating these values in time. However, this does not necessarily result in smooth synchronous changes in each parameter, as is shown for the smoothed true airspeed. We suggest that it is the effect

of the asynchronous change, due to the precision of the data, that gives rise to the variability shown in the corresponding derived Mach Temperature.

Figure 6-14a(i) depicts the vertical temperature profiles before and after applying the low-pass-filters. The red profile is constructed using the aggregated observation before applying the low-pass-filter. The remaining profiles are constructed after applying the low-pass filters: CMA (blue), BA (black), LIN (green) and IRR (yellow). Figure 6-14a(ii) shows the effects of the low-pass filters as the difference between the non-smoothed (red) and smoothed Mach Temperature profiles. Above 1000 m the differences range between $\pm 0.5 K$ while below 1000 m all except the IRR profile show increasing differences. These increases may be the result of the quality threshold filtering that is applied.

For all low-pass filters except IRR, no smoothed-report is generated if it would contain two successive reports with a time difference greater than δt_{max} , which was set at 6 s. These reports are removed from the filtered time-series of the aircraft's trajectory. We do this so that the horizontal spatial and temporal resolutions (approximately 500 m for 6 s) of the time-series is reasonably consistent along the aircraft trajectory. Time differences between 2 s and 6 s correspond to horizontal spatial scales between 300 m and 800 m. We assume that a break in time-series of reports >6 s arise as a result of either (a) the aircraft exiting from a turning point on its approach to land, (b) that it passed out of then re-entered the airport domain or (c) that the aircraft was not within the line of sight reception to the Mode-S EHS receiver. The effect of applying the quality control criterion on the number of reports is shown in figure 6-14b(ii). The quality control criterion removes between 10% to 30% of reports for the CMA and LIN when compared to the IRR. The number of reports for BA is expected to be lower since no report is used more than once. The quality control criterion is not applied to the IRR low-pass-filter, instead the time-difference is used in the weighting function applied to the report, so all reports are used.

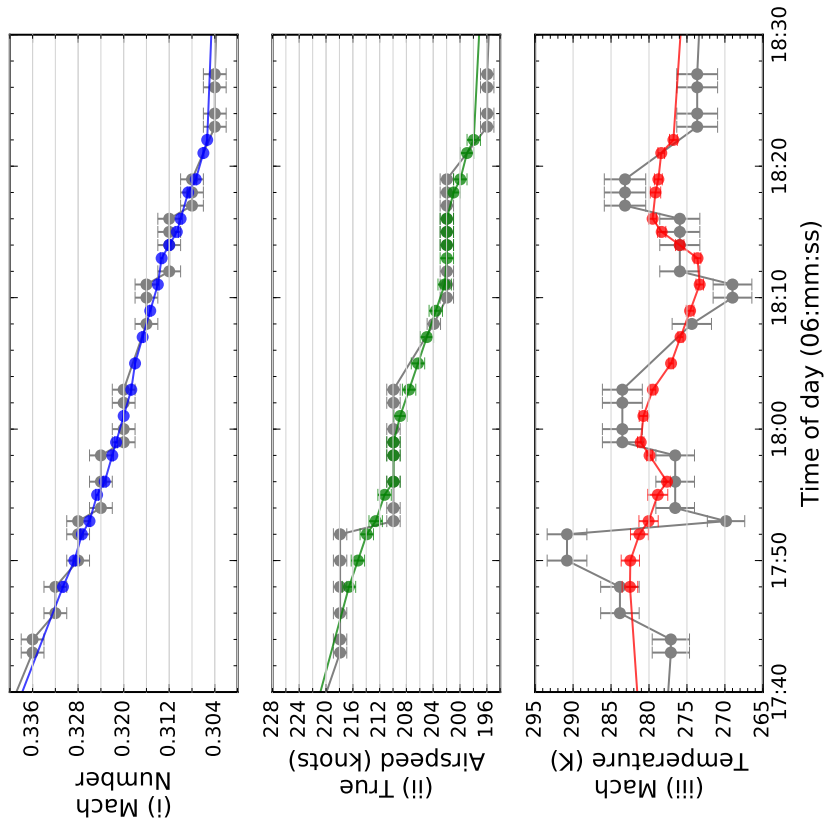
The effect of the low-pass-filters is to reduce the variability in the aggregated Mach Temperature observation as shown by the corresponding profiles of the standard deviation for each low-pass filter in figure 6-14b. For altitudes above 1000 m there appears to be little difference between the four methods, all reduce the variability in the aggregated reports when compared with unfiltered reports (red profile). Below 1000 m the IRR method appears less successful at reducing the variability when compared with CMA, LIN and BA methods. However, the IRR method utilises all the reports whereas the other three methods do not do so because quality control criterion removes reports. This might account for their better performance at reducing the variability in the standard deviation at low levels. We note that the vertical profile of the standard deviation



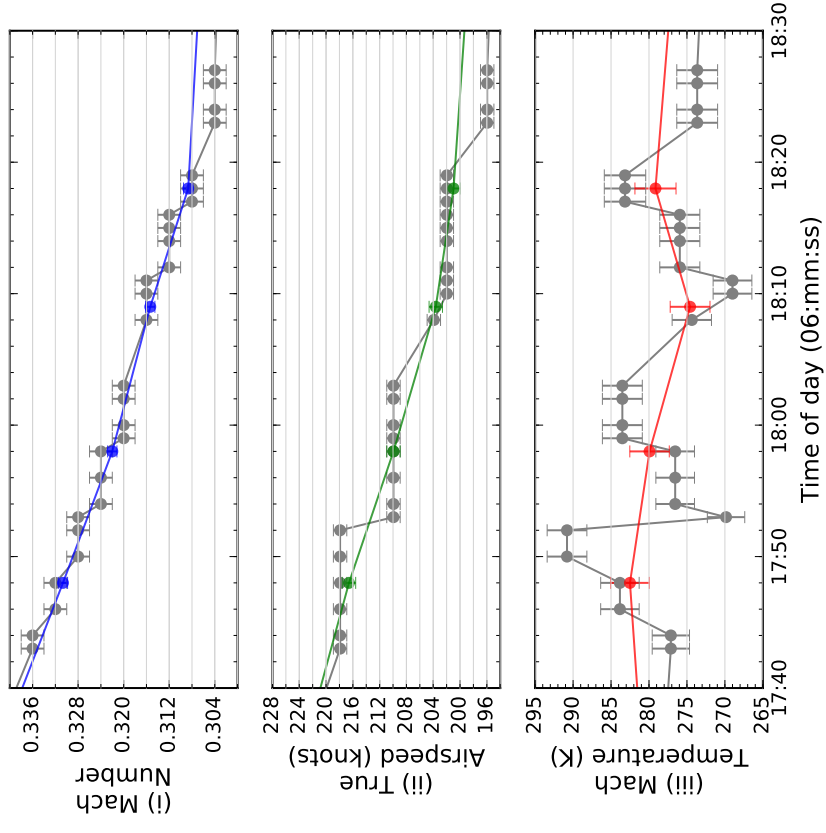
(a) Irregular Exponential Smoothing

(b) Centred Moving Average

Figure 6-13: Effect of applying a low-pass-filter on the Mode-S EHS reports of (i) Mach number, (ii) true airspeed for aircraft track 4006C4.1. This aircraft was descending in the London Heathrow Domain, between 06:12 to 06:22 UTC, 4th January 2015. The smoothed Mode-S EHS reports for Mach number (blue) and true airspeed (green) are used to recompute the Mach Temperature (red). In each panel the original reports for Mach number and true airspeed are shown as grey circles and the grid lines represent the step changes between values. Error bars for the smoothed report are the estimated standard deviation for the reports used.



(d) Linear Regression



(c) Block Average

Figure 6-13: Continuation of figure on page 145.

increases from 2 K at 3000 m to 4 K at 300 m. This is similar to the quantisation error profile that arises from Mode-S EHS processing, as shown in figure 4-9.

6.10 Estimating the Observation Error for Aggregated Mach Temperature

In this section we use the error equation we derived in section 4.5.2 to characterise the observation error standard deviation for the aggregated observations of Mach Temperature.

We use aggregated Mode-S EHS reports for Mach number and aggregated true airspeed for altitude bins at 150 m and equation 3.4 to estimate the standard deviation of the aggregated Mach Temperature reports. We model three different precisions of the Mach number and true airspeed first we assume the precision is half the magnitude of the data increment, $\Delta M = \frac{1}{2}(0.004)$ and $\Delta V = \frac{1}{2}(1.2) \text{ ms}^{-1}$; next we assume that the precision of the input data is represented as the standard deviation of quantisation, $\Delta M = 0.002/\sqrt{12}$ and $\Delta V = 1.0/\sqrt{12} \text{ ms}^{-1}$; finally we assume the precision of the input data could be represented as twice the standard deviation of quantisation. Profiles of the resulting standard deviations for these are shown in figure 6-14b(i) as the Full Precision (FP) profile (grey squares), Quantisation Error (QE) profile (grey triangles) and as twice the Quantisation Error (2QE) profile (grey circles). We compare the effect of the low-pass-filter on the standard deviation with these estimated errors.

Figure 6-14 shows the non-smoothed profile (red) lies between the estimated error profiles due to $1 \times \text{QE}$ and $2 \times \text{QE}$. The effect of the low-pass filters (blue, black, green) is to reduce the standard deviation, the magnitude of which now follows the estimated error profile due to $1 \times \text{QE}$. There are two regions, between 300 m and 600 m and between 1700 m and 2000 m, where the standard deviation departs from the $1 \times \text{QE}$ profile. These departures are in regions where temperature inversions occur, as identified by the radiosonde report in figure 6-1 (page 112). We suggest that the increased error in the aggregated Mach Temperature is due to presence of low-level wind-shear, which would affect the speed of the aircraft as it transits through it; by increasing or decreasing the headwind causing the aircraft to decelerate or accelerate.

We found that there was some benefit to using a low-pass filter to reduce the effect of the ‘high-frequency’ noise component. We found that the difference between the aggregated Mach Temperature using the smoothed and non-smoothed results differed only by $\pm 0.5 \text{ K}$ above 1000 m, with the difference below 1000 m ranging between 0.25 K and -1.25 K. However, the low level difference may be the result of removing reports from the time-series as a result of the quality control criterion that was applied. The

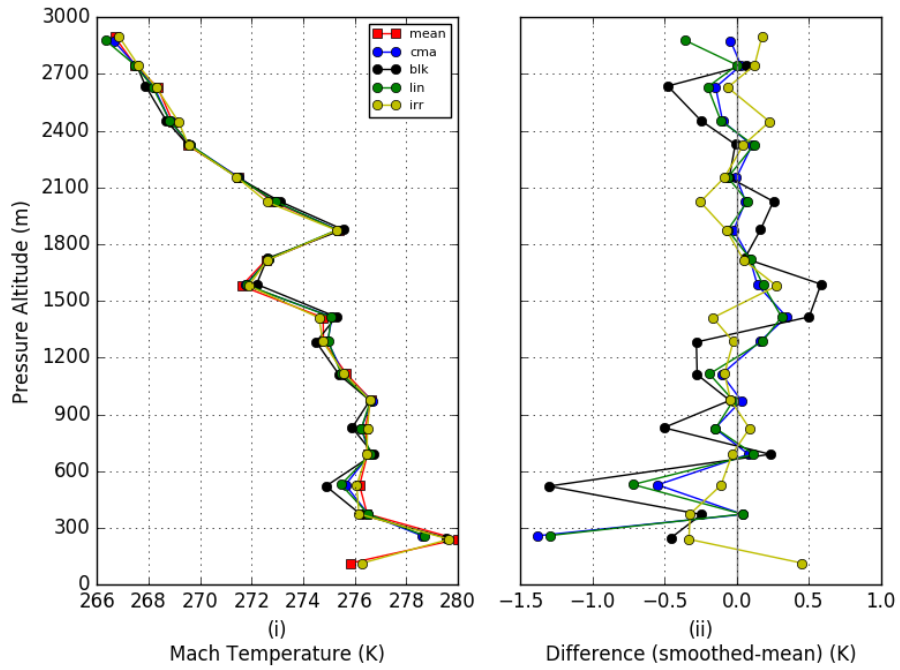
greater benefit arises with the corresponding estimates of the observation error standard deviation for the smoothed results. The magnitude of these were reduced by as much as 30% when compared with the non-smoothed results: the magnitudes were reduced at 3000 m from 2 K to 1.5 K and near the surface from 7 K to 5 K.

6.11 Summary and Conclusion

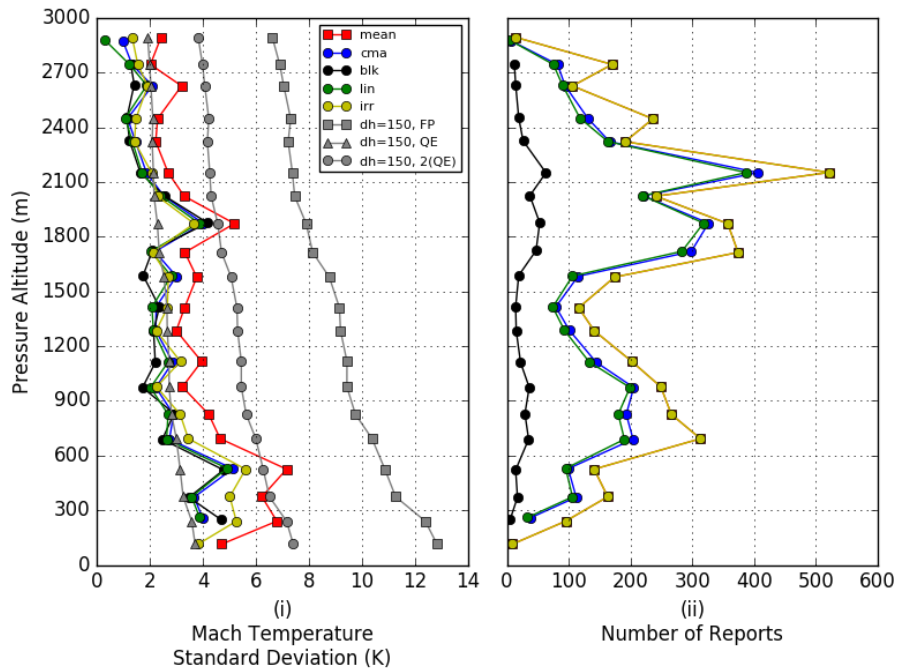
This chapter provides a systematic study for using Mode-S EHS Mach Temperature to identify a meteorological feature, temperature inversion, which is important for operational aviation weather forecasting and numerical weather prediction. We do this with vertical temperature profiles constructed using aggregated Mode-S EHS Mach Temperatures, derived from multiple aircraft. The Mode-S EHS reports used were collected by Met Office Mode-S EHS receiver network (described in section 5.5, page 99).

We compared hourly aggregated Mach Temperature profiles with in situ observations of temperature reported by radiosonde and AMDAR, when available. We found that the aggregated Mach Temperature profile between 1000 m and 3000 m show some agreement with these in situ observations. However, we found that below 1000 m there was less agreement. The magnitude of the difference between the in situ observations and the aggregated Mach Temperature was as great as 6 K. However, comparison is difficult against in situ observations since these are point based instantaneous values, measured on time-scales of seconds to minutes, compared with the hourly mean of the aggregated Mach Temperature. Moreover, the radiosonde observations are not located within the airport domains. However, the temperature differences observed below 1000 m are unlikely to be due to changes in the ambient temperature; nor the prevailing meteorological conditions at the surface on the day (near freezing conditions, low wind speed and fog).

We also compared the hourly aggregated Mach Temperature against the UKV NWP model forecasts. (We note that the in situ observations that we used in our comparison were not assimilated by the UKV NWP model since they were received after the observation processing cut-off time.) We found similar results to our comparison with in situ observations, that the hourly mean Mach Temperature profiles between 1000 m and 3000 m compared favourably with the hourly mean profiles forecast by the UKV NWP. Below 1000 m there was less correspondence. Furthermore, we found that the Mach Temperature profiles identified regions where temperature inversions may be present but which were not present in the UKV NWP forecast, thus showing that Mach Temperature profiles may provide additional information for use in NWP.

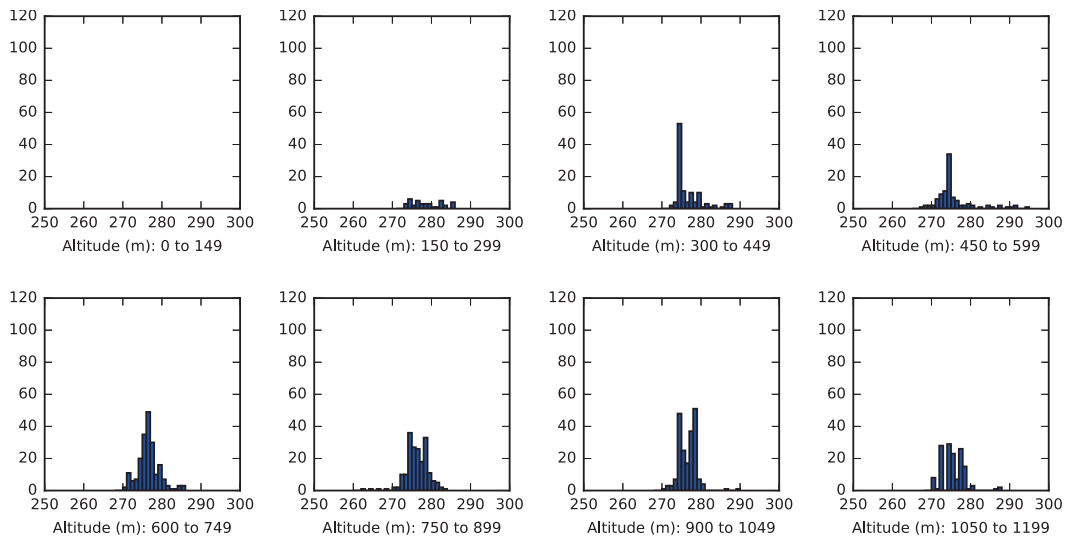


(a) Mach Temperature Profiles.

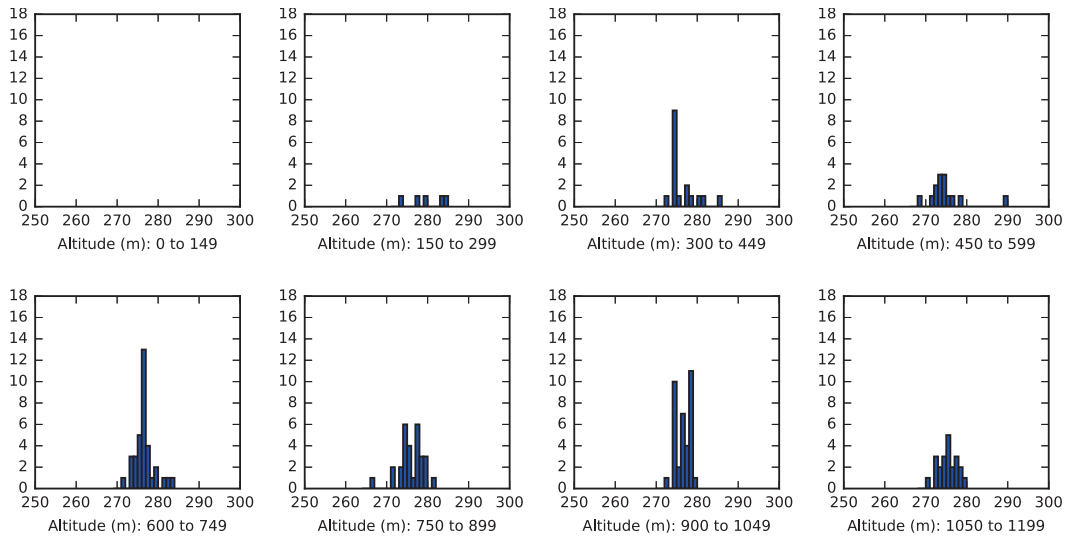


(b) Mach Temperature Standard Deviation Profiles.

Figure 6-14: Effect of the low-pass-filter on (a) the aggregated Mach Temperature and (b) the standard deviation.

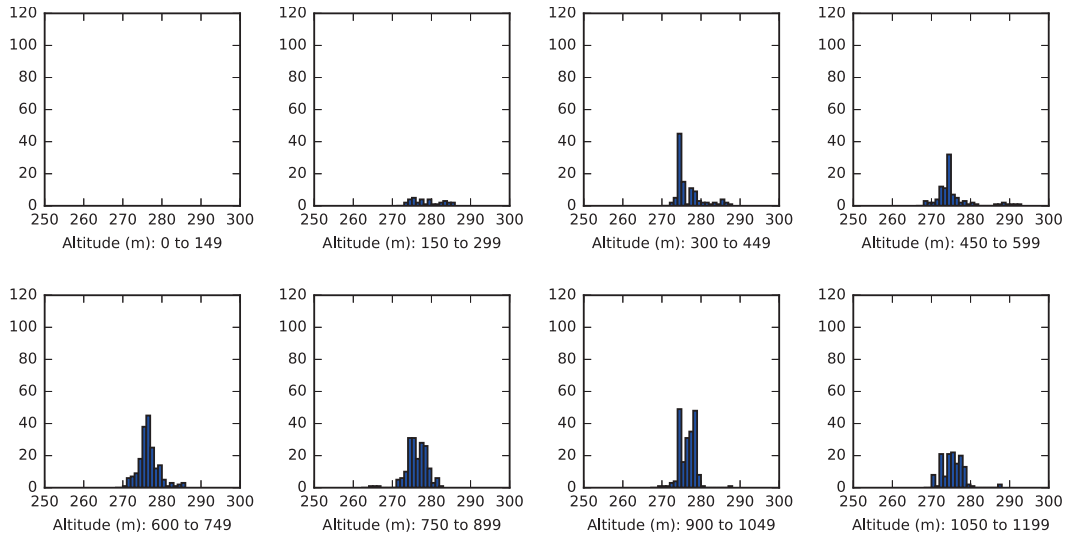


(a) low-pass-filter - Moving Centred Average, width = 7. Time Filter < 6s

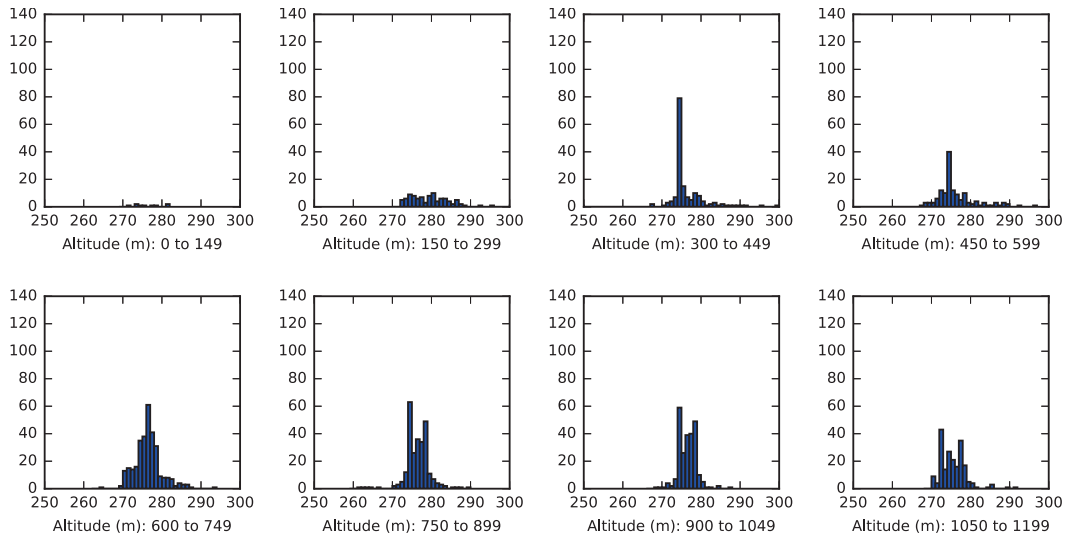


(b) low-pass-filter - Boxcar Average, width = 7. Time Filter = 6s

Figure 6-15: The effect of different low-pass-filter schemes on the distribution of Mach Temperature reports for the altitude range 0 m to 1200 m. Mach Temperature bin width = 1 K, altitude bin width = 150 m. For (a), (b) and (c) there are no reports below 150 m.



(c) low-pass-filter - Linear regression, width = 7. Time Filter = 6s



(d) low-pass-filter - Exponential Weighted Average. Time Filter = Exponential Weighting.

Figure 6-15: Continuation of figure on page 150

We also investigated further the observation error in the Mach Temperature. We know from our results in chapter 4 that the precision of the Mach number and true airspeed causes an increase in the measurement error of the Mach Temperature at low altitudes. We found that the Mode-S EHS processing also results in step changes in the reports of Mach number and true airspeed that are asynchronous in time. This results in very large fluctuations in the corresponding Mach Temperature, ranging from 5 K to 9 K between adjacent reports. In effect, the asynchronous changes introduce a ‘high-frequency’ noise component. To reduce the effect of this ‘high-frequency’ noise component we applied low-pass-filters to the time-series of reports of Mach number and true airspeed for each aircraft.

We used four low-pass-filters: centred moving average (CMA), block average (BA), linear regression (LR) and irregular exponential smoothing (IRR). The low-pass-filters CMA, BA and LR are based on a moving window containing $(2m+1)$ reports (see section 6.5) which are used to compute the average Mach number and true airspeed. The IRR low-pass-filter used a weighting function for the summation of the running average of all previous reports and the current report of Mach number and true airspeed. The weighting function was tuned to weight the running average of reports higher than the current report and was a function of the time difference between between the reports.

For smoothing the time-series of reports above 1000 m the performance of each of the low-pass-filters was similar. Below 1000 m there was a small difference between using the moving window methods and the IRR. The former methods reduce variance more than the IRR. However, the advantage of the IRR method is that it uses all the available reports whereas the moving window methods removed reports as a result of the imposed quality control criterion. The IRR method differs because it contains parameters that can be used to fine tune the performance of the low-pass-filter.

However, each of the methods used to minimise the fluctuations in the Mode-S EHS derived observations, i.e., aggregation and low-pass filtering, effectively reduces the space and time resolution of the data. This in turn affects the meteorological phenomena that can be detected. If the Mode-S EHS reports could be used directly then small scale features such as turbulence or short gravity waves may be detected (Orlanski 1975, Fig 1). But as we smooth the derived observations these features are averaged out.

We conclude that applying a low-pass-filter to the time-series reports of Mach number and true airspeed could be beneficial as a pre-processing step prior to NWP data assimilation but further research would be needed in order to tune the filter parameters. Moreover, the IRR method could be used as the basis for a Kalman filter.

Chapter 7

Assimilation of Aircraft Derived Observations using a Convection-Permitting Configuration of the Met Office Unified Model.

7.1 Introduction

In chapter 3 (page 33) it was shown how meteorological observations can be derived from routine messages exchanged between an aircraft and air traffic management. In chapter 4 (page 55) we derived equations to estimate the errors for these derived observations and validated these estimates against in situ observations. In chapter 6 (page 109) we showed that by aggregating these derived observations potentially useful information could be gained on the state of the atmosphere. We used nearby observations from AMDAR and radiosonde to verify qualitatively that useful information was available. This was shown using a case study to identify the occurrence of temperature inversions. We also showed that the vertical profile of the estimated error for aggregated reports of Mach Temperature was between one- and two-times the quantisation error obtained in chapter 4. In this chapter we examine the impact on NWP forecasts when we assimilate Mode-S EHS derived observations in a convection-permitting NWP model. We also use the observation-minus-background and observation-minus-analysis residuals to estimate the observation error for Mach Temperature.

Previous studies by de Haan & Stoffelen (2012) and Lange & Janjic (2016) have

shown that assimilation of Mode-S EHS observations have a positive impact on short-range forecasts. However, the impact will be very dependent on the data assimilation system used, the background error used and how many other sources of observations are used (as shown in table 2.5, page 29). The previous studies that assimilated Mode-S EHS were conducted using NWP models with horizontal grid spacings of 11 km and 2.2 km respectively, the latter being an ensemble-based convection-permitting model. Lange & Janjic (2016) and de Haan & Stoffelen (2012) used Mode-S EHS observations of wind and temperature that were derived from time-averaged Mode-S EHS reports - 60 s for aircraft in level flight and 12 s for aircraft ascents and descents. We note here that the study by Strajnar et al. (2015) did not use Mode-S EHS rather it used Mode-S MRAR. While the focus of our studies is based on Mode-S EHS we include Strajnar et al. (2015) for the purpose of comparing the benefits of assimilation of Mode-S EHS observations.

De Haan & Stoffelen (2012) found that for forecast lead times of one- and two-hours ahead, the Mode-S EHS observation-minus-forecast error for Mach Temperature ranges between 2.0 K near the surface, 1.5 K at 800 hPa and 1.0 K at 300 hPa (de Haan & Stoffelen 2012, Fig 13). Lange & Janjic (2016, Fig 9) used the Desroziers et al. (2005) diagnostic to estimate the observation error for Mach Temperature. They found that the observation error ranges between 1.2 K near the surface, 1.0 K at 850 hPa, 0.8 K at 700 hPa and 0.6 K at 400 hPa. Qualitatively these estimated observation errors have a similar vertical structure to each other with errors increasing significantly in the altitude range 700 hPa to 1000 hPa when compared with the altitude range above 700 hPa. Estimates of the Mach Temperature observation errors by Lange & Janjic (2016) are much lower than those of de Haan & Stoffelen (2012) and those found using in situ observations by Mirza et al. (2016) (chapter 4). The difference in the results between Lange & Janjic (2016) and de Haan & Stoffelen (2012) may be due to the difference in background error used in each NWP model.

Our experiments differ from these previous studies in the following ways:

- we use Mode-S EHS reports collected by the Met Office receiver network, described in section 5.5 (page 99);
- we use a higher resolution convection-permitting NWP model with horizontal grid spacing 1.5 km, described in section 2.10 (page 22);
- using a variational assimilation scheme we assimilate Mode-S EHS derived observations directly, i.e., without smoothing; and assimilate Mode-S EHS over AMDAR;

- we use the Desroziers et al. (2005) diagnostic to obtain estimates of observation error for AMDAR and Mode-S EHS derived observations that results from their assimilation in the NWP model UKV.

We choose this as our initial configuration for two reasons: (i) the technical limitations of the current UKV NWP data assimilation processing and (ii) so that we can evaluate the benefit of Mode-S EHS aircraft derived observations of wind and temperature on UKV NWP forecasts.

This chapter is organised as follows: in section 7.2 we describe briefly how the diagnostic proposed by Desroziers et al. (2005) can use the output of residuals from the variational assimilation system to estimate the observation error. In section 7.3 we describe our design for data assimilation experiments, in particular the configuration of the pre-operational version of the UKV. In section 7.4 we present results of our experiments with an assessment on the impact of assimilation of Mode-S EHS observations. In section 7.5 we estimate the Desroziers et al. (2005) diagnosed error for Mode-S EHS and AMDAR horizontal wind and temperature. We close this chapter with a summary of findings in section 7.6.

7.2 Desroziers et al (2005) Diagnosis of Observation Errors

In this section we describe the Desroziers et al. (2005) diagnosis method which is used to estimate error covariances. This is done by using a combination of the statistical average of the observation-minus-background, $[o - b]$, called the innovation vector (Talagrand 1997), and the observation-minus-analysis, $[o - a]$, called the residual vector. These differences can be obtained from our variational data assimilation system. The term o is the observation measurement, the background term b is the NWP value obtained from a previous forecast, and the analysis term a is obtained from the current analysis after the data assimilation processing is completed. This method was originally posed to provide a consistency check for an analysis scheme, such as 3-D Var. The diagnostic has been applied to estimate observation error statistics for a number of observation sources, e.g., Doppler radial winds (Waller et al. 2016a) and satellite radiance channels (Stewart 2010, Bormann & Bauer 2010, Bormann et al. 2010, Weston et al. 2014, Bormann et al. 2016, Waller et al. 2016b). Lange & Janjic (2016) used this diagnostic method to estimate the observation error standard deviation, σ_{DD} , for AMDAR and Mode-S EHS using the innovation and residual statistics output from an ensemble data assimilation system. They found that the observation error for Mode-S EHS winds is comparable with AMDAR but the observation error for temperature is 50%

greater than AMDAR at levels below 700 hPa. We will apply the diagnostic method to the innovations and residuals for AMDAR and Mode-S EHS obtained from the Met Office UKV 1.5 km NWP model, which is a deterministic model and variational data assimilation system. The results will be discussed in section 7.5.

Using the notation defined in section 2.11 (page 25), Desroziers et al. (2005, sec. 2.) showed that the definition of the innovation vector is given by,

$$\mathbf{d}_b^o = \mathbf{y}_o - \mathbf{H}(\mathbf{x}_b) = \mathbf{y}_o - \mathbf{H}(\mathbf{x}_t) + \mathbf{H}(\mathbf{x}_t) - \mathbf{H}(\mathbf{x}_b) \simeq \epsilon_o - \mathbf{H}\epsilon_b. \quad (7.1)$$

Using linear statistical expectation theory (Walpole et al. 2011, Ch. 4), it can be shown that,

$$E[\mathbf{d}_b^o(\mathbf{d}_b^o)^T] = E[\epsilon_o(\epsilon_o)^T] - E[\epsilon_o(\epsilon_b)^T]\mathbf{H}^T - \mathbf{H}E[\epsilon_b(\epsilon_o)^T] + \mathbf{H}E[\epsilon_b(\epsilon_b)^T]\mathbf{H}^T, \quad (7.2)$$

and assuming that ϵ_o and ϵ_b errors are mutually uncorrelated, i.e., the terms with the products $\epsilon_o\epsilon_b$ are zero, then

$$E[\mathbf{d}_b^o(\mathbf{d}_b^o)^T] = \mathbf{R} + \mathbf{H}\mathbf{B}\mathbf{H}^T. \quad (7.3)$$

Similarly, Desroziers et al. (2005) show that, by using the same methodology, the expectation between the innovation vector \mathbf{d}_b^o and the residual vector \mathbf{d}_a^o , which is given by,

$$\mathbf{d}_a^o = \mathbf{y} - \mathbf{H}(\mathbf{x}_a), \quad (7.4)$$

is related to the covariance matrix of the observation errors as,

$$E[\mathbf{d}_a^o(\mathbf{d}_b^o)^T] = \mathbf{R}, \quad (7.5)$$

provided that the exact values of the observation error covariance and background error covariance, are used to generate the innovations and residuals. However, if these are not known exactly then Desroziers et al. (2005) suggest that their approximations may be obtained by applying the diagnostic iteratively. In our initial study we do not apply the iterative method because the observation error covariance for Mode-S EHS is unknown with respect to the UKV NWP model. Waller et al. (2016) provide guidance on interpreting the results of the diagnostic determined non-iteratively.

7.3 Experiment Design

In this section we give an overview on how we configured the NWP model used for our data assimilation experiments. We used a version of the UKV NWP model trial suite that was undergoing pre-operational tests. This is the 1.5 km limited-area mesoscale convection-permitting model used for routine weather forecasts for the United Kingdom. This model is described in section 2.10. However, this version of the model required modification to assimilate Mode-S EHS derived observations. We describe the modifications in section 7.3.1.

To determine a practicable configuration for the data assimilation process used in the UKV we carried out five short experiments consisting of a control run and four experiment runs. The control run used, unless thinned, all the available routine observations (listed in table 2.4, page 25) for the routine weather forecasts but excluded aircraft-based observations. The experimental runs used the configuration of the control run and, in addition to the routine observations, included (i) AMDAR, (ii) AMDAR and all Mode-S EHS derived observations, (iii) AMDAR and Mode-S EHS derived horizontal wind and (iv) AMDAR and Mode-S EHS derived ambient temperature. Once the UKV was configured then experiments were performed using extended runs.

For these extended runs the data assimilation used, unless thinned, all the available derived observations from Mode-S EHS reports. These reports were collected using the Met Office Mode-S EHS receiver network (section 5.5). The reports used were collected between 03Z 2nd January to 06Z 8th January 2015 and which were retrieved from the Met Office MetDB observations archive. This period includes the case study dates used in chapter 6, where on the 4th January fog persisted for a longer period than forecast by the UKV. In addition, we used the Desroziers et al. (2005) diagnosis method (section 7.2, page 155) to estimate the observation error variance.

7.3.1 Configuration of the UKV

The basic configuration of the UKV used for these experiments was the same as the pre-operational parallel suite version 37, hereafter referred to as UKV-ps37 (see section 2.10). All routine observations, from surface-, air- and space-based observing systems, available to the operational forecast system were also available to the experimental system (see tables 2.5 and 2.4) (Ballard et al. 2016). Observations received from up to 90 minutes before, and those received no later than 75 minutes after, the analysis time are assimilated. The horizontal resolution of the data assimilation grid is 3 km. The data assimilation process used is the three dimensional variation (3D-Var) with first guess at appropriate time (FGAT) (Lorenc & Rawlins 2005). (FGAT uses the full

model state, saved at regular intervals, to obtain the NWP model background value, using linear interpolation, that corresponds to the actual time and position of each observation. The observation-minus-background fields are then treated as if they were received at the analysis time.) Three hourly data assimilation with 36 hour forecasts were run every six hours, starting at analysis times 0300, 0900, 1500 and 2100 UTC and with only 6 hour forecasts at intermediate cycles.

7.3.2 Observation Operator

For aircraft-based observations, the atmospheric observations reported are the horizontal wind speed and wind direction and the ambient temperature. These variables are reported directly for AMDAR whereas for Mode-S EHS they are derived (as shown in chapter 4).

The observation for the horizontal wind report from aircraft is expressed as its latitudinal component in the direction from south to north, V , and its longitudinal component in the direction from west to east, U ,

$$U = -V_w \sin(\alpha_w), \quad (7.6)$$

and

$$V = -V_w \cos(\alpha_w), \quad (7.7)$$

where V_w is the magnitude of the wind speed and α_w is the angular wind direction, measured clockwise from geographic North, from which the wind blows. The unit of measurement for wind speed is metres per second and for wind direction it is radians. Thus there may be additional steps to convert reports which use units of knots for wind speed and angular degrees for wind direction.

In NWP model space the wind is represented by these latitudinal and longitudinal components on a rotated grid and its vertical component in the direction from the surface upwards, W . Hereafter, we do not consider further the vertical wind component since it is not a state variable that is reported by aircraft.

Similarly, in model space the ambient temperature is represented by its potential temperature, θ_{pt} , which is defined as the ambient temperature of a parcel of dry-air when moved adiabatically to the surface (or a reference pressure) (Stull 2000, p. 47),

$$\theta_{pt} = T \left(\frac{P_{ref}}{P} \right)^{\frac{R_a}{C_p}}, \quad (7.8)$$

where T is the reported ambient temperature, P is the ambient pressure, P_{ref} , is the

reference pressure, normally taken to be 1000 hPa, R_a is the characteristic gas constant for dry air, and C_p is the specific heat of dry air under constant pressure.

The observation operator does not correct for the effects of humidity on the potential temperature, nor for the departure of the environmental atmospheric state from the ISA (ICAO 1993), excepting that these differences are assumed to be within the model’s errors of representation.

The observation operators for horizontal wind and potential temperature also contain interpolation steps to transform the model state variable from the model grid to the geographic position of the observation report. For the horizontal position the transform uses bi-linear interpolation using the four nearest horizontal grid points surrounding the position of the observation report. For the vertical position the transform uses log-linear interpolation between the adjacent model pressure levels for the pressure altitude of the observation report.

7.3.3 Observation Error Profiles

In equation 2.8, \mathbf{R} represents the observation error covariance matrix. It is a square matrix of dimension $p \times p$, where p is the number of observations. It is assumed that the observation errors are uncorrelated so that only non-zero elements of the matrix are the observation variances, σ_p^2 (Kalnay 2003, Ch 5).

For most of the data assimilation trials in this study the initial assumption is that the observation errors for AMDAR and Mode-S EHS are the same and they are uncorrelated. We make these assumptions because we aim firstly to obtain a practicable configuration of the data assimilation system, using the existing Met Office operational framework for the UKV NWP model. Secondly, that aircraft-based observations are reported by aircraft that are independent of each other.

Assumed Observation Error Standard Deviation

Figure 7-1a shows the assumed vertical profile of observation error standard deviations, σ_{AOBS} , for temperature as used in three NWP models: HIRLAM, COSMO-KENDA and UKV (table 2.6, page 30) lists some of their properties. Similarly figure 7-1b shows the corresponding vertical profile of σ_{AOBS} for horizontal wind. For the UKV the observation error for AMDAR used operationally had been determined from comparisons between the Met Office Unified Model and Radiosondes (Bell et al. 1999). For COSMO-KENDA the observation error for AMDAR was derived (Schraff et al. 2016, Lange & Janjic 2016, p1457, Table 1) using the Desroziers et al. (2005) diagnosis. For the de Haan & Stoffelen (2012) HIRLAM study the assumed profile for

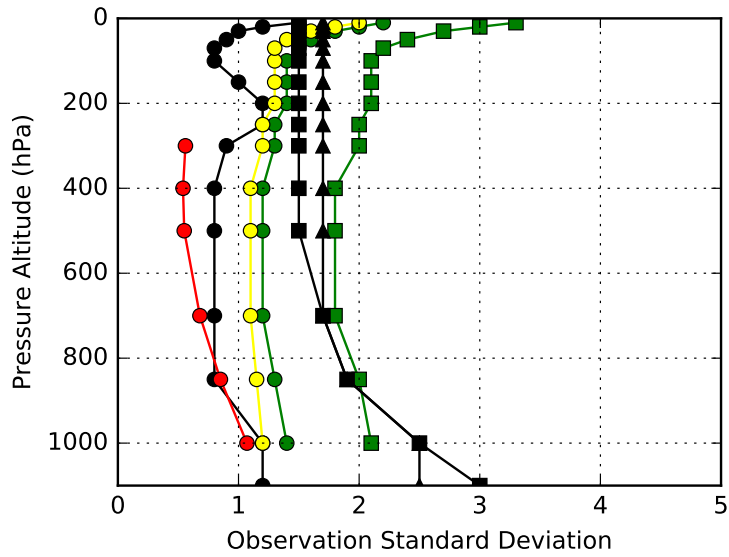
Mode-S EHS temperature (fig 7-1a green squares) is $1.5 \times$ AMDAR. The HIRLAM AMDAR observation errors are cited by de Haan & Stoffelen (2012, p.920 Table 1) and Lindskog et al. (2001, p.452 Table 1). Both of these are identical to the profile derived by Courtier et al. (1998, p.1803 Table B1). Clearly, as the σ_{AOBS} profiles for each model differ so this will affect the interpretation of the results and the assessment of the benefits of assimilating Mode-S EHS observations. Strajnar et al. (2015) uses an AMDAR σ_{AOBS} profile for Mode-S MRAR since these observations are assumed to be of the same quality as AMDAR (Strajnar 2012). Similarly, Strajnar (2012) uses the same observation errors as stated by Courtier et al. (1998, p.1803 Table B1).

We also show in figure 7-1a a second larger σ_{AOBS} profile (T2) for Mode-S EHS temperature for the UKV. This error profile was the ad-hoc profile estimated from routine monitoring of the observation-minus-background statistics (Hall 1992, Hollingsworth et al. 1986) using the operational version of the UKV, which does not assimilate Mode-S EHS observations.

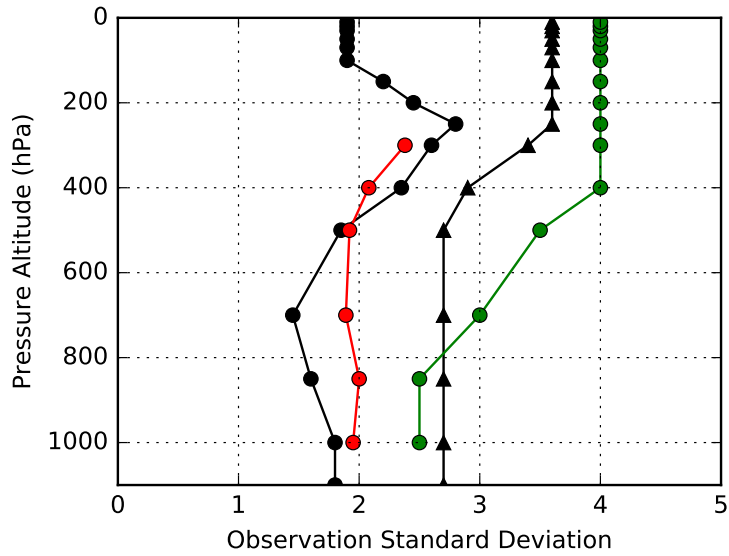
Observation-minus-Background Statistics

Figure 7-2 shows the Met Office's routine monitoring of the observation-minus-background error for Mode-S EHS temperature for the period 2nd to 8th January 2015. The left panel shows the mean bias and mean standard deviation and the right panel shows the total number of Mode-S EHS reports. The operational UKV NWP model provides the background fields and, at the time of our research, did not assimilate Mode-S EHS observations. We note that the bias is negative between the altitudes 4000 m and 6000 m, and positive above. The positive bias steadily increases from 0.0 K to 1.0 K between 4000 m and 2000 m, and is approximately 1.5 K below 2000 m. The bias below 4000 m may have contributions from background errors since the operational UKV does not assimilate Mode-S EHS, and from Mode-S EHS errors, since we have shown in chapter 6 that Mach Temperature becomes increasingly variable below 1000 m. We suggest that observation bias is more likely to be result of Mode-S EHS processing than due to the ambient temperature. This is because during this period weather conditions were calm in the south east for England, as evident from the prevailing foggy conditions.

We note that the root mean square error increases from 1.5 K at 9000 m to 2.0 K at 5000 m, 2.5 K at 2000 m, with a sharp increase to 3.5 K at the surface. This vertical profile appears to be similar to the quantisation error studied in chapter 4 (page 55). We note the similarity between figure 7-2 and profiles (a) and (b) in figure 4-2 (page 69) Between 9000 m to 2000 m the RMSE is similar to profile (b), which results from the



(a) Temperature (K). UKV AMDAR (T1) (black circles), UKV AIREP (black triangles), UKV Mode-S EHS (T2) (black squares).



(b) Horizontal Wind Speed Component (ms^{-1}). For NWP models, the Mode-S EHS observation standard deviation is the same as that used for AMDAR.

Figure 7-1: Assumed observation error standard deviation, σ_{AOBS} , profiles for (a) temperature and (b) horizontal wind components for data types AMDAR (circles), AIREP (triangles) and Mode-S EHS (squares), as used in NWP models UKV (black), HIRLAM (green) (de Haan & Stoffelen 2012, p.920 Table 1) and COSMO-KENDA (red) (Schraff et al. 2016, p1457, Table 1) and ALADIN (yellow) (Strajnar et al. 2015)

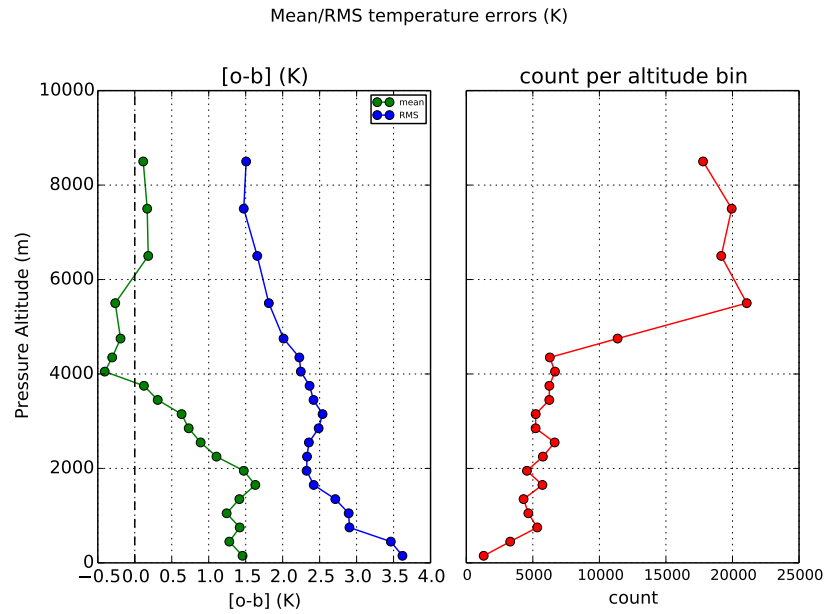


Figure 7-2: The mean observation-minus-background [o-b] for Mode-S EHS temperature for the period 2nd to 8th January 2015. The left panel shows the mean bias (green) and root mean square error (blue). The right panel shows the total number of reports for altitude bin widths 150 m. The operational version of the UKV provides the background.

standard deviation of quantisation error, and the increase in error between 2000 m and 0 m appears to be closer to profile (a) for the full precision error. We note that Ballard et al. (2017) show the observation-minus-background mean bias profile for March 2016 is approximately 0.5 K for all altitudes but the RMSE profile is similar to that shown in figure 7-2.

The Met Office’s routine observation monitoring shows that the Mode-S EHS temperature error is greater than the assumed AMDAR observation error, and the error increases significantly below 1000 m. The monitoring suggests that for Mode-S EHS temperature in the altitude range 15,000 m (100 hPa) to 3000 m (700 hPa) σ_{AOBS} lies somewhere between AMDAR and AIREP, between 3000 m and 100 m (1000 hPa) the σ_{AOBS} is approximately the same as AIREP, and near the surface the σ_{AOBS} is at its greatest. From this monitoring we construct an ad-hoc σ_{AOBS} profile, T2, which we can use for Mode-S EHS σ_{AOBS} temperature.

The profile of this observation-minus-background error is similar to those shown in figures 4-9 (page 83) and 6-14b (page 149), which suggests that quantisation error is a significant contributor to the observation error for Mode-S EHS Mach Temperature. The rationale for adapting the the AIREP σ_{AOBS} is that it is already used in the

operational UKV NWP model. We assume that it is in reasonable balance with the other observation types (Ballard et al. 2017) since we know that the operational data assimilation accepts aircraft observations using the σ_{AOBS} for AMDAR and AIREP.

7.3.4 Mode-S EHS Observation Thinning

Previous studies have shown that the practical use of Mode-S EHS observations require thinning prior to their data assimilation (de Haan & Stoffelen 2012, Lange & Janjic 2016). Therefore short-run trials were conducted to estimate the amount of data-thinning required so that the data assimilation system would reach an acceptable level of convergence prior to the NWP forecasting step. Thinning is a distinct process from the temporal averaging used to minimise the variance of the Mode-S EHS observations (as discussed in section 6.9, page 142).

In our experiments we used two methods available to thin the number of Mode-S EHS observations available prior to data assimilation: temporal thinning and spatial thinning. For temporal thinning, the time-window for accepting observations is $T \pm \Delta t$ minutes, where T is the data assimilation time, i.e., 0000, 0300, 0600 UTC, and Δt is the time window for accepting observations. The default time window for accepting observations is in the range $0 < \Delta t < 90$ minutes. The temporal thinning could be applied separately to the different types of aircraft-based observations. For the trial runs, only the time window for accepting Mode-S EHS observations was varied, between 15, 30, 60 and 90 minutes. The time window for AMDAR and AIREPS was left at its default value, $\Delta t = 90$ minutes.

For spatial thinning, we applied thinning down to the data assimilation horizontal grid length, 3 km, and observation-type selection. If there was more than one aircraft-based observation type available within a grid box then the Mode-S EHS observation type was preferentially selected. Only the observation which is closest to the centre of a grid box was selected. The spatial thinning is applied to all available aircraft-based observations, i.e., AIREP, AMDAR and Mode-S EHS. For the trial runs, the spatial thinning grid-box dimensions were: 40 hPa vertical depth between the surface and 11 km and the horizontal dimensions at the surface being 3.0 km in longitude and 3.0 km in latitude. The vertical depth of 40 hPa corresponds approximately to the vertical separation between aircraft flight levels (1000 feet or 330 m) near the surface under ISA conditions. The time difference between reports within the grid box was varied between 5 mins and 15 mins.

For these initial trials we aim to understand what effect the density of Mode-S EHS reports has on the data assimilation process. Thus we do not aggregate the observations nor apply any temporal smoothing or a low-pass filter as discussed in chapter 6.

Incorporating these methods was beyond the scope of the present study. In section 2.13 (page 27) we reviewed previous data assimilation studies. Essentially, de Haan & Stoffelen (2012) and Lange & Janjic (2016) used hourly and three hourly assimilation cycles, Mode-S EHS observations that were smoothed using a linear regression low-pass filter and Mode-S EHS observations thinning.

7.3.5 Quality Control

Mode-S EHS observations undergo quality control at two stages. The first stage is at the point of collection where erroneous or invalid reports are removed before being submitted to the observations database, this is described in section 5.5 (page 99). The second stage is applied by the Observation Processing System (OPS) prior to data assimilation. The OPS performs several checks on the observation. Firstly, the observations are passed through a gross-error filter. Secondly, observations are compared to nearby observations in a so-called ‘buddy check’. Finally, the probability of gross error is computed.

The gross error filter is simply a threshold filter. The observation is marked for rejection if it exceeds a pre-defined constant value. The buddy check computes the difference between the current observation and nearby observations. The observation is marked for rejection if the difference exceeds a pre-defined constant value. The probability of gross error is based on Bayes Rule (Walpole et al. 2011, Ch. 2). The framework for implementing this method in the Met Office 3-D Var scheme is described more fully in Ingleby & Lorenc (1993). If the probability of gross error is computed to be greater than 0.5 then the observation is rejected.

7.3.6 Trials of Data Assimilation Performance

In this section we aim to find a configuration for the UKV data assimilation that processes Mode-S EHS derived observations with a similar performance to that achieved without them. Our aim is to obtain a data assimilation performance that is similar in terms of the computational time and to ensure that adding Mode-S EHS observations does not negatively impact on the fit to other less numerous observations. We do this by running short trials of the UKV. We assess the performance of the data assimilation processing by checking the number of iterations, n_{iter} , required for the cost function (eq. (2.8)) to reach a minimum value. This would be an important factor for operational implementation. The assimilation is stopped when

- $\|\nabla J(\mathbf{x}_a)\| \leq Q$ or
- the change in the cost function $\frac{|J(x_{n+1}) - J(x_n)|}{J(x_o)} < threshold$ or

- $n_{iter} > n_{max}$, where n_{iter} is the actual number of iterations and n_{max} is the threshold for stopping the data assimilation process; for the parallel suite UKV-ps37, $n_{max} = 100$.

A large number of iterations implies slow convergence to the minimum value which may not be suitable for operational implementation.

Table 7.1 lists the technical trials for assimilation of Mode-S EHS observations. The notation for these trials is as follows:

1. CONT is the control experiment where no aircraft observations are assimilated.
2. A is for AMDAR, S is for Mode-S EHS aircraft observations
3. For all trials the time window of accepted observations for AMDAR is ± 90 minutes. Assimilation of AMDAR includes AIREP.
4. The restricted time window for data assimilation of observations (d) for Mode-S EHS observations is ± 90 minutes of the analysis time *unless otherwise stated*. The letter combination dyy indicates that a different data assimilation window is used, where yy is the time in minutes.
5. The time window for the spatial-temporal thinning window (t), described in section 7.3.4 is 300 seconds *unless otherwise stated*. The letter combination txxx indicates the time window used, where xxx is the time in seconds.
6. Where thinning is applied it applies to all aircraft observations between the surface and 11 km. This is a separate process that is applied after the data assimilation time window.

These trials ran the data assimilation in a continuous cycle starting from 0300 UTC and finishing at 0900 UTC 2nd January 2015. This would provide at least three data assimilation cycles in which Mode-S EHS data would be assimilated. For these technical trials we use the AMDAR winds σ_{AOBS} profile for both AMDAR and Mode-S EHS winds; and the profile for AMDAR temperature σ_{AOBS} T1 for both AMDAR and Mode-S EHS temperatures, these are shown in figure 7-1 (page 161). (In our longer trials we use the revised σ_{AOBS} T2 profile for Mode-S EHS temperatures.)

The UKV-ps37 was configured to initialise its run from the operational analysis obtained 3 hours earlier at 0000 UTC. This was to allow the NWP model a short spin-up time before starting to assimilate Mode-S EHS observations. Moreover, the start time of the trial was chosen to allow for the gradual increase in the number of available Mode-S EHS observations. This is because there is minimal air traffic operating within

UK airspace between the hours from 2300 to 0500 UTC. During this time any Mode-S EHS observations are likely to be from air traffic transiting UK airspace at high altitude (≈ 10 km).

Trial runs were conducted as follows: (a) without aircraft-based observations (CONT), (b) with AMDAR only, (c) with AMDAR and Mode-S EHS winds and temperatures, (d) with AMDAR plus Mode-S EHS winds and (e) with AMDAR plus Mode-S EHS temperatures. AMDAR wind and temperature observations were used in all these trials. The number of aircraft-based observations was controlled either by changing the data assimilation window for the type of observation or applying temporal and spatial thinning. In all trials where AMDAR reports were assimilated this also included AIREPS. The number of available AIREPS is around 100 per day. The number of AMDAR reports can be around 1000 per day.

The results of these trials are listed in table 7.2. The table shows the number of iterations required at each data assimilation cycle (0300, 0600 and 0900 UTC) to achieve minimisation of the cost function and the corresponding number of aircraft reports assimilated for temperature (T) and wind (W) observations. We see that for experiment CONT the number of iterations decreases over the three cycles, with the average number of iterations being 20. Trial CONT has not assimilated aircraft observations, so provides a metric for assessing the impact of assimilating aircraft observations on the number of iterations.

Trial AO assimilated only AMDAR and AIREP reports which were available to the operational version of the UKV. The number of observations increased from around 250 at 0300 UTC to around 900 at 0900 UTC. The average number of iterations to minimise the cost function is 18, which is comparable to the trial CONT.

Trial AS was designed to assimilate all available aircraft-based observations, AMDAR, AIREP and Mode-S EHS. We can see that the number of assimilated aircraft-based observations is 100 times greater than for trial AO. At the beginning of the experiment the number of iterations is three-times that of AO. At subsequent cycles, where the number Mode-S EHS observations increases by a factor of 10, the maximum number of iterations, n_{max} , has been reached. Also the assimilated aircraft observations are dominated by the Mode-S EHS. From this trial, it is clear that for the UKV-ps37 using 3-hourly 3-D Var, assimilating all available Mode-S EHS observations is not practicable.

Trials AStxxxddy (see table 7.1), were used to explore the options available to thin the available aircraft-based observations. We begin with spatial thinning, indicated with txxx then change the time range for the time-window for accepting observations, indicated with dyy. The spatial thinning control was set to prioritise assimilation of

Mode-S EHS reports. For spatial thinning alone we note that the number of iterations to reach minimisation is two- to four-times that of AO. The cost of spatial thinning is to reduce the number of assimilated observations by a factor of 10 when compared with trial AS. However, whilst thinning has achieved the desired effect on the number of iterations required to reach minimisation of the cost function it is still too high when compared to the trial AO. The trial ASt300d30 uses a time window of ± 30 minutes around the analysis validity time to accept Mode-S EHS observations. We see that the trial ASt300d30 does reduce the number of iterations to that comparable to the operational version, AO. The number of iterations is halved when thinning of Mode-S EHS observations is included.

Trials ASt300d30W and ASt300d30T were used to assess which of the Mode-S EHS observation types causes the increase in the number of iterations. For these experiments the impact on the data assimilation for assimilating only winds or only temperatures is about the same. The last trial, AOsto, was performed due to a major technical change that was made to the UKV-ps37 prior to its operational deployment. This involved a change in the order in which the background error covariance transformation operations were performed from vertical then horizontal to horizontal then vertical. The reasons for this change are beyond the scope of this study. Suffice to say trial AOsto shows that the effects of these changes appear to have had only a small effect on the number of iterations when compared to the trial AO.

Based on the number of iterations required to achieve a minimisation we conclude from these technical trials that spatial thinning and reducing the data assimilation window would provide a UKV-ps37 suite that would be comparable to the operational version of the UKV in terms of the number of iterations required for the cost function to be minimised. The number of Mode-S EHS observations would be reduced to around 10% of those available, this is still around 20 times more than the available AMDAR. This reduction is comparable to previous studies (2.13, page 27) which used Mode-S EHS reports of 5% within SSR range of Schipol Airport (de Haan & Stoffelen 2012); 10% and 50% within German airspace (Lange & Janjic 2016), supplied by Maastricht Upper Air Centre; and between 5% and 15% for Mode-S MRAR (Strajnar et al. 2015).

The limitations of these technical trials is that we used a version of the UKV suite that mirrored closely the version to be used in operational weather forecasting, UKV-ps37. There are technical limitations with using UKV-ps37. The data assimilation system for UKV-ps37 does not distinguish between AMDAR and Mode-S EHS observations in its diagnostic output. So it is not possible to assess the impact of assimilating Mode-S EHS observations separately from the assimilation of AMDAR observations. Nonetheless useful information can still be obtained by performing an extended run

using the configuration of the trial ASt300d30.

7.3.7 Desroziers et al. (2005) Diagnostic Calculation

We used the Desroziers et al. (2005) diagnosis method to derive an estimated observation error standard deviation vertical profile, σ_{DD} , for aircraft-based observations within the UKV inner domain (fig 2-6). To do this we adapted the method developed by Waller et al. (2016b).

Waller et al. (2016b) developed a method to obtain the Desroziers et al. (2005) diagnosed observation error variance, R , and the horizontal covariance, for SEVERI satellite observations at different radiance wavelengths. We adapted the Waller et al. (2016b) method to obtain R for aircraft-based observations at different altitudes. In Waller et al. (2016b) the method described in Stewart (2010, sec 4.2) was used to compute the Desroziers et al. (2005) diagnostic for R , (section 7.2, page 155 and section 7.3.3, page 159)

$$R = \frac{1}{N} \sum_{i=1}^N (d_a^o)_i (d_b^o)_i - \left(\frac{1}{N} \sum_{i=1}^N (d_a^o)_i \right) \left(\frac{1}{N} \sum_{i=1}^N (d_b^o)_i \right), \quad (7.9)$$

where d_b^o and d_a^o are the innovation and residual respectively, N is the total number of observations in the altitude band. The mean residual and innovation are subtracted to make the result unbiased.

We used the innovations and residuals from the longer trial run LT_AST1 (table 7.3) to compute R for a range of pressure altitudes. We computed R at pressure-altitude intervals of 100 hPa between 1100 hPa (near the surface) and 100 hPa (top of the troposphere), this represents the range of altitudes for aircraft flight trajectories.

The geographic distribution of the reports for AMDAR and Mode-S EHS is shown in figure 5-9. We would expect to see the largest number of observations being reported during the cruise phase of flight, which occurs mostly in the region between 300 hPa and 200 hPa, because this is where most of the flight time is spent.

Only those observations that passed the initial quality control (section 7.3.5, page 164) were used in our analysis. For our initial investigation, the innovations and residuals were computed using the assumption that AMDAR σ_{AOBS} profiles (fig 7-1, page 161) apply for AMDAR and Mode-S EHS reports of wind and temperature.

We use our adapted Waller et al. (2016b) method to construct σ_{DD} for the different types of aircraft-based observations. We discuss the results of the Desroziers et al. (2005) diagnostic calculation for AMDAR and Mode-S EHS in section 7.5 (page 179).

Table 7.1: List of technical trials for data assimilation of AMDAR and Mode-S EHS. Suite refers to the identification number of the UKV suite which contains the set-up parameters used for the technical trial. Technical trials were run for the period 0300 UTC to 0900 UTC on 2nd January 2015. The label indicates which aircraft-based observations were used, A is for AMDAR and S is for Mode-S EHS. Unless otherwise indicated both wind (W) and temperature (T) observations were assimilated.

Suite	Label	Configuration details
ah418a	CONT	Control. No aircraft-based observations. No Thinning.
ah319a	AO	AMDAR only observations. No Thinning.
ai775	AS	AMDAR+MODES. No Thinning applied. Data assimilation window ± 90 min
aj232a	AS+300	AMDAR+MODES. Thinning applied. Data assimilation window ± 90 min
aj232b	AS+060	AMDAR+MODES. Thinning with time difference of 1 minute. Data assimilation window ± 90 min
aj232c	AS+030	AMDAR+MODES. Thinning with time difference of 30 seconds. Data assimilation window ± 90 min
aj232d	AS+900	AMDAR+MODES. Thinning with time difference of 15 minutes. Data assimilation window ± 90 min
aj232e	AS+300d30	AMDAR+MODES. Thinning applied. Data assimilation window ± 30 min
aj232f	AS+300d30W	AMDAR+MODES. Thinning applied. Data assimilation window ± 30 min. Assimilation Winds only.
aj232g	AS+300d30T	AMDAR+MODES. Thinning applied. Data assimilation window ± 30 min. Assimilation Temperature only.
aj232h	AOsto	a major technical change for UKV-ps37 prior to its operational implementation otherwise same as ah319a.

Table 7.2: Metrics for the technical trials for the data assimilation (DA) cycles 0300, 0600 and 0900 UTC for 2nd January 2015. The label column describes the technical trial used and is matched with the technical trial defined in table 7.1

Label	Number of Iterations			Number of Assimilated Observations								
	0300	0600	0900	0300			0600			0900		
UTC				T	W	T	W	T	W	T	W	
CONT	27	20	13	0	0	0	0	0	0	0	0	
AO	17	21	17	251	251	693	694	887	887	887	887	
AS	56	100	100	28334	29935	166850	176216	272098	292872	292872	292872	
ASt	42	46	61	4722	4997	29730	30845	57170	60303	60303	60303	
ASt060	23	48	73	5200	5498	33282	34683	64395	68546	68546	68546	
ASt030	33	52	74	5738	6072	36749	38443	71582	76357	76357	76357	
ASt900	52	41	56	4533	4783	27940	28847	53023	55540	55540	55540	
ASt300d30	20	32	35	2127	2167	11728	12204	22438	23923	23923	23923	
ASt300d30W	17	32	34	252	2167	701	12202	879	23923	23923	23923	
ASt300d30T	20	36	22	2127	262	11721	697	22429	885	885	885	
AOsto	19	14	19	252	262	701	697	879	879	879	885	

Table 7.3: List of longer trials (LT) for data assimilation using the UKV-ps37. The UKV observation error profile for temperature (shown in figure 7-1a) were also kept the same for all trials except for LT_AST2, when it was changed to the revised profile based on observation monitoring. The UKV observation error profile for winds (shown in figure 7-1b) were kept the same for all trials. The table also lists whether the trial was configured to output the additional results for the innovations [o-b] and the residuals [o-a].

Experiment ID	Experiment Label	Mode-S EHS Observation Error Profile		Comments
		Temperature	Winds	
al417	LT_CONT	AMDAR	AMDAR	No assimilation of A/C data
aj232	LT_AO	AMDAR	AMDAR	Assimilate AMDAR Only
al756	LT_SO	AMDAR	AMDAR	Assimilate Mode-S EHS Only
al754	LT_AST1	AMDAR	AMDAR	Assimilate Mode-S EHS & AMDAR
al972	LT_AST2	New T	AMDAR	Assimilate Mode-S EHS & AMDAR

7.4 Results of Data Assimilation Experiments

In this section we present the results of longer trial runs. These use the configuration of trial ASt300d30 discussed in section 7.3.6 and, to ensure that trials were consistent with the UKV-ps37, the technical change used in ASsto. The key parameters used in ASt300d30 are that at the analysis time the assimilation window for accepting observations is ± 90 minutes except Mode-S EHS for which we use different thinning strategies.

Table 7.3 lists the longer trials, where LT indicates this is a longer trial for the period from 0300 UTC 2nd January 2015 to 0600 UTC 8th January 2015. Starting from 0300 UTC 2nd January there were 50 data assimilation cycles. The time between each data assimilation cycle is three hours. The LT were conducted for AMDAR only (AO), Mode-S EHS only (SO); AMDAR and Mode-S EHS (AST1) using the AMDAR σ_{AOBS} T1 for Mode-S EHS temperature; and AMDAR and Mode-S EHS (AST2) using the ad-hoc σ_{AOBS} T2 for Mode-S EHS temperature. (For trail AST2, the ad-hoc σ_{AOBS} T2 is based on the results obtained from the Met Office’s observation-minus-background monitoring, as discussed in section 7.3.3.) For each LT the same type and number of observations were available for assimilation.

7.4.1 Impact of Assimilated Mode-S EHS Observations on the Fit to Aircraft Observations

Our technical trials had shown that for data assimilation in the UKV_ps37 it was necessary to reduce the number of Mode-S EHS observations. This was done in two ways: (i) reducing the time window used for Mode-S EHS observation around the analysis validity time and (ii) applying spatial and temporal thinning for all aircraft observations. The spatial and temporal thinning also prioritised Mode-S EHS observations over AMDAR. So where the density of Mode-S EHS observations is high the effect is to replace AMDAR. Conversely in the absence of Mode-S EHS then AMDAR are used if available. Figure 5-9 shows that for the period 03Z 2nd January to 06Z 8th January 2015 Mode-S EHS observations are confined to the southern half of the United Kingdom whereas AMDAR observations are distributed across the whole country. Thus replacement of AMDAR by Mode-S EHS is mostly likely to occur in the southern region.

To estimate the impact of assimilating Mode-S EHS derived observations we consider, in the first instance, the initial and final values of the total cost function, eq. (2.8) (page 27). After each assimilation cycle, we would expect the final value to be smaller than the initial value for each experiment. However, we can only meaningfully compare results between experiments when they use the same set of observations. For

each of the trials listed in table 7.3, figure 7-3 shows the assimilation time-series of the total cost function (i) at the start and (ii) at the end of assimilation processing.

In all trials the final cost is lower than its start cost. This suggests that the assimilation cycles are extracting useful information from the observations but it is not clear from the total cost result how much this is due to the addition of Mode-S EHS observations. The reduction in the cost function at the start and end of the AMDAR & Mode-S EHS (T2), LT_AST2, trial is due to the lower weight given to Mode-S EHS observations as result of using the revised observation error profile. Nonetheless there is an impact on the cost function between the start and end of the assimilation cycle. The lack of difference in total penalties between LT_SO and LT_AST1 is mainly due to the dominance of the number of Mode-S EHS observations compared to AMDAR, and the small detectable difference is probably due to the Mode-S EHS thinning method.

The total penalty is dependant on the number of observations assimilated. This is clearly indicated by the diurnal changes in the total penalty which appears to correspond with the diurnal changes in the availability of aircraft-based observations (fig 5-8). We note also that in the period between 4th and 7th January calm conditions persisted as a high-pressure system was present over the UK. The periods before and after were subject to changing conditions resulting from the passage of low-pressure systems with accompanying weather fronts. The passage of these weather fronts brought higher wind speeds which may have increased the forecast error. This may explain the higher values in the total penalty before and after the calm period.

7.4.2 Impact of Assimilated Mode-S EHS Observations on the Fit to Non-aircraft Observations

In this section we consider the impact of assimilating the Mode-S EHS observations on other observation systems that report temperature and horizontal wind namely surface synoptic reporting, satellite and Doppler radar. We use the same observation set for comparison with each experiment. Previous studies by de Haan & Stoffelen (2012) and Lange & Janjic (2016) do not report the effect of Mode-S EHS assimilation on Doppler and satellite derived wind. We choose to look at winds and temperature because these are easily comparable. We also consider the impact on forecasts of weather types, visibility and precipitation, but there is a less clear link between the input observations and the forecast weather types.

Figure 7-4 (page 176) shows the assimilation time series of the innovations for surface based observations 10 m horizontal wind component U (fig 7-4a) and 2 m screen temperature (fig 7-4b). For all trials the overall impact appears to be neutral, there being only small differences between the innovations and residuals of the trials. The

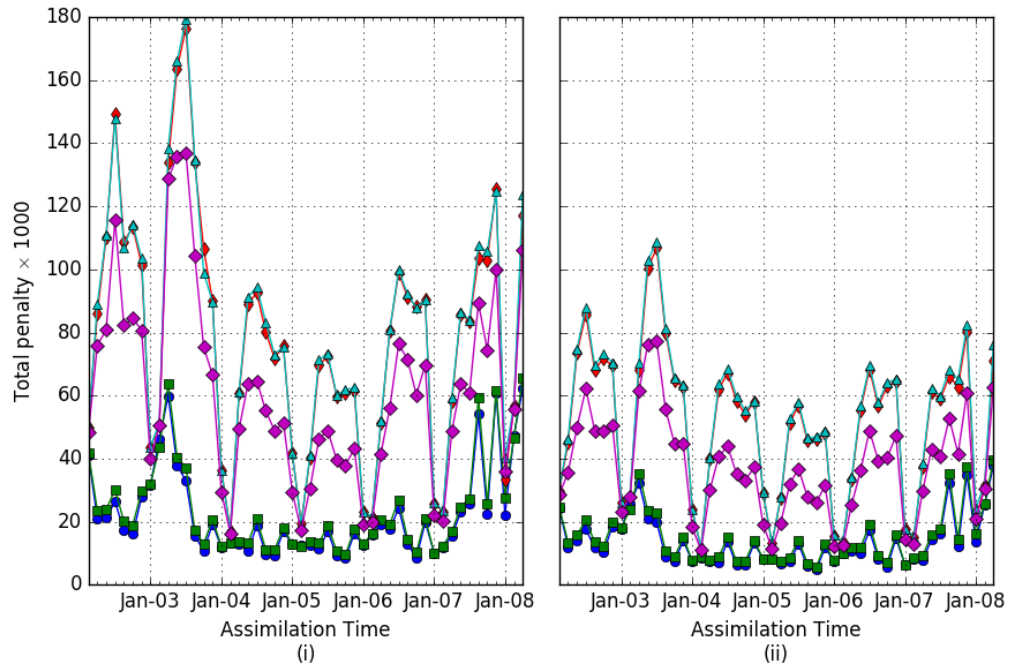


Figure 7-3: Time series of the total penalty metric (i) at the start and (ii) at the end of assimilation processing for the trials listed in table 7.3. LT_CONT, No aircraft data assimilated (blue circles); LT_AO, AMDAR only (green squares); LT_SO, Mode-S EHS only (red narrow diamonds); AMDAR and Mode-S EHS LT_AST1 (light blue triangles) and LT_AST2 (purple large diamonds). T1 indicates the use of AMDAR observation error for temperature was used for Mode-S EHS. T2 indicates the revised observation error temperature was used for Mode-S EHS.

results for horizontal wind component V (not shown) are similar. Clearly the influence of the aircraft-based observations has not extended to the near surface conditions. This may be due to the lack of aircraft-based observations below the altitude of 300 m (see section 6.4).

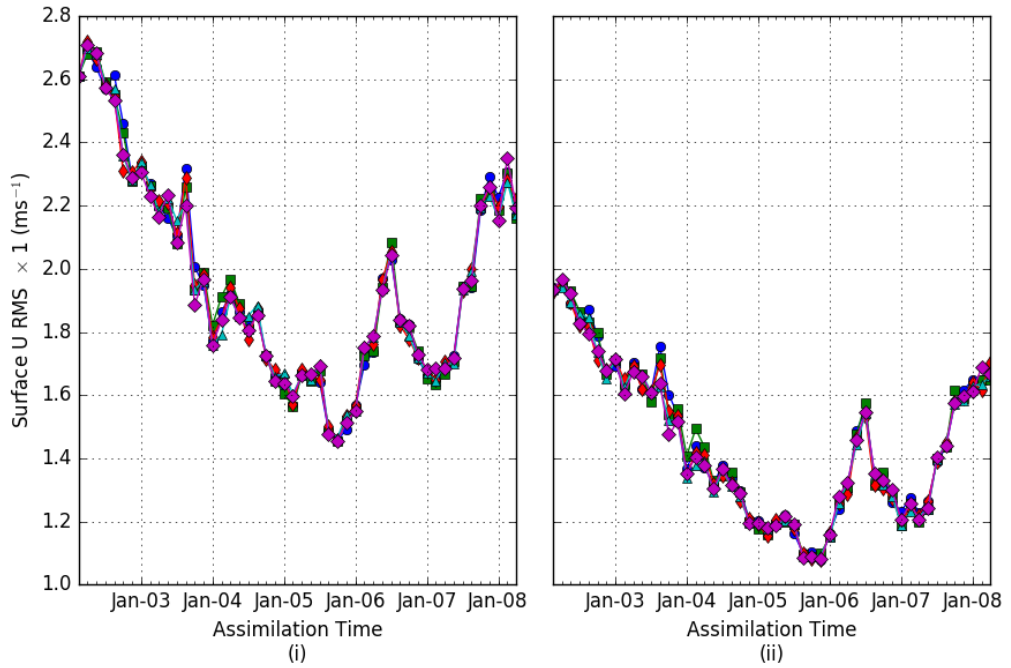
Figure 7-5 shows the assimilation time series of the innovations for remotely sensed observations, satellite horizontal wind component U (fig 7-5a) and Doppler radial wind component (fig 7-5b). As for the surface observations, for all trials the overall impact is neutral. The results for satellite horizontal wind component V (not shown) are similar. The assimilation of the Mode-S EHS has had little impact since the residuals of the trials are of similar magnitude. However, there are some small differences resulting from the revised observation error for Mach Temperatures.

In complex operational NWP systems, it not unusual for changes in the system to produce a neutral impact on assimilation statistics such as these. In the next section we consider the impact on short range forecasts.

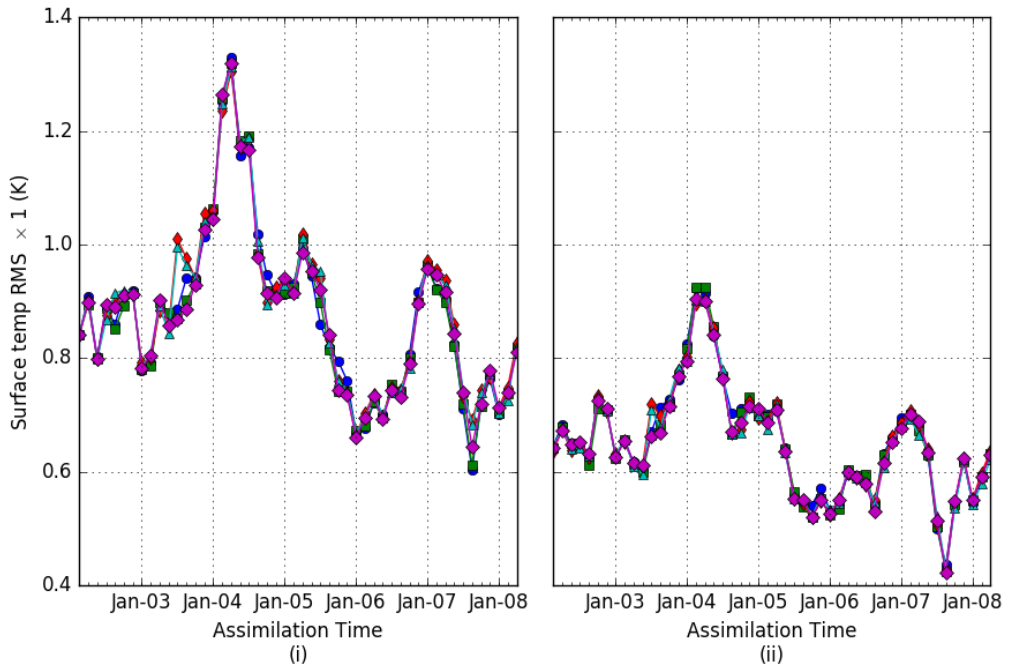
7.4.3 Forecast Verification against Radiosonde

In this section we consider verification of the wind and temperature forecasts output by the trial suites. The trial suites were configured for analysis every three hours followed by a short run of forecasts, hourly forecasts for a lead time of up to six hours ahead. The short run forecasts were chosen because previous studies by de Haan & Stoffelen (2012) have shown that the benefit of assimilating AMDAR reports persists up to lead times of six hours while for Mode-S EHS the benefit persists for up to three hours. The forecasts were verified against radiosonde using the Met Office application TRUI (TRials User Interface). This application provides a standardised framework for evaluating trial suite forecasts and for comparing the verification between trials. TRUI verification of wind and temperature forecasts uses available radiosonde and surface based observations. Table 7.4 lists the trial comparisons and figures 7-6 and 7-7 (page 181) show the results of the comparisons for vertical profiles of temperature and wind respectively.

Figure 7-6a shows the mean RMSE vertical profile of the forecast temperature for the long trials with AMDAR only (LT_AO) and AMDAR+Mode-S EHS using observation profile T1 (figure 7-1, page 161) (LT_AST1). The RMSE magnitudes for each profile are similar. The differences are less than 0.1 K, as shown in fig. 7-6b. The small differences suggest that assimilation of Mode-S EHS Mach temperatures has not made a significant change in the forecast at lead times of six hours. Figure 7-6d shows the difference when using using observation profile T2 (figure 7-1, page 161) (LT_AST2) for Mach temperature, the magnitude of the differences are again within 0.1 K. There

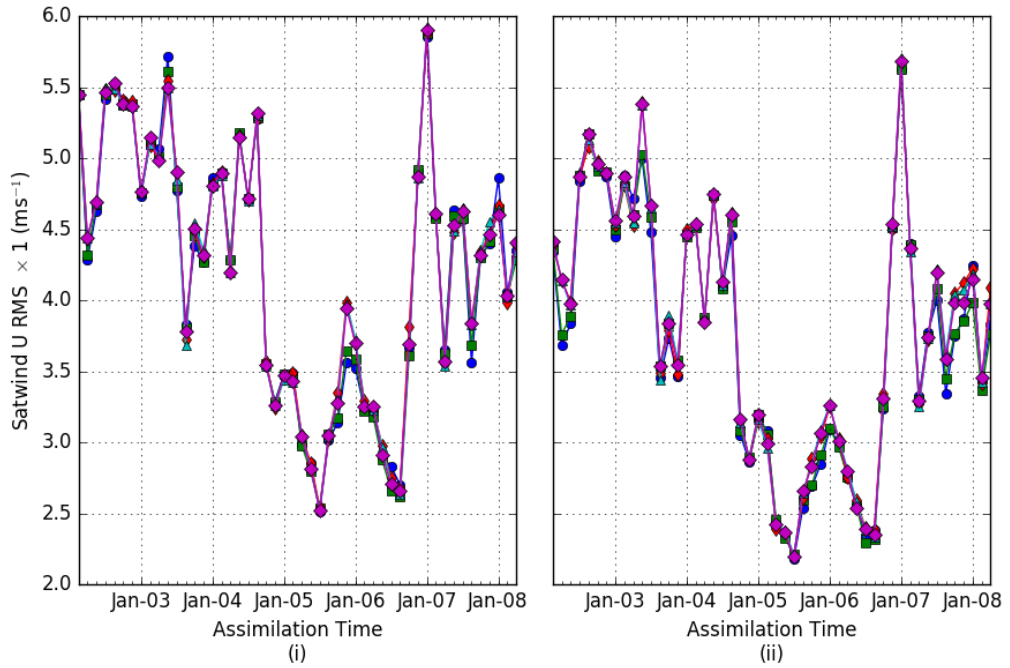


(a)

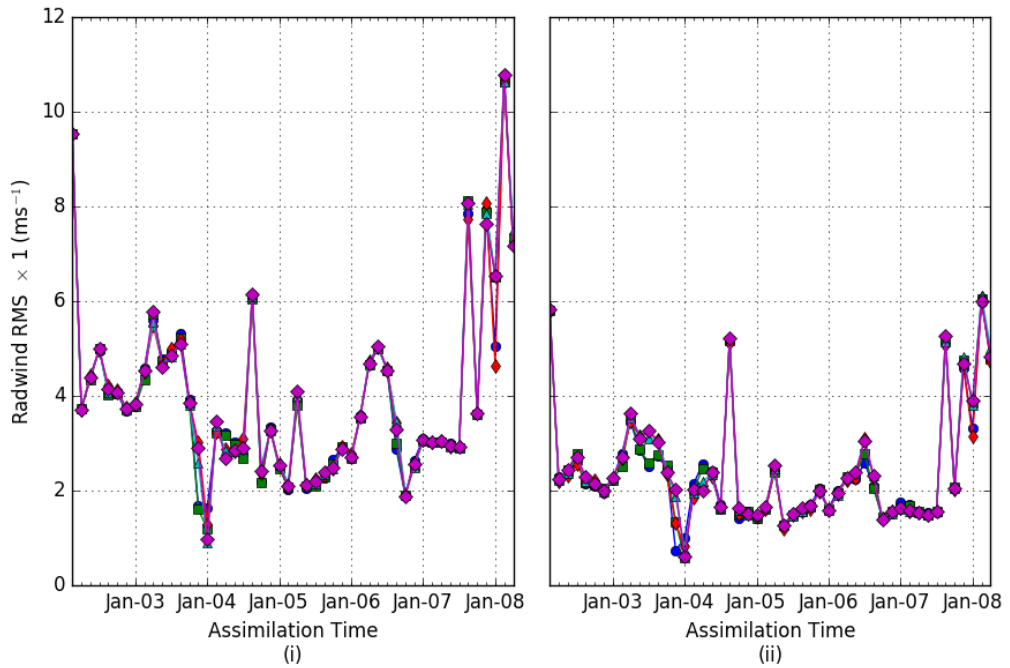


(b)

Figure 7-4: Assimilation cycle time series of the (i) RMSE innovations at the start and (ii) RMSE residuals at the end of assimilation for surface observations (a) 10 m horizontal wind component U and (b) 2 m potential temperature. Legend is the same as in figure 7-3.



(a)



(b)

Figure 7-5: Assimilation cycle time series of the (i) RMSE innovations at the start and (ii) RMSE residuals at the end of assimilation for remote sensed observations (a) satellite horizontal wind component U and (b) Doppler radial wind. Legend is the same as in figure 7-3.

is an increase in RMSE difference between 300 hPa and 200 hPa otherwise there is little to distinguish between LT_AST1 and LT_AST2, as shown in fig. 7-6c where the magnitude of the difference is less than 0.02 K. Similar results are seen in the wind vertical profiles (figure 7-7). Comparing figure 7-7b with 7-7d we note that the revised observation error for temperature appears to have had greater effect on the horizontal wind, particularly the distribution at levels below 300 hPa. However, the magnitude of the RMSE differences are small being 0.1 ms^{-1} , which could be due to computational noise resulting from floating point binary representation.

In figure 7-7a (page 181) it is notable that the mean RMSE for AMDAR wind appears to be larger than expected, ranging between 3 ms^{-1} to 5 ms^{-1} compared with the more generally accepted range 2 ms^{-1} to 3 ms^{-1} (Painting 2003). This difference may be due to NWP background model error.

The change in the observation error profile for Mach Temperature seems not to have significantly affected the subsequent forecasts. The larger the observation error standard deviation the lower the weighting of the observation in the data assimilation processing, eq. (2.8) (page 27). It is unclear from these results whether the higher observation error standard deviation for the Mode-S EHS Mach Temperature means that they are not contributing much information to the analysis field when compared with the AMDAR temperature. This may account for the neutral impact on the analysis discussed in section 7.4.2. Previous studies by de Haan & Stoffelen (2012) and Lange & Janjic (2016) have shown better forecast accuracy for the first few hours with the assimilation of Mode-S EHS than with AMDAR only when forecasts are verified against radiosonde observations. Two main differences between these studies and this present work are (i) we use a higher horizontal grid length and (ii) we do not apply a low pass filter, e.g., linear regression, to smooth the Mach Temperature prior to its assimilation (see section 6.9.2).

Furthermore, we specified two observation error standard deviation profiles for the Mode-S EHS Mach Temperature, T1 and T2. The profile T1 is identical to the AMDAR observation error standard deviation while the profile T2 is closer to our estimated error due to quantisation error (figure 4-9, page 83). We found that in both cases the impact on the UKV NWP forecasts was neutral.

We conclude from our studies that, using our UKV_ps37 configuration, the assimilation of Mode-S EHS has a neutral impact on the forecasts of wind and temperatures, with no adverse impact on the observations from other sources. Therefore there appears to be no additional benefit to the assimilation of Mode-S EHS observations, in terms of improving forecast accuracy of horizontal wind and ambient temperature. Further study is required to understand whether this is due to a saturation effect, as reported

Table 7.4: Met Office TRUI verification and comparison of forecasts from UKV trials, listed in table 7.3.

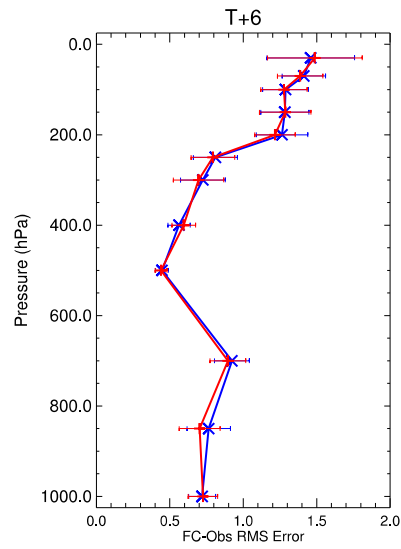
TRUI trials
LT_AO v LT_AST1
LT_AO v LT_AST2
LT_AST2 v LT_AST1

by Lange & Janjic (2016), or due to the assimilation of non-smoothed Mach temperature, which gives a lower weighting to these observations in the assimilation process.

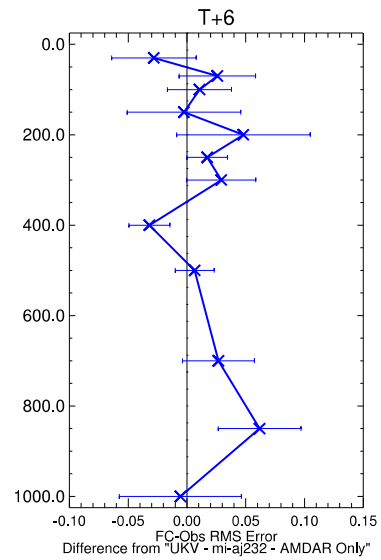
7.5 Diagnosed Observation Errors

We noted in section 2.14 (page 29) that the accurate representation of the observation error standard deviation is important for the data assimilation process. In section 7.3.3 (page 159) we showed the σ_{AOBS} profile for winds and temperature that have been used for data assimilation experiments using AMDAR and Mode-S EHS reports. In this section we investigate the correctness of the σ_{AOBS} profile for AMDAR and Mode-S EHS observations for wind and temperature. We compare the σ_{DD} profile, using the Desroziers et al. (2005) diagnosed method (section 7.2), with the σ_{AOBS} profiles shown in figure 7-1 (page 161).

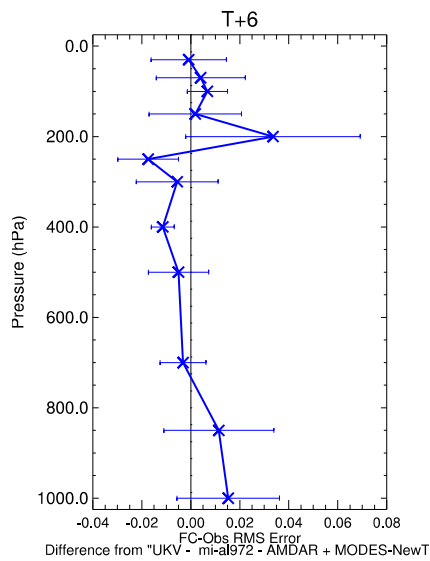
Figures 7-8 and 7-9 show the Desroziers et al. (2005) diagnosis of the observation error standard deviation profile, $\sqrt{R(i, i)}$, for AMDAR and Mode-S EHS horizontal wind components. The results are plotted at the centre of the pressure level interval. The operational UKV assumed observation error standard deviation profile is shown for comparison. The blue bars indicate the number of reports used for each pressure level interval. For Mode-S EHS the number of reports decreases steadily between 250 hPa and 950 hPa. This is expected since the shape of an SSR detection zone resembles an inverted truncated cone centred at the SSR site. Furthermore, the higher number of reports at 250 hPa is expected since this is the region where an aircraft trajectory is in its en-route phase. Moreover, in this region the number of reports will include aircraft transiting UK airspace. For AMDAR below 1000 hPa and above 200 hPa there are too few reports to interpret meaningfully the diagnosed results, similarly for Mode-S EHS. For AMDAR between 950 hPa and 550 hPa the assumed and diagnosed observation error standard deviation are similar, above 550 hPa we see the diagnosed observation error standard deviation is larger than the assumed, with greatest departure at 450 hPa. In contrast, the Mode-S EHS diagnosed observation profile is less than the assumed



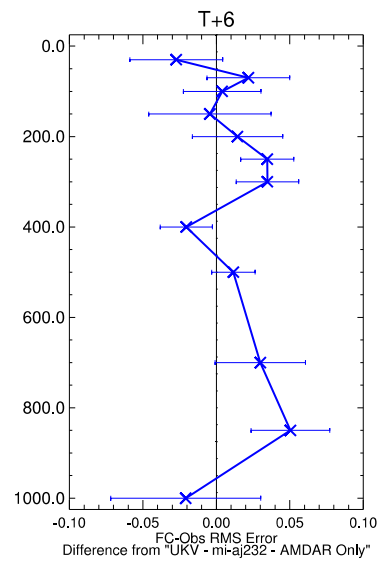
(a)



(b)

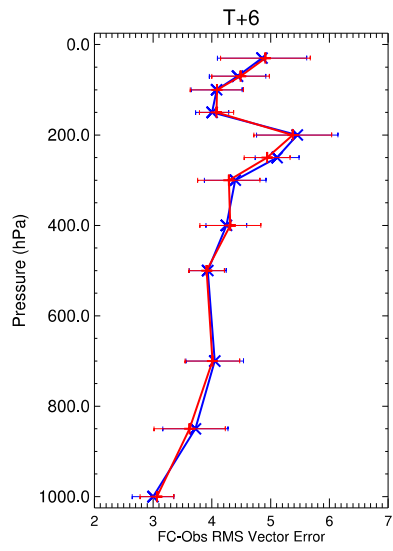


(c)

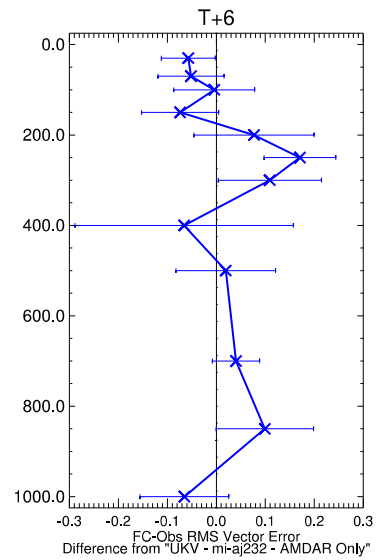


(d)

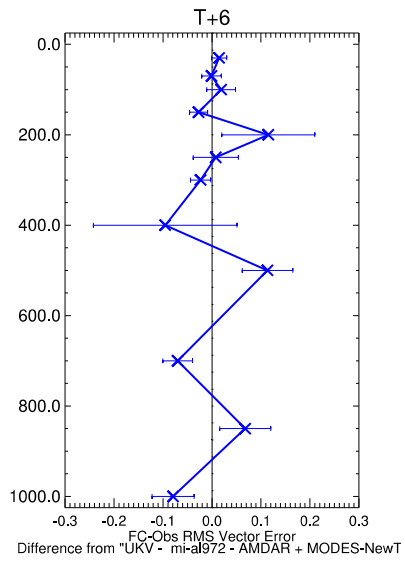
Figure 7-6: Mean RMSE of forecast vertical temperature profile against radiosonde for the trials, using the notation defined in table 7.3 (page 171), (a) LT_AO (red), LT_AST1 (blue). RMSE differences for (b) LT_AST1 – LT_AO, (c) LT_AST1 – LT_AST2 and (d) RMSE difference for LT_AST2 – LT_AO. Error bars are the standard error of the mean.



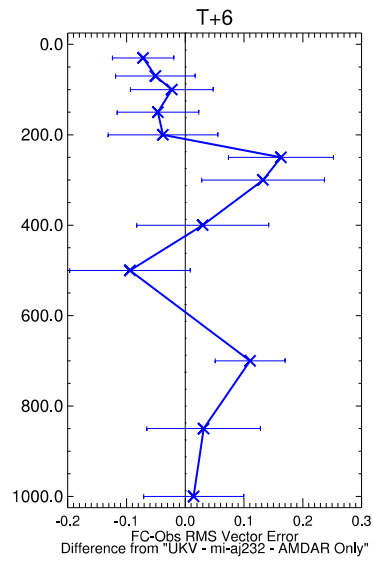
(a)



(b)



(c)



(d)

Figure 7-7: Mean RMSE of forecast vertical wind profile against radiosonde for the data assimilation trials, using the same notation given in figure 7-6.

error. However, care must be taken when interpreting these results for three reasons. Firstly, the spatial distribution of the reports differs. Mode-S EHS is concentrated in the South of England while AMDAR is distributed more widely throughout the United Kingdom. Secondly, for the trial period the weather regime in Northern England and Scotland changed when compared to Southern England. The change in weather regime in the north was due to the passage of weather fronts associated with a low pressure system near Iceland (see section 5.2). In the south, the weather regime was under the influence of a high pressure region and would have impacted on the AMDAR reports in this region. Thirdly, these results are for a limited period of time and so may not be fully representative. Furthermore the diagnosis method may under-represent the true observation error value (Waller et al. 2016).

The Desroziers et al. (2005) diagnosed σ_{DD} profile for AMDAR and Mode-S EHS temperature are shown in figure 7-10. The σ_{AOBS} profile used in the operational UKV is shown for comparison. The blue bars and their distribution is as discussed for figure 7-8 above. The σ_{DD} profile for AMDAR (fig 7-10a) between 950 hPa and 250 hPa is in good agreement with that used in the operational UKV NWP model. In contrast, the diagnosed Mode-S EHS σ_{DD} profile for temperature (fig 7-10b) is clearly greater than that used in the operational UKV NWP model, if we assume it is the same as the AMDAR values. This result suggests that we greatly underestimate the σ_{AOBS} profile for the Mode-S EHS temperature. Our result is qualitatively similar to those found by Lange & Janjic (2016) and de Haan & Stoffelen (2012) in so far that the profile of σ_{AOBS} profile increases towards the surface. But our result differs in magnitude being almost twice that found by Lange & Janjic (2016) and one-and-half times that found by de Haan & Stoffelen (2012). However, Lange & Janjic (2016) and de Haan & Stoffelen (2012) used smoothed Mode-S EHS reports.

We suggest that the diagnosed σ_{DD} profile is due to quantisation error that arises from the reduced precision of the Mode-S EHS reports used to derive Mach Temperature, we identified evidence for this effect in chapter 4 (page 55) and chapter 6 (page 147). Further research is needed to compute the Desroziers et al. (2005) diagnosis from the innovations and residuals output from the data assimilation experiments that used the ad-hoc σ_{AOBS} profile T2, for Mode-S EHS Mach temperature. However, we were unable to do this analysis for this thesis due to lack of time. But we expect the σ_{DD} profile T2 to be similar to our results for σ_{DD} profile T1. This is because while the error for the background NWP model may change, the observation error due Mode-S EHS processing appears to have the greater effect.

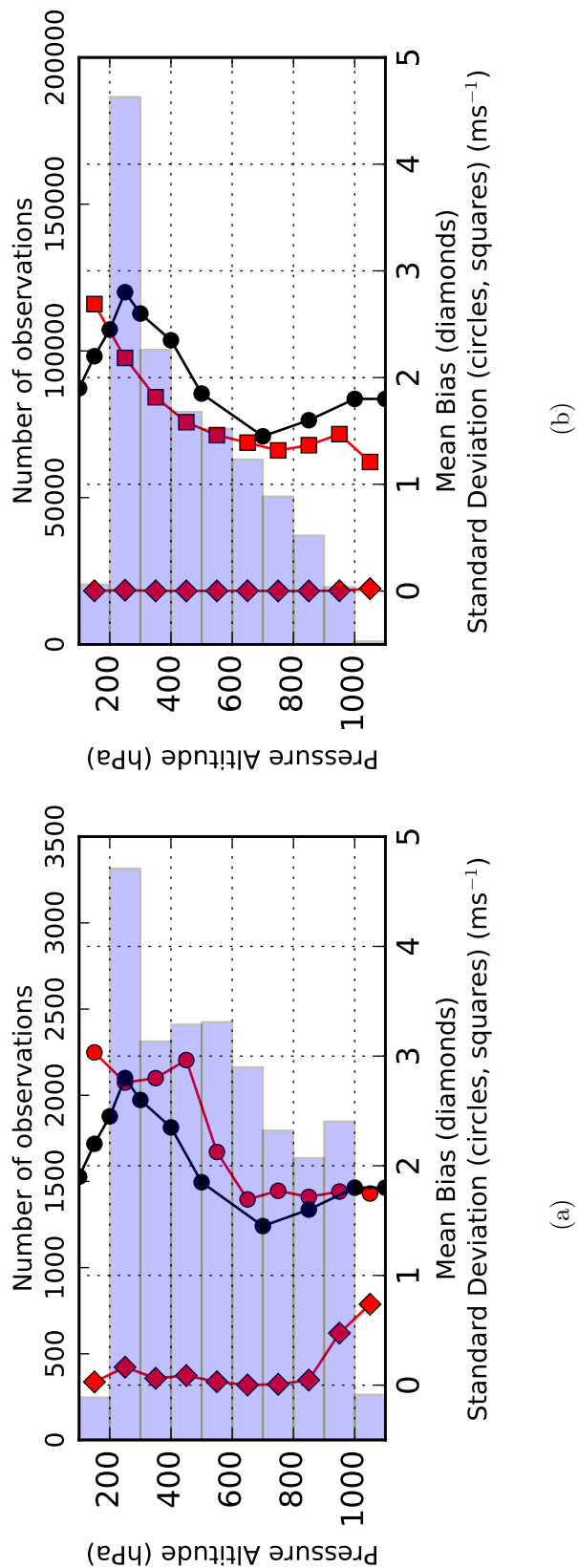
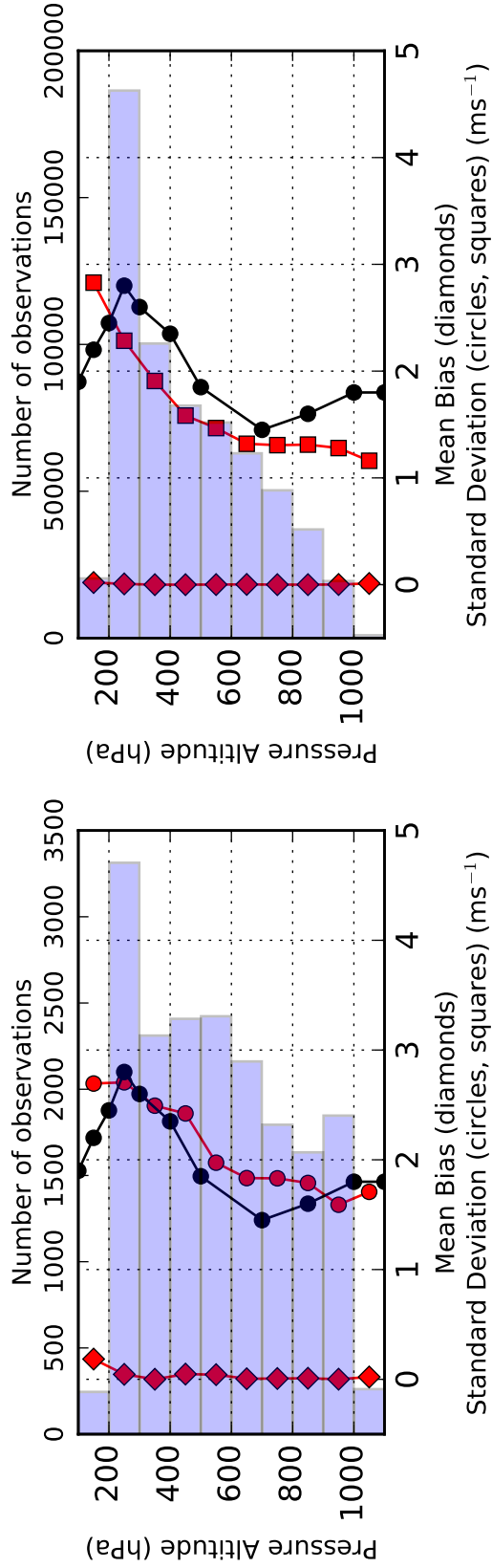


Figure 7-8: Desroziers et al. (2005) diagnosed (red) and UKV assumed (black) observation error standard deviation for horizontal u-wind components (a) AMDAR (circles) (b) Mode-S EHS (squares) for data assimilation trial LT_AST1 for the period 03Z 2nd Jan to 06Z 8th Jan 2015. Desroziers et al. (2005) diagnosed results are computed over 100 hPa intervals and plotted at the centre of the interval. Blue bars indicate the number of observation pairs used.



(a)

(b)

Figure 7-9: Destroziere et al. (2005) diagnosed (red) and UKV assumed (black) observation error standard deviation for horizontal v-wind component (a) AMDAR (b) Mode-S EHS. Keys to plots are the same as for figure 7-8.

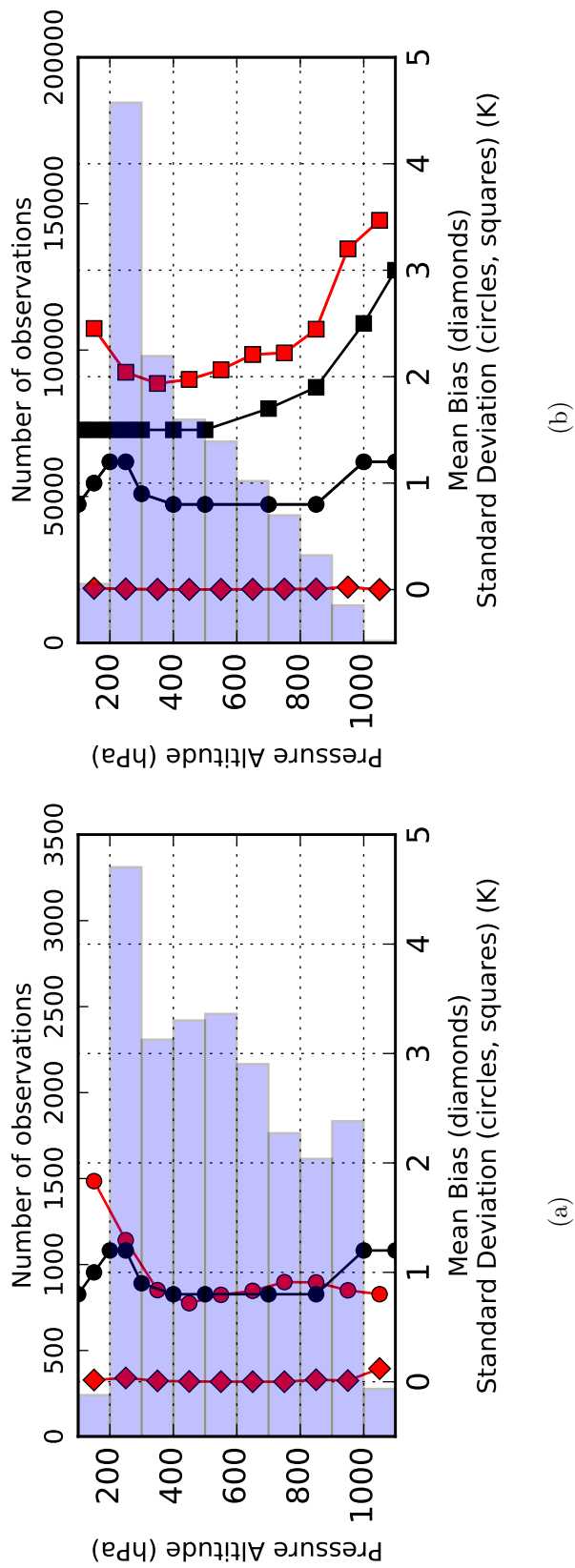


Figure 7-10: Destroziere et al. (2005) diagnosed (red) and UKV assumed (black) observation error standard deviation for temperature (a) AMDAR (circles) (b) Mode-S EHS (squares). Keys to plots are the same as for figure 7-8 (page 183).

7.6 Summary and Conclusions

In this chapter we have shown how we configured a version of the Met Office operational limited area NWP model, the UKV, to assimilate Mode-S EHS derived observations. This is the first study to evaluate the impact of using Mode-S EHS observations with the highest horizontal grid length, 1.5 km, convection-permitting NWP model .

The UKV NWP model trials used 3-D variational data assimilation with first guess at appropriate time (FGAT). The trials assimilated Mode-S EHS reports collected using the Met Office receiver network rather than these being supplied directly by an Air Traffic Management such as used by de Haan (2011). It was found that for a practical application it is necessary to spatially and temporally thin the Mode-S EHS observations. To evaluate the impact of assimilation of AMDAR observations and Mode-S EHS derived observations four trials were conducted using the period 2nd to 8th January 2015.

The results of the trials showed that the impact of assimilation of AMDAR observations within the UKV domain was beneficial but only very marginally when compared to not assimilating them. The assimilation of the thinned Mode-S EHS observations did not adversely affect the assimilation of other observation types, suggesting that the configuration of the data assimilation processing was acceptable. When wind and temperature forecasts were verified against available observations the inclusion of Mode-S EHS observations overall had a neutral impact. We note, however, that it was not possible to perform a passive assimilation of the aircraft-based observations by their type. Therefore it is difficult to draw any firm conclusion about the impact of Mode-S EHS observations. Our result differs from previous studies (Cardinali et al. 2003, de Haan & Stoffelen 2012, Lange & Janjic 2016) which show that AMDAR and Mode-S EHS observations have a positive impact on forecasts. Our results are not conclusive since we ran our trials for five days whereas previous studies have used longer trials. Moreover, we found that because of a technical limitation of the UKV NWP model data assimilation it was not possible to set-up the trials to use the same set of observations.

A key requirement for the data assimilation of the observations is an accurate representation of the assumed observation error standard deviation profile, σ_{AOBS} . To assess whether σ_{AOBS} for AMDAR, σ_{AOBS-A} , was representative we applied the Desroziers et al. (2005) diagnosis using the innovations and residuals from trials LT_AST1 and LT_AST2 for horizontal wind and temperature. We found that the diagnosed observation error standard deviation profile, σ_{DD} , for AMDAR, σ_{DD-A} , horizontal wind was of the order 10% higher than σ_{AOBS-A} . By contrast we found the σ_{DD} for Mode-S EHS, σ_{DD-S} , horizontal wind to be of the order 10% lower than σ_{AOBS-A} . The differences

in the results for σ_{AOBS} and σ_{DD} may be affected by the limited period chosen, the different spatial distributions of AMDAR and Mode-S EHS reports, and the different wind regimes that were present across the United Kingdom for this period.

When considering the results for temperature using σ_{AOBS-A} , we found that the Desroziers et al. (2005) σ_{DD-A} were in good agreement σ_{AOBS-A} . We found σ_{DD-S} for temperature to be at least twice as large as σ_{AOBS-A} . The σ_{DD-S} for temperature is similar to that seen in Mach Temperature standard deviation profiles discussed in section 4.5 (page 66) and shown in figure 4-9 (page 83), and in section 6.9.2 (page 143) and shown in figure 6-14 (page 149). Hence we suggest that σ_{DD-S} profile shows that quantisation error, that arises from the reduced precision of the Mode-S EHS reports used to derive Mach Temperature, makes the stronger contribution to the observation error.

We found that it was not possible to use all of the available Mode-S EHS observations. This was because the density of Mode-S EHS observations was too great, which may cause problems. There is a computational overhead to assimilate a large number of observations, especially if these are in close proximity to each other and reporting almost the same value, thus assimilating potentially redundant information. For example, the horizontal length scales of atmospheric phenomena measured by aircraft could be of the order 500 m at an altitude of 3000 m and 200 m near the surface. These scales are less than the UKV NWP model data assimilation, which has a horizontal grid length of 3.0 km, so the smallest length scale that it could represent is 12.0 km (Inness & Dorling 2012, Ch. 5). Furthermore, the errors in high frequency observations may be highly correlated in time and space. To minimise the effects of these problems we could either thin or combine these observations.

Thinning is a method that removes observations. For example thinning could provide a representative sample of aircraft-based observations that is commensurate with the NWP model's data assimilation horizontal grid length, e.g., one observation every 3 km for the UKV NWP data assimilation. However, thinning does not mean the observations are wholly representative since selection criteria are applied in terms of their position relative to the NWP model grid points and the time difference between observations and the NWP model integration time. Furthermore, while thinning may reduce correlated error between observations it does not reduce the random error associated with a single observation. Previous studies that have assimilated Mode-S EHS have spatially thinned Mode-S EHS observations: de Haan & Stoffelen (2012) used 6 km, half the horizontal grid length for the HIRLAM NWP model; Strajnar et al. (2015) used 25 km, six-times the horizontal grid length for the ALADIN NWP model; while Lange & Janjic (2016) used random thinning to either 10% or 50% of

the original dataset. However, these studies used thinning to reduce the computational load for data assimilation of Mode-S EHS observations rather than to account for their observation error.

For our data assimilation trials we thinned our Mode-S EHS observations. This was done in two stages. First we thinned by observation time, removing Mode-S EHS observations that were older or later than ± 30 minutes of the data assimilation analysis time. Then the resulting subset of Mode-S EHS observations were spatially thinned to one observation every 3 km and we thinned temporally to one observation every five minutes. The effect of this method of thinning reduced the number of observations to be processed by the data assimilation system to 10% of the available Mode-S EHS observations. This reduced the computational overhead to a level that was comparable to the current operational version of the UKV NWP model. However, this method removes information and the selected observations may not be representative of the atmospheric state, especially given the large observation error standard deviation for Mode-S EHS temperature below 1000 m.

The alternative to thinning is to combine observations to form a representative super-observation, such as discussed in section 3.6 (page 39). Before forming a representative super-observation, this method could remove observations with large differences, which may be unrealistic, when compared with corresponding UKV NWP model value. The method of super-observations is capable of averaging out random errors so that the error of the super-observation may be less than the error on a single observation, where random error makes the stronger contribution to the total observation error. However, any method that averages or combines observations in space and time, while reducing the computational impact on the data assimilation, also changes the scale of the meteorological phenomena that can be represented by the averaged observation, since by averaging, either in space or time or both, there is the loss of finer scale structure. Furthermore, the error characteristics of the combined observation, whether aggregated or super-observation, will differ from the error characteristics of the individual observations, e.g., a reduction in random error.

However, we note that there are no previous studies that evaluate using super-observation of aircraft-based observations. Furthermore, the assumption of uncorrelated observations errors may not apply, therefore further research would be required to evaluate the suitability of using the super-observation method. For our data assimilation trials, using the method of super-observations required non-trivial technical changes to the UKV NWP data assimilation scheme which was beyond the scope of our research.

Chapter 8

Discussion and Further Work.

Accurate observations of the atmospheric state are needed for operational meteorological forecasting and for numerical weather prediction. The need for accuracy in operational meteorology is to aid decision making especially during adverse weather conditions such as fog and low-level wind shear. The uncertainty in numerical weather predictions arises from the uncertainty in the initial conditions. The initial conditions are calculated from observations and previous forecasts, which are weighted by their respective error statistics. When the state of the atmosphere is represented by observations from measurement sensors they are subject errors. These errors may be random, correlated or systematic. These errors may be expressed in terms of their statistical properties, e.g., mean bias, standard deviation and root mean square error (Wilks 2011, Jolliffe & Stephenson 2012). These statistical properties can be used to represent the accuracy and precision of these measurements (Taylor 1982). During the past two decades, a significant source of observations of the state of the atmosphere are obtained from commercial air traffic.

In this thesis we expand on the existing body of knowledge for the utilisation of aircraft-based observations for operational meteorology and numerical weather prediction. In chapter 1 of this thesis we posed three questions which we have answered through a series of experiments, case studies and their analysis:

1. How accurately do observations derived from routine messages exchanged between an aircraft and air-traffic-control represent the state of the atmosphere in terms of the horizontal wind and ambient temperature?
2. What atmospheric phenomena within the boundary layer can be observed using high-frequency observations derived from these routine messages?
3. What benefit does assimilation of these high-frequency observations bring to the

Met Office’s convection-permitting numerical weather prediction model?

In section 8.1 we summarise the results and conclusions of our research. In section 8.2 we discuss our results in more detail. To complete our thesis, in section 8.3 we make recommendations for further areas of research investigating the utility of aircraft-based observations, as more of this observation data type becomes available.

8.1 Summary of Results and Conclusion

In this section we summarise our results as follows:

- Mode-S EHS is a new source of aircraft-based observations which can provide high frequency observations of temperature and horizontal wind, within the terminal manoeuvring area of airports.
- We developed novel error models to characterise the observation error standard deviation for Mode-S EHS horizontal wind and Mach temperature. We have shown that the standard deviation of quantisation error, which is the result of Mode-S EHS processing, makes a significant contribution to the observation error standard deviation for Mach temperature and places a lower limit on the same for horizontal wind.
- We have shown that by aggregating the high frequency observations of Mach temperature useful meteorological information can be obtained above 1000 m, e.g., the presence of elevated temperature inversions. However, we also found that below 1000 m there is greater uncertainty in the aggregated Mach temperature, which fluctuates rapidly. We showed that these fluctuations are due to the asynchronous changes in the reported Mach number and true airspeed. We showed that by applying a low-pass filter to smooth out the fluctuations the observation uncertainty can be reduced to the level of quantisation error.
- We performed trials to assimilate Mode-S EHS horizontal wind and Mach temperature using the Met Office’s UKV, a high-resolution convection-permitting NWP model. We found it was necessary to thin spatially and temporally the number of Mode-S EHS observations so that we would obtain a UKV NWP analysis that would be acceptable for use in operational meteorology. We found for our trials, 2nd to 8th January 2015, there was a neutral impact on the UKV NWP model analysis and forecasts, with lead times of six-hours, when compared with radiosonde observations. However, this result is not conclusive since we assumed

that the observation error standard deviation for Mode-S EHS and AMDAR were the same and we used non-smoothed non-aggregated observations.

- We performed a Desroziers et al. (2005) diagnosis using the observation-minus-background and observation-minus-analysis output by the UKV NWP model. We found that for AMDAR and Mode-S EHS horizontal wind the diagnosed observation error standard deviation was within 10% of the corresponding assumed observation error standard deviation. We found that for AMDAR temperature the assumed and diagnosed observation error standard deviation was in agreement but for the Mode-S EHS Mach temperature the observation error standard deviation was greater than the assumed; its magnitude similar to the magnitude obtained from our novel error model.

We conclude that Mode-S EHS has the potential for providing useful meteorological information at a frequency that is greater and for a lower cost than is currently available by AMDAR. With suitable pre-processing Mode-S EHS observations may provide benefits to operational meteorological forecasting and numerical weather prediction, particularly for rapid update forecasts with lead times of up to a few hours. However, further research is required. The results from such research may help inform the development of new aviation standards for the automated reporting of meteorological observations by commercial aircraft.

For example, to demonstrate to the aviation community that reporting meteorological observations to a higher precision would be beneficial to improving short-range high-resolution numerical weather prediction. In particular, direct reports of the higher precision temperature would be better than using the derived method of temperature based on Mach number.

8.2 Discussion of Results

Aircraft-based observations are an important source of in situ measurements (Cardinali et al. 2003, Petersen et al. 2004, Cardinali 2013, Petersen et al. 2016) of horizontal wind and ambient temperature. Currently, AMDAR (Painting 2003) is the main source of these observations. Their accuracy and precision have been subject to a number of studies (section 2.8, page 16). A newer source of observations is Mode-S EHS (de Haan 2011, Stone & Pearce 2016, Mirza et al. 2016). The advantage of Mode-S EHS are that observations can be 100-times more than AMDAR observations, and can be collected more cheaply, when compared with the cost of AMDAR reports, due to the lower cost of collection. However, the statistical properties of this observation type are poorly

understood. For numerical weather prediction, it is important that the assumed observation error standard deviation, $\sigma_{A OBS}$, is specified correctly so that during data assimilation the correct weighting of the observation can be applied.

Our thesis adds new knowledge that increases our understanding of (a) the observation error standard deviation of the horizontal wind and ambient temperature derived from Mode-S EHS reports and (b) the usefulness of these observations for operational meteorology and numerical weather prediction.

8.2.1 Quality of Mode-S EHS Reports

In our thesis we present new evidence that Mode-S EHS processing determines the quality of the observations and, therefore, the Mode-S EHS. Previous work assimilating Mode-S EHS horizontal wind data has assumed a similar observation error standard deviation to AMDAR horizontal wind (de Haan & Stoffelen 2012, Lange & Janjic 2016). However, an inflated observation error standard deviation (compared to AMDAR) has been assumed for temperature (de Haan & Stoffelen 2012, Lange & Janjic 2016). De Haan (2011) identified that the reporting precision of the Mode-S EHS Mach number and true airspeed may account for the lower quality but did not investigate this further.

In chapters 3 and 4 we developed novel models for the observation error standard deviation, which we use to answer our first thesis question on the accuracy of the Mode-S EHS observations. In contrast we use section 3.9 (page 51) that Mode-S EHS processing results in quantisation error, which arises from the rounding then truncation of the binary representation of the data. We assume that the quantisation error is uniformly distributed for each of the reports that comprise the aircraft's state vector (section 2.7, page 15). We use the statistics of the uniform distribution to estimate the precision of the Mode-S EHS observations of horizontal wind and Mach Temperature. Our assumption differs from that used by de Haan (2011) who estimated the precision by comparing the differences between two successive Mode-S EHS derived observations but makes no suggestion about how these might be distributed. However, we suggest that the de Haan (2011) method may not be robust because the Mode-S EHS processing introduces asynchronous changes in the reported Mach number and true airspeed (section 3.8, page 48). In contrast, we use in situ data recorded by the FAAM research aircraft (Smith & Gratton 2004) to validate our novel error models for Mode-S EHS observations. This is the first study to perform this type of validation for Mode-S EHS.

In chapter 4 we showed that our novel error models can be used to estimate the precision of the derived observations using the precision of the reports in the aircraft

state vector. We used the FAAM in situ data to emulate the Mode-S EHS processing (EUROCAE 2008) of the aircraft state vector prior to its broadcast. We compared the Mode-S EHS derived observations with the in situ measurements of the horizontal wind and temperature. We showed that their differences are not uniformly distributed but have the character of a uni-modal distribution. We concluded that the derived observation error standard deviation for Mode-S EHS Mach Temperature error can be modelled if we assume the precision of the input Mach number and true airspeed are represented by the standard deviation of quantisation error. Furthermore, the quantisation error statistic places a lower limit on the estimate of the derived observation error standard deviation for the Mode-S EHS horizontal wind error. The results of this study provides a more robust characterisation of the observation error standard deviation for the Mode-S EHS observations.

However, we note that we used an emulation of the Mode-S EHS processing. This was because the FAAM research aircraft is not equipped with a Mode-S EHS transponder. If a similar experiment were to be conducted using an installed Mode-S EHS transponder then we might expect a refinement our result.

8.2.2 Identifying Atmospheric Phenomena using Mode-S EHS Observations

In chapter 6 we used our knowledge and understanding gained from chapters 3 (page 33), 4 (page 55) and 5 (page 91) to answer our second thesis question, identifying atmospheric phenomena within the boundary layer using the high-frequency Mode-S EHS derived observations. We constructed vertical profiles of Mode-S EHS Mach Temperature using our method to aggregate observations from Mode-S EHS reports of Mach number and true airspeed from multiple aircraft (section 3.6, page 39). Our method of aggregation uses only the reported observations, unlike the method of super-observations (Lorenc 1981, Berger et al. 2004) which, in effect performs a local optimal interpolation between an NWP model background value and observation innovations. We use only the aggregated observations so that we can compare their meteorological information with that available from other in situ observations and the UKV NWP model forecasts.

We compared the vertical structure of the constructed profiles with observations reported by nearby AMDAR reporting aircraft and radiosonde. We showed that there is good agreement between the aggregated Mode-S EHS Mach temperature and these observations above 1000 m. However, below 1000 m we found large fluctuations in the aggregated Mode-S EHS Mach temperature. We believe that for our case study such fluctuations could not be due to the prevailing state of the atmosphere: calm

conditions, low wind speed and fog. We also compared the structure of the constructed profiles with forecasts from the UKV NWP model. (We note that the AMDAR and radiosonde reports used in our comparison were not assimilated by the UKV NWP model.) We found similar results: agreement is good above 1000 m and poor below 1000 m. Moreover, we found the constructed profiles showed the presence of an elevated temperature inversion not forecast by the UKV NWP model. We demonstrated that aggregated Mode-S EHS reports contain useful information. We investigated further the large fluctuations in Mach temperature below 1000 m.

We showed that the large fluctuations are due to the asynchronous change in the Mach number and true airspeed, which is introduced by the Mode-S EHS processing. These fluctuations are greater during ascents and descents because of the aircraft's airspeed changes. We also found an apparent bias in the derived temperatures, as there was a tendency toward cooler temperatures for ascending aircraft and warmer temperatures for descending aircraft when compared with the mean surface ambient temperature. This finding differs to that found by Petersen & Moninger (2006) who report that aircraft, equipped with an external sensor package, have a warm temperature bias for ascents and cool temperature bias for descents when compared with the NOAA Rapid Update Cycle NWP model analysis. Ballish & Kumar (2008) also suggest that aircraft temperature reports, when compared to an NWP model analysis, are subject to a mean bias which is aircraft-type specific. Clearly there remains some uncertainty over the cause of this apparent bias which requires further investigation.

We used low-pass-filters to smooth the asynchronous changes in the Mode-S EHS reports of Mach number and true airspeed. The low pass filters used were the centred-moving average, block average, linear regression and the irregular exponential filter (IRR). The first three filters use a moving window to compute a mean value. The IRR filter differs as it is a weighted mean between the current observation and mean of the of past observations. We found all these filters produced similar results for the resulting mean Mach temperature and reduced its variance by at most 30%. The average time difference between reports is 2 s and the maximum time difference is 6 s. The moving window filters used five reports. Therefore the sampling times can range between 10 s and 30 s respectively. These sampling times are comparable with AMDAR reports, which uses a moving window of 10 s (Painting 2003) and the low pass filter used by de Haan (2011), which used a moving window of 12 s for ascents and descents. The horizontal sampling length scales of atmospheric processes which these sampling times correspond to range from 0.5 km to 4.5 km. Thus the smoothed Mode-S EHS reports provide observations that are comparable to the 3.0 km horizontal grid length for data assimilation using the UKV NWP model. Useful meteorological information would be

contained within at least four times this horizontal scale (Inness & Dorling 2012, p. 87). Moreover, we found the observation error standard deviation for the smoothed aggregated observations of Mach temperature could be modelled using our novel error model developed in chapter 4.

8.2.3 Assimilation Experiments using Mode-S EHS Observations

In chapter 7 we addressed our third thesis question, the benefit of using Mode-S EHS observations in a convection-permitting numerical weather prediction model. We configured a version of the Met Office’s operational limited area NWP model, the UKV, to assimilate Mode-S EHS derived observations for the case study period 2nd to 8th January 2015. This is the first study to evaluate the impact of using Mode-S EHS observations with such a short horizontal grid length, 1.5 km, convection-permitting NWP model. De Haan & Stoffelen (2012) performed their data assimilation trials using the HIRLAM 11 km NWP model while Lange & Janjic (2016) trials used the COSMO-KENDA 4.4 km ensemble prediction system. However, our data assimilation trials were only for a period of six days therefore our initial results should be treated with caution.

In order to achieve a practical configuration of the UKV NWP model it was necessary to spatially and temporally thin the Mode-S EHS observations, otherwise the data assimilation processing would not converge to an acceptable analysis for use in operational weather forecasts. Thus we assimilated only Mode-S EHS observations reported ± 30 minutes of the analysis time and then spatially thinned these reports to one observation every 3 km horizontally. This reduced the number of Mode-S EHS observations at each assimilation cycle to around 10% of those available, e.g., at 1200 UTC there are up to 300,000. The number of observations we used is comparable to that used by de Haan & Stoffelen (2012) and Lange & Janjic (2016).

Our data assimilation trials used Mode-S EHS horizontal wind and temperature directly. For technical reasons we did not implement the low pass filters discussed in section 6.5. The horizontal wind was corrected using the Jacobs et al. (2014) method, which estimates the aircraft heading error using an NWP model, in our case the operational UKV. The results of our data assimilation showed that assimilating Mode-S EHS has a neutral impact on the UKV NWP model analysis and forecasts with lead times of up to six hours, when compared to radiosonde observations. This contrasts with the results obtained by de Haan & Stoffelen (2012) and Lange & Janjic (2016). De Haan & Stoffelen (2012) found improvement in the short range forecasts of horizontal wind and temperature with lead times of up to three hours. Results were similar for Lange & Janjic (2016), who showed improvements were mostly above 1000 m.

However, our results are not conclusive since we only performed our experiments over six days. In our configuration the assumed observation error standard deviation for Mode-S EHS and AMDAR were the same; we did not use smoothed Mode-S EHS reports; our experiments included the full range of observations types used for operational data assimilation in the UKV NWP model; and the meteorological conditions were calm, i.e., changing slowly over the six days, for the region where Mode-S EHS reports were collected. Using the non-smoothed Mode-S EHS and the assumed observation error standard deviation for AMDAR may have resulted in these observations being given a lower weighting in the data assimilation processing, especially if the observation-minus-background for Mach temperature is large.

We also investigated our assumption to use the same assumed observation error standard deviation for Mode-S EHS and AMDAR. For the horizontal wind de Haan & Stoffelen (2012) and Lange & Janjic (2016) used the same assumed observation error standard deviation for Mode-S EHS and AMDAR. For Mode-S EHS Mach temperature they used an inflated assumed observation error standard deviation for AMDAR temperature. We used the observation-minus-background and observation-minus-analysis output by the UKV NWP model to obtain the Desroziers et al. (2005) diagnosed observation error standard deviation for Mode-S EHS and AMDAR. Our analysis showed that for AMDAR horizontal wind the diagnosed observation error standard deviation was approximately 10% greater than the assumed observation error standard deviation, while for Mode-S EHS it was approximately 10% less. This result suggests that the quality of the observations for AMDAR and Mode-S EHS, after applying heading corrections, are similar. For temperature, we found that for AMDAR assumed and diagnosed observation error standard deviation are in agreement. However, we found that diagnosed observation error standard deviation for Mode-S EHS Mach temperature to be greater than the assumed observation error standard deviation. The vertical profile of diagnosed observation error standard deviation for Mach temperature was found to have similar characteristics of our result from chapter 4. We conclude from this result that the standard deviation of quantisation error makes a strong contribution to the Mach temperature observation error. This result is in contrast with Lange & Janjic (2016) who found diagnosed observation error standard deviation to be less than the assumed observation error standard deviation used by de Haan & Stoffelen (2012).

8.3 Further work

The results from the data assimilation experiments conducted in chapter 7 are not conclusive with respect to assessing the benefit of aircraft-based observations of tem-

perature and horizontal wind for both Mode-S and AMDAR. We suggest that further research is needed to:

- **Investigate further the benefits of assimilating Mode-S EHS observations in the Met Office UKV NWP Model**

To configure the UKV NWP Model to run longer data assimilation trials. These trials should be representative of the climatology of the UKV, thus trials of at least 30 consecutive days covering a summer and winter period are suggested. These trials should use Mode-S EHS reports collected by the entire Met Office receiver network. Conducting longer trials also affords the opportunity to re-apply the Desroziers et al. (2005) diagnostic method to affirm our results. An extension to this work would be to test the sensitivity of the results of the diagnostic to the choice of background error covariance matrix.

- **Investigate the use of super-observations**

The data assimilation configuration of the UKV, and other studies, suggest that Mode-S EHS observations should be thinned to around 10%. The study by Lange & Janjic (2016) also showed that too many Mode-S EHS observations may cause saturation, i.e., where additional observations beyond a certain fraction of the total do not improve the NWP analysis.

Further work to assess using aggregated observations or super-observations may afford a way to utilise more of the available observations. In addition, implementation of a low-pass filter to smooth reports along aircraft trajectories requires further investigation. This may reduce some of the uncertainty in the derived observations for operational meteorological forecasting and numerical weather prediction.

- **Investigate further the observation error standard deviation for Mode-S EHS derived observations using data from the FAAM research aircraft**

There may be a further opportunity to study the observation errors for Mode-S EHS derived observations. From 2018 all aircraft operating within European airspace will be required to be equipped with a Mode-S transponder. Thus the FAAM aircraft will have a Mode-S transponder, which will receive its input from the aircraft's flight management system.

This investigation could also assess the space-time length scales that could be represented by using smoothed and non-smoothed Mode-S EHS reports of Mach

number and true airspeed. Such further work may investigate the origin of aircraft temperature biases and their correction; derive more refined methods to correct for aircraft heading errors; and investigate the effects of correlated error resulting from the increased temporal resolution of the meteorological observations.

- **Investigate correlated error in aircraft-based observations**

It has been suggested by Carrière & Autonés (2001) that high frequency aircraft-based observations may have correlated errors. Given that Mode-S EHS observations are reported with high frequency we can suppose that these may be subject to correlated error in space and time. Methods used to account for correlated error range from spatial and temporal thinning, e.g., such as used by Lange & Janjic (2016), aggregated-observations or super-observations performed over small areas (Berger et al. 2004) or inflation of the assumed observation error standard deviation (Stewart et al. 2013). The Desroziers et al. (2005) diagnostic could be used to estimate the spatial correlations and hence evaluate whether the chosen thinning distance is appropriate (Waller et al. 2016a).

Appendix A

Symbols and Abbreviations

Symbol	Units	Comment
<i>ARINC</i>		Subscript used to indicate that the observation was derived using the precision-level of ARINC reports.
<i>MODES</i>		Subscript used to indicate that the observation was derived using the precision-level of Mode-S reports.
<i>REF</i>		Subscript used to indicate that the measurement was obtained from the FAAM's measuring instruments
<i>MB</i>		Mean bias of the sample.
<i>RMSE</i>		Root Mean Square Error of the sample.
<i>RMSVE</i>		Root Mean Square Vector Error of the sample.
ϵ		Precision of measurement or quantisation step.
η		general symbol used to represent atmospheric phenomenon.
γ	none	Ratio of the constants for dry air at constant volume and constant pressure under International Standard Atmosphere conditions.
λ	degrees	Geographic longitude.
ϕ	degrees	Geographic latitude.
μ		Mean value of the sample.
σ		Standard deviation of the sample.
$\delta\sigma$		Standard error of the standard deviation.
σ_e		Standard error of the mean.

Symbol	Units	Comment
σ_{AOBS}		Assumed observation error standard deviation for data assimilation.
σ_{DD}		Desroziers diagnosed observation error standard deviation.
dh	m	Altitude bin width for aggregated observations.
dz	m	Change in altitude.
dT	K	Change in ambient temperature.
dt	K	Change in time.
Γ	Km^{-1}	Environmental lapse rate.
θ_A	radians	True heading measured clockwise from geographic North of the aircraft's air vector.
θ_G	radians	Ground heading measured clockwise from geographic North of the aircraft's air vector.
θ_R	radians	Rotation of aircraft about its longitudinal axis, clockwise is positive.
θ_{mag}	radians	Magnetic direction measured clockwise from magnetic North.
θ_{var}	radians	Magnetic variation which is the difference between true heading and magnetic North, $\theta_A - \theta_{mag}$.
θ_{dev}	radians	Magnetic deviation is the compass error and represents the angular difference between the true heading and compass-heading.
ξ	-	A general symbol used to represent a meteorological phenomenon.
f	-	FAAM flight number.
k	-	positive integer counter
o_i		The i^{th} derived observation from Mode-S.
r_i		The i^{th} reference observation recorded by the FAAM instruments.
m		number of binary bits, where $m < n$.
n		number of binary bits.
t	seconds	Unit of time.
t_s	seconds	Sampling Period.
A	ms^{-1}	Local speed of sound in air.

Symbol	Units	Comment
A_0	ms^{-1}	Local speed of sound in air at the Earth's surface under International Standard Atmosphere conditions.
$C(t)$	none	Time varying continuous waveform.
C_{max}		Magnitude of the maximum of the time varying continuous waveform.
$D(t)$	none	Time varying discrete waveform.
$S(t)$	none	Sample of the time varying continuous waveform at time t.
$Z_n(t)$		digitised value of the varying waveform at time t.
$Z_m(t)$		truncated value of the digitised value at time t.
M	none	Mach number.
N_f	none	The total number of observation and reference pairs that passed quality control for FAAM flight f .
P_0	hPa	Static pressure at the Earth's surface under International Standard Atmosphere conditions..
P_S	hPa	Static pressure.
P_T	hPa	Total pressure.
Q	hPa	Dynamic pressure, i.e., the pitot-static pressure difference, $P_T - P_S$.
R_a	$\text{JKg}^{-1}\text{K}^{-1}$	Characteristic gas constant for dry air for the International Standard Atmosphere.
T_b	K	Ambient temperature at the base of a temperature inversion layer.
T_t	K	Ambient temperature at the top of a temperature inversion layer.
T_s	K	Strength of a temperature inversion layer.
T_A	K	Ambient temperature.
T_0	K	Ambient temperature at the Earth's surface under International Standard Atmosphere conditions.
T_{Mach}	K	Mach temperature, ambient temperature derived from Mode-S reports.

Symbol	Units	Comment
T_{REF}	K	Reference temperature, ambient temperature measurements recorded by the FAAM's de-iced temperature sensor.
U	ms^{-1}	Zonal component of the horizontal wind vector.
V	ms^{-1}	Meridional component of the horizontal wind vector.
\mathbf{V}_A		Aircraft's air vector.
\mathbf{V}_G		Aircraft's ground vector.
\mathbf{V}_W		Horizontal wind vector from which the wind blows, direction measured clockwise from geographic North
V_A	ms^{-1}	True airspeed relative to the surrounding air of the aircraft's air vector.
V_G	ms^{-1}	Ground speed relative to the Earth's surface of the aircraft's ground vector.
V_{ws}	ms^{-1}	Wind speed, magnitude of the wind vector.
V_{wd}	degrees	Meteorological wind direction, direction of the wind vector from which the wind blows and measured clockwise from geographic North.
ΔM	none	Mach number precision.
ΔT	none	Estimated precision in the Mach Temperature.
ΔU	ms^{-1}	Estimated precision in the zonal component of the horizontal wind vector.
ΔV	ms^{-1}	Estimated precision in the meridional component of the horizontal wind vector.
ΔV_A	ms^{-1}	True airspeed precision.
ΔV_G	ms^{-1}	Ground speed precision.
$\Delta \theta_A$	radians	True heading precision.
$\Delta \theta_G$	radians	Ground heading precision.
z	m	Altitude above mean sea level.
z_d	m	Depth of a temperature inversion layer.
z_b	m	Altitude of the base of a temperature inversion layer.
z_t	m	Altitude of the top of a temperature inversion layer.

Acronyms	Comment
3-D Var	Three dimensional variational data assimilation.
ACARS	Aircraft Communications Addressing and Reporting System. A digital datalink system provided by ARINC and SITA, for transmission of short messages between aircraft and ground stations via radio or satellite. ACARS is also a message format transmitted to the ground using ARINC 620 protocol
ADS-B	Automatic Dependent Surveillance - Broadcast mode. Part of the secondary surveillance radar system which broadcasts automatically a limited set of aircraft state parameters among which are altitude, latitude, longitude.
AIREP	Pilot report of a meteorological observation or event, also called a PIREP.
ALADIN	a numerical weather prediction model.
AMDAR	Aircraft Meteorological Data Relay program. A system for reporting the state of the atmosphere which uses an aircraft's existing instrumentation.
ANSP	Air Navigation Service Provider.
ARINC	Aeronautical Radio Incorporated, a communications service provider. Develops and maintains standards for the distribution of aircraft state parameters between subsystems on the aircraft, between aircraft and between aircraft and the ground.
ARINC-429	A standard used for the exchange of data between an aircraft's subsystems.
AROME	a numerical weather prediction model.
ATM	Air Traffic Management.
COPE	Convective Precipitation Experiment. A series of flights conducted by FAAM to investigate convective conditions.
COSMO	Consortium for small scale modelling, a numerical weather prediction model.
DA	Data Assimilation is a statistical method used to combine observations and NWP model data.
E-AMDAR	EUMETNET-AMDAR (E-AMDAR) Programme serves EUCOS requirements for upper air measurements of wind and temperature and to maximize the efficiency/cost ratio of implementing AMDAR systems for EUMETNET.
EGKK	ICAO airport identifier used for the London Gatwick domain.

Acronyms	Comment
EGLL	ICAO airport identifier used for the London Heathrow domain.
EUMETNET	European Meteorological Network
ECMWF	European Centre for Medium Range Weather forecasting.
EUCOS	EUMETNET Composite Observing System
FMS	Flight Management System, used to control the motion of the aircraft.
FGAT	First Guess at Appropriate Time.
FAAM	Facility for Atmospheric Airborne Measurements.
GPS	Global Positioning System. Uses a constellation of low-earth orbit satellites to provide an accurate position report at the Earth's surface.
HARMONIE	
HIRLAM	High Resolution Limited Area Model, a numerical weather prediction model.
HRRR	High Resolution Rapid Refresh, a numerical weather prediction model which updated at least once every hour.
WGS84	World Geodetic System 1984 (WGS84) which defines the reference ellipsoid for the Earth's surface for navigation co-ordinates, altitude and mean sea level.
ICAO	International Civil Aviation Authority, an executive agency of the United Nations which encourages and co-ordinates co-operation between air navigation service providers, airlines, airframe manufacturers and aircraft equipment. Develops and maintains standards for the measurement, collection, transmission and exchange of aircraft state parameters for operational air navigation.
INS	Inertial Navigation System. Uses the Earth's rotation to fix a geographic position at the surface.
ISA	International Standard Atmosphere as defined by ICAO Technical Report Document 7488
ISMAR	International Sub-millimetre Airborne Radiometer calibration flight.
LIDAR	Light detection and Ranging.
LLJ	Low-level jet.
LAM	Limited Area Model.
LTMA	London Terminal Manoeuvring Area
MetDB	Met Office Meteorological Observations Database.
MDCRS	Meteorological Data Collection and Reporting System is the United States AMDAR programme.

Acronyms	Comment
MODE-A	The capability of the secondary surveillance radar to request an aircraft's identification code.
MODE-C	The capability of the secondary surveillance radar to request aircraft's altitude altitude.
Mode-S	Mode-Select. The capability of the secondary surveillance radar to request aircraft state parameters from an aircraft.
Mode-S EHS	Mode-Select Enhanced. The capability of the secondary surveillance radar to request parameters for an aircraft's state vector. A subset of these parameters are true airspeed, magnetic heading, ground speed, ground heading, Mach number and additional data such as MRAR. This is sometimes referred to as Mode-S Extended Squitter or 1090 MHz Squitter.
Mode-S ELS	Mode-Select Elementary. The capability of the secondary surveillance radar to request parameters for an aircraft's state vector. A subset of these parameters are true airspeed, magnetic heading, ground speed, ground heading, Mach number and additional data such as MRAR. This is sometimes referred to as Mode-S Extended Squitter or 1090 MHz Squitter.
Mode-S MRAR	Meteorological Routine Air Report which may be sent as part of Enhanced Mode-Selective. The capability of the secondary surveillance radar to request meteorological state parameters such as ambient temperature and horizontal wind vector.
NATS	National Air Traffic Services, the air navigation service provider for the United Kingdom.
NCAS	National Centre for Atmospheric Science, United Kingdom.
NCEP	National Centre for Environmental Prediction, United States of America.
NMS	National Meteorological Service, the service provider for the national or region's weather service.
NOAA	National Oceanic and Atmospheric Administration.
NWP	Numerical Weather Prediction. A numerical model of the atmosphere which when integrated forward in time generate forecasts of the atmospheric state, for example, temperature, wind, cloud.
OPS	Observation Processing System, Met Office application used to pre-process observations prior to data assimilation.

Acronyms	Comment
PIREP	Pilot report of a meteorological observation or event, also called an AIREP.
RASS	Radio acoustic sounding system.
RMSE	Root mean square error.
SD	Standard deviation.
SEVIRI	Spinning Enhanced Visible and InfraRed Imager.
SODAR	Sonic Detection and Ranging.
SSR	Secondary Surveillance Radar.
SYNOP	Surface Observations.
TAMDAR	Tropospheric Airborne Meteorological Data Reporting, an integrated sensor suite and satellite communications system (Iridium) package for installation on regional aircraft which typically do not have airtoground communications or highquality sensors.
TRUI	TRials User Interface, Met Office software application used to quantify the performance of NWP models.
UK	United Kingdom.
UKV	Met Office limited area NWP model for the United Kingdom.
UKV-ps37	Development version of the Met Office UKV - parallel suite (ps) number 37.
UM	Unified Model, a numerical weather prediction model.
UTC	Universal Coordinated Time.
WMO	World Meteorological Organisation, an executive agency of the United Nations which encourages and co-ordinates co-operation between national meteorological and hydrological organisations, in addition develops and maintains standards for the measurement, collection, transmission and exchange of meteorological observations for operational meteorology and climate monitoring.
WTR	Wind and temperature radar
WMO ABO	Aircraft-Based Observations. An international effort within the World Meteorological Organization (WMO) to coordinate the collection of environmental observations from commercial aircraft.

Bibliography

- AEEC (2004), Mark 33 Digital Information Transfer System (DITS) Part 1 Functional Description, Electrical Interface, Label Assignments And Word Formats ARINC Specification 429 Part 1-17, Technical report, Airlines Electronic Engineering Committee.
- Andreas, E. L., Claffy, K. J. & Makshtas, A. P. (2000), ‘Low-Level Atmospheric Jets And Inversions Over The Western Weddell Sea’, *Boundary-Layer Meteorology* **97**(3), 459–486.
- Applanix (2006), POS AV V5 Installation and Operation Guide, Technical report, Applanix Corporation.
- Arakawa, A. & Lamb, V. R. (1977), ‘Computational Design of the Basic Dynamical Processes of the UCLA General Circulation Model’, *Methods in Computational Physics: Advances in Research and Applications* **17**, 173 – 265.
- Baldauf, M., Seifert, A., Färstner, J., Majewski, D., Raschendorfer, M. & Reinhardt, T. (2011), ‘Operational Convective-Scale Numerical Weather Prediction with the COSMO Model: Description and Sensitivities’, *Monthly Weather Review* **139**(12), 3887–3905.
- Ball, M., Barnhart, C., Nemhauser, G. & Odoni, A. (2007), Chapter 1 Air Transportation: Irregular Operations and Control , in C. Barnhart & G. Laporte, eds, ‘Transportation’, Vol. 14 of *Handbooks in Operations Research and Management Science*, Elsevier, pp. 1 – 67.
- Ballard, S. P., L., Z., Simonin, D. & C., J.-F. (2016), ‘Performance of 4-D Var NWP-based nowcasting of precipitation at the Met Office for summer 2012’, *Quarterly Journal of the Royal Meteorological Society* **142**(694), 472–487.

- Ballard, S. P., Mirza, A. K., Maycock, A., Stone, E. K., Dance, S. L., Kelly, G., Dow, G. & Rooney, G. G. (2017), Report on Extended Trial of Mode-S EHS data in UKV., Technical report, Met Office, Exeter, United Kingdom.
- Ballard, S. P., Zhihong, L., Simonin, D., Buttery, H., Charlton-Perez, C., Gaussiat, N. & Hawkness-Smith, L. (2012), ‘Use Of Radar Data In NWP-Based Nowcasting In The Met Office’, *IAHS-AISH Publication* **351**, 336–341.
- Ballish, B. A. & Kumar, V. K. (2008), ‘Systematic Differences in Aircraft and Radiosonde Temperatures Implications for NWP and Climate Studies’, *Bulletin of the American Meteorological Society* pp. 1689–1707.
- Bannister, R. N. (2008), ‘A review of forecast error covariance statistics in atmospheric variational data assimilation. I: Characteristics and measurements of forecast error covariances’, *Quarterly Journal of the Royal Meteorological Society* **134**(637), 1951–1970.
- Barnhart, C., Fearing, D., Odoni, A. & Vaze, V. (2012), ‘Demand and capacity management in air transportation’, *EURO Journal on Transportation and Logistics* **1**(1), 135–155.
- Barry, R. G. & Chorley, R. J. (2009), *Atmosphere, Weather And Climate*, Routledge.
- Begueret, J. B., Mariano, A. & Dallet, D. (2008), High-Speed A/D; D/A conversion: A survey, in ‘Bipolar/BiCMOS Circuits and Technology Meeting, 2008. BCTM 2008. IEEE’, pp. 260–264.
- Bell, R. S., Dalby, T. D., Li, D. & Saunders, F. W. (1999), The autumn 1999 global data assimilation upgrade package forecasting research technical report no. 280, Technical report, Met Office.
- Benjamin, S. G. & Schwartz, B. E. (1999), ‘Accuracy Of ACARS Wind And Temperature Observations Determined By Collocation’, *Weather and Forecasting* **14**, 1032–1038.
- Benjamin, S. G., Weygandt, S. S., Brown, J. M., Hu, M., Alexander, C. R., Smirnova, T. G., Olson, J. B., James, E. P., Dowell, D. C., Grell, G. A., Lin, H., Peckham, S. E., Smith, T. L., Moninger, W. R., Kenyon, J. S. & Manikin, G. S. (2016), ‘A North American Hourly Assimilation and Model Forecast Cycle: The Rapid Refresh’, *Monthly Weather Review* **144**(4), 1669–1694.
- Bennett, W. R. (1948), ‘Spectra of quantized signals’, *Bell System Technical Journal* **27**(3), 446–472.

- Berger, H., Forsythe, M., Eyre, J. & Healy, S. (2004), A Superobbing scheme for Atmospheric Motion Vectors, Technical report, Met Office Forecasting Research Technical Report No. 451.
- Blackader, A. K. (1957), ‘Boundary Layer Wind Maxima And Their Significance For The Growth Of Nocturnal Inversions.’, *Bulletin of the American Meteorological Society* **38**, 283–290.
- Boisvert, R. & Orlando, V. (1993), ADS-Mode S system overview, *in* ‘Digital Avionics Systems Conference, 1993. 12th DASC., AIAA/IEEE’, pp. 104–109.
- Bormann, N. & Bauer, P. (2010), ‘Estimates of spatial and interchannel observation-error characteristics for current sounder radiances for numerical weather prediction. I: Methods and application to ATOVS data’, *Quarterly Journal of the Royal Meteorological Society* **136**(649), 1036–1050.
- Bormann, N., Bonavita, M., Dragani, R., Eresmaa, R., Matricardi, M. & McNally, A. (2016), ‘Enhancing the impact of IASI observations through an updated observation-error covariance matrix’, *Quarterly Journal of the Royal Meteorological Society* **142**(697), 1767–1780.
- Bormann, N., Collard, A. & Bauer, P. (2010), ‘Estimates of spatial and interchannel observation-error characteristics for current sounder radiances for numerical weather prediction. II: Application to AIRS and IASI data’, *Quarterly Journal of the Royal Meteorological Society* **136**(649), 1051–1063.
- Boutle, I. A., Finnenkoetter, A., Lock, A. P. & Wells, H. (2016), ‘The London Model: forecasting fog at 333 m resolution’, *Quarterly Journal of the Royal Meteorological Society* **142**(694), 360–371.
- Brockwell, P. & Davis, R. (2002), *Introduction to Time Series and Forecasting*, Springer Texts in Statistics, Springer New York.
- Brown, P. R. A. (2004a), Turbulence Probe: Flow Angle and TAS Calibration, Technical report, Facility for Airborne Atmospheric Measurements.
- Brown, R. (2004b), *Smoothing, Forecasting and Prediction of Discrete Time Series (Reprint)*, Dover Phoenix Editions, Dover Publications.
- Brown, R. & Roach, W. T. (1976), ‘The physics of radiation fog: II – a numerical study’, *Quarterly Journal of the Royal Meteorological Society* **102**(432), 335–354.

- Cardinali, C. (2013), *Observation Influence Diagnostic of a Data Assimilation System*, Springer Berlin Heidelberg, Berlin, Heidelberg, pp. 89–110.
- Cardinali, C., Isaksen, L. & Andersson, E. (2003), ‘Use and Impact of Automated Aircraft Data in a Global 4D-Var Data Assimilation System’, *Monthly Weather Review* **131**, 1865–1877.
- Carlberg, S. R. (2012), The EUMETNET AMDAR Optimization Program (E-ADOS) - A Component of the E-AMDAR Programme, Technical report, WMO AMDAR Panel Newsletter.
- Carrière, J.-M. & Autonés, F. (2001), ‘Evaluation of a wind/temperature nowcasting model using aircraft data for the benefit of air traffic management’, *Meteorological Applications* **8**(2), 177–188.
- Civil Aviation Authority (2013), CAP 562 Civil Aircraft Airworthiness Information and Procedures, Chapter 34, Navigation Leaflet 34-10 Compass Base Surveying and Leaflet 34-20 Compasses, Technical report, Safety and Airspace Regulation Group, Civil Aviation Authority, United Kingdom.
- Civil Aviation Authority (2014), CAP 760 Air Traffic Services Safety Requirements, Technical report, Civil Aviation Authority, United Kingdom.
- Civil Aviation Authority (2015*a*), Environmental Research and Consultancy Department Report 1501 Noise Exposure Contours for Heathrow Airport 2014, Technical report, Department for Transport.
- Civil Aviation Authority (2015*b*), Environmental Research and Consultancy Department Report 1502 Noise Exposure Contours for Gatwick Airport 2014, Technical report, Department for Transport.
- Civil Aviation Authority (2016), United Kingdom Aeronautical Information Publication AIRAC 7/2016 (Part 2) – Effective Date: 23 JUNE 2016, Technical report, National Air Traffic Services.
- Clark, P., Roberts, N., Lean, H., Ballard, S. P. & Charlton-Perez, C. (2016), ‘Convection-permitting models: a step-change in rainfall forecasting’, *Meteorological Applications* **23**(2), 165–181.
- Collard, A., Hilton, F., Forsythe, M. & Candy, B. (2011), ‘From Observations to Forecasts Part 8: The use of satellite observations in numerical weather prediction’, *Weather* **66**(2), 31–36.

- Collinson, R. P. G. (2011), *Introduction to Avionics Systems*, third edn, Springer.
- Courtier, P., Andersson, E., Heckley, W., Vasiljevic, D., Hamrud, M., Hollingsworth, A., Rabier, F., Fisher, M. & Pailleux, J. (1998), ‘The ECMWF implementation of three-dimensional variational assimilation (3D-Var). I: Formulation’, *Quarterly Journal of the Royal Meteorological Society* **124**(550), 1783–1807.
- Daley, R. (1991), *Atmospheric Data Analysis*, Cambridge Atmospheric and Space Science Series, Cambridge University Press.
- Dance, S. L. (2004), ‘Issues In High Resolution Limited Area Data Assimilation For Quantitative Precipitation Forecasting ’, *Physica D: Nonlinear Phenomena* **196**(12), 1–27.
- Davies, T., Cullen, M. J. P., Malcolm, A. J., Mawson, M. H., Staniforth, A., White, A. A. & Wood, N. (2005), ‘A new dynamical core for the Met Office’s global and regional modelling of the atmosphere’, *Quarterly Journal of the Royal Meteorological Society* **131**(608), 1759–1782.
- de Haan, S. (2011), ‘High-resolution wind and temperature observations from aircraft tracked by Mode-S EHS air traffic control radar’, *Journal of Geophysical Research: Atmospheres* **116**(D10).
- de Haan, S. (2013), An improved correction method for high quality wind and temperature observations derived from Mode-S EHS. Technical report TR-338, Technical Report TR-338, Royal Netherlands Meteorological Institute, De Bilt, Netherlands.
- de Haan, S. (2015), ‘Estimates of Mode-S EHS aircraft derived wind observation errors using triple collocation’, *Atmospheric Measurement Techniques Discussions* **8**, 12633–12661.
- de Haan, S. & Stoffelen, A. (2010), Assimilation Of High Resolution Mode-S EHS Wind And Temperature Observations In A Limited Area NWP Model, Scientific Report 2010-03, KNMI, Netherlands.
- de Haan, S. & Stoffelen, A. (2012), ‘Assimilation of High-Resolution Mode-S EHS Wind and Temperature Observations in a Regional NWP Model for Nowcasting Applications’, *Weather and Forecasting* **27**(4), 918–937.
- de Leege, A. M. P., Van Paassen, M. M. & Mulder, M. (2012), ‘Using Automatic Dependent Surveillance-Broadcast for Meteorological Monitoring’, *Journal of Aircraft* **50**(1), 249–261.

- de Villiers, M. P. & White, D. (2014), ‘Near-surface winds and wind shear at four airports during the St Jude’s day storm’, *Weather* **69**(11), 288–294.
- Desroziers, G., Berre, L., Chapnik, B. & Poli, P. (2005), ‘Diagnosis of observation, background and analysis-error statistics in observation space’, *Quarterly Journal of the Royal Meteorological Society* **131**(613), 3385–3396.
- Drue, C., Frey, W., Hoff, A. & Hauf, T. (2008), ‘Aircraft Type-Specific Errors In AMDAR Weather Reports From Commercial Aircraft’, *Quarterly Journal of the Royal Meteorological Society* **134**, 229–239.
- Drue, C., Hauf, T. & Hoff, A. (2010), ‘Comparison of Boundary-Layer Profiles and Layer Detection by AMDAR and WTR/RASS at Frankfurt Airport’, *Boundary-Layer Meteorology* **135**(3), 407–432.
- Eden, P. (2012), ‘Monthly Weather Log: 201210’, *Weather* **67**(12), i–iv.
- Eden, P. (2013a), ‘Monthly Weather Log: 201306’, *Weather* **68**(8), i–iv.
- Eden, P. (2013b), ‘Monthly Weather Log: 201307’, *Weather* **68**(9), i–iv.
- EUROCAE (2008), Minimum Operational Performance Specification for Secondary Surveillance Radar Mode-S Transponders: Document ED-73C, Technical report, The European Organisation for Civil Aviation Equipment.
- Flyvbjerg, H. & Petersen, H. G. (1989), ‘Error estimates on averages of correlated data’, *The Journal of Chemical Physics* **91**(1), 461–466.
- Fowler, A., Bannister, R. & Eyre, J. (2012), ‘A new floating model level scheme for the assimilation of boundary-layer top inversions: the univariate assimilation of temperature’, *Quarterly Journal of the Royal Meteorological Society* **138**(664), 682–698.
- Fowler, A. M. (2010), The assimilation of misplaced boundary layer features. PhD Thesis., PhD thesis, University of Reading.
- Frehlich, R. (2011), ‘The definition of ‘truth’ for Numerical Weather Prediction error statistics’, *Quarterly Journal of the Royal Meteorological Society* **137**(654), 84–98.
- Fujita, T. T. (1986), Mesoscale classifications: their history and their application to forecasting, in P. Ray, ed., ‘Mesoscale meteorology and forecasting’, Springer, pp. 18–35.
- Golding, B., Clark, P. & May, B. (2005), ‘The Boscastle flood: Meteorological analysis of the conditions leading to flooding on 16 August 2004’, *Weather* **60**(8), 230–235.

- Golding, B. W., Ballard, S. P., Mylne, K., Roberts, N., Saulter, A. and Wilson, C., Agnew, P., Davis, L. S., Trice, J., Jones, C. et al. (2013), ‘Forecasting Capabilities For The London 2012 Olympics’, *Bulletin of the American Meteorological Society* .
- Grahame, N., Riddaway, B., Eadie, A., Hall, B. & McCallum, E. (2009), ‘Exceptional hailstorm hits Ottery St Mary on 30 October 2008’, *Weather* **64**(10), 255–263.
- Hagelin, S., Auger, L., Brovelli, P. & Dupont, O. (2014), ‘Nowcasting with the AROME Model: First Results from the High-Resolution AROME Airport’, *Weather and Forecasting* **29**(4), 773–787.
- Hall, C. (1992), ‘The use of output from a numerical model to monitor the quality of radiosonde observations.’, *Meteorological Magazine* **121**, 91–99.
- Hernandez-Carrascal, A. & Bormann, N. (2014), ‘Atmospheric Motion Vectors from Model Simulations. Part II: Interpretation as Spatial and Vertical Averages of Wind and Role of Clouds’, *Journal of Applied Meteorology and Climatology* **53**(1), 65–82.
- Hirahara, Y., J. I. & Ishimizu, T. (2011), ‘Trial operation of the Local Forecast Model at JMA’, *CAS/JSC WGNE Res. Activ. Atmos. Oceanic Modell.*, *41*, 0511-0512 .
- Hoel, P. (1984), *Introduction to mathematical statistics*, Wiley series in probability and mathematical statistics, Wiley.
- Hollingsworth, A., Shaw, D. B., Lonnberg, P., Illari, L., Arpe, K. & Simmons, A. J. (1986), ‘Monitoring of Observation and Analysis Quality by a Data Assimilation System’, *Monthly Weather Review* **114**(5), 861–879.
- Horowitz, P. & Hill, W. (2015), *The Art of Electronics*, Cambridge University Press.
- Houghton, E. & Carpenter, P. (2003), *Aerodynamics For Engineering Students*, Elsevier Science.
- ICAO (1993), Manual of the ICAO Standard Atmosphere: Extended to 80 Kilometres (262 500 Feet) Third Edition, Technical Report Doc 7488-CD, International Civil Aviation Organisation.
- ICAO (2010), Annex 10 to the Convention on International Civil Aviation Aeronautical Telecommunications Volume IV Surveillance radar and Collision Avoidance Systems Ed 5, Technical report, International Civil Aviation Organisation.
- ICAO (2012), Technical Provisions for Mode S Services and Extended Squitter, Technical Report Doc 9871, International Civil Aviation Organisation.

- Ingleby, B. & Edwards, D. (2015), ‘Changes to radiosonde reports and their processing for numerical weather prediction’, *Atmospheric Science Letters* **16**(1), 44–49.
- Ingleby, N. B. & Lorenc, A. C. (1993), ‘Bayesian quality control using multivariate normal distributions’, *Quarterly Journal of the Royal Meteorological Society* **119**(513), 1195–1225.
- Inness, P. & Dorling, S. (2012), *Operational Weather Forecasting*, Advancing Weather and Climate Science, Wiley.
- Jacobs, N. A., Mulally, D. J. & Anderson, A. K. (2014), ‘Correction of Flux Valve-Based Heading for Improvement of Aircraft Wind Observations’, *Journal of Atmospheric and Oceanic Technology* .
- Jacobs, W., Nietosvaara, V., Bott, A., Bendix, J., Cermak, J., Michaelides, S. & Gultepe, I. (2008), *EUR 22978 COST Action 722 Earth System Science and Environmental Management Short range forecasting methods of fog, visibility and low clouds.*, Office for Official Publications of the European Communities.
- Jacobs, W., Nietosvaara, V., Michaelides, S. C. & Gmoser, H. (2005), *EUR 21451 COST Action 722 Short-range Forecasting Methods of Fog, Visibility and Low Clouds - Phase I Report*, Office for Official Publications of the European Communities.
- Jolliffe, I. T. & Stephenson, D. B. (2012), *Forecast Verification: A Practitioner’s Guide In Atmospheric Science*, John Wiley & Sons.
- Jones, C. D. & Macpherson, B. (1997), ‘A latent heat nudging scheme for the assimilation of precipitation data into an operational mesoscale model’, *Meteorological Applications* **4**(3), 269–277.
- Kahl, J. D. (1990), ‘Characteristics of the low level temperature inversion along the Alaskan Arctic coast’, *International Journal of Climatology* **10**(5), 537–548.
- Kalman, R. E. (1960), ‘A New Approach to Linear Filtering and Prediction Problems’, *Transactions of the ASME—Journal of Basic Engineering* **82**(Series D), 35–45.
- Kalnay, E. (2003), *Atmospheric Modeling, Data Assimilation And Predictability*, Cambridge University Press, New York.
- Kim, P. & Huh, L. (2011), *Kalman Filter for Beginners: With MATLAB Examples*, CreateSpace Independent Publishing Platform.

- Kitchen, M. (2012*a*), Observations Research and Development Seminar: Upper Air Observations, Technical report, Met Office.
- Kitchen, M. (2012*b*), Provision of High Resolution Observations over the UK, Met office science advisory committee, Met Office.
- Lange, H. & Janjic, T. (2016), ‘Assimilation of Mode-S EHS Aircraft Observations in COSMO-KENDA’, *Monthly Weather Review* .
- Lawson, R. P. & Cooper, W. A. (1990), ‘Performance Of Some Airborne Thermometers In Clouds’, *Journal of Atmospheric and Oceanic Technology* **7**(3), 480–494.
- Lean, H. W., Clark, P. A., Dixon, M., Roberts, N. M., Fitch, A., Forbes, R. & Halliwell, C. (2008), ‘Characteristics of High-Resolution Versions of the Met Office Unified Model for Forecasting Convection over the United Kingdom’, *Monthly Weather Review* **136**(9), 3408–3424.
- Lenschow, D. H. & Stankov, B. B. (1986), ‘Length Scales in the Convective Boundary Layer’, *Journal of the Atmospheric Sciences* **43**(12), 1198–1209.
- Leon, D. C., French, J. R., Lasher-Trapp, S., Blyth, A. M., Abel, S. J., Ballard, S., Barrett, A., Bennett, L. J., Bower, K., Brooks, B., Brown, P., Charlton-Perez, C., Chouarton, T., Clark, P., Collier, C., Crosier, J., Cui, Z., Dey, S., Dufton, D., Eagle, C., Flynn, M. J., Gallagher, M., Halliwell, C., Hanley, K., Hawkness-Smith, L., Huang, Y., Kelly, G., Kitchen, M., Korolev, A., Lean, H., Liu, Z., Marsham, J., Moser, D., Nicol, J., Norton, E. G., Plummer, D., Price, J., Ricketts, H., Roberts, N., Rosenberg, P. D., Simonin, D., Taylor, J. W., Warren, R., Williams, P. I. & Young, G. (2015), ‘The CONvective Precipitation Experiment (COPE): Investigating the origins of heavy precipitation in the southwestern UK’, *Bulletin of the American Meteorological Society* .
- Lindskog, M., Gustafsson, N., Navascués, B., Mogensen, K. S., Huang, X.-Y., Yang, X., Andrae, U., Berre, L., Thorsteinsson, S. & Rantakokko, J. (2001), ‘Three-dimensional variational data assimilation for a limited area model. Part II: Observation handling and assimilation experiments’, *Tellus A* **53**(4), 447–468.
- Lock, A. P., Brown, A. R., Bush, M. R., Martin, G. M. & Smith, R. N. B. (2000), ‘A New Boundary Layer Mixing Scheme. Part I: Scheme Description and Single-Column Model Tests’, *Monthly Weather Review* **128**(9), 3187–3199.
- Lorenc, A. C. (1981), ‘A Global Three-Dimensional Multivariate Statistical Interpolation Scheme’, *Monthly Weather Review* **109**(109), 701–721.

- Lorenc, A. C. (1986), ‘Analysis methods for numerical weather prediction’, *Quarterly Journal of the Royal Meteorological Society* **112**(474), 1177–1194.
- Lorenc, A. C., Ballard, S. P., Bell, R. S., Ingleby, N. B., Andrews, P. L. F., Barker, D. M., Bray, J. R., Clayton, A. M., Dalby, T., Li, D., Payne, T. J. & Saunders, F. W. (2000), ‘The Met. Office global three-dimensional variational data assimilation scheme’, *Quarterly Journal of the Royal Meteorological Society* **126**(570), 2991–3012.
- Lorenc, A. C. & Rawlins, F. (2005), ‘Why does 4D-Var beat 3D-Var?’, *Quarterly Journal of the Royal Meteorological Society* **131**(613), 3247–3257.
- Lorenz, E. N. (1963), ‘Deterministic Nonperiodic Flow’, *Journal of the Atmospheric Sciences* **20**(2), 130–141.
- Mahashabde, A., Wolfe, P., Ashok, A., Dorbian, C., He, Q., Fan, A., Lukachko, S., Mozdzanowska, A., Wollersheim, C., Barrett, S. R., Locke, M. & Waitz, I. A. (2011), ‘Assessing the environmental impacts of aircraft noise and emissions’, *Progress in Aerospace Sciences* **47**(1), 15 – 52.
- Malcher, J. & Kraus, H. (1983), ‘Low-level jet phenomena described by an integrated dynamical PBL model’, *Boundary-Layer Meteorology* **27**(4), 327–343.
- Markovic, D., Hauf, T., Rhner, P. & Spehr, U. (2008), ‘A statistical study of the weather impact on punctuality at Frankfurt Airport’, *Meteorological Applications* **15**(2), 293–303.
- Maus, S., Macmillan, S., McLean, S., Hamilton, B., Thomson, A., Nair, M. & Rollins, C. (2010), The US/UK World Magnetic Model for 2010-2015, NOAA Technical Report NESDIS/NGDC, Technical report, British Geological Survey.
- Met Office (2011), Fact sheet No. 11 - Interpreting weather charts, Technical report, National Meteorological Library and Archive.
- Met Office (2012), Daily Weather Summaries 2012, Technical report, National Meteorological Library and Archive, Met Office.
- Met Office (2015*a*), Daily Weather Summaries 2015, Technical report, National Meteorological Library and Archive, Met Office.
- Met Office (2015*b*), High Resolution Radiosonde Reports., Technical report, National Meteorological Library and Archive.

- Mirza, A. K., Ballard, S. P., Dance, S. L., Maisey, P., Rooney, G. G. & Stone, E. K. (2016), 'Comparison of aircraft derived observations with in situ research aircraft measurements', *Quarterly Journal of the Royal Meteorological Society* .
- Montmerle, T. (2016), Statement of Guidance for High Resolution Numerical Weather Prediction, Technical report, ET- EGOS -7, World Meteorological Organisation.
- Moyna, B., Lee, C., Charlton, J., Rule, I., King, R., M, O. & Kangas, V. (2010), 'IS-MAR: Towards a Sub Millimetre-Wave Airborne Demonstrator for the Observation of Precipitation and Ice Clouds'.
- Mulally, D. & Anderson, A. (2011), Correction of Aircraft Flux Valve Based Heading for Two-Dimensional Winds Aloft Calculations Using Weather Model Comparisons, *in* '15th Symposium on Integrated Observing and Assimilation Systems for Atmosphere, Oceans, and Land Surface (IOAS-AOLS)'.
- Nakamura, D. (2013), 'Magnetic Variation Review and Recommendations', *Performance Based Operations, Aviation Rulemaking Committee, Federal Aviation Administration* . Last accessed 2015-10-14.
- Nicholls, S. (1980), The Measurement Of Flight Level Wind And Aircraft Position By The MRF Hercules, Technical report, Meteorological Research Flight - Farnborough, Meteorological Office, United Kingdom. MRF Internal Note No. 9.
- Oldham, K., Myland, J. & Spanier, J. (2010), *An Atlas of Functions: with Equator, the Atlas Function Calculator*, An Atlas of Functions, Springer New York.
- Orlanski, I. (1975), 'A Rational Subdivision Of Scales For Atmospheric Processes', *Bulletin of the American Meteorological Society* **56**, 527–530.
- Painting, C. (2003), *Aircraft Meteorological Data Relay (AMDAR) Reference Manual*, wmo no. 958 edn, World Meteorological Organisation, Secretariat of the World Meteorological Organization, Geneva, Switzerland.
- Pelgrom, M. (2017), *Analog-to-Digital Conversion - 3rd Edition*, Springer International Publishing.
- Petersen, R. A., Crouce, L., Mamrosh, R., Baker, R. & Pauley, P. (2016), 'On the Impact and Future Benefits of AMDAR Observations in Operational Forecasting: Part II: Water Vapor Observations', *Bulletin of the American Meteorological Society* **97**(11), 2117–2133.

- Petersen, R. A., Manikin, G. & Keyser, D. (2004), Summary of Impact Tests of Automated Wind / Temperature Reports from Commercial Aircraft., *in* H. Böttger, P. Menzel & J. Pailleux, eds, ‘Proceedings of the Third WMO Workshop on the Impact of Various Observing Systems on Numerical Weather Prediction.’, Vol. WMO/TD No. 1228, pp. 298–307.
- Petersen, R. A. & Moninger, W. R. (2006), ‘Assessing Two Different Commercial Aircraft-based Sensing Systems’, *10th Symposium on Integrated Observing and Assimilation Systems for Atmosphere, Oceans, and Land Surface* .
- Piccolo, C. & Cullen, M. (2011), ‘Adaptive mesh method in the Met Office variational data assimilation system’, *Quarterly Journal of the Royal Meteorological Society* **137**(656), 631–640.
- Prichard, B. (2015), ‘Weather Summaries January 2015’, *Weather* **70**(3), i–iv.
- Reitebuch, O. (2012), *The Spaceborne Wind Lidar Mission ADM-Aeolus*, Springer Berlin Heidelberg, Berlin, Heidelberg, pp. 815–827.
- Reitebuch, O., Lemmerz, C., Nagel, E., Paffrath, U., Durand, Y., Endemann, M., Fabre, F. & Chaloupy, M. (2009), ‘The Airborne Demonstrator for the Direct-Detection Doppler Wind Lidar ALADIN on ADM-Aeolus. Part I: Instrument Design and Comparison to Satellite Instrument’, *Journal of Atmospheric and Oceanic Technology* **26**(12), 2501–2515.
- Rennie, S. J., Dance, S. L., Illingworth, A. J., Ballard, S. P. & Simonin, D. (2011), ‘3D-Var Assimilation Of Insect-Derived Doppler Radar Radial Winds In Convective Cases Using A High-Resolution Model’, *Monthly Weather Review* **139**(4), 1148–1163.
- Renshaw, R. & Francis, P. N. (2011), ‘Variational assimilation of cloud fraction in the operational Met Office Unified Model’, *Quarterly Journal of the Royal Meteorological Society* **137**(661), 1963–1974.
- Roach, W. T. (1994), ‘Back to basics: Fog: Part 1 — Definitions and basic physics’, *Weather* **49**(12), 411–415.
- Roach, W. T. (1995a), ‘Back to basics: Fog: Part 2 — The formation and dissipation of land fog’, *Weather* **50**(1), 7–11.
- Roach, W. T. (1995b), ‘Back to basics: Fog: Part 3 — The formation and dissipation of sea fog.’, *Weather* **50**(3), 80–84.

- Roach, W. T., Brown, R., Caughey, S. J., Garland, J. A. & Readings, C. J. (1976), 'The physics of radiation fog: I – a field study', *Quarterly Journal of the Royal Meteorological Society* **102**(432), 313–333.
- Ross, S. M. (2009), *Introduction to Probability and Statistics for Engineers and Scientists*, Fourth edn, Academic Press, Boston.
- Saito, K., Fujita, T., Yamada, Y., Ishida, J.-i., Kumagai, Y., Aranami, K., Ohmori, S., Nagasawa, R., Kumagai, S., Muroi, C., Kato, T., Eito, H. & Yamazaki, Y. (2006), 'The Operational JMA Nonhydrostatic Mesoscale Model', *Monthly Weather Review* **134**(4), 1266–1298.
- Schmelling, M. (1995), 'Averaging correlated data', *Physica Scripta* **51**(6), 676.
- Schraff, C., Reich, H., Rhodin, A., Schomburg, A., Stephan, K., Perianez, A. & Potthast, R. (2016), 'Kilometre-scale ensemble data assimilation for the COSMO model (KENDA)', *Quarterly Journal of the Royal Meteorological Society* .
- Schwartz, B. E. & Benjamin, S. (1995), 'A Comparison of Temperature and Wind Measurements from ACARS Equipped Aircraft and Rawinsondes', *Weather and Forecasting* **10**, 528–544.
- Seity, Y., Brousseau, P., Malardel, S., Hello, G., Banard, P., Bouttier, F., Lac, C. & Masson, V. (2011), 'The AROME France Convective-Scale Operational Model', *Monthly Weather Review* **139**(3), 976–991.
- Sharman, R. & Lane, T. (2016), *Aviation Turbulence: Processes, Detection, Prediction*, Springer International Publishing.
- Simonin, D., Ballard, S. P. & Li, Z. (2014), 'Doppler Radar Radial Wind Assimilation Using An Hourly Cycling 3D-Var With A 1.5 Km Resolution Version Of The Met Office Unified Model For Nowcasting', *Quarterly Journal of the Royal Meteorological Society* **140**(684), 2298–2314.
- Skamarock, W. C. & Klemp, J. B. (2008), 'A time-split nonhydrostatic atmospheric model for weather research and forecasting applications ', *Journal of Computational Physics* **227**(7), 3465–3485. Predicting weather, climate and extreme events.
- Smith, M. & Gratton, G. (2004), 'Facility for Airborne Atmospheric Measurements; Met Office; Natural Environment Research Council'.
- Spitzer, C. R. (2006), *Avionics: Elements, Software and Functions*, The Avionics Handbook, Second Edition, CRC Press.

- Staniforth, A. & Wood, N. (2008), ‘Aspects of the dynamical core of a nonhydrostatic, deep-atmosphere, unified weather and climate-prediction model’, *Journal of Computational Physics* **227**(7), 3445–3464.
- Stewart, L., Dance, S. & Nichols, N. (2013), ‘Data assimilation with correlated observation errors: experiments with a 1-D shallow water model’, *Tellus A* **65**(0).
- Stewart, L. M. (2010), Correlated observation errors in data assimilation., PhD thesis, University of Reading.
- Stickland, J. & Grooters, A. T. F. (2005), The Global AMDAR Programme, in ‘International Symposium on Remote Sensing of the Environment’, International Symposium on Remote Sensing of the Environment, St. Petersburg, Russian Federation.
- Stickney, T. M., Shedlov, M. W. & Thompson, D. I. (1994), Goodrich Total Temperature Sensors Technical Report 5755 Revision C, 1994, Technical report, Rosemount Aerospace Inc.
- Stone, E. K. & Kitchen, M. (2015), ‘Introducing an Approach for Extracting Temperature from Aircraft GNSS and Pressure Altitude Reports in ADS-B Messages’, *Journal of Atmospheric and Oceanic Technology* **32**(4), 736–743.
- Stone, E. K. & Pearce, G. (2016), ‘A Network of Mode-S Receivers for Routine Acquisition of Aircraft-Derived Meteorological Data’, *Journal of Atmospheric and Oceanic Technology* **33**(4), 757–768.
- Strajnar, B. (2012), ‘Validation Of Mode-S Meteorological Routine Air Report Aircraft Observations’, *Journal of Geophysical Research* **117**.
- Strajnar, B., Aagar, N. & Berre, L. (2015), ‘Impact of new aircraft observations Mode-S MRAR in a mesoscale NWP model’, *Journal of Geophysical Research: Atmospheres* **120**(9), 3920–3938.
- Strajnar, B. & Trojáková, A. (2015), Analysis and preprocessing of Czech Mode-S observations, Technical report, Czech Hydrometeorological Institute.
- Stull, R. (1988), *An Introduction to Boundary Layer Meteorology*, Atmospheric and Oceanographic Sciences Library, Kluwer Academic Publishers.
- Stull, R. (2000), *Meteorology for Scientists and Engineers*, Earth Science Series, Brooks Cole.

- Sun, J., Xue, M., Wilson, J. W., Zawadzki, I., Ballard, S. P., Onvlee-Hooimeyer, J., Joe, P., Barker, D. M., Li, P., Golding, B., Xu, M. & Pinto, J. (2014), ‘Use of NWP for Nowcasting Convective Precipitation’, *Bulletin of the American Meteorological Society* pp. 409–426.
- Talagrand, O. (1997), ‘Assimilation of Observations, an Introduction, Special Issue Data Assimilation in Meteorology and Oceanography: Theory and Practice’, *Journal of the Meteorological Society of Japan. Ser. II* **75**(1B), 191–209.
- Tang, Y., Lean, H. & Bornemann, J. (2013), ‘The Benefits of the Met Office Variable Resolution NWP Model for Forecasting Convection’, *Meteorological Applications* **20**, 417–426.
- Taylor, G. I. (1938), ‘The Spectrum of Turbulence’, *Proceedings of the Royal Society of London A: Mathematical, Physical and Engineering Sciences* **164**(919), 476–490.
- Taylor, J. R. (1982), *An Introduction to Error Analysis - The Study of Uncertainties in Physical Measurements*, 2nd edn, University Science Books, 55D Gate Five Road, Sausalito, CA 94965.
- Theodore, T. & Caracena, F. (1977), ‘An Analysis of Three Weather-Related Aircraft Accidents’, *Bulletin of the American Meteorological Society* **58**(11), 1164–1181.
- Thorpe, A. J. & Guymer, T. H. (1977), ‘The Nocturnal Jet’, *Quarterly Journal of the Royal Meteorological Society* **103**(438), 633–653.
- Tjernstram, M. & Friehe, C. A. (1991), ‘Analysis of a Radome Air-Motion System on a Twin-Jet Aircraft for Boundary-Layer Research’, *Journal of Atmospheric and Oceanic Technology* **8**(1), 19–40.
- Waller, J. A., Ballard, S. P., Dance, S. L., Nichols, N. K., Simonin, D. & Kelly, G. (2016b), ‘Diagnosing Horizontal and Inter-Channel Observation Error Correlations for SEVIRI Observations Using Observation-Minus-Background and Observation-Minus-Analysis Statistics’, *Journal of Remote Sensing* **8**(7), 581.
- Waller, J. A., Dance, S. L., Lawless, A. S., Nichols, N. K. & Eyre, J. R. (2014), ‘Representativity error for temperature and humidity using the Met Office high-resolution models’, *Quarterly Journal of the Royal Meteorological Society* **140**(681), 1189–1197.
- Waller, J. A., Dance, S. L. & Nichols, N. K. (2016), ‘Theoretical insight into diagnosing observation error correlations using observation-minus-background and observation-minus-analysis statistics.’, *Quarterly Journal of the Royal Meteorological Society* **142**(694), 418–431.

- Waller, J. A., Simonin, D., Dance, S. L., Nichols, N. K. & Ballard, S. P. (2016a), ‘Diagnosing observation error correlations for Doppler radar radial winds in the Met Office UKV model using observation-minus-background and observation-minus-analysis statistics’, *Monthly Weather Review* **144**(10), 3533–3551.
- Walpole, R. E., Myers, R. H., Myers, S. L. & Ye, K. (2011), *Probability & Statistics for Engineers & Scientists 9th Edition*, Pearson Education.
- Walters, D., Brooks, M., Boutle, I., Melvin, T., Stratton, R., Vosper, S., Wells, H., Williams, K., Wood, N., Allen, T., Bushell, A., Copsey, D., Earnshaw, P., Edwards, J., Gross, M., Hardiman, S., Harris, C., Heming, J., Klingaman, N., Levine, R., Manners, J., Martin, G., Milton, S., Mittermaier, M., Morcrette, C., Riddick, T., Roberts, M., Sanchez, C., Selwood, P., Stirling, A., Smith, C., Suri, D., Tennant, W., Vidale, P. L., Wilkinson, J., Willett, M., Woolnough, S. & Xavier, P. (2016), ‘The Met Office Unified Model Global Atmosphere 6.0/6.1 and JULES Global Land 6.0/6.1 configurations’, *Geoscientific Model Development Discussions* **2016**, 1–52.
- Weinstein, B. (2009), ‘Correcting the Effects of Magnetic Variation’, *Boeing AERO Magazine* .
- Weston, P. P., Bell, W. & Eyre, J. R. (2014), ‘Accounting for correlated error in the assimilation of high-resolution sounder data’, *Quarterly Journal of the Royal Meteorological Society* **140**(685), 2420–2429.
- Widrow, B., Kollar, I. & Liu, M. (1996), ‘Statistical theory of quantization’, *IEEE Transactions on Instrumentation and Measurement* **45**(2), 353–361.
- Wilks, D. S. (2011), *Statistical Methods in the Atmospheric Sciences 3rd Edition*, Vol. 100 of *International Geophysics Series*, Elsevier, Amsterdam.
- Woodfield, A. A. & Hayne, P. I. (1965), *C.P. No. 809 Ministry Of Aviation Aeronautical Research Council Current Papers Measurement of Air Temperature on an Aircraft Travelling at High Subsonic and Supersonic Speeds*, London:Her Majesty’s Stationery Office.
- Woolley, A. (2008a), GPS/Inertial Navigation unit installation test report. FAAM Core GPS-aided Inertial Navigation System, providing attitude, position and velocity data., Technical report, Facility for Airborne Atmospheric Measurements.
- Woolley, A. (2008b), Rosemount Temperature Data, Technical report, Facility for Airborne Atmospheric Measurements.

- Woolley, A. (2009), Temperature Instrumentation - Science Requirments Temperature Working Group Report 2008, Technical report, Facility for Airborne Atmospheric Measurements.
- Woolley, A. (2014*a*), FAAM - Aircraft horizontal wind vectors, Technical report, Facility for Airborne Atmospheric Measurements.
- Woolley, A. (2014*b*), FAAM Primary Systems, Technical report, Facility for Airborne Atmospheric Measurements.
- World Meteorological Organisation (2008), ‘Guide to Meteorological Instruments and Methods of Observation Seventh Edition (WMO-No. 8)’, *World Meteorological Organisation, Geneva, Switzerland* .
- Wright, D. J. (1986), ‘Forecasting Data Published at Irregular Time Intervals Using an Extension of Holt’s Method’, *Management Science* **32**(4), 499–510.